TU Delft

Delft University of Technology

Magnetostriction in 2D material nanomechanical resonators

Houmes, M.J.A.

DOI
10.4233/uuid:3af58913-06c6-4d8d-8e27-a5f75d34aadf

Publication date
2024

Document Version
Final published version

Citation (APA)
Houmes, M. J. A. (2024). *Magnetostriction in 2D material nanomechanical resonators*. [Dissertation (TU Delft), Delft University of Technology]. https://doi.org/10.4233/uuid:3af58913-06c6-4d8d-8e27-a5f75d34aadf

Important note
To cite this publication, please use the final published version (if applicable).
Please check the document version above.

Copyright
Other than for strictly personal use, it is not permitted to download, forward or distribute the text or part of it, without the consent of the author(s) and/or copyright holder(s), unless the work is under an open content license such as Creative Commons.

Takedown policy
Please contact us and provide details if you believe this document breaches copyrights.
We will remove access to the work immediately and investigate your claim.

This work is downloaded from Delft University of Technology.
For technical reasons the number of authors shown on this cover page is limited to a maximum of 10.

MAGNETOSTRICTION IN 2D MATERIAL NANOMECHANICAL RESONATORS

MAGNETOSTRICTION IN 2D MATERIAL NANOMECHANICAL RESONATORS

Proefschrift

ter verkrijging van de graad van doctor
aan de Technische Universiteit Delft,
op gezag van de Rector Magnificus prof. dr.ir. T. H. J. J. van der Hagen,
voorzitter van het College voor Promoties,
in het openbaar te verdedigen op

door

Maurits Jan Adriaan HOUMES

Master of Science, Physics,
Universiteit Leiden, Nederland,
geboren te Dordrecht, Nederland.

Dit proefschrift is goedgekeurd door de promoteren.

Samenstelling promotiecommissie:

Rector Magnificus,	voorzitter
Prof. Dr. P. G. Steeneken,	Technische Universiteit Delft, promotor
Prof. Dr. Ir. H. S. J. van der Zant,	Technische Universiteit Delft, promotor
Onafhankelijke leden:	
Prof. Dr. Y. M. Blanter,	Technische Universiteit Delft
Prof. Dr. G. A. Steele	Technische Universiteit Delft
Prof. Dr. S. Berciaud	Université de Strasbourg
Dr. S. Bhattacharyya	Leiden University
Prof. Dr. K.I. Bolotin	Freie Universität Berlin

Keywords: Two-dimensional materials, nanomechanics, phase transition, membranes, resonance, NEMS, magnetic materials, anisotropy, laser interferometry.

Printed by: Proefschriftmaken

Front & Back: A $CoPS_3$ crystal lattice deforming. Image: Maurits J.A. Houmes

Copyright © 2024 by M.J.A. Houmes

ISBN 978-94-6510-372-3

An electronic version of this dissertation is available at
http://repository.tudelft.nl/.

CONTENTS

SUMMARY

This thesis discusses several studies on magnetic two-dimensional (2D) materials, focusing on their nanomechanical properties and the behavior of resonance frequencies in response to temperature changes. These studies employ nanomechanical resonators, specifically suspended membranes (drum resonators) of 2D magnetic materials. The frequency response of these resonators is measured using optical excitation combined with an interferometric setup, allowing identification of resonance frequencies.

By altering the temperature of the resonators, the resonance frequency shifts as the strain within the 2D material changes. This strain change is partially magnetostrictive in origin due to changes in the magnetic order within the materials, offering a method to study these magnetic characteristics.

Chapter 1 introduces two-dimensional materials and the nanomechanical techniques used in this thesis, while Chapter 2 provides a theoretical foundation for the mechanics of the resonators and the coupling between the mechanics and the magnetic order.

Chapters 3 and 4 present findings from studies on $FePS_3$, $CoPS_3$, $NiPS_3$, and $CrPS_4$. The anisotropic nature of the coupling between the magnetic order and the crystalline lattice in these materials allows for the extraction of magnetic order behavior from the resonators' responses.

Chapter 5 examines how optothermal modulation of drum resonators in magnetic 2D materials can enhance drive efficiency, particularly near the transition temperature due to magnetostrictive coupling effects.

Chapter 6 explores the nonlinear behavior observed in a $FePS_3$-based drum resonator, showing that near the transition temperature, nonlinear response and the nonlinear damping is significantly influenced by a time delay between the magnetic and lattice responses.

SAMENVATTING

Dit proefschrift behandelt enkele onderzoeken naar magnetische tweedimensionale (2D) materialen, met de focus op hun nanomechanische eigenschappen en het gedrag van resonantiefrequenties als functie van temperatuur. Deze onderzoeken maken gebruik van nanomechanische resonatoren, specifiek vrijhangende membranen (drumresonatoren) van 2D magnetische materialen. De frequentierespons van deze resonatoren wordt gemeten met behulp van optische excitatie in combinatie met een interferometrische detectie, waarmee de resonantiefrequenties kunnen worden geïdentificeerd.

Door de temperatuur van de resonatoren te veranderen, verschuift de resonantiefrequentie, doordat de deformatie binnen het 2D-materiaal verandert. Deze spanningsverandering is gedeeltelijk magnetostrictief in oorsprong door de veranderingen in de magnetische orde in de materialen. Dit biedt een methode om de magnetische eigenschappen te bestuderen.

Hoofdstuk 1 introduceert tweedimensionale materialen en de nanomechanische technieken die in dit proefschrift worden gebruikt. Hoofdstuk 2 biedt een theoretische basis voor de mechanica van de resonatoren en de koppeling tussen de mechanica en de magnetische orde.

Hoofdstukken 3 en 4 presenteren resultaten van studies over $FePS_3$, $CoPS_3$, $NiPS_3$ en $CrPS_4$. De anisotrope aard van de koppeling tussen de magnetische orde en het kristalrooster in deze materialen maakt het mogelijk om het gedrag van de magnetische orde uit de respons van de resonatoren af te leiden.

Hoofdstuk 5 onderzoekt hoe optothermische modulatie van drumresonatoren in magnetische 2D-materialen de efficiëntie van excitatie kan verbeteren, vooral dichtbij de overgangstemperatuur, door magnetostrictieve koppelingseffecten.

Hoofdstuk 6 bespreekt niet-lineair gedrag waargenomen in $FePS_3$ drumresonatoren, en laat zien dat nabij de overgangstemperatuur de niet-lineaire respons en de niet-lineaire demping aanzienlijk worden beïnvloed door een tijdsvertraging tussen de magnetische en roosterresponsen.

1

INTRODUCTION

If I have seen further, it is by standing on the shoulders of giants.

- Isaac Newton

1

ERAS in history are often categorised by the capability of a civilisation to produce and utilise materials. This categorisation is clear in the case of the Stone, Bronze, and Iron Age, continuing to the modern era, which is often referred to as the Silicon or Semiconductor Age. The reason for this categorisation is intuitive: the tools, vehicles, and buildings a civilisation creates are limited in strength to that of the strongest material it has access to. Thus, the study of materials forms a foundational pillar for societal advancement. Material research broadly consists of three main areas: theory, fabrication, and characterisation. This thesis focuses on the latter, specifically on developing and applying a method for characterising two-dimensional (2D) materials. This chapter introduces the relevant context for subsequent chapters, beginning with an overview of 2D materials, a class that includes the strongest known material, graphene.

1.1. 2D MATERIALS

Two-dimensional materials, also known as van der Waals (vdW) materials[1], are crystalline materials consisting of strongly bound layers that are stacked on top of one another, held together by the relatively weak vdW forces. This weak interlayer binding allows for cleaving, or exfoliation, essentially peeling off one or a few layers at a time. This process enables the isolation and study of individual layers, revealing some of their properties to be distinct to those of the bulk material. Many material properties differ significantly between 3D and 2D systems and it remains an open question exactly how and where the transition between these two regimes occurs. For instance, the theoretical behaviour of magnetic phases varies significantly between 3D and 2D systems (see section 1.2).

Before the isolation of graphene in 2004 [1], it was believed that 2D materials could not to exist in a free form because thermal fluctuations would cause any sheet to crumple or deform to a 3D structure, such as nanotubes [1]. However when stabilised by a substrate or by boundary clamping, these sheets can maintain their 2D structure, providing an opportunity to investigate vdW materials in their 2D limit.

Since 2004, there has been a large research effort around 2D materials. Following graphene, many other materials have become available, such as hexagonal boron nitride (hBN), transition metal dichalcogenides (TMDs), Xenes, and metal thiophosphates. These research efforts generally focus on either *material science*, *fabrication* and *applications*. This thesis primarily contributes to the field of material science, but it will also briefly discuss aspects of fabrication and applications relevant to this work.

1.1.1. MATERIAL SCIENCE

From a material science perspective 2D materials provide a highly intriguing platform for research. The ability to fabricate different layers from various materials and stack them together allows for a bottom-up approach to building materials. Each material in the stack contributes different properties to the composite structure, enabling a certain

[1] Definition in literature sometimes describes van der Waals materials as a strict subset of 2D materials. Grouping any a single unit cell thick system, such as a one unit cell thick film of complex oxide, together with 2D materials . Throughout this thesis we will not make this distinction and use the terms 2D and vdW materials interchangeably.

level of control over the resulting material properties. In some cases, the interactions between the different layers may even give rise to new physics not present in either layer (or their bulk variant) separately [2]. This control and the potential to explore new physics, makes 2D materials an excellent platform for material science research.

Most of the fundamental[2] research on 2D materials uses either a form of electrical transport measurements (e.g, Hall measurements or transistor structures) or optical probing (e.g., MOKE or ARPES experiments). These studies, as is the case for most condensed matter physics experiments, typically explore the behaviour of (quasi-)particles, such as electrons, Cooper pairs, phonons, excitons, plasmons, and magnons and their interactions. The emphasis is often put on understanding the behaviour of these systems from the perspective of the band structure of electrons and is then discussed in terms of a single or few particle picture. To isolate these few particle behaviours, the field relies on cooling systems to cryogenic temperatures to minimize thermal population of excited states, which could obscure the observations.

The work in this thesis deviates somewhat from this traditional approach by focusing on larger ensembles and predominantly considering them from a classical perspective. Commonly researchers working with 2D materials are concerned with imperfections such as crystal defects and doping as they have a significant impact on their measurements. However for the mechanical measurements in this thesis contribution from such imperfections are small.[3] Of course if defect densities get large enough their contribution should be taken into account [3].

In nanomechanical structures a role equivalent to crystal defects for transport measurements is played by strain related imperfections such as wrinkles, ripples, non-uniform strains, and geometrical defects like partially covered holes, cracks or steps. These defects often result from the transfer process and are difficult to control or even reproduce, providing the main source of the sample-to-sample variability in the studies presented in this thesis [4]. Thus, the fabrication significantly influences the final properties and behaviour of the 2D materials. Understanding and optimizing both crystal growth and transfer techniques are essential for achieving consistent, high-quality samples. The next subsection discusses the fabrication methods for 2D materials samples, focusing on crystal growth and the transfer process.

1.1.2. FABRICATION

Under the term fabrication as it pertains to 2D materials, there are broadly two categories: material fabrication and device fabrication. Material fabrication focuses on finding and growing 2D material crystals, while device fabrication deals with shaping these crystals into desired geometries. This thesis primarily utilises the resulting materials without engaging in the material fabrication process itself; therefore, we will not delve into that aspect in detail [5–7].

Device fabrication consists of broadly two approaches: bottom-up or top-down. A bottom-up approach involves growing and stacking individual layers of the desired ma-

[2] Here meaning: not fabrication or application focused.

[3] Although the contribution of such crystal defects has not been specifically quantified they are expected to be present in the samples. However measured data can be reasonably well explained without accounting for such defects indicating they do not significantly contribute to the observed phenomena.

terial into a specific geometry. A top-down approach starts from a bulk crystal and thins this down to the desired thicknesses. Both approaches have their respective challenges and benefits and are in practise often used congruently. The samples in this work utilise a mostly top-down approach, where thin layers obtained from bulk crystals are transferred and stacked onto a target substrate (see section 1.4.1).

1.1.3. APPLICATIONS

Since the isolation of graphene, there has been a surge in potential applications for it and other 2D materials. For graphene alone, one can find wide range of applications at several stages of development, including material additives, conductive inks, coatings, and sensors. Examples of the latter include biosensors based on functionalised graphene, pressure and gas sensors, microphones, and graphene-based hall sensors [8–11]. Beyond graphene, there are several examples of applications involving other 2D materials, for instance metal dicalcogenide gas and electrochemical sensors, demonstrating the versatility and potential of these materials [12, 13].

The aforementioned examples are not exhaustive but highlight the significant potential of 2D materials. Another field where 2D materials could provide the material platform for future devices is that of spintronics, which focuses on using spin degrees of freedom for information storage and transfer. This can have the benefit of faster computing and eliminating Joule heating as pathway of energy loss. This could result in substantial energy saving, particularly given the increasing computational demands from increased automation and usage of artificial intelligence (AI).

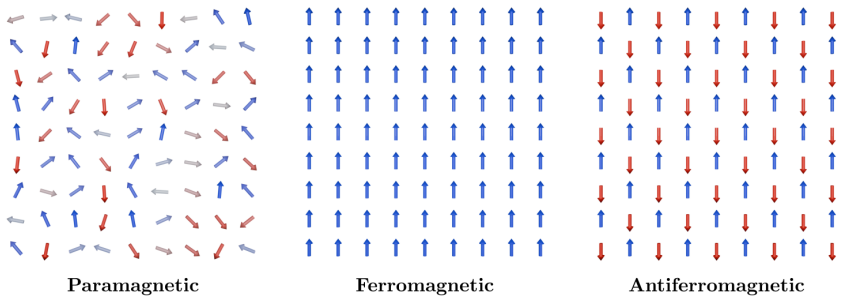

Figure 1.1: **Magnetic ordering.** From left to right are depicted examples of spin orientations corresponding to a paramagnetic, ferromagnetic, and antiferromagnetic system respectively.

1.2. MAGNETISM

Magnetism is the the property of a material to have an intrinsic ordered magnetic field. This requires interaction between its magnetic components, namely its spins. Generally, materials are split into three types of magnetism: non-magnetic (also called paramagnetic), ferromagnetic, and antiferromagnetic.[4] The difference between these categories

[4] This categorisation could be further refined to smaller categories such as ferri-magnetism or the recently introduced altermagnetism [14], but the three mentioned categories will be enough for this work.

lies in the nature of the spin coupling and the resulting magnetic structure, as shown in figure 1.1, which can be significantly more complex than these basic types. While a comprehensive discussion of magnetism is far beyond the scope of this thesis, an overview of the relevant theory is provided in chapter 2. For a more detailed discussion, readers are referred to [15].

1.2.1. MAGNETIC 2D MATERIALS

Historically, it was believed that 2D materials could not host magnetic order because thermal fluctuations were expected to destroy long range magnetic order at non-zero temperatures [16, 17]. However, since the discovery of $FePS_3$, the first magnetic 2D material, many more have been identified, demonstrating that 2D materials can indeed exhibit a variety of magnetic orders [18].

This diversity of magnetic 2D materials provides a fertile ground to explore several open questions, such as how the magnetic order of a system changes when going from the 3D to 2D limit. Or how the external interactions affect 2D magnetic systems, such as when several 2D magnets are stacked atop each other. Furthermore, by combining magnetic 2D materials with other 2D materials allows access new material regimes otherwise inaccessible [19].

Despite their potential, 2D magnetic materials pose unique challenges, particularly in their characterisation. These materials tend to be insulating or semi-conducting, limiting the utility of electrical transport measurements. Traditional methods for characterizing magnetic systems often fail to achieve the necessary signal-to-noise ratio (SNR) due to the low volume of these materials. While optical methods can be more successful, they frequently encounter similar SNR problems due to limited thickness of the material, which restricts reflection and absorption and thus signal strength [20].

This thesis discusses a complementary method that utilises nanomechanical resonators to probe the magnetic phase transition in these materials. This approach offers a novel way to avoid the limitations of traditional characterization techniques, providing additional insights to the properties of magnetic 2D materials.

1.3. NANOMECHANICS

Nano-electromechanical systems (NEMS) and their larger counterparts, Micro-electromechanical systems (MEMS), have become ubiquitous in modern devices. They are found in a wide variety of applications, such as in mobile devices where they are used as gyroscopes, accelerometer, microphones, and speakers. In telecom networks, they are used as thin-film bulk acoustic resonators (FBARs) for filtering. These devices can often be described using classical mechanics. However, at the small scale of these devices, certain effects, such as stiction forces, often negligible at the macroscale need be considered. Since the relevance of such effects becomes significant at small scales, these devices also provide a platform to study these effects. One can think of contributions coming from material properties or thermodynamic effects that for macro systems are small or negligible.

Combining this with resonators that operate at higher frequencies and have higher quality factors, which can easily driven into non-linear regimes, results in very sensitive

sensors both to external stimuli as to internal (material) changes. Due to these high sensitivities, NEMS resonators form a natural platform to study 2D materials.

Particularly drum resonators, consisting of a thin layer of the 2D material suspended over a cavity, are interesting systems. The suspended nature of such resonators allows the 2D material to be isolated from external stimuli, such as a substrate, allowing for precise control and manipulation of their environment. Moreover, the mechanical vibrations of the drum resonator serve as sensitive probes, enabling the detection of subtle changes in the material properties. Such resonators are especially suited to study changes in strain, as the resonance frequency of these systems has a strong dependence on its strain. This is particular advantageous for the study of 2D materials, where strain is an important parameter. Strain has been shown to couple to electrical, magnetic, and thermal properties of these materials [21–23]. These couplings are generally reciprocal, meaning that small changes in any of these properties can induce a significant change in the strain in the system.

It is this coupling and sensitivity that lies at the heart of many results of the work discussed in this thesis. In the next section we will discuss the fabrication and measurement techniques used, and in chapter 2 we will discuss the underlying theory.

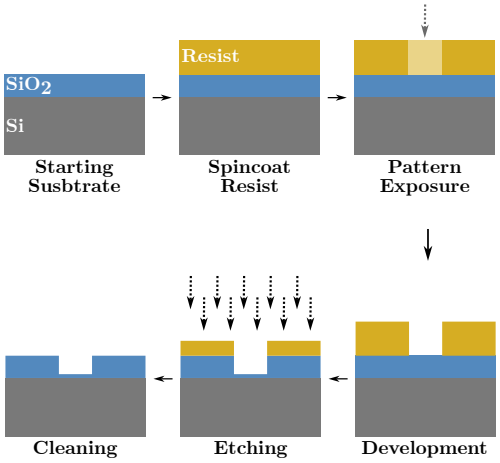

Figure 1.2: **Substrate fabrication.** The starting substrate consists of a highly doped silicon wafer with a thermally grown silicon-dioxide layer, typically 285 nm thick. Then a layer of resist is spin-coated onto the sample, the thickness of which is determined by the desired cavity depth and the relative etch rate when compared to SiO_2. During the exposure step the desired pattern is exposed. The sample is then submerged in a developer suited for the resist. This washes away the exposed area (in case of positive resit) exposing the SiO_2 layer. The sample is then placed in a reactive ion etcher and anisotropically etched until the desired cavity depth is reached, typically around 300 nm. After this, the remaining resist is cleaned off and the sample is ready for transfer.

1.4. METHODS

1.4.1. DEVICE FABRICATION

The fabrication of the substrates used in this thesis was developed by a former PhD candidate in the group, Martin Lee, and is discussed in [24]. To this recipe only minor changes are made to used parameters to compensate for the drift of machines over time and by making several updates to the exact layout of the design pattern, each with a corresponding dose test. Unless electrical contact was needed the steps to create embedded electrodes were skipped resulting in samples with only holes in the SiO2, with typical dimensions ranging from 2 to 10 μm in lateral size. The fabrication flow is depicted in figure 1.2.

The samples presented in this thesis were fabricated using a top-down approach. Starting from a bulk crystal a few layers are exfoliated and placed on a target substrate using a dry transfer technique [25, 26]. A dry transfer technique was chosen to avoid exposing the suspended structures to liquids, as previous experience has shown that the capillary and other surface forces present in a liquid are often strong enough to collapse suspended structures.

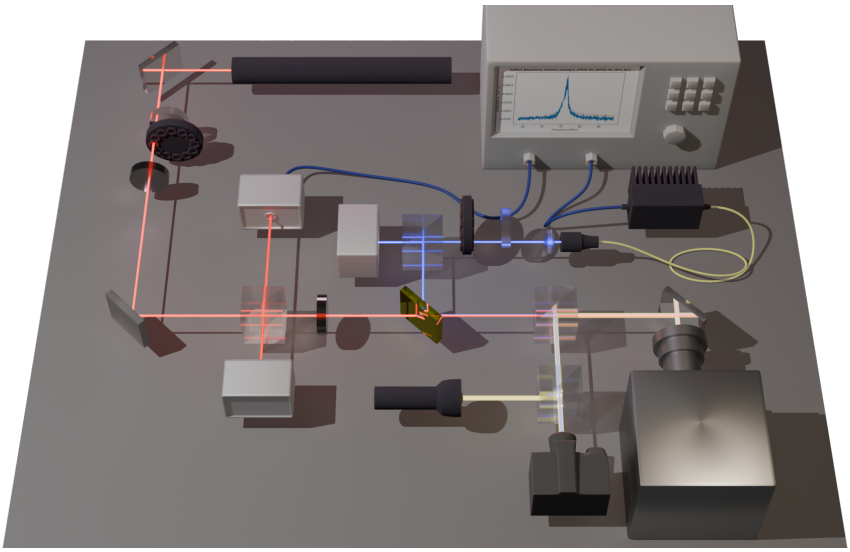

Figure 1.3: **3D impression of interferometry setup.** Shown are the basic components of interferometry setup. Visible are the 3 light paths, as explained in figures 1.4, 1.5, 1.6, and the cabling to and from the vector network analyser (blue cables) and the optical cable from the laser diode to the free-space coupler (yellow cable).

1.4.2. INTERFEROMETRY

Let's walk through the interferometers that form the basis of the results in this thesis. The work presented here combines results collected from two very similar setups. We will describe the general version of these setups, an impression of which is shown in figure 1.3, but the reader should keep in mind that small variations between them exist, both in the optical paths and in the exact equipment used. Where relevant, these variations

1

shall be highlighted. The interferometer consist of three light paths, referred to as red, blue, and white, corresponding with the red laser ($\lambda = 632$ nm), blue laser ($\lambda = 405$ nm) and the white light path.

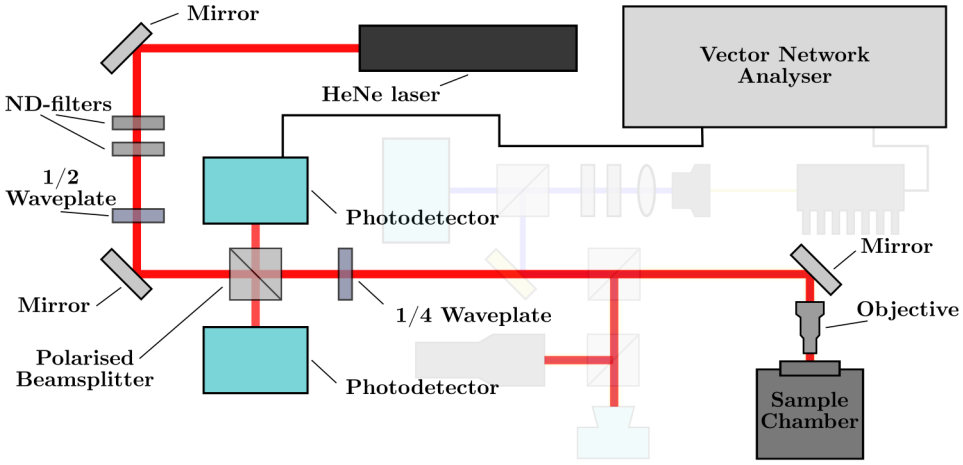

Figure 1.4: **Red laser path.** A schematic of the setup highlighting the components pertaining to the red laser path, see text for details.

RED

The red laser is used for the readout and is thus the most crucial part. It utilises interference effects to measure the membrane's response. As shown in figure 1.4, starting from the laser source, we use a HeNe laser because it provides a very stable laser source. This laser produces elliptically polarised laser light, which we first send through 2 neutral density filters (ND-filters) to reduce the intensity, preventing overheating of our samples to below an acceptable range, generally less than 0.5 K.

One of these ND-filters is a manual continuous density wheel, which is manually tuned to bring the intensity in the right order of magnitude. The second ND-filter is a filter wheel containing 12 different filter intensities, which can be computer controlled. Using two filters in conjunction allows for the manual wheel to be set initially and then use the filter wheel to achieve more repeatable intensity variations.

After intensity filtering, the laser passes through a half-wave plate to rotate its polarisation. This is done such that when the red light later passes through the polarised beamsplitter, the maximum intensity is directed towards the sample, optimizing the signal. The laser light then passes through the polarised beamsplitter, which splits the light beam based on the polarisation. One polarisation is send to the sample and the other is directed towards a photo detector that acts as a reference for the laser intensity.

The light directed towards the sample passes through a second waveplate to convert the now linear polarised light into circular polarised light, preventing unwanted effects coming from bifringent materials as well as ensuring that upon return from the sample the reflected signal is fully reflected towards the dection photodiode by the polarised

beamsplitter. The resulting circularly polarised light is then combined with the other light paths and directed into the sample chamber through an objective lens, focusing onto the sample. Upon interaction with the sample, the light is reflected back into the objective lens.

This reflected light passes back through the quarter waveplate converting it to linear polarisation. It then passes through the polarised beamsplitter and is reflected onto the measurement photodiode, which detects the reflected light intensity. This photodiode splits the intensity signal into a constant (low frequency) part and an oscillating (high frequency) component. The constant signal is used as a proxy for the overall reflection intensity and is used to optimize the position of the sample in the beam. The high frequency signal contains the information of the mechanical oscillating membrane and is fed into the Vector Network Analyser (VNA).

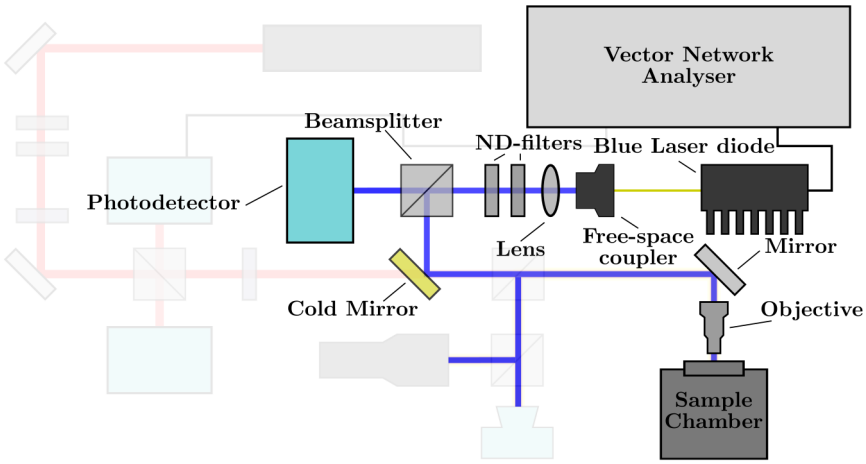

Figure 1.5: **Blue laser path.** A schematic of the setup with the components pertaining to the blue laser path highlighted, see text for details.

BLUE

The blue laser is used for driving the membranes; for cases where alternative driving is used, like electrostatic driving, the blue laser is not required. The output AC signal of the VNA is fed into the laser driver, where it is combined with a DC signal to regulate the intensity of the blue laser diode (see figure 1.5). The AC signal causes a intensity modulation on top of the DC-regulated intensity.

The laser diode is connected to an optical fiber which terminates in a free-space coupler mounted in an optomechanical mount, easing the aligning of the laser beam. Directly after the free-space coupler is a lens used to tune the focal plane of the blue laser to coincide with that of the red laser. The beam is then directed to two ND-filters: one manual continuous intensity wheel, and the second a discrete electronic filter wheel, similar to those used for the red laser.

After passing through the ND-filters, a reference beam is split off using a beamsplitter

and directed at a photodiode to serve as a intensity reference. The remaining beam is then directed onto a cold mirror, which is reflective for the blue laser but transparent for the red, allowing for combination of the beams. This cold mirror also ensures that any reflected blue laser light will not reach the final measurement diode, preventing an unwanted offset on top of the signal of interest.

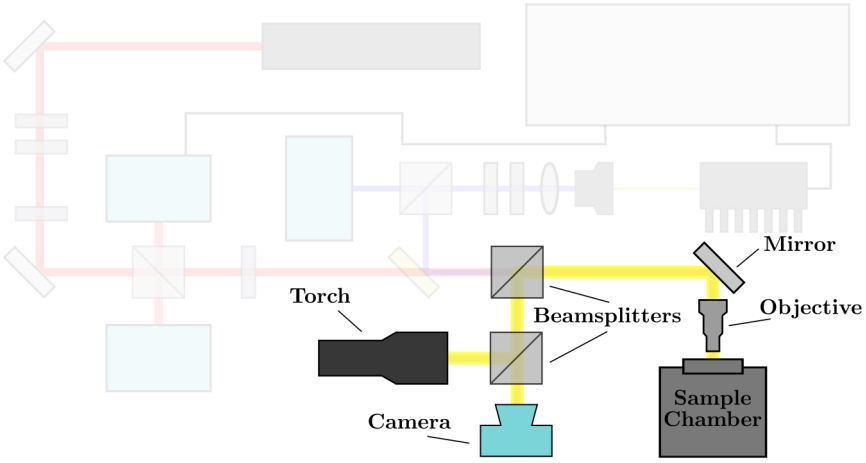

Figure 1.6: **White light path.** A schematic of the setup with the components pertaining to the white light path highlighted, see text for details. This section can be entirely bypassed by removing the top indicated beamsplitter, which is typically done during measurements.

WHITE

The white light serves as basic illumination for positioning of the sample. As shown in figure 1.6 a simple torch, modified to be powered by a voltage source for easy control, is used as the white light source. The voltage source allows for adjustment of the light intensity, and remote control of the torch.

The white light is combined with the laser beam paths using a beamsplitter and is focused onto the sample through the objective. The reflected signal is passed through the same beamsplitter and directed onto an off-the-shelf Canon camera without objective lens, providing visual feedback for the positioning of the sample. The camera's live feed is fed to the measurement PC and used to position the desired drum under the laser spot. After alignment the torch is turned off and the beamsplitter used for the white light is flipped out of the optical path to minimise loss of signal.

1.5. THESIS OUTLINE

Chapter 2 discusses the theory underlying coupling between the mechanics and magnetic order. Chapters 3 and chapter 4 present results of using anisotropy and mechanics to investigate magnetic 2D materials. Chapter 5 describes the effect of an additional actuation mechanism that is present in the magnetic phase. Chapter 6 investigates the effects of a magnetic phase transition on the behaviour of the drum resonators in the

non-linear regime. The references are listed at the end of each chapter and supplementary section as well as at the end of the thesis, the numbering is consistent through out the thesis, meaning that the same reference will have the same number in each chapter.

REFERENCES

1. Novoselov, K. S. *et al.* Electric Field Effect in Atomically Thin Carbon Films. *Science* **306,** 666–669 (Oct. 2004).
2. Novoselov, K. S., Mishchenko, A., Carvalho, A. & Neto, A. H. C. 2D materials and van der Waals heterostructures. *Science* **353,** aac9439 (2016).
3. López-Polín, G. *et al.* Increasing the elastic modulus of graphene by controlled defect creation. *Nature Physics* **11,** 26–31 (Jan. 2015).
4. Chen, W., Gui, X., Yang, L., Zhu, H. & Tang, Z. Wrinkling of two-dimensional materials: methods, properties and applications. *Nanoscale Horiz.* **4,** 291–320 (2019).
5. Gao, W., Zhi, G., Zhou, M. & Niu, T. Growth of Single Crystalline 2D Materials beyond Graphene on Non-metallic Substrates. *Small,* 2311317.
6. Dong, J., Zhang, L. & Ding, F. Kinetics of Graphene and 2D Materials Growth. *Advanced Materials* **31,** 1801583 (2019).
7. Geng, D. & Yang, H. Y. Recent Advances in Growth of Novel 2D Materials: Beyond Graphene and Transition Metal Dichalcogenides. *Advanced Materials* **30,** 1800865 (2018).
8. Sulleiro, M. V., Dominguez-Alfaro, A., Alegret, N., Silvestri, A. & Gómez, I. J. 2D Materials towards sensing technology: From fundamentals to applications. *Sensing and Bio-Sensing Research* **38,** 100540 (2022).
9. Yang, S., Jiang, C. & Wei, S.-h. Gas sensing in 2D materials. *Applied Physics Reviews* **4,** 021304 (May 2017).
10. Baglioni, G. *et al.* Ultra-sensitive graphene membranes for microphone applications. *Nanoscale* **15,** 6343–6352 (2023).
11. Guo, Y. *et al.* Review of the pressure sensor based on graphene and its derivatives. *Microelectronic Engineering* **288,** 112167 (2024).
12. Kim, Y. *et al.* Recent Advances in Functionalization and Hybridization of Two-Dimensional Transition Metal Dichalcogenide for Gas Sensor. *Adv. Eng. Mater.* **26,** 2301063 (2024).
13. Acosta, S. & Quintana, M. Chemically Functionalized 2D Transition Metal Dichalcogenides for Sensors. *Sensors* **24** (2024).
14. Šmejkal, L., Sinova, J. & Jungwirth, T. Beyond Conventional Ferromagnetism and Antiferromagnetism: A Phase with Nonrelativistic Spin and Crystal Rotation Symmetry. *Phys. Rev. X* **12,** 031042 (Sept. 2022).
15. Landau, L., Lifshitz, E. & Pitaevskii, L. *Electrodynamics of Continuous Media: Volume 8* (Elsevier Science, 1995).

16. Mermin, N. D. & Wagner, H. Absence of Ferromagnetism or Antiferromagnetism in One- or Two-Dimensional Isotropic Heisenberg Models. *Phys. Rev. Lett.* **17,** 1133 (Nov. 1966).

17. Hohenberg, P. C. Existence of Long-Range Order in One and Two Dimensions. *Phys. Rev.* **158,** 383–386 (June 1967).

18. Cortie, D. L. *et al.* Two-Dimensional Magnets: Forgotten History and Recent Progress towards Spintronic Applications. *Adv. Funct. Mater.* **30,** 1901414 (2020).

19. Ghiasi, T. S. *et al. Quantum Anomalous Hall and Spin Hall Effects in Magnetic Graphene* 2023. arXiv: 2312.07515 [cond-mat.mes-hall].

20. Yin, P., Lin, Q. & Duan, Y. Applications of Raman spectroscopy in two-dimensional materials. *Journal of Innovative Optical Health Sciences* **13,** 2030010 (2020).

21. Lee, M. *et al.* Study of charge density waves in suspended 2H-TaS_2 and 2H-$TaSe_2$ by nanomechanical resonance. *Appl. Phys. Lett.* **118,** 193105 (May 2021).

22. Šiškins, M. *et al.* Magnetic and electronic phase transitions probed by nanomechanical resonators. *Nat. Commun.* **11,** 2698 (June 2020).

23. Baglioni, G. *et al.* Thermo-Magnetostrictive Effect for Driving Antiferromagnetic Two-Dimensional Material Resonators. *Nano Lett.* **23,** 6973–6978 (2023).

24. Lee, M. *Applied and fundamental studies of vibrating 2D membranes* PhD thesis (Delft Univerisity of Technology, 2021).

25. Kim, C., Yoon, M.-A., Jang, B., Kim, J.-H. & Kim, K.-S. A Review on Transfer Process of Two-dimensional Materials. *Tribology and Lubricants* **36,** 1–10 (Feb. 2020).

26. Schranghamer, T. F., Sharma, M., Singh, R. & Das, S. Review and comparison of layer transfer methods for two-dimensional materials for emerging applications. *Chem. Soc. Rev.* **50,** 11032–11054 (2021).

2

THEORY

All models are wrong, but some are useful.

- George Box

In this chapter we will layout the theory from which the following chapters draw. Although the theory presented here can be found in numerous text books, such as [27] [28] and [15], it will be presented starting from rather basic definitions, for two reasons. Firstly for consistency, as everyone who used several sources to study a theory will know that notation and convention even at the level of definitions is not always consistent or compatible. Secondly, completeness the aim for this thesis is to be as self complete as possible, requiring the reader to look up little to no external references in order to follow the discussion. The definitions and theory are mostly based on [27] and [28]. This chapter will first discuss basic concepts from elasticity theory followed by the application of elasticity to thin structures to setup a plate theory. We will derive this plate theory from an energy perspective as it allows for an intuitive way to add couplings of other degrees of freedom to the elastic degrees of freedom, which we will use at the end of the chapter to couple the mechanical and magnetic degrees of freedom. The second part of the chapter will discuss Landau theory of magnetism, and the chapter concludes by linking the developed plate theory and theory of magnetism using magnetostriction.

2.1. ELASTICITY

When a force is applied to a material it deforms. There are two important regimes for these kinds of deformations, elastic and plastic. Elastic deformation means that upon removal of the force the material returns to it's original shape where as in plastic deformation the shape remains altered from the original shape even after the force is removed. For purposes of understanding the results in this thesis we can limit ourselves mostly to the elastic regime.

Elasticity revolves around describing deformation under forces, to construct a theory we will first introduce the mathemetical objects corresponding to each of these concepts. Deformation can be described using a displacement field, which we will denote $\boldsymbol{u}$. This is a vector valued field defined over the volume corresponding with the material in it's undeformed state, $V \subset \mathbb{R}^3$. Where the value of $\boldsymbol{u}(\boldsymbol{x})$ with $\boldsymbol{x} \in V$ is the vector connecting the initial point $\boldsymbol{x}$ with $\boldsymbol{x'}$ where $\boldsymbol{x'} \in V' \subset \mathbb{R}^3$ is the point that the volume of material at $\boldsymbol{x}$ moves to in the deformed state, such that $\boldsymbol{x} + \boldsymbol{u}(\boldsymbol{x}) = \boldsymbol{x'}$. Here V' corresponds to the volume occupied by the material in the deformed state. We will assume that V and V' are similar in topology, by which we mean that there are no additional holes or tears that appear as a result of the deformation.

In order to calculate the energy corresponding to a given deformation we need to calculate the work done on the material. This can be done using two tensor fields, the strain tensor field, $\boldsymbol{\epsilon}$, and the stress tensor field, $\boldsymbol{\sigma}$. For ease we will drop the 'field' in further discussion understanding that the discussed tensors in general vary over the volume of interest. The strain tensor corresponds to the deformation of an infinitesimal volume element and can be calculated form the displacement field as[1]:

$$\epsilon_{ij} = \frac{1}{2}(\partial_j u_i + \partial_i u_j). \tag{2.1.1}$$

Here we use the Einstein notation implying a summation over repeated indices, also we

[1] This definition is sometimes called the harmonic strain, to distinguish it from strain defined as $\epsilon_{ij} = \frac{1}{2}(\partial_j u_i + \partial_i u_j + \partial_k u_i \partial_k u_j)$ which includes a higher order term that is often neglected [28].

write ∂_i for the partial derivative along the i-th coordinate direction.[2] From the definition it is easy to see that the strain tensor is symmetric, i.e. $\epsilon_{ij} = \epsilon_{ji}$. As the strain tensor is used to describe the deformation so is stress tensor used to describe the forces acting on a infinitesimal volume element. The energy density is then given by the contraction of the two tensors,

$$\frac{1}{2}\sigma : \epsilon = \frac{1}{2}\sigma_{ij}\epsilon_{ij}. \tag{2.1.2}$$

Thus one can define the stress tensor from the energy formulation as for a given potential energy density, $U_{\text{el}} = \sigma_{ij}\epsilon_{ij}$, the stress tensor is defined as:

$$\sigma_{ij} = \frac{\partial U_{\text{el}}}{\partial \epsilon_{ij}}, \tag{2.1.3}$$

and therefore also the stress tensor is symmetric, $\sigma_{ij} = \sigma_{ji}$. This definition, although general, is often of limited use as it requires knowledge of the potential energy density. Luckily most materials are adequately described using Hooke's law relating the the stress and strain tensor as

$$\sigma_{ij} = C_{ijkl}\epsilon_{kl}, \tag{2.1.4}$$

where C_{ijkl} is the elasticity tensor corresponding with the material of study. The elasticity tensor has the following symmetries:

$$C_{ijkl} = C_{jikl} = C_{ijlk} = C_{klij}. \tag{2.1.5}$$

For such systems the potential energy density is then given by:

$$U_{\text{el}} = \frac{1}{2}\sigma_{ij}\epsilon_{ij} = \frac{1}{2}C_{ijkl}\epsilon_{kl}\epsilon_{ij}. \tag{2.1.6}$$

Aside from the potential energy density a volume of material in motion also has kinetic energy density, which is relevant for dynamic systems such as the ones under study in this thesis. The kinetic energy density, T_{el}, of a material is given by:

$$T_{\text{el}} = \frac{1}{2}\rho(\partial_t \boldsymbol{u})^2. \tag{2.1.7}$$

Here ρ is the mass density of the material, ∂_t is the time derivative and $(\partial_t \boldsymbol{u})^2$ should be read as the dot product between the vector $\partial_t \boldsymbol{u}$ with itself.

2.2. PLATE THEORY

The main system of study in this thesis is that of a suspended material where the thickness of the material, typically ranging from 1×10^{-9}m to 1×10^{-7}m, is significantly smaller than the lateral size of the suspended area, typically ranging from 1×10^{-6}m to 1×10^{-5}m. For such systems there is a difference in behaviour along the thin out-of-plane direction when compared to the large in-plane directions. Such systems are called plates and often described using Kirchhoff-Love plate theory or variations there on. We will exchange the assumption of non-varying thickness of standard Kirchhoff-Love plate theory for that of plane stress and derive the dynamic equations of motion for a plate of a general material.

[2] So for a standard Cartesian coordinate system consisting of x, y, z directions $\partial_1 = \frac{\partial}{\partial x}$.

2.2.1. DISPLACEMENT FIELD

Firstly we will define the mid-plane as the plane corresponding with the center of the plate along the out-of-plane, read the thin, direction.[3] We will define our coordinates such that the 3rd coordinate, x_3, corresponds to the out-of-plane direction and the mid-plane corresponds to $x_3 = 0$. So $x_3 \in [-\frac{h}{2}, \frac{h}{2}]$ where h is the thickness of the plate. We will make the following simplifying assumptions:

1. Straight lines normal to the mid-plane remain straight after deformation.

2. Straight lines normal to the mid-plane remain normal to the mid-plane after deformation.

3. The top and bottom of the plate are free, such that the stress components perpendicular to the plate are zero. $\sigma_{i3}(x_3 = \pm\frac{h}{2}) = 0$ and the plate is thin enough to assume this condition holds throughout the plate $\sigma_{i3} = 0$.

Assumptions 1 and 2 allow for the displacement field to be decomposed in three contributions, the translation of the mid-plane, the rotation of the mid-plane, scaling along the normals to the mid-plane.[4] Figure 2.1 shows a schematic of a deformed plate in reference to its undeformed state.

For a given point p in the plate there is a point r on the mid-plane of the plate such that p lies on a normal of the mid-plane trough r. The displacement field at p, $\boldsymbol{u}(p)$, is given by the vector connecting p to q, where q corresponds to p after deformation. The first contribution to $\boldsymbol{u}(p)$ is the given by the translation of the mid-plane, $\boldsymbol{u}^0(p) = \boldsymbol{u}^0(r)$, figure 2.1B). The remaining contribution is then $\boldsymbol{u}(p) - \boldsymbol{u}^0(p)$ corresponding to the rotation of the mid-plane, translating p to p' in figure 2.1 and a scaling along the normal, translating p' to q' in figure 2.1C). The lateral translation due to the rotation is given by $p_3 \sin(\partial_\alpha u_3^0)$, where p_3 is the out-of-plane coordinate of p and α is the in-plane coordinate corresponding to the translation. For small values of $\partial_\alpha u_3^0$ this translation can be approximated, using the small angle approximation, as $p_3 \partial_\alpha u_3^0$. The scaling along the normal is generally very small and as such can be neglected.[5]

This leads to the following form of the in-plane displacement field:

$$u_1 = u_1^0 - x_3 \partial_1 u_3^0 \tag{2.2.1}$$

$$u_2 = u_2^0 - x_3 \partial_2 u_3^0, \tag{2.2.2}$$

where $\boldsymbol{u}^0$ is the displacement field of the mid-plane, i.e. $\boldsymbol{u}^0 = \boldsymbol{u}(x_3 = 0)$.

[3] The term mid-plane is not to be confused with neutral-plane which corresponds to the plane where the out of plane strain component equals zero. For homogeneous plates the two often coincide, but in general they are different.

[4] Note that we assume that the mid-plane remains the mid-plane after deformation implying that any scaling along the normals is mirrored along the mid-plane. This is not generally true, such as for non-homogeneous plates, but will be a good enough approximation for this thesis.

[5] This scaling will be captured by the later introduced $\tilde{u_3}(x_1, x_2, x_3)$, by neglecting the contribution here we neglect the effect this term has on the in-plane displacement. This contribution is on the order of $\tilde{u_3}(x_1, x_2, x_3) \sin(\partial_\alpha u_3^0)$ and as such small enough to safely neglect in our discussion.

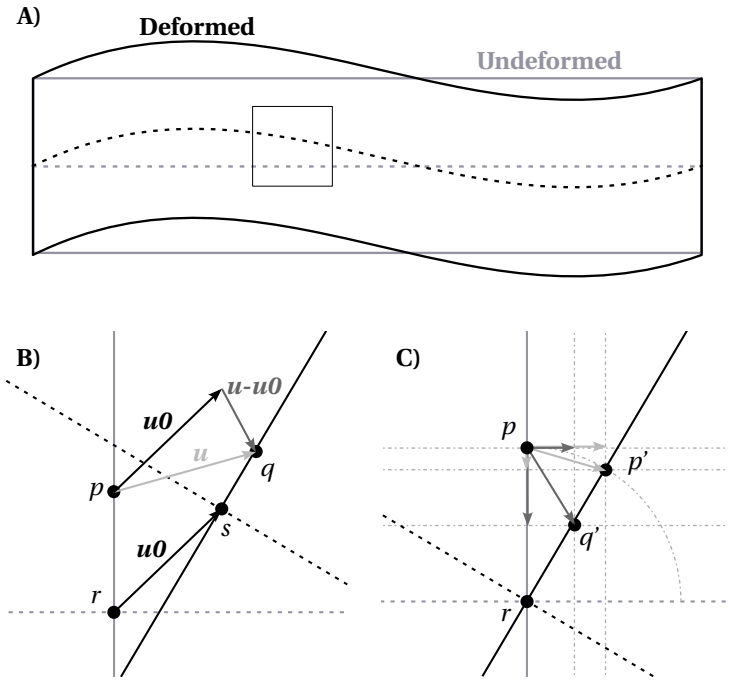

Figure 2.1: **Schematic displacement field of a plate. A)** A schematic cut-through of a plate in the undeformed (grey) and deformed (black) state. The grey and black dashed lines are the mid-plane of the undeformed and deformed plate, respectively. The indicated square is shown magnified in panel B). **B)** A zoom-in of panel A). The grey and black dashed lines correspond to the mid-plane of the undeformed and deformed plate and the continous lines are normal to the mid-plane of the corresponding colour. Indicated are a point r on the mid-plane and p in the undeformed plate that translate to s and q under deformation respectively. The corresponding deformation vectors $\boldsymbol{u}^0(r)$ and $\boldsymbol{u}(p)$ are shown and the $\boldsymbol{u}(p)$ is decomposed into a $\boldsymbol{u}^0$ component and the remainder $\boldsymbol{u}-\boldsymbol{u}^0$. **C)** shows the same as panel B) except that the deformed system is translated by $-\boldsymbol{u}^0$, so that the points r and s coincide. The translated point q is indicated as q'. Also indicated is the point p' corresponding to a translation of p resulting solely by a change in slope of the mid-plane. The grey vectors correspond to the translation of p by, $\boldsymbol{u}-\boldsymbol{u}^0$ (dark) and it's constituents, and the translation as a result of only rotating the mid-plane (light) and it's constituents. The dotted and dashed lines are added for clarification.

From assumption 3 and the definitions of the stress (2.1.4) and strain tensor (2.1.1) we find

$$\epsilon_{33} = -\frac{\lambda}{\lambda+2\mu}(\epsilon_{11}+\epsilon_{22}) \tag{2.2.3}$$

$$\partial_3 u_3 = -\frac{\lambda}{\lambda+2\mu}(\partial_1 u_1 + \partial_2 u_2). \tag{2.2.4}$$

Note that here we have assumed our material to be isotropic meaning that the elasticity tensor is of the form:

$$C_{ijkl} = \lambda\delta_{ij}\delta_{kl} + \mu(\delta_{ik}\delta_{jl} + \delta_{il}\delta_{jk}) \tag{2.2.5}$$

where λ, μ are the first and second Lamé parameters[6] and δ is the Kronecker delta. Substituting (2.2.1) and (2.2.2) in (2.2.4) we find:

$$\begin{aligned}\partial_3 u_3 &= -\frac{\lambda}{\lambda+2\mu}(\partial_1(u_1^0 - x_3\partial_1 u_3^0) + \partial_2(u_2^0 - x_3\partial_2 u_3^0)) \\ &= -\frac{\lambda}{\lambda+2\mu}(\partial_1 u_1^0 + \partial_2 u_2^0) + \frac{\lambda}{\lambda+2\mu}x_3(\partial_1\partial_1 u_3^0 + \partial_2\partial_2 u_3^0) \\ &= -\frac{\lambda}{\lambda+2\mu}f(x,y) + \frac{\lambda}{\lambda+2\mu}x_3(\nabla_{2\mathrm{D}}^2 u_3^0),\end{aligned} \tag{2.2.6}$$

where $f(x,y) = \partial_1 u_1^0 + \partial_2 u_2^0$ and $\nabla_{2\mathrm{D}}^2 = \partial_1\partial_1 + \partial_2\partial_2$. Considering (2.2.6) at the mid-plane we find a differential equation for u_3^0 in terms of the in-plane displacements of the mid-plane.

$$(\partial_3 u_3)\big|_{x_3=0} = -\frac{\lambda}{\lambda+2\mu}(\partial_1 u_1^0 + \partial_2 u_2^0) \tag{2.2.7}$$

Note that this is the same as evaluating (2.2.4) at the mid-plane. We can write the out-of-plane displacement as:

$$u_3(x_1,x_2,x_3) = u_3^0(x_1,x_2) + \tilde{u_3}(x_1,x_2,x_3). \tag{2.2.8}$$

Substituting this into (2.2.6) results in:

$$\begin{aligned}\partial_3 u_3^0 + \partial_3\tilde{u_3} &= -\frac{\lambda}{\lambda+2\mu}f(x,y) + \frac{\lambda}{\lambda+2\mu}x_3(\nabla_{2\mathrm{D}}^2 u_3^0) \\ \partial_3\tilde{u_3} &= -\frac{\lambda}{\lambda+2\mu}f(x,y) + \frac{\lambda}{\lambda+2\mu}x_3(\nabla_{2\mathrm{D}}^2 u_3^0).\end{aligned} \tag{2.2.9}$$

Integrating both sides results in

$$\begin{aligned}\tilde{u_3} &= \int_0^{x_3}\partial_3\tilde{u_3}\,dx_3 = \int_0^{x_3} -\frac{\lambda}{\lambda+2\mu}f(x,y) + \frac{\lambda}{\lambda+2\mu}x_3(\nabla_{2\mathrm{D}}^2 u_3^0)\,dx_3 \\ &= -\frac{\lambda}{\lambda+2\mu}f(x,y)x_3 + \frac{\lambda}{\lambda+2\mu}(\nabla_{2\mathrm{D}}^2 u_3^0)\frac{1}{2}x_3^2.\end{aligned} \tag{2.2.10}$$

An interesting consequence of this is that under the made assumptions variations in the thickness of the plate are proportional to the in-plane strains and the thickness of the plate, as the variation in thickness, Δh becomes

$$\begin{aligned}\Delta h &= u_3(x_3 = \frac{h}{2}) - u_3(x_3 = -\frac{h}{2}) \\ &= u_3^0 + \tilde{u_3}(x_3 = \frac{h}{2}) - u_3^0 - \tilde{u_3}(x_3 = -\frac{h}{2}) \\ &= -\frac{\lambda}{\lambda+2\mu}f(x,y)h.\end{aligned} \tag{2.2.11}$$

[6] μ is also know as the shear modulus.

2.2.2. EQUATIONS OF MOTION

Even though the previous derivation for u_3 was based on the assumption of an isotropic material we will assume the resulting form of the displacement field to be the same for the case of an anisotropic material. In order to derive the equations of motion (EOM) we will use the Euler-Lagrange formalism. Starting with a Lagrangian of the form:

$$L = \int_V \mathscr{L} dV = \int_V \frac{1}{2}\rho(\partial_t \boldsymbol{u})^2 - \frac{1}{2}\sigma_{ij}\epsilon_{ij} dV. \tag{2.2.12}$$

Where $\mathscr{L}$ is the Lagrangian density given by (2.1.6) and (2.1.7) resulting in:

$$\mathscr{L} = T_{\text{el}} - U_{\text{el}} = \frac{1}{2}\rho(\partial_t \boldsymbol{u})^2 - \frac{1}{2}\sigma_{ij}\epsilon_{ij} = \frac{1}{2}\rho(\partial_t \boldsymbol{u})^2 - \frac{1}{2}C_{ijkl}\epsilon_{kl}\epsilon_{ij}. \tag{2.2.13}$$

We take the displacement field to be of the same form as in the previous section:

$$\begin{aligned} u_1 &= u_1^0 - x_3\partial_1 u_3^0 \\ u_2 &= u_2^0 - x_3\partial_2 u_3^0 \\ u_3 &= u_3^0 + \tilde{u_3}. \end{aligned} \tag{2.2.14}$$

From substituting this displacement field into the definition of the strain tensor (2.1.1) we find the following components:

$$\begin{aligned} \epsilon_{11} &= \partial_1 u_1^0 - x_3\partial_1\partial_1 u_3^0 \\ \epsilon_{22} &= \partial_2 u_2^0 - x_3\partial_2\partial_2 u_3^0 \\ \epsilon_{33} &= \partial_3(u_3^0 + \tilde{u_3}) = \partial_3\tilde{u_3} \\ \epsilon_{23} &= \frac{1}{2}(\partial_2(u_3^0 + \tilde{u_3}) - \partial_2 u_3^0) = \frac{1}{2}\partial_2\tilde{u_3} \\ \epsilon_{13} &= \frac{1}{2}(\partial_1(u_3^0 + \tilde{u_3}) - \partial_1 u_3^0) = \frac{1}{2}\partial_1\tilde{u_3} \\ \epsilon_{12} &= \frac{1}{2}(\partial_2 u_1^0 + \partial_1 u_2^0) - x_3\partial_1\partial_2 u_3^0. \end{aligned} \tag{2.2.15}$$

The terms of the potential energy density then becomes:

$$\begin{aligned}
\frac{1}{2}C_{ijkl}\epsilon_{kl}\epsilon_{ij} = \frac{1}{2}\Big(&C_{1111}\epsilon_{11}^2 + C_{2222}\epsilon_{22}^2 + C_{3333}\epsilon_{33}^2 \\
&+ 2C_{1122}\epsilon_{12}\epsilon_{22} + 2C_{1133}\epsilon_{11}\epsilon_{33} + 2C_{2233}\epsilon_{22}\epsilon_{33} + 4C_{1112}\epsilon_{11}\epsilon_{12} \\
&+ 4C_{1113}\epsilon_{11}\epsilon_{13} + 4C_{1123}\epsilon_{11}\epsilon_{23} + 4C_{1212}\epsilon_{12}\epsilon_{12} + 4C_{1222}\epsilon_{12}\epsilon_{22} \\
&+ 4C_{1233}\epsilon_{12}\epsilon_{33} + 8C_{1223}\epsilon_{12}\epsilon_{23} + 8C_{1213}\epsilon_{12}\epsilon_{13} + 4C_{1313}\epsilon_{13}\epsilon_{13} \\
&+ 4C_{1322}\epsilon_{13}\epsilon_{22} + 4C_{1333}\epsilon_{13}\epsilon_{33} + 8C_{1323}\epsilon_{13}\epsilon_{23} \\
&+ 4C_{2223}\epsilon_{22}\epsilon_{23} + 4C_{2323}\epsilon_{23}\epsilon_{23} + 4C_{2333}\epsilon_{23}\epsilon_{33}\Big), \qquad (2.2.16)
\end{aligned}$$

$$\begin{aligned}
= \frac{1}{2}\Big(&C_{1111}\left(\partial_1 u_1^0 - x_3\partial_1\partial_1 u_3^0\right)^2 \\
&+ 4C_{1112}\left(\partial_1 u_1^0 - x_3\partial_1\partial_1 u_3^0\right)\left(\left(\partial_2 u_1^0 + \partial_1 u_2^0\right) - x_3\partial_1\partial_2 u_3^0\right) \\
&+ 2C_{1113}\left(\partial_1 u_1^0 - x_3\partial_1\partial_1 u_3^0\right)\partial_1\tilde{u}_3 \\
&+ 2C_{1122}\left(\partial_2 u_2^0 - x_3\partial_2\partial_2 u_3^0\right)\left(\partial_1 u_1^0 - x_3\partial_1\partial_1 u_3^0\right) \\
&+ 2C_{1123}\left(\partial_1 u_1^0 - x_3\partial_1\partial_1 u_3^0\right)\partial_2\tilde{u}_3 + 2C_{1133}\left(\partial_1 u_1^0 - x_3\partial_1\partial_1 u_3^0\right)\partial_3\tilde{u}_3 \\
&+ 4C_{1212}\left(\left(\partial_2 u_1^0 + \partial_1 u_2^0\right) - x_3\partial_1\partial_2 u_3^0\right)^2 \\
&+ 4C_{1213}\left(\left(\partial_2 u_1^0 + \partial_1 u_2^0\right) - x_3\partial_1\partial_2 u_3^0\right)\partial_1\tilde{u}_3 \\
&+ 4C_{1222}\left(\partial_2 u_2^0 - x_3\partial_2\partial_2 u_3^0\right)\left(\left(\partial_2 u_1^0 + \partial_1 u_2^0\right) - x_3\partial_1\partial_2 u_3^0\right) \\
&+ 4C_{1223}\left(\left(\partial_2 u_1^0 + \partial_1 u_2^0\right) - x_3\partial_1\partial_2 u_3^0\right)\partial_2\tilde{u}_3 \\
&+ 4C_{1233}\left(\left(\partial_2 u_1^0 + \partial_1 u_2^0\right) - x_3\partial_1\partial_2 u_3^0\right)\partial_3\tilde{u}_3 \\
&+ C_{1313}(\partial_1\tilde{u}_3)^2 + 2C_{1322}\left(\partial_2 u_2^0 - x_3\partial_2\partial_2 u_3^0\right)\partial_1\tilde{u}_3 \\
&+ 2C_{1323}\partial_2\tilde{u}_3\partial_1\tilde{u}_3 + 2C_{1333}\partial_3\tilde{u}_3\partial_1\tilde{u}_3 + C_{2222}\left(\partial_2 u_2^0 - x_3\partial_2\partial_2 u_3^0\right)^2 \\
&+ 2C_{2223}\left(\partial_2 u_2^0 - x_3\partial_2\partial_2 u_3^0\right)\partial_2\tilde{u}_3 + 2C_{2233}\left(\partial_2 u_2^0 - x_3\partial_2\partial_2 u_3^0\right)\partial_3\tilde{u}_3 \\
&+ C_{2323}(\partial_2\tilde{u}_3)^2 + 2C_{2333}\partial_3\tilde{u}_3\partial_2\tilde{u}_3 + C_{3333}(\partial_3\tilde{u}_3)^2\Big). \qquad (2.2.17)
\end{aligned}$$

Similarly the kinetic energy density is given by:

$$\frac{1}{2}\rho(\partial_t \boldsymbol{u})^2 = \frac{1}{2}\rho\Big((\partial_t u_1)^2 + (\partial_t u_2)^2 + (\partial_t u_3)^2\Big) \qquad (2.2.18)$$

$$= \frac{1}{2}\rho\Big((\partial_t u_1^0 - x_3\partial_t\partial_1 u_3^0)^2 + (\partial_t u_2^0 - x_3\partial_t\partial_2 u_3^0)^2 + (\partial_t u_3^0 + \partial_t\tilde{u}_3)^2\Big) \qquad (2.2.19)$$

$$\begin{aligned}
= \frac{1}{2}\rho\Big(&(\partial_t u_1^0)^2 + (\partial_t u_2^0)^2 + (\partial_t u_3^0)^2 + (\partial_t\tilde{u}_3)^2 + 2(\partial_t u_3^0)(\partial_t\tilde{u}_3) \\
&- 2x_3(\partial_t u_1^0)(\partial_t\partial_1 u_3^0) - 2x_3(\partial_t u_2^0)(\partial_t\partial_2 u_3^0) \\
&+ x_3^2(\partial_t\partial_1 u_3^0)^2 + x_3^2(\partial_t\partial_2 u_3^0)^2\Big). \qquad (2.2.20)
\end{aligned}$$

Meaning the Lagrangian density becomes:

$$\begin{aligned}
\mathscr{L} &= \frac{1}{2}\rho(\partial_t \boldsymbol{u})^2 - \frac{1}{2}\sigma_{ij}\epsilon_{ij} \qquad (2.2.21)\\
&= \frac{1}{2}\rho\Big((\partial_t u_1^0)^2 + (\partial_t u_2^0)^2 + (\partial_t u_3^0)^2 + (\partial_t \tilde{u_3})^2 + 2(\partial_t u_3^0)(\partial_t \tilde{u_3})\\
&\quad - 2x_3(\partial_t u_1^0)(\partial_t\partial_1 u_3^0) - 2x_3(\partial_t u_2^0)(\partial_t\partial_2 u_3^0)\\
&\quad + x_3^2(\partial_t\partial_1 u_3^0)^2 + x_3^2(\partial_t\partial_2 u_3^0)^2\Big)\\
&\quad - \frac{1}{2}\Big(C_{1111}\left(\partial_1 u_1^0 - x_3\partial_1\partial_1 u_3^0\right)^2\\
&\quad + 4C_{1112}\left(\partial_1 u_1^0 - x_3\partial_1\partial_1 u_3^0\right)\left(\left(\partial_2 u_1^0 + \partial_1 u_2^0\right) - x_3\partial_1\partial_2 u_3^0\right)\\
&\quad + 2C_{1113}\left(\partial_1 u_1^0 - x_3\partial_1\partial_1 u_3^0\right)\partial_1\tilde{u_3}\\
&\quad + 2C_{1122}\left(\partial_2 u_2^0 - x_3\partial_2\partial_2 u_3^0\right)\left(\partial_1 u_1^0 - x_3\partial_1\partial_1 u_3^0\right)\\
&\quad + 2C_{1123}\left(\partial_1 u_1^0 - x_3\partial_1\partial_1 u_3^0\right)\partial_2\tilde{u_3} + 2C_{1133}\left(\partial_1 u_1^0 - x_3\partial_1\partial_1 u_3^0\right)\partial_3\tilde{u_3}\\
&\quad + 4C_{1212}\left(\left(\partial_2 u_1^0 + \partial_1 u_2^0\right) - x_3\partial_1\partial_2 u_3^0\right)^2 + 4C_{1213}\left(\left(\partial_2 u_1^0 + \partial_1 u_2^0\right) - x_3\partial_1\partial_2 u_3^0\right)\partial_1\tilde{u_3}\\
&\quad + 4C_{1222}\left(\partial_2 u_2^0 - x_3\partial_2\partial_2 u_3^0\right)\left(\left(\partial_2 u_1^0 + \partial_1 u_2^0\right) - x_3\partial_1\partial_2 u_3^0\right)\\
&\quad + 4C_{1223}\left(\left(\partial_2 u_1^0 + \partial_1 u_2^0\right) - x_3\partial_1\partial_2 u_3^0\right)\partial_2\tilde{u_3} + 4C_{1233}\left(\left(\partial_2 u_1^0 + \partial_1 u_2^0\right) - x_3\partial_1\partial_2 u_3^0\right)\partial_3\tilde{u_3}\\
&\quad + C_{1313}(\partial_1\tilde{u_3})^2 + 2C_{1322}\left(\partial_2 u_2^0 - x_3\partial_2\partial_2 u_3^0\right)\partial_1\tilde{u_3}\\
&\quad + 2C_{1323}\partial_2\tilde{u_3}\partial_1\tilde{u_3} + 2C_{1333}\partial_3\tilde{u_3}\partial_1\tilde{u_3} + C_{2222}\left(\partial_2 u_2^0 - x_3\partial_2\partial_2 u_3^0\right)^2\\
&\quad + 2C_{2223}\left(\partial_2 u_2^0 - x_3\partial_2\partial_2 u_3^0\right)\partial_2\tilde{u_3} + 2C_{2233}\left(\partial_2 u_2^0 - x_3\partial_2\partial_2 u_3^0\right)\partial_3\tilde{u_3}\\
&\quad + C_{2323}(\partial_2\tilde{u_3})^2 + 2C_{2333}\partial_3\tilde{u_3}\partial_2\tilde{u_3} + C_{3333}(\partial_3\tilde{u_3})^2\Big). \qquad (2.2.22)
\end{aligned}$$

Where we see that $\mathscr{L}$ depends on x_3, $\partial_t u_1^0$, $\partial_t u_2^0$, $\partial_t u_3^0$, $\partial_t \tilde{u_3}$, $\partial_1 u_1^0$,$\partial_1 u_2^0$,$\partial_1 \tilde{u_3}$, $\partial_2 u_1^0$, $\partial_2 u_2^0$, $\partial_2 \tilde{u_3}$, $\partial_3 \tilde{u_3}$, $\partial_1\partial_1 u_3^0$, $\partial_2\partial_2 u_3^0$, and $\partial_1\partial_2 u_3^0$. In order to find then the EOM we will use the Euler-Lagrange equations. Since we are mostly interested in the out-of-plane displacements we will derive the EOM for u_3^0. The EOM for the other displacement field components are discussed in section 2.A.1. In order to find then the EOM for u_3^0 we start with the Euler-Lagrange equation:

$$0 = \frac{\partial\mathscr{L}}{\partial u_3^0} - \frac{d}{dt}\frac{\partial\mathscr{L}}{\partial\partial_t u_3^0} + \frac{d^2}{dx_1^2}\frac{\partial\mathscr{L}}{\partial\partial_1\partial_1 u_3^0} + \frac{d^2}{dx_2^2}\frac{\partial\mathscr{L}}{\partial\partial_2\partial_2 u_3^0} + \frac{d^2}{dx_1x_2}\frac{\partial\mathscr{L}}{\partial\partial_1\partial_2 u_3^0}. \qquad (2.2.23)$$

So we find that the EOM for u_3^0 becomes:

$$
\begin{aligned}
0 = x_3\Big(&C_{1111}\partial_1\partial_1\partial_1\partial_1 u_1^0 + C_{2222}\partial_2\partial_2\partial_2\partial_2 u_2^0 \\
&+ C_{1112}\left(3\partial_1\partial_1\partial_2 u_1^0 + \partial_1\partial_1\partial_1 u_2^0\right) + C_{1222}\left(3\partial_1\partial_2\partial_2 u_2^0 + \partial_2\partial_2\partial_2 u_1^0\right) \\
&+ (C_{1122} + 2C_{1212})(\partial_1\partial_2\partial_2 u_1^0 + \partial_1\partial_1\partial_2 u_2^0)\Big) \\
- x_3^2\Big(&C_{1111}\partial_1\partial_1\partial_1\partial_1 u_3^0 + C_{2222}\partial_2\partial_2\partial_2\partial_2 u_3^0 \\
&+ 4C_{1112}\partial_1\partial_1\partial_1\partial_2 u_3^0 + 4C_{1222}\partial_1\partial_2\partial_2\partial_2 u_3^0 + 2(C_{1122} + 2C_{1212})\partial_1\partial_1\partial_2\partial_2 u_3^0\Big) \\
- \rho\Big(&\partial_t\partial_t u_3^0 + x_3\left(\partial_1\partial_t\partial_t u_1^0 + \partial_2\partial_t\partial_t u_2^0\right) - x_3^2\left(\partial_1\partial_1\partial_t\partial_t u_3^0 + \partial_2\partial_2\partial_t\partial_t u_3^0\right)\Big) \\
+ x_3\Big(&+ C_{1133}\partial_1\partial_1\partial_3\tilde{u}_3 + C_{2233}\partial_2\partial_2\partial_3\tilde{u}_3 + 2C_{1233}\partial_1\partial_2\partial_3\tilde{u}_3 \\
&+ C_{1113}\partial_1\partial_1\partial_1\tilde{u}_3 + C_{2223}\partial_2\partial_2\partial_2\tilde{u}_3 \\
&+ (2C_{1223} + C_{1322})\partial_1\partial_2\partial_2\tilde{u}_3 + (C_{1123} + 2C_{3121})\partial_1\partial_1\partial_2\tilde{u}_3\Big) \\
- \rho\partial_t\partial_t\tilde{u}_3 &
\end{aligned}
\tag{2.2.24}
$$

We remark that in the case that $\tilde{u}_3$ vanishes the last two terms vanish, resulting in:

$$
\begin{aligned}
0 = x_3\Big(&C_{1111}\partial_1\partial_1\partial_1\partial_1 u_1^0 + C_{2222}\partial_2\partial_2\partial_2\partial_2 u_2^0 \\
&+ C_{1112}\left(3\partial_1\partial_1\partial_2 u_1^0 + \partial_1\partial_1\partial_1 u_2^0\right) + C_{1222}\left(3\partial_1\partial_2\partial_2 u_2^0 + \partial_2\partial_2\partial_2 u_1^0\right) \\
&+ (C_{1122} + 2C_{1212})(\partial_1\partial_2\partial_2 u_1^0 + \partial_1\partial_1\partial_2 u_2^0)\Big) \\
- x_3^2\Big(&C_{1111}\partial_1\partial_1\partial_1\partial_1 u_3^0 + C_{2222}\partial_2\partial_2\partial_2\partial_2 u_3^0 \\
&+ 4C_{1112}\partial_1\partial_1\partial_1\partial_2 u_3^0 + 4C_{1222}\partial_1\partial_2\partial_2\partial_2 u_3^0 + 2(C_{1122} + 2C_{1212})\partial_1\partial_1\partial_2\partial_2 u_3^0\Big) \\
- \rho\Big(&\partial_t\partial_t u_3^0 + x_3\left(\partial_1\partial_t\partial_t u_1^0 + \partial_2\partial_t\partial_t u_2^0\right) - x_3^2\left(\partial_1\partial_1\partial_t\partial_t u_3^0 + \partial_2\partial_2\partial_t\partial_t u_3^0\right)\Big).
\end{aligned}
\tag{2.2.25}
$$

In (2.2.25) the x_3 dependence is all explicit since the u_i^0 do not depend on x_3. This means we can integrate over the thickness of the plate, $x_3 \in [-\frac{h}{2}, \frac{h}{2}]$, which results in the terms odd in x_3 to vanish.

$$
\begin{aligned}
0 = \frac{h^3}{12}\Big(&C_{1111}\partial_1\partial_1\partial_1\partial_1 u_3^0 + 4C_{1112}\partial_1\partial_1\partial_1\partial_2 u_3^0 + 2(C_{1122} + 2C_{1212})\partial_1\partial_1\partial_2\partial_2 u_3^0 \\
&+ 4C_{1222}\partial_1\partial_2\partial_2\partial_2 u_3^0 + C_{2222}\partial_2\partial_2\partial_2\partial_2 u_3^0\Big) \\
&+ \rho\partial_t\partial_t u_3^0 - \frac{h^3}{12}(\partial_t\partial_t\partial_1\partial_1 u_3^0 + \partial_t\partial_t\partial_2\partial_2 u_3^0).
\end{aligned}
\tag{2.2.26}
$$

In order to make the comparison to the known literature model for an isotropic plate we can substitute in the corresponding elasticity tensor. Note that due to the assumption 3 we alter the behaviour of the material, this leads to a renormalisation of the elasticity tensor, see section 2.A.2. The renormalised elasticity tensor for an isotropic material

then becomes:

$$C_{1111} = C_{2222} = \lambda + 2\mu = \frac{E}{(1-\nu^2)}, \tag{2.2.27a}$$

$$C_{1112} = C_{2212} = 0, \tag{2.2.27b}$$

$$C_{1122} = \lambda = \frac{\nu E}{(1-\nu^2)}, \tag{2.2.27c}$$

$$C_{1212} = \mu = \frac{E}{2(1+\nu)}, \tag{2.2.27d}$$

where E is the materials Young's modulus and ν is its Poisson ratio. Plugging the renormalised values of the elasticity tensor into (2.2.26) we find:

$$\begin{aligned} -\frac{h^3}{12}\big((\lambda+2\mu)(\partial_1\partial_1\partial_1\partial_1 u_3^0) + (\lambda+2\mu)(\partial_2\partial_2\partial_2\partial_2 u_3^0) \\ + 2\lambda(\partial_1\partial_1\partial_2\partial_2 u_3^0) + 4\mu(\partial_1\partial_2\partial_1\partial_2 u_3^0)\big) \\ = \rho h(\partial_t\partial_t u_3^0) - \rho\frac{h^3}{12}(\partial_t\partial_t\partial_1\partial_1 u_3^0) - \rho\frac{h^3}{12}(\partial_t\partial_t\partial_2\partial_2 u_3^0). \end{aligned} \tag{2.2.28}$$

Which can be rewritten as follows:

$$-D\big(\Delta^2 u_3^0\big) = \rho h(\partial_t\partial_t u_3^0) - \rho\frac{h^3}{12}(\partial_t\partial_t\partial_1\partial_1 u_3^0) - \rho\frac{h^3}{12}(\partial_t\partial_t\partial_2\partial_2 u_3^0) \tag{2.2.29}$$

Where $\Delta^2 = (\partial_1\partial_1 + \partial_2\partial_2)^2$ and $D = \frac{h^3}{12}\frac{E}{(1-\nu^2)}$, which is known as the flexural stiffness. Commonly the last two terms in (2.2.29), those with the prefactor $\rho\frac{h^3}{12}$, are neglected in which case (2.2.29) becomes the standard Kirchoff-Love equation for an undriven isotropic plate.

$$D\big(\Delta^2 u_3^0\big) + \rho h(\partial_t\partial_t u_3^0) = 0 \tag{2.2.30}$$

Equation (2.2.30) can be used to find the resonances of the plate, given the boundary conditions, examples of which are discussed in [29]. Throughout the following chapters we will use analysis of such resonances. The theory presented so far provides a starting point for future work to account for more complex behaviours. For example, the general from presented in (2.2.24) allows to include also the dynamics of $\tilde{u_3}$.

2.3. MAGNETISM

As mentioned in section 1.2 the relevant microscopic origin for magnetism are spins, particularly electron spins. Since all electrons have spin and all materials contain electrons one might expected that all materials are magnetic. To a certain extend this is true, but in practise for a lot of materials the interaction with magnetic fields is quite weak as such these materials can be considered to be not magnetic. This is a result from the fact that the spins in these materials tend to be aligned oppositely, as is the case of for two electrons in the same orbital, or aligned randomly resulting in an overall cancellation of the magnetic moments through out the material. However there are materials where some spins are ordered, i.e. not randomly oriented, or uncompensated resulting

in a magnetic structure. It is these materials that we generally refer to when discussing magnets.

One should however realise that magnetic materials are not magnetic at all temperatures, as this ordering of spins is affected by temperature effects, such as thermal fluctuations. This means that magnets exhibit a phase transition. These phase transitions can be described using Landau theory [15, 30] which makes use of a quantity know as the order parameter. In this section we will provide an introduction to this theory starting from the definitions of this order paramter.

2.3.1. MAGNETIC ORDER PARAMETER

For magnetic phases the order parameter can be understood as a measure for how aligned the spins, by which we mean the magnetic moments, in the system are. If we consider a ferromagnetic system, then if the system is fully ordered all spins are aligned parallel to each other, whereas if the system is fully disordered the spins are not aligned but rather point in random directions. An intuitive measure for how ferromagnetically ordered a state is would be to then add all spins together. This quantity would be zero in the case where the spins are not aligned, called the paramagnetic state, and maximal in the fully ordered state, the ferromagnetic state. If we consider the set all spins in the system, $\{\boldsymbol{S}_1, \boldsymbol{S}_2, ..., \boldsymbol{S}_N\}$, then summing over this set and dividing by the volume of the system, V, gives us the ferromagnetic order parameter:

$$\boldsymbol{M} = \frac{1}{V}\sum_{i=1}^{N} \boldsymbol{S}_i \tag{2.3.1}$$

Note that this ferromagnetic order parameter, $\boldsymbol{M}$, is a vector quantity with units of A/m. Often we don't really care about the direction of this order parameter and only the magnitude, $M = |\boldsymbol{M}|$, is considered. We will consider $\boldsymbol{M}$ to be a field varying over space, which can be understood from the definition in (2.3.1) by taking V to be an infinitesimal volume element and only sum over the spins in that volume element.

Using the same order parameter for antiferromagnetic systems as for ferromagnetic systems does not work, in the sense that there is not a difference in value between the paramagnetic and antiferromagnetic state. This is due to the fact that when the spins start to order in anti alignment the fact that neighboring spins have opposite direction means that they cancel in the summation. To take this into account we can define a slightly different order parameter, called the antiferromagnetic order parameter, which corresponds to the total staggered magnetisation [31], which we will denote with $\boldsymbol{L}$. If we consider the system in a completely ordered state we can divide the set of spins, $\{\boldsymbol{S}_1, \boldsymbol{S}_2, ..., \boldsymbol{S}_N\}$, in the system in to two disjointed subsets whose union form the entire set, $\{\boldsymbol{S}'_1, \boldsymbol{S}'_2, ..., \boldsymbol{S}'_{N_A}\}$ and $\{\boldsymbol{S}''_1, \boldsymbol{S}''_2, ..., \boldsymbol{S}''_{N_B}\}$, where one subset consist of all spins that are parallel with other spins of that subset but are anti-parallel with the spins in the other subset. We can then define the antiferromagnetic order parameter to be the the difference between the sums of each of these subsets,

$$\boldsymbol{L} = \frac{1}{V}\Big(\sum_{i=1}^{N_A} \boldsymbol{S}'_i - \sum_{j=1}^{N_B} \boldsymbol{S}''_j\Big). \tag{2.3.2}$$

For an antiferromagnet there is no macroscopic magnetization which requires that the two subsets are of equal size, i.e. $N_A = N_B$. If this is not the case the two subsets do not completely cancel each others total magnetization resulting in some macroscopic magnetization, this case corresponds to that of a ferrimagnet.[7] It is interesting to note that we can actually consider the ferromagnetic system to be a special case where one of the subsets is the empty set, in which case we see that the definition of $\boldsymbol{L}$ and $\boldsymbol{M}$ coincide. And one could generalize this definition further to include systems where the total ordered state can be naturally partitioned into more than two subsets, such as for certain frustrated lattices.

2.3.2. FREE ENERGY

The order parameter is thus zero in the non-magnetic state and non-zero in the magnetic state. This suggest that at the transition point the order parameter is small [8] allowing for an expansion of the energy in terms of the order parameter. So close to the transition the free energy can be written as:

$$F = F_0 + A_{1i}M_i + A_{2ij}M_iM_j + A_{3ijk}M_iM_jM_k + A_{4ijkl}M_iM_jM_kM_l + \dots. \tag{2.3.3}$$

Where the indices run over $\{1,2,3\}$ and M_i is the ith component of the vector $\boldsymbol{M}$. Here the A's are the expansion coefficients and F_0 represents the contributions to the free energy not coming from the magnetic order, such as phonon contributions. Since free energy has to be invariant under time reversal and the order parameters of interest to us, both $\boldsymbol{M}$ and $\boldsymbol{L}$, are anti-symmetric under time reversal any term of odd order in the order parameter has to vanish [32] [15]. If we then also drop terms of order higher than 4th order in the order parameter we are left with:

$$F = F_0 + A_{2ij}M_iM_j + A_{4ijkl}M_iM_jM_kM_l \tag{2.3.4}$$

Equation (2.3.4) uses the general vector form of the order parameter with the corresponding coefficients, A_2, A_4, written as tensor components. Often it is sufficient to simply consider the order parameter in a scalar form, such as the magnitude of the order parameter $M = \sqrt{M_iM_i}$. Simplifying (2.3.4) in this way we get:

$$F = F_0 + a(T - T_N)^{2\beta}M^2 + BM^4. \tag{2.3.5}$$

Here a, B are positive constants[9], T is the temperature, T_N the transition temperature, and β a critical exponent describing the transition.

2.4. MAGNETOSTRICTION

Some materials deform when subjected to a magnetic field, this phenomenon is called magnetostriction. This effect is the reason that transformers hum, as the metal core,

[7] This definition assumes that the total system has an even amount of spins. In practice this is not always the case even for systems that we would consider an antiferromagnet and a more rigorous definition involves considering the infinite size limit of the system.

[8] Note that we make the implicit assumption that the order parameter is continues. This is the case for the transitions discussed in this thesis and so we will proceed without further discussion on this assumption.

[9] a can also be negative, this is dependent on if the disordered state is at higher or lower temperature with respect to the ordered state. Since for all transitions discussed in the this thesis the disordered state is at a higher temperature which corresponds to $a > 0$ we will treat a as being positive.

usually iron, expands and contracts along with the changing magnetisation induced by the coils in the transformer. This deformation does not only happen due to externally induced magnetisation changes, such as with the transformer example, but also when a material changes magnetisation itself, such as when exhibiting a magnetic phase transition, the latter case is called spontaneous magnetostriction.

The simplest coupling in the free energy expression that that satisfies the symmetries mentioned earlier in this chapter is of the form:

$$\lambda_{ijkl}\sigma_{ij}M_kM_l. \tag{2.4.1}$$

Here λ_{ijkl} are the magnetostrictive coupling coefficients with units of m^2/A^2. It will be more convenient to rephrase (2.4.1) in terms of strain using (2.1.4).

$$\lambda_{ijkl}C_{ijpq}\epsilon_{pq}M_kM_l = \bar{\lambda}_{ijkl}\epsilon_{ij}M_kM_l. \tag{2.4.2}$$

Where we defined $\bar{\lambda}_{pqkl} = \lambda_{ijkl}C_{ijpq}$ for ease of notation. If we consider the magnetic free energy and the coupling as an additional potential to the Lagrangian density from (2.2.13) we can find the effects this coupling has on the EOM of u_3^0 for a plate made from a magnetostrictive material. The purely magnetic terms, i.e. not containing any strain component, will not contribute to the EOM of u_3^0 as the functional derivatives in the Euler-Lagrange equation will vanish. So the only new contribution to the EOM of u_3^0 can come from the coupling term itself. Taking the strain tensor to be the same as in (2.2.15) and substituting those into (2.4.2) we find:

$$\begin{aligned}\bar{\lambda}_{ijkl}\epsilon_{ij}M_kM_l = M_kM_l\Big(&\bar{\lambda}_{11kl}(\partial_1 u_1^0 - x_3\partial_1\partial_1 u_3^0) + \bar{\lambda}_{22kl}(\partial_2 u_2^0 - x_3\partial_2\partial_2 u_3^0)\\ &+ \bar{\lambda}_{33kl}\partial_3\tilde{u_3} + 2\bar{\lambda}_{23kl}\frac{1}{2}\partial_2\tilde{u_3} + 2\bar{\lambda}_{13kl}\frac{1}{2}\partial_1\tilde{u_3}\\ &+ 2\bar{\lambda}_{12kl}(\frac{1}{2}(\partial_2 u_1^0 + \partial_1 u_2^0) - x_3\partial_1\partial_2 u_3^0)\Big)\end{aligned} \tag{2.4.3}$$

If we consider the EOM for u_3^0 as in (2.2.23) adding the contribution coming from (2.4.3), see section 2.B.1, we find that the only non-zero functional derivatives are:

$$\frac{\delta L_{\text{ms}}}{\delta\partial_1\partial_1 u_3^0} = -x_3M_kM_l\bar{\lambda}_{11kl} \tag{2.4.4a}$$

$$\frac{\delta L_{\text{ms}}}{\delta\partial_2\partial_2 u_3^0} = -x_3M_kM_l\bar{\lambda}_{22kl} \tag{2.4.4b}$$

$$\frac{\delta L_{\text{ms}}}{\delta\partial_1\partial_2 u_3^0} = -x_3M_kM_l\bar{\lambda}_{12kl}. \tag{2.4.4c}$$

Where $L_{\text{ms}} = \int_V \mathscr{L}_{\text{ms}}dV = \int_V \bar{\lambda}_{ijkl}\epsilon_{ij}M_kM_l dV$ is the magnetostriction term in the Lagrangian.

In the case of a homogeneous plate where M_i and $\bar{\lambda}_{ijkl}$ are constant through out the plate the terms described by (2.4.4) have no x_1 or x_2 dependence. Therefore there is no contribution to the EOM for u_3^0 as a result from this magnetostrictive coupling, as these non-zero functional derivatives only appear in (2.2.23) in combination with the derivative operators $\frac{d}{dx_1}$ and or $\frac{d}{dx_2}$.

However the magnetostriction term also has an effect on the EOM for the magnetic DOF's. To see this we will follow the same procedure as for the displacement field for the magnetic field. We start from the Lagrangian:

$$\begin{aligned} L &= L_{\text{el}} + L_{\text{mag}} + L_{\text{ms}} \\ &= L_{\text{el}} - F_0 - A_{2ij}M_iM_j - A_{4ijkl}M_iM_jM_kM_l - \bar{\lambda}_{ijkl}\epsilon_{ij}M_kM_l, \end{aligned} \tag{2.4.5}$$

where L_{el} is the elastic part given by (2.2.12) and L_{mag} is the purely magnetic part. The EOM for M_i is then given by:

$$\begin{aligned} 0 &= \frac{\delta L}{\delta M_i} - \frac{d}{dt}\frac{\delta L}{\delta \partial_t M_i} \\ &= -2A_{2ij}M_j - 4A_{4ijkl}M_jM_kM_l - \bar{\lambda}_{klij}\epsilon_{kl}M_j. \end{aligned} \tag{2.4.6}$$

Which can be rewritten this as:

$$0 = \Big((2A_{2ij} + \bar{\lambda}_{klij}\epsilon_{kl}) + 4A_{4ijkl}M_kM_l\Big)M_j. \tag{2.4.7}$$

If we are only interested in the magnitude of the magnetic order we can replace the M_i simply with M and find:

$$0 = \Big((2a(T-T_N)^{2\beta} + \bar{\lambda}_{klij}\epsilon_{kl}) + 4BM^2\Big)M. \tag{2.4.8}$$

For which there are three possible solutions:

$$M = 0 \tag{2.4.9}$$

$$M = \pm\sqrt{\frac{2a(T-T_N)^{2\beta} + \bar{\lambda}_{klij}\epsilon_{kl}}{4B}}. \tag{2.4.10}$$

The $M = 0$ solution corresponds with no magnetisation as in the paramagnetic phase. The second set of solutions correspond with the 2 orientations of the magnetisation in the magnetic phase. We remark that for the case that $\beta = \frac{1}{2}$ we can rewrite (2.4.10) to interpret the magnetostriction contribution as simply renormalising the transition temperature. This results in:

$$M = \pm\sqrt{\frac{2a(T-T_N) + \bar{\lambda}_{klij}\epsilon_{kl}}{4B}} = \pm\sqrt{\frac{2a(T-T_N^*)}{4B}}, \tag{2.4.11}$$

where

$$T_N^* = T_N - (\frac{\bar{\lambda}_{klij}\epsilon_{kl}}{2a}). \tag{2.4.12}$$

This result shows that when considering a magnetic phase transition in a system with magnetostriction the transition temperature becomes dependent on the strain in the system. This will be relevant for the rest of this thesis as they discuss precisely such systems.

REFERENCES

15. Landau, L., Lifshitz, E. & Pitaevskii, L. *Electrodynamics of Continuous Media: Volume 8* (Elsevier Science, 1995).

27. Sadd, M. H. *Elasticity: Theory, Applications, and Numerics* (Elsevier, 2004).

28. Landau, L. D. & Lifshitz, E. M. *Theory of Elasticity* 3rd ed. (Elsevier, 1986).

29. Leissa, A. W. & Qatu, M. S. *Vibrations of continuous systems* (New York: McGraw-Hill, 2011).

30. Landau, L. On the theory of phase transitions. *Ukrainian journal of physics* **53,** 25–35 (2008).

31. Neirotti, J. P. & de Oliveira, M. J. Spontaneous staggered magnetization in antiferromagnetic Heisenberg-Ising chains. *Phys. Rev. B* **54,** 6351–6355 (9 Sept. 1996).

32. Landau, L. D., Lifshitz, E. M., Sykes, J. B. & M.J, K. *Statistical Physics* 3rd ed. (Elsevier, 1980).

2.A. SUPPLEMENTARY PLATE THEORY

2.A.1. EQUATIONS OF MOTION OF ELASTIC DEGREES OF FREEDOM

In the main text we used the Euler-Lagrange formalism to derive the EOM of the elastic DOF. This method is based on principle of least action which when discussed in undergraduate physics classes is often only discussed in the context of a single variable, commonly time, and single function, commonly position. This section will give a brief recap of this one variable one function case and discuss the more general case, for the readers that are unfamiliar with the generalisation. We will apply the generalised case to the elastic DOF in the plate theory discussed in the main text to derive the complete set of EOM for all elastic DOF of the model.

EULER-LAGRANGE FORMALISM

In order to derive the EOM for a dynamical system we look for a stationary point of the action functional, this principle is the well know principle of least action. Let S be the action of our system then:

$$S[f] = \int_{t_0}^{t_1} L(t, f(t), \partial_t f(t))\, dt, \tag{2.A.1}$$

where $L(t, f)$ is the systems Lagrangian dependent on time, t, and a function f that describes the variable of interest, such as the position of a particle, and t_0 and t_1 are the boundary times of our problem. In this system dependent on one function f, its first derivative $\partial_t f(t)$, and one variable t a stationary point is given by the well known Euler-Lagrange equation:

$$\frac{\delta L}{\delta f} - \partial_t \frac{\delta L}{\delta \partial_t f(t)} = 0. \tag{2.A.2}$$

This formalism can be generalised to systems with multiple variables, functions, and higher order derivatives, such as the case of a plate in elasticity theory [33]. In that case the action will have the form:

$$S[f_1, \ldots, f_p] = \int_\Omega \mathscr{L}(t, x_1, \ldots, x_m, f_1, \ldots, f_p, \partial_t f_1, \ldots, \partial_m f_p, \partial_t^n f_1, \ldots, \partial_m^n f_p)\, dx, \tag{2.A.3}$$

where $\Omega = [t_0, t_1] \times V$ is the parameter space of interest, the product space of the temporal interval $[t_0, t_1]$ with the spacial volume V, and $\mathscr{L}$ is the Lagrangian (density) dependent on the variables $t, x_1, \ldots, x_m$ as well as the functions $f_1, \ldots, f_p$ and their derivatives up to order n, we use the notation ∂_m^n for $\frac{\partial^n}{\partial x_m^n}$.[10] In such a system a stationary point satisfies the system of Euler-Lagrange equations given by:

$$\frac{\partial \mathscr{L}}{\partial f_i} + \sum_{j=1}^{n} \sum_{\mu_1 \leq \cdots \leq \mu_j} (-1)^j \partial_{\mu_1 \ldots \mu_j} \frac{\partial \mathscr{L}}{\partial \partial_{\mu_1 \ldots \mu_j} f_i} = 0, \tag{2.A.4}$$

where $\mu_1 \ldots \mu_j$ run over the variables $t, x_1, \ldots, x_m$.

[10] Note that this also includes combination of derivatives such as $\partial_t \partial_1 \partial m$.

EQUATIONS OF MOTION

We see from (2.2.22) that $\mathscr{L}$ depends on x_3, $\partial_t u_1^0$, $\partial_t u_2^0$, $\partial_t u_3^0$, $\partial_t \tilde{u}_3$, $\partial_1 u_1^0$, $\partial_1 u_2^0$, $\partial_1 \tilde{u}_3$, $\partial_2 u_1^0$, $\partial_2 u_2^0$, $\partial_2 \tilde{u}_3$, $\partial_3 \tilde{u}_3$, $\partial_1\partial_1 u_3^0$, $\partial_2\partial_2 u_3^0$, and $\partial_1\partial_2 u_3^0$. Plugging this in to (2.A.4) we get an EOM for each field, u_1^0, u_2^0, $\tilde{u}_3$, and u_3^0.

$$0 = \frac{\partial \mathscr{L}}{\partial u_1^0} - \partial_t \frac{\partial \mathscr{L}}{\partial \partial_t u_1^0} - \partial_1 \frac{\partial \mathscr{L}}{\partial \partial_1 u_1^0} - \partial_2 \frac{\partial \mathscr{L}}{\partial \partial_2 u_1^0} \tag{2.A.5a}$$

$$0 = \frac{\partial \mathscr{L}}{\partial u_2^0} - \partial_t \frac{\partial \mathscr{L}}{\partial \partial_t u_2^0} - \partial_1 \frac{\partial \mathscr{L}}{\partial \partial_1 u_2^0} - \partial_2 \frac{\partial \mathscr{L}}{\partial \partial_2 u_2^0} \tag{2.A.5b}$$

$$0 = \frac{\partial \mathscr{L}}{\partial \tilde{u}_3} - \partial_t \frac{\partial \mathscr{L}}{\partial \partial_t \tilde{u}_3} - \partial_1 \frac{\partial \mathscr{L}}{\partial \partial_1 \tilde{u}_3} - \partial_2 \frac{\partial \mathscr{L}}{\partial \partial_2 \tilde{u}_3} - \partial_3 \frac{\partial \mathscr{L}}{\partial \partial_3 \tilde{u}_3} \tag{2.A.5c}$$

$$0 = \frac{\partial \mathscr{L}}{\partial u_3^0} - \partial_t \frac{\partial \mathscr{L}}{\partial \partial_t u_3^0} + \partial_1\partial_1 \frac{\partial \mathscr{L}}{\partial \partial_1\partial_1 u_3^0} + \partial_2\partial_2 \frac{\partial \mathscr{L}}{\partial \partial_2\partial_2 u_3^0} + \partial_1\partial_2 \frac{\partial \mathscr{L}}{\partial \partial_1\partial_2 u_3^0} \tag{2.A.5d}$$

Substituting (2.2.22) into (2.A.5) we find the following set of coupled EOM:

For u_1^0 we find:

$$\begin{aligned}
&C_{1111}\partial_1\partial_1 u_1^0 + C_{1112}2\partial_1\partial_2 u_1^0 + C_{1212}\partial_2\partial_2 u_1^0 \\
&+ C_{1112}\partial_1\partial_1 u_2^0 + (C_{1122} + C_{1212})\partial_1\partial_2 u_2^0 + C_{1222}\partial_2\partial_2 u_2^0 \\
&+ C_{1113}\partial_1\partial_1 \tilde{u}_3 + C_{1223}\partial_2\partial_2 \tilde{u}_3 \\
&+ C_{1233}\partial_2\partial_3 \tilde{u}_3 + C_{1133}\partial_1\partial_3 \tilde{u}_3 + (C_{1123} + C_{3121})\partial_1\partial_2 \tilde{u}_3 \\
&\quad = \rho\partial_t\partial_t u_1^0 + x_3\Big(- \rho\partial_1\partial_t\partial_t u_3^0 \\
&\qquad\qquad + C_{1111}\partial_1\partial_1\partial_1 u_3^0 + C_{1222}\partial_2\partial_2\partial_2 u_3^0 \\
&\qquad\qquad + 3C_{1112}\partial_1\partial_1\partial_2 u_3^0 + (C_{1122} + 2C_{1212})\partial_1\partial_2\partial_2 u_3^0\Big).
\end{aligned} \tag{2.A.6}$$

For u_2^0 we find:

$$\begin{aligned}
&C_{1112}\partial_1\partial_1 u_1^0 + (C_{1122} + C_{1212})\partial_1\partial_2 u_1^0 + C_{1222}\partial_2\partial_2 u_1^0 \\
&+ C_{1212}\partial_1\partial_1 u_2^0 + C_{1222}2\partial_1\partial_2 u_2^0 + C_{2222}\partial_2\partial_2 u_2^0 \\
&+ C_{3121}\partial_1\partial_1 \tilde{u}_3 + C_{2223}\partial_2\partial_2 \tilde{u}_3 \\
&+ C_{2233}\partial_2\partial_3 \tilde{u}_3 + C_{1233}\partial_1\partial_3 \tilde{u}_3 + (C_{1223} + C_{1322})\partial_1\partial_2 \tilde{u}_3 \\
&\quad = \rho\partial_t\partial_t u_2^0 + x_3\Big(- \rho\partial_2\partial_t\partial_t u_3^0 \\
&\qquad\qquad + C_{1112}\partial_1\partial_1\partial_1 u_3^0 + C_{2222}\partial_2\partial_2\partial_2 u_3^0 \\
&\qquad\qquad + (C_{1122} + 2C_{1212})\partial_1\partial_1\partial_2 u_3^0 + 3C_{1222}\partial_1\partial_2\partial_2 u_3^0\Big).
\end{aligned} \tag{2.A.7}$$

For $\tilde{u_3}$ we find:

$$
\begin{aligned}
&C_{1113}\partial_1\partial_1 u_1^0 + (C_{1123}+C_{3121})\partial_1\partial_2 u_1^0 + C_{1223}\partial_2\partial_2 u_1^0 \\
&+ C_{3121}\partial_1\partial_1 u_2^0 + (C_{1223}+C_{1322})\partial_1\partial_2 u_2^0 + C_{2223}\partial_2\partial_2 u_2^0 \\
&+ C_{1313}\partial_1\partial_1 \tilde{u_3} + C_{2323}\partial_2\partial_2 \tilde{u_3} + C_{3333}\partial_3\partial_3 \tilde{u_3} \\
&+ 2C_{2333}\partial_2\partial_3 \tilde{u_3} + 2C_{1333}\partial_1\partial_3 \tilde{u_3} + 2C_{1323}\partial_1\partial_2 \tilde{u_3} \\
&= \rho\partial_t\partial_t \tilde{u_3} \\
&\quad + \rho\partial_t\partial_t u_3^0 + C_{1133}\partial_1\partial_1 u_3^0 + 2C_{1233}\partial_1\partial_2 u_3^0 + C_{2233}\partial_2\partial_2 u_3^0 \\
&\quad + x_3\Big(C_{1113}\partial_1\partial_1\partial_1 u_3^0 + C_{2223}\partial_2\partial_2\partial_2 u_3^0 \\
&\qquad + (2C_{1223}+C_{1322})\partial_1\partial_2\partial_2 u_3^0 + (C_{1123}+2C_{3121})\partial_1\partial_1\partial_2 u_3^0\Big).
\end{aligned}
\tag{2.A.8}
$$

And for u_3^0 we find:

$$
\begin{aligned}
&x_3\Big(C_{1111}\partial_1\partial_1\partial_1 u_1^0 + C_{1112}3\partial_1\partial_1\partial_2 u_1^0 + C_{1222}\partial_2\partial_2\partial_2 u_1^0 + (C_{1122}+2C_{1212})\partial_1\partial_2\partial_2 u_1^0 \\
&\quad + C_{1112}\partial_1\partial_1\partial_1 u_2^0 + C_{1222}3\partial_1\partial_2\partial_2 u_2^0 + C_{2222}\partial_2\partial_2\partial_2 u_2^0 + (C_{1122}+2C_{1212})\partial_1\partial_1\partial_2 u_2^0\Big) \\
&- x_3^2\Big(C_{1111}\partial_1\partial_1\partial_1\partial_1 u_3^0 + 2(C_{1122}+2C_{1212})\partial_1\partial_1\partial_2\partial_2 u_3^0 + C_{2222}\partial_2\partial_2\partial_2\partial_2 u_3^0 \\
&\quad + 4C_{1112}\partial_1\partial_1\partial_1\partial_2 u_3^0 + 4C_{1222}\partial_1\partial_2\partial_2\partial_2 u_3^0\Big) \\
&= \rho\Big(\partial_t\partial_t u_3^0 + x_3\left(\partial_1\partial_t\partial_t u_1^0 + \partial_2\partial_t\partial_t u_2^0\right) - x_3^2\left(\partial_1\partial_1\partial_t\partial_t u_3^0 + \partial_2\partial_2\partial_t\partial_t u_3^0\right)\Big) \\
&\quad - x_3\Big(C_{1133}\partial_1\partial_1\partial_3 \tilde{u_3} + C_{2233}\partial_2\partial_2\partial_3 \tilde{u_3} + 2C_{1233}\partial_1\partial_2\partial_3 \tilde{u_3} \\
&\qquad + C_{1113}\partial_1\partial_1\partial_1 \tilde{u_3} + C_{2223}\partial_2\partial_2\partial_2 \tilde{u_3} \\
&\qquad + (2C_{1223}+C_{1322})\partial_1\partial_2\partial_2 \tilde{u_3} + (C_{1123}+2C_{3121})\partial_1\partial_1\partial_2 \tilde{u_3}\Big) \\
&\quad + \rho\partial_t\partial_t \tilde{u_3}
\end{aligned}
\tag{2.A.9}
$$

The equations (2.A.6), (2.A.7), (2.A.8), and (2.A.9) form the total set of coupled EOM for the displacement fields of a plate. They are here presented in a general format to provide a starting point for different systems, such as anisotropic materials or non homogeneous systems.

2.A.2. FROM 3D TO 2D ELASTICITY

If we have an plate of isotropic material the elasticity tensor is given by:

$$
C_{ijkl}^{3D} = \lambda\delta_{ij}\delta_{kl} + \mu(\delta_{ik}\delta_{jl} + \delta_{il}\delta_{jk}), \tag{2.A.10}
$$

where λ and μ are the standard Lamé parameters for a three dimensional system. Under assumption 3 calculating the σ_{zz} component for an isotropic material results in:

$$
\begin{aligned}
\sigma_{zz} &= C_{zzkl}^{3D}\epsilon_{kl} \\
&= \lambda\epsilon_{xx} + \lambda\epsilon_{yy} + \lambda\epsilon_{zz} + 2\mu\epsilon_{zz} \\
&= (\lambda+2\mu)\epsilon_{zz} + \lambda(\epsilon_{xx}+\epsilon_{yy}).
\end{aligned}
\tag{2.A.11}
$$

Applying the assumption of plane stress, $\sigma_{zz} = 0$, this results in:

$$\epsilon_{zz} = \frac{-\lambda}{(\lambda + 2\mu)}(\epsilon_{xx} + \epsilon_{yy}). \tag{2.A.12}$$

2

For the other diagonal stress components we find:

$$\begin{aligned}
\sigma_{xx} &= C^{3D}_{xxkl}\epsilon_{kl} \\
&= (\lambda + 2\mu)\epsilon_{xx} + \lambda(\epsilon_{zz} + \epsilon_{yy}) \\
&= (\lambda + 2\mu)\epsilon_{xx} + \lambda\epsilon_{yy} - \frac{\lambda^2}{(\lambda + 2\mu)}(\epsilon_{xx} + \epsilon_{yy}) \\
&= \frac{4\mu(\lambda + \mu)}{(\lambda + 2\mu)}\epsilon_{xx} + \frac{2\lambda\mu}{(\lambda + 2\mu)}\epsilon_{yy}, \qquad (2.A.13) \\
\sigma_{yy} &= C^{3D}_{yykl}\epsilon_{kl} \\
&= (\lambda + 2\mu)\epsilon_{yy} + \lambda(\epsilon_{zz} + \epsilon_{xx}) \\
&= (\lambda + 2\mu)\epsilon_{yy} + \lambda\epsilon_{xx} - \frac{\lambda^2}{(\lambda + 2\mu)}(\epsilon_{xx} + \epsilon_{yy}) \\
&= \frac{4\mu(\lambda + \mu)}{(\lambda + 2\mu)}\epsilon_{yy} + \frac{2\lambda\mu}{(\lambda + 2\mu)}\epsilon_{xx}. \qquad (2.A.14)
\end{aligned}$$

From this we can see that there appears to be a renomalisation of the elasticity tensor due to the plane stress assumption. We define a new elasticity tensor in the 2D (plane stress) case as satisfying:

$$\sigma_{ij} = C^{2D}_{ijkl}\epsilon_{kl}, \tag{2.A.15}$$

where the indices now run over $\{x, y\}$. We already found some of the components of C^{2D}.

$$C^{2D}_{xxxx} = C^{2D}_{yyyy} = \frac{4\mu(\lambda + \mu)}{(\lambda + 2\mu)} \tag{2.A.16a}$$

$$C^{2D}_{xxyy} = C^{2D}_{xxyy} = \frac{2\lambda\mu}{(\lambda + 2\mu)} \tag{2.A.16b}$$

$$C^{2D}_{xxxy} = C^{2D}_{xxyx} = C^{2D}_{xyxx} = C^{2D}_{yxxx} = 0 \tag{2.A.16c}$$

$$C^{2D}_{yyyx} = C^{2D}_{yyxy} = C^{2D}_{yxyy} = C^{2D}_{xyyy} = 0 \tag{2.A.16d}$$

Leaving just 4 components, which can be determined from:

$$\begin{aligned}
\sigma_{xy} &= C^{3D}_{xykl}\epsilon_{kl} \qquad (2.A.17a) \\
&= \mu\epsilon_{yx} + \mu\epsilon_{xy}. \qquad (2.A.17b)
\end{aligned}$$

Showing that:

$$C^{2D}_{xyxy} = C^{2D}_{yxxy} = C^{2D}_{xyyx} = C^{2D}_{yxyx} = \mu. \tag{2.A.18}$$

The 2D analogues of the 3D Lamé parameters are then given by:

$$C^{2D}_{xxxx} = C^{2D}_{yyyy} = \frac{4\mu(\lambda+\mu)}{(\lambda+2\mu)} = \lambda^{2D} + 2\mu^{2D} \tag{2.A.19a}$$

$$C^{2D}_{xxyy} = C^{2D}_{xxyy} = \frac{2\lambda\mu}{(\lambda+2\mu)} = \lambda^{2D} \tag{2.A.19b}$$

$$C^{2D}_{xyxy} = C^{2D}_{yxxy} = C^{2D}_{xyyx} = C^{2D}_{yxyx} = \mu = \mu^{2D}. \tag{2.A.19c}$$

Rewriting this in terms of the Youngs modulus and Poisson's ratio E, ν as per:

$$\lambda = \frac{E\nu}{(1+\nu)(1-2\nu)}, \tag{2.A.20a}$$

$$\mu = \frac{E}{2(1+\nu)}, \tag{2.A.20b}$$

results in:

$$\lambda^{2D} = \frac{E\nu}{(1+\nu)(1-\nu)} = \frac{E\nu}{(1-\nu^2)} \tag{2.A.21a}$$

$$\mu^{2D} = \frac{E}{2(1+\nu)} \tag{2.A.21b}$$

$$\lambda^{2D} + 2\mu^{2D} = \frac{E}{(1+\nu)(1-\nu)} = \frac{E}{(1-\nu^2)}. \tag{2.A.21c}$$

This provides the renormalised values for the Lamé parameters to be used in EOM for the displacement fields of a isotropic plate, as is done in the main text following (2.2.26).

2.B. SUPPLEMENTARY MAGNETOSTRICTION

2.B.1. EQUATIONS OF MOTION WITH MAGNETOSTRICTION

When incorporating the magnetic degrees of freedom into our consideration of our system we start from a Lagrangian combining the elastic and magnetic DOFs.

$$\begin{aligned} L &= L_{\text{el}} + L_{\text{mag}} + L_{\text{ms}} \\ &= L_{\text{el}} - F_0 - A_{2ij} M_i M_j - A_{4ijkl} M_i M_j M_k M_l - \bar{\lambda}_{ijkl} \epsilon_{ij} M_k M_l \end{aligned} \tag{2.B.1}$$

As mentioned in the main text the purely magnetic part of this Lagrangian does not contribute to the EOM for the elastic degrees of freedom as it does not contain any dependence on the displacement fields. The contributions of L_{ms} to the EOM of the displacement fields can be found by substituting L_{ms} into the right hand sides of equations

(2.A.5):

$$\frac{\partial \mathscr{L}_{\text{ms}}}{\partial u_1^0} - \partial_t \frac{\partial \mathscr{L}_{\text{ms}}}{\partial \partial_t u_1^0} - \partial_1 \frac{\partial \mathscr{L}_{\text{ms}}}{\partial \partial_1 u_1^0} - \partial_2 \frac{\partial \mathscr{L}_{\text{ms}}}{\partial \partial_2 u_1^0} \tag{2.B.2a}$$

$$\frac{\partial \mathscr{L}_{\text{ms}}}{\partial u_2^0} - \partial_t \frac{\partial \mathscr{L}_{\text{ms}}}{\partial \partial_t u_2^0} - \partial_1 \frac{\partial \mathscr{L}_{\text{ms}}}{\partial \partial_1 u_2^0} - \partial_2 \frac{\partial \mathscr{L}_{\text{ms}}}{\partial \partial_2 u_2^0} \tag{2.B.2b}$$

$$\frac{\partial \mathscr{L}_{\text{ms}}}{\partial \tilde{u}_3} - \partial_t \frac{\partial \mathscr{L}_{\text{ms}}}{\partial \partial_t \tilde{u}_3} - \partial_1 \frac{\partial \mathscr{L}_{\text{ms}}}{\partial \partial_1 \tilde{u}_3} - \partial_2 \frac{\partial \mathscr{L}_{\text{ms}}}{\partial \partial_2 \tilde{u}_3} - \partial_3 \frac{\partial \mathscr{L}_{\text{ms}}}{\partial \partial_3 \tilde{u}_3} \tag{2.B.2c}$$

$$\frac{\partial \mathscr{L}_{\text{ms}}}{\partial u_3^0} - \partial_t \frac{\partial \mathscr{L}_{\text{ms}}}{\partial \partial_t u_3^0} + \partial_1 \partial_1 \frac{\partial \mathscr{L}_{\text{ms}}}{\partial \partial_1 \partial_1 u_3^0} + \partial_2 \partial_2 \frac{\partial \mathscr{L}_{\text{ms}}}{\partial \partial_2 \partial_2 u_3^0} + \partial_1 \partial_2 \frac{\partial \mathscr{L}_{\text{ms}}}{\partial \partial_1 \partial_2 u_3^0}. \tag{2.B.2d}$$

Here equations a-d correspond with a-d of (2.A.5). Writing out the magnetostriction term:

$$\begin{aligned}
\mathscr{L}_{\text{ms}} &= \bar{\lambda}_{ijkl} \epsilon_{ij} M_k M_l \\
&= M_k M_l \big(\bar{\lambda}_{11kl} (\partial_1 u_1^0 - x_3 \partial_1 \partial_1 u_3^0) + \bar{\lambda}_{22kl} (\partial_2 u_2^0 - x_3 \partial_2 \partial_2 u_3^0) \\
&\quad + \bar{\lambda}_{33kl} \partial_3 \tilde{u}_3 + \bar{\lambda}_{23kl} \partial_2 \tilde{u}_3 + \bar{\lambda}_{13kl} \partial_1 \tilde{u}_3 \\
&\quad + 2\bar{\lambda}_{12kl} (\frac{1}{2} (\partial_2 u_1^0 + \partial_1 u_2^0) - x_3 \partial_1 \partial_2 u_3^0) \big)
\end{aligned} \tag{2.B.3}$$

and substituting this in (2.B.2) results in[11]:

$$-\partial_1 (M_k M_l \bar{\lambda}_{11kl}) - \partial_2 (M_k M_l \bar{\lambda}_{12kl}) \tag{2.B.4a}$$

$$-\partial_1 (M_k M_l \bar{\lambda}_{(12kl)}) - \partial_2 (M_k M_l \bar{\lambda}_{22kl}) \tag{2.B.4b}$$

$$-\partial_1 (M_k M_l \bar{\lambda}_{13kl}) - \partial_2 (M_k M_l \bar{\lambda}_{23kl}) - \partial_3 (M_k M_l \bar{\lambda}_{33kl}) \tag{2.B.4c}$$

$$-\partial_1 \partial_1 (M_k M_l \bar{\lambda}_{11kl} x_3) - \partial_2 \partial_2 (M_k M_l \bar{\lambda}_{22kl} x_3) - \partial_1 \partial_2 (2 M_k M_l \bar{\lambda}_{12kl} x_3). \tag{2.B.4d}$$

These are the additional terms to the EOM for the displacement fields originating from the magnetostrictive coupling. An interesting observation to be made at this point is that when both the magnetisation and the magnetostriction do not vary over the material volume, i.e. $\partial_i M_j = 0$ and $\partial_m \bar{\lambda}_{ijkl} = 0$, as in a homogeneus system, all terms in (2.B.4) vanish.

REFERENCES

33. Gelfand, I. M., Fomin, S. V. & Silverman, R. A. *Calculus of Variations* (Prentice-Hall, Englewood Cliffs, N. J., 1963).

[11] Note that this term does not include any new dependencies on the displacement fields or their derivatives meaning no new terms need to be added to the Euler-Lagrange equations given in (2.A.5).

3

MAGNETIC ORDER IN 2D ANTIFERROMAGNETS REVEALED BY SPONTANEOUS ANISOTROPIC MAGNETOSTRICTION

The temperature dependent order parameter provides important information on the nature of magnetism. Using traditional methods to study this parameter in two-dimensional (2D) magnets remains difficult, particularly for insulating antiferromagnetic (AF) compounds. Here, we show that its temperature dependence in AF MPS_3 (M(II) = Fe, Co, Ni) can be probed via the anisotropy in the resonance frequency of rectangular membranes, mediated by a combination of anisotropic magnetostriction and spontaneous staggered magnetization. Density functional calculations followed by a derived orbital-resolved magnetic exchange analysis confirm and unravel the microscopic origin of this magnetization inducing anistropic strain. We further show that the temperature and thickness dependent order parameter allows to deduce the material's critical exponents characterising magnetic order. Nanomechanical sensing of magnetic order thus provides a future platform to investigate 2D magnetism down to the single-layer limit.

Parts of this chapter have been published in [34].

3.1. INTRODUCTION

LAYERED two-dimensional (2D) magnetic materials offer an emerging platform for fundamental studies of magnetism in the 2D limit. Their stackability into van der Waals heterostructures opens pathways to non-trivial magnetic phases and technological applications, including sensors, memories and spintronic logic devices [35]. In addition to ferromagnetism, first observed in CrI_3 [36] and $Cr_2Ge_2Te_6$ [37], antiferromagnetism in 2D materials has also been studied in $FePS_3$ [38] and CrSBr [39]. Antiferromagnetic (AF) materials are of particular technological interest due to their high spin-wave propagation speed and lack of macroscopic stray fields, making them strong candidates for spintronic and magnonic applications [40–44].

For insulating, thin AF materials, such as MPS_3 (M(II) = Fe, Co, Ni), few methods are available to study their intrinsic magnetism. Conventional techniques, such as neutron scattering, magnetization measurement by a superconducting quantum interference device (SQUID) or vibrating sample magnetometry are challenging, due to the small volumes of exfoliated 2D materials. Other methods, suited to 2D materials, require electrical conductance, the presence of specific optical modes or ferromagnetic order; they are therefore difficult to apply [35]. In contrast, strain applied to 2D magnetic materials was shown to be an extremely powerful tool to modify the magnetic properties, inducing magnetization reversal [45], reorientating the easy-axis [46], or reversing the exchange interaction [47]. In addition, the direct coupling between strain, resonance frequency and magnetization in membranes of 2D magnets, makes nanomechanical resonance a sensitive method for studying their phase transitions [22, 48, 49]. Here, we show, guided by density functional theory (DFT), that the magnetic order parameter of MPS_3 AF membranes can be quantified through the anisotropy in their magneto-elastic response; from its temperature dependence the critical exponents are determined, and their thickness dependence is investigated.

3.2. RESULTS AND DISCUSSION

3.2.1. FIRST PRINCIPLES ANALYSIS OF SPONTANEOUS MAGNETOSTRICTION IN MPS_3

Transition-metal phosphorus trisulphides, with general formula MPS_3, are layered materials stacked in a monoclinic lattice with symmetry group C2/m [50], as shown in the top view of a single-layer in the paramagnetic phase, figure 3.1a, top panel. The spins of $FePS_3$ point out-of-plane, whereas both $CoPS_3$ and $NiPS_3$ are in-plane systems with their spins preferentially aligned along the *a* axis. The intralayer AF order forms a zigzag configuration, as shown in bottom panel of figure 3.1a, leading to two opposite aligned magnetic sub-latices. The difference of the magnetisation between these sub-latices is the Néel vector. In bulk $CoPS_3$ and $NiPS_3$, these layers with this staggered magnetism are stacked in a ferromagnetic (FM) fashion with Néel transition temperatures, T_N, around 119 and 155 K, respectively [51, 52]. The interlayer magnetic interactions in $FePS_3$ are AF with a transition around 118 K [53].

To analyse the effect of magnetic ordering on the lattice, a first principles structural optimization of $FePS_3$, $CoPS_3$ and $NiPS_3$ based on density functional theory (DFT) was preformed. For the ground state zigzag magnetic configuration, the calculations pre-

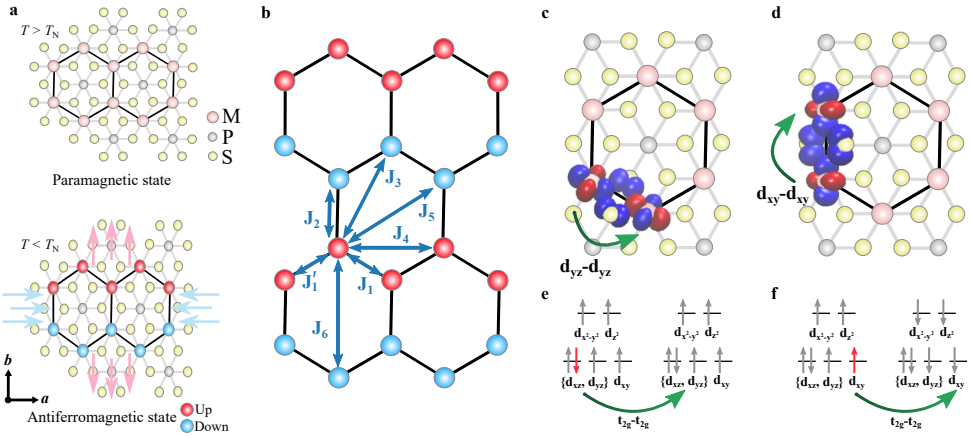

Figure 3.1: **Magnetostriction in MPS_3 membranes. a, top panel,** Crystalline structure of MPS_3 in the paramagnetic phase ($T > T_N$). Black hexagons indicate the organisation of magnetic atoms in the lattice. **a, bottom panel,** Crystalline structure of MPS_3 at the AF phase ($T < T_N$) as it elongates in the b and contracts in the a direction. Light blue and red arrows indicate the axial lattice distortion. **b,** Illustration of the exchange interaction parameters included into the Heisenberg spin Hamiltonian. **c-d,** Calculated maximally localized Wannier orbitals. Green arrows illustrate the most relevant FM superexchange channels for J_1 (J_1') (**c**) and J_2 (**d**), corresponding with the d_{yz}-d_{yz} (d_{xz}-d_{xz}) and d_{xy}-d_{xy} orbitals, respectively. **e-f,** Electron configuration of the Fe^{2+} magnetic ions connected by J_1 (**e**) and J_2 (**f**), showing parallel and antiparallel spin orientations, respectively.

dict a compression of the a lattice parameter with respect to the crystallographic, non-magnetic structure of 2.545% and 1.328% for the Co and Fe derivatives respectively (see Table 3.1). In addition, the b axis expands by 0.402% (Co) and 0.359% (Fe). In contrast, in $NiPS_3$ the lattice parameters remain almost unchanged. The crystal and magnetic structures are strongly connected in these compounds, which is further corroborated by simulations of different spin configurations. The results of which are available in the supplementary information of [34].

The 2D nature of the magnetostriction was studied by simulating the evolution of lattice parameters in multilayer monoclinic $FePS_3$ (which presents AF interlayer coupling), obtaining similar results (1.462% compression in the a axis and 0.437% expansion in the b axis). This indicates that the anisotropic magnetostiction is independent of the stacking and interlayer interactions.

The microscopic mechanism governing the spontaneous magnetostriction in these materials is studied using orbital-resolved magnetic exchange analyses based on maximally localized Wannier functions, (see supplementary information of [34]). The analysis shows that the spontaneous magnetostriction calculated in $FePS_3$ and $CoPS_3$ arises from isotropic magnetic exchange interactions between t_{2g}-t_{2g} orbitals. Specifically, for $FePS_3$ the main magnetic exchange channels, substantially affected by the compression of the a and expansion of the b lattice parameters, are the ones involving t_{2g}-t_{2g} interactions of FM nature. The changes in the lattice parameters result in an increase in J_1 and J_1', see figure 3.1, due to a decrease in distance between the d_{yz}-d_{yz} and d_{xz}-d_{xz} orbitals, respectively, shown in figure 3.1c. Simultaneously, these changes cause a decrease of

	$CoPS_3$		$FePS_3$		$NiPS_3$	
Lattice parameter (Å)	***a***	***b***	***a***	***b***	***a***	***b***
NM	5.895	10.19	5.947	10.301	5.812	10.07
AF-zigzag	5.745	10.231	5.868	10.338	5.817	10.061
Change (%)	-2.545	+0.402	-1.328	+0.359	+0.086	-0.089

Table 3.1: $CoPS_3$, $FePS_3$ and $NiPS_3$ lattice parameters of the crystallographic non-magnetic (NM) and fully optimized zigzag antiferromagnetic (AF-zigzag) configurations, as calculated by DFT (see supplementary information of [34]).

J_2 due to a larger separation of the d_{xy}-d_{xy} orbitals, see figure 3.1d. This is compatible with the electron configuration of Fe^{2+} (d^6), which has these orbitals partially filled and allows FM hopping between them, see figure 3.1e,f.

This hopping effect also occurs for Co^{2+} (d^7) although the additional electron present for Co blocks the d_{xy}-d_{xy} pathway. This results in a stronger effect along J_1 and J_1' for the optimized structure, maximizing FM interactions in the zigzag chain, which involve the d_{yz}-d_{yz} and d_{xz}-d_{xz} orbitals, respectively. For the Ni^{2+} derivative (d^8), the t_{2g} energy levels are fully occupied, which results in a blocking of the t_{2g}-t_{2g} magnetic super-exchange channels. This leads to an almost negligible modification in the lattice parameters of the optimized structure with respect to the crystallographic non-magnetic one.

3.2.2. RESONANCE FREQUENCY CHANGES DUE TO SPONTANEOUS MAGNETOSTRICTIVE STRAIN

The predicted anisotropic change of lattice parameters when going from the paramagnetic to the AF phase, causes compressive stress, σ_a, and tensile stress, σ_b, along the a axis and b axis respectively, as illustrated in figure 3.1a, bottom pannel. To quantify this anisotropy appearing at the phase transition, we use rectangular membranes, shown in figure 3.2b, to nanomechanically probe stress variations, along a specific crystallographic axis [54] (see section 3.A.1). In the following analysis, we neglect the stress contribution from the thermal expansion of the substrate, as this is small compared to that of the MPS_3 compounds [22].

The resonance frequency of the fundamental mode of a rectangular membrane, f_{res}, is approximately given by [29]:

$$f_{res} \approx \frac{1}{2}\sqrt{\frac{1}{\rho}\left[\frac{1}{w^2}\sigma_w + \frac{1}{l^2}\sigma_l\right]}, \tag{3.2.1}$$

where ρ is the mass density, w and l are respectively the width and length of the membrane, as indicated in figure 3.2b, and $\sigma_{w,l}$ are the stresses parallel to these directions. For high-aspect-ratio membranes ($w \ll l$), the mechanical resonance frequency is mostly determined by the stress along the shortest direction, σ_w. The membranes shown in this chapter range in aspect ratio from 1 to 5 up to 1 to 12, corresponding to the σ_l pre-factor being smaller by a factor of 25 up to 144 as compared to the σ_w pre-factor.

We study the resonance frequency of thin MPS_3 flakes suspended over star-shaped cavities with 30° angular resolution, as shown in an example device in figure 3.2b. When the longest side of the cavity is aligned along a crystallographic axis (a or b) and $w \ll l$, its fundamental resonance frequency (f_a or f_b) is determined by the stress along the perpendicular axis (σ_b or σ_a):

$$f_a \approx \frac{1}{2}\sqrt{\frac{1}{\rho w^2}\sigma_b} \text{ and } f_b \approx \frac{1}{2}\sqrt{\frac{1}{\rho w^2}\sigma_a}. \tag{3.2.2}$$

On cavities oriented at an intermediate angle, θ, (defined with respect to the b axis), the resonance frequency is:

$$\begin{aligned} f_\theta(T) &\approx \frac{1}{2}\sqrt{\frac{1}{\rho w^2}\left[\sigma_{a,\theta} + \sigma_{b,\theta}\right]}, \\ \sigma_{a,\theta} &= \frac{E}{(1-\nu^2)}(\cos^2\theta + \nu\sin^2\theta)(\bar{\epsilon} - \epsilon_{ms,a}), \\ \sigma_{b,\theta} &= \frac{E}{(1-\nu^2)}(\sin^2\theta + \nu\cos^2\theta)(\bar{\epsilon} - \epsilon_{ms,b}), \end{aligned} \tag{3.2.3}$$

where we have used the constitutive equations for a magnetostrictive membrane with plane stress [55], while only keeping the anisotropy in the magnetostriction coefficient, see section 3.A.1. Here, E is the Young's modulus and ν is Poisson's ratio of the material. Moreover, we have $\bar{\epsilon} = \epsilon_{fab} - \epsilon_{th}$, with ϵ_{fab} the residual fabrication strain and ϵ_{th} the phononic thermal expansion induced strain variation. The magnetostrictive strain along the a and b-axes is given by $\epsilon_{ms,a,b} = \lambda_{a,b}L^2$, see section 3.A.2 for a detailed derivation of equation (3.2.3), here $\lambda_{a,b}$ are magnetostriction coefficients and L^2 is the AF order parameter squared.

The temperature dependence of the resonance frequency comprises two contributions: one due to the phononic thermal expansion coefficient α, given by

$$\epsilon_{th}(T) = \int_{T_0}^{T} \alpha(\tilde{T})\mathrm{d}\tilde{T}, \tag{3.2.4}$$

where T_0 is a reference temperature and $\tilde{T}$ the integration variable, and the magnetostrictive contribution $\epsilon_{ms,a,b}(T) = \lambda_{a,b}L^2(T)$. The former contribution is a slowly varying function of T, while the latter term contains the staggered magnetization, which increases abruptly near the phase transition; it thus can be used to determine $L(T)$, as we will show below. We assume $\lambda_{a,b}$ to be T independent, as its temperature dependence will be negligible when compared to that of $L(T)$.

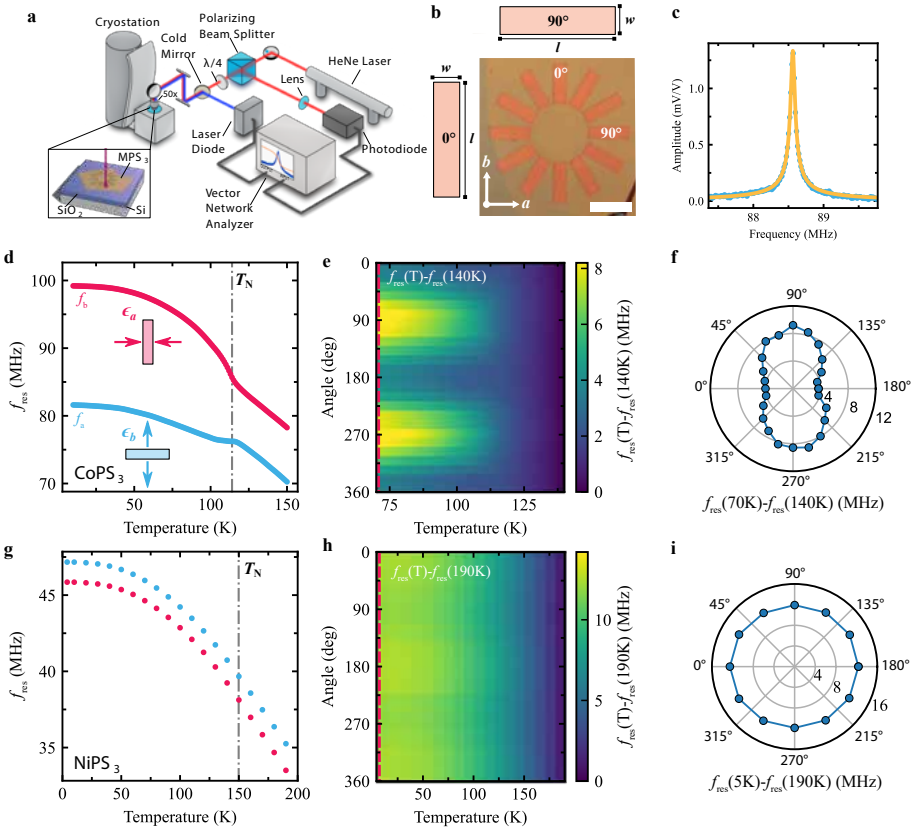

Figure 3.2: **Angle-resolved mechanical characterization via laser interferometry. a,** Schematic illustration of the laser interferometry setup and sample with rectangular cavity array. **b,** Optical image of the rectangular membranes array for a $CoPS_3$ sample. The a and b axis are determined from the resonance frequency behaviour. Scale bar: 12 μm. Schematic of 0° and 90° membranes from the array where w is the width of the membrane and l its length. **c,** Measured amplitude of the fundamental resonance peak in a $CoPS_3$ drum at $T = 10$ K and Lorentzian fit used to extract the fundamental resonance frequency, f_{res}, and quality factor, Q. **d,** Temperature dependence of f_{res} of a $CoPS_3$ rectangular membrane, shown are f_{a} (blue) and f_{b} (red) as defined in equation (3.2.2). The arrows show the dominant magnetostrictive strain contributions for the corresponding cavities. The dashed line indicates the transition temperature T_{N} extracted from the data. **e,** Resonance frequency difference, $f_{\text{res}}(T) - f_{\text{res}}(140\,\text{K})$, as a function of angle and temperature. The dashed line indicates the transition as in **d f,** Polar plot of $f_{\text{res}}(T) - f_{\text{res}}(140\,\text{K})$ taken along the red dashed line in (e). Panels **g-i,** follow the same structure as (c-e) for $NiPS_3$ resonators with negligible anisotropy, measured between 5 K and 190 K.

3.2.3. NANOMECHANICAL DETERMINATION OF THE ORDER PARAMETER

To quantify the anisotropy in the magnetic membranes, a laser interferometry technique is used to measure their resonance frequency as a function of temperature [56]. A MPS_3 flake, suspended over holes in a patterned Si/SiO_2 chip, figure 3.2b, is placed inside a cryostat with optical access as shown in figure 3.2a. Both actuation and detection are

done optically, by means of a power-modulated blue laser which opto-thermally excites the membrane, and a constant red laser which measures the change in the reflected signal resulting from the membrane's motion [22]. A typical resonance is shown in figure 3.2c, along with the damped harmonic oscillator model fit defining the resonance frequency. Figure 3.2d shows that in $CoPS_3$ f_a and f_b exhibit a similar temperature dependence for $T > T_N$, while diverging behaviour below the phase transition $T < T_N$ is visible, namely an increase of f_a and a decrease of f_b relative to an overall isotropic increase. This sudden change in $f(T)$ for the perpendicular cavities, occurring near T_N, constitutes, in accordance with the DFT calculations, the central result of this chapter as it shows that the magnetic ordering in MPS_3 leads to anisotropic strain and thus spontaneous magnetostriction. We further note that strictly speaking, T_N should be replaced by T_N^* which includes the effects of strain (see section 3.A.1). For simplicity, we here use the notation T_N for the measured transition temperatures.

The anisotropic behavior of $CoPS_3$ in the AF state is even more evident in figure 3.2e, where $f_{res}(T) - f_{res}(140\,K)$ for the different cavities of the star-shaped sample are plotted as a function of θ and temperature. The polar plot in figure 3.2f shows the data along the red dashed line at $T = 70$ K in figure 3.2e and results in a characteristic dumbbell-shape. Similar anisotropic behaviour is observed in $FePS_3$ as shown in section 3.A.3. On the contrary, for $NiPS_3$ negligible anisotropy is observed in the angle-resolved magnetostriction data in figure 3.2g-i.

To obtain $L(T)$ from the data, we first subtract the pretension contribution from the resonance frequency $f_\theta(T_0)$ by calculating $\tilde{f}_\theta^2(T) = f_\theta^2(T) - f_\theta^2(T_0)$, for each angle, where $T_0 = 150$ K is the highest temperature in our measurements. The resulting values of $\tilde{f}_\theta^2(T)$ along the crystalline axes a and b are shown in figure 3.3a,d,g for the three MPS_3 compounds. Note that this is not the same data as shown in figure 3.2, but of a sample with thickness and geometry closer to that of the sample figure 3.3d,e,f, for ease of comparison. With equation (3.2.3), we then calculate the difference $\tilde{f}_b^2(T) - \tilde{f}_a^2(T)$ which yields

$$\tilde{f}_b^2 - \tilde{f}_a^2 = \frac{E}{4\rho w^2(1+\nu)}\,[\lambda_a - \lambda_b]\,L^2. \tag{3.2.5}$$

We can now use equation (3.2.5) to access the critical behaviour of L below T_N by plotting $\tilde{f}_b^2 - \tilde{f}_a^2$ as a function of temperature. As shown in figure 3.3b,e,h, the trend presents the typical critical behaviour with a non-zero order parameter appearing in the ordered state for $T < T_N$. Figures 3.3c,f,i show the same critical curve as figure 3.3b,e,h respectively, plotted on a logarithmic scale against the reduced temperature $(1 - T/T_N)$. Note that the difference $\tilde{f}_b^2 - \tilde{f}_a^2$ for $NiPS_3$, is substantially smaller than that of the $Fe/CoPS_3$ membranes indicative of a weaker anisotropic magnetostrictive behaviour.

The angle dependence of the resonance frequencies allows us to estimate the ratio $r_{ab} = \lambda_a/\lambda_b$ between the magnetostriction parameters, $\lambda_{a,b}$, see section 3.A.2. This ratio we directly compare to DFT calculations: Experimentally, we find for $FePS_3$, $r_{ab} = -2.3 \pm 0.3$ while from the DFT calculations we estimate $r_{ab} = -3.70$. For $CoPS_3$ (taking [57] $\nu_{CoPS_3} = 0.293$), the experimental value is -1.42 ± 0.07 and the DFT one -6.33. We conclude that although both the sign and order of magnitude of the magnetostrictive anisotropy in these compounds are well reproduced in the current work, more detailed studies will be needed to obtain full quantitative correspondence with theory.

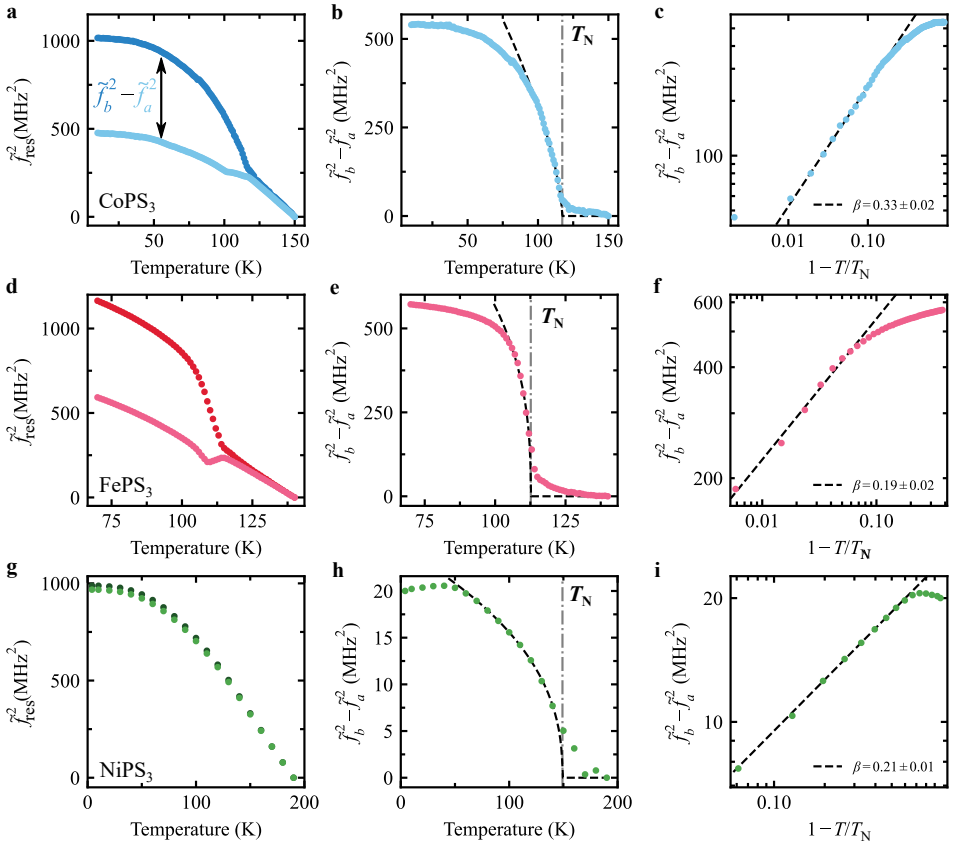

Figure 3.3: **Anisotropy and critical behaviour in resonance frequency of MPS_3 (M(II) = Co, Fe, Ni) membranes. a,** Pretension corrected resonance frequency ($\tilde{f}_a^2(T) = f_a^2(T) - f_a^2(150\text{K})$ (light) and $\tilde{f}_b^2(T) = f_b^2(T) - f_b^2(150\text{K})$ (dark)) of rectangular membranes of $CoPS_3$. **b,** Difference of the corrected frequency squared $\tilde{f}_b^2 - \tilde{f}_a^2$ proportional to the order parameter L^2 from equation 3.2.5. The dashed-dotted line indicates the measured transition temperature T_N. The dashed black line is a powerlaw fit through the data close to T_N (see Supplementary Note 6). **c,** Difference of the corrected frequency squared $\tilde{f}_b^2 - \tilde{f}_a^2$ as a function of the reduced temperature $1 - T/T_N$. The dashed black line is the fit from b where the slope defines the critical exponent 2β. **d-f,** and **g-i,** follow the same structure as (a-c) for $FePS_3$ and $NiPS_3$ resonators, respectively.

3.2.4. THICKNESS DEPENDENCE OF CRITICAL BEHAVIOUR

When transitioning from 3D systems to 2D systems the magnetic order is generally changed. For isotropic 2D systems the Mermin-Wagner theorem forbids magnetic order as it will be destroyed by thermal fluctuations. However, for anisotropic 2D systems different magnetic orders can exist, such as Ising, XY and Kosterlitz-Thouless phases [59]. By varying the thickness, i.e., the number of layers, of the MPS_3 compounds we are able to investigate the transition from the bulk 3D behaviour to the 2D behaviour.

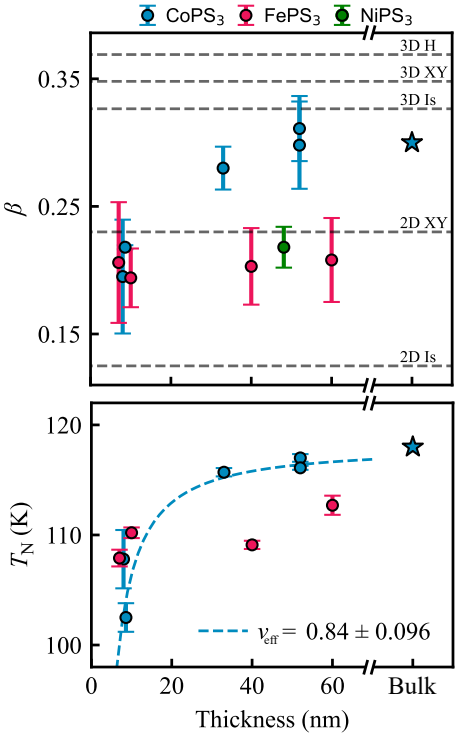

Figure 3.4: **Thickness dependence of critical behaviour.** Average critical exponent, β, and critical temperature, T_N, of MPS_3 resonators plotted as a function of thickness. The blue stars indicate $CoPS_3$ bulk values from [58]. Critical parameters have been determined from power law fits to $\tilde{f}_b^2 - \tilde{f}_\theta^2$, as shown in figure 3.3b,e,h, and then taking the average value over the fit parameter for all angles $\theta \neq 0$. Error bars are calculated from standard deviation of fit results for all θ. The horizontal gray dashed lines in the upper plot indicate the expected values of β for the 3D or 2D versions of the Heisenberg (H), XY or Ising (Is) models. The blue dashed line in the lower panel indicates a fit to equation (3.2.7) through the $CoPS_3$ data with $\nu_{eff} = 0.84 \pm 0.13$.

As follows from Landau's theory of phase transitions (see section 3.A.1), $L(T)$ near T_N is given by

$$L^2(T) = \begin{cases} 0 & \text{if } T > T_N \\ \frac{A}{2B}(T_N - T)^{2\beta} & \text{if } T < T_N, \end{cases} \tag{3.2.6}$$

where A and B are constants and β is a critical exponent representative of the magnetic order. We fit equation (3.2.6) to the data in figure 3.3b,e,h in the region close to T_N (indicated by the black dashed line in figure 3.3b,e,h) to extract the critical exponent β and T_N for the three materials (see section 3.A.5 for more details on the fitting procedure). In the logarithmic plot of the critical curve the fitting of a straight line shows good agreement to the data points, consistent with the result of equation (3.2.6). The values for β and T_N are plotted in figure 3.4 as a function of thickness, t, and listed in section 3.A.5, table 3.2.

For the weakly anisotropic $NiPS_3$, $\beta = 0.218 \pm 0.016$, comparable to the value ($\beta = 0.22 \pm 0.02$) found in Ref. [60], and consistent with the expected 2D XY magnetic dimensionality ($\beta_{2DXY} = 0.233$) of $NiPS_3$ [61]. For $FePS_3$ we find $\beta = 0.208 \pm 0.033$, comparable with literature values [62]. For both β and T_N no appreciable thickness dependence is observed, similar to what has previously been reported in Ref. [63], where changes in the critical behaviour mostly become visible in the monolayer limit.

For thicker $CoPS_3$ samples ($t = 40 - 60$ nm) we find $\beta = 0.289 \pm 0.034$ close to what is reported in literature for the bulk ($\beta_{bulk} = 0.3 \pm 0.01$ [51]) and consistent with the 3D Ising model. For samples with $t < 10$ nm the measured β, on the other hand, is 0.195 ± 0.045,

closer to β_{2DXY} as shown in the top panel of figure 3.4. This constitutes a noticeable change in β while going from bulk to thinner samples. Similarly, we observe for $CoPS_3$ a decrease in T_N from the bulk value of 118 K down to ~ 100 K, similar to what was previously reported in Ref. [58]. We fit a power law to the dependence of T_N on thickness,

$$T_N(t)/T_N^{3D} \propto 1-(C/t)^{1/\nu_{eff}}, \tag{3.2.7}$$

where C is a non-universal constant related to the interlayer coupling, and ν_{eff} is an effective critical exponent related to the correlation length [64]. Fitting the $CoPS_3$ data points with $T_N^{3D} = 118$ K [58] yields $C = 1.43 \pm 0.457$ nm and $\nu_{eff} = 0.84 \pm 0.096$. This value of ν_{eff} is intermediate between the expected values of $\nu_{eff} = 0.630$ for the 3D Ising and $\nu_{eff} = 1$ for the 2D Ising models, and indicative of a transition regime [59].

3.3. CONCLUSIONS

In conclusion, we provide a comprehensive analysis of the anisotropic magnetostriction effect in MPS_3 compounds and its implications to the dynamics of membrane made from them. DFT calculations provide a microscopic explanation for the anisotropic lattice deformation in $CoPS_3$, $FePS_3$ and $NiPS_3$ which are consistent with our measurements. We further demonstrate the relation between magnetic ordering and anisotropy in the mechanical resonance frequency of suspended MPS_3 resonators, providing a direct measure of the AF order parameter in absence of an external magnetic field. We observe a thickness dependence in the critical behaviour of $CoPS_3$ resonators [51, 58], which is absent in the case of $FePS_3$. The presented technique is of particular interest for the study of 2D magnetism given the scarcity of methods available to investigate critical phenomena of van der Waals materials in the atomically thin limit.

REFERENCES

22. Šiškins, M. *et al.* Magnetic and electronic phase transitions probed by nanomechanical resonators. *Nat. Commun.* **11,** 2698 (June 2020).

29. Leissa, A. W. & Qatu, M. S. *Vibrations of continuous systems* (New York: McGraw-Hill, 2011).

34. Houmes, M. J. A. *et al.* Magnetic order in 2D antiferromagnets revealed by spontaneous anisotropic magnetostriction. *Nat. Commun.* **14,** 8503 (Dec. 2023).

35. Mak, K. F., Shan, J. & Ralph, D. C. Probing and controlling magnetic states in 2D layered magnetic materials. *Nat. Rev. Phys.* **1,** 646–661 (Sept. 2019).

36. Huang, B. *et al.* Layer-dependent ferromagnetism in a van der Waals crystal down to the monolayer limit. *Nature* **546,** 270–273 (June 2017).

37. Gong, C. *et al.* Discovery of intrinsic ferromagnetism in two-dimensional van der Waals crystals. *Nature* **546,** 265–269 (Apr. 2017).

38. Lee, J.-U. *et al.* Ising-Type Magnetic Ordering in Atomically Thin $FePS_3$. *Nano Lett.* **16,** 7433–7438 (Nov. 2016).

39. Telford, E. J. *et al.* Layered Antiferromagnetism Induces Large Negative Magnetoresistance in the van der Waals Semiconductor CrSBr. *Adv. Mater.* **32,** 2003240 (2020).
40. Němec, P., Fiebig, M., Kampfrath, T. & Kimel, A. V. Antiferromagnetic opto-spintronics. *Nat. Phys.* **14,** 229–241 (Mar. 2018).
41. Rahman, S., Torres, J. F., Khan, A. R. & Lu, Y. Recent Developments in van der Waals Antiferromagnetic 2D Materials: Synthesis, Characterization, and Device Implementation. *ACS Nano* **15,** 17175–17213 (Nov. 2021).
42. Mertens, F. *et al.* Ultrafast Coherent THz Lattice Dynamics Coupled to Spins in the van der Waals Antiferromagnet $FePS_3$. *Adv. Mater.,* 2208355 (2022).
43. Boix-Constant, C. *et al.* Probing the Spin Dimensionality in Single-Layer CrSBr van der Waals Heterostructures by Magneto-Transport Measurements. *Adv. Mater.* **34,** 2204940 (2022).
44. Esteras, D. L., Rybakov, A., Ruiz, A. M. & Baldoví, J. J. Magnon Straintronics in the 2D van der Waals Ferromagnet CrSBr from First-Principles. *Nano Lett.* **22,** 8771–8778 (2022).
45. Wang, Y. *et al.* Strain-Sensitive Magnetization Reversal of a van der Waals Magnet. *Adv. Mater.* **32,** 2004533 (2020).
46. Ni, Z. *et al.* Imaging the Néel vector switching in the monolayer antiferromagnet $MnPSe_3$ with strain-controlled Ising order. *Nat. Nanotechnol.* **16,** 782–787 (Apr. 2021).
47. Cenker, J. *et al.* Reversible strain-induced magnetic phase transition in a van der Waals magnet. en. *Nat. Nanotechnol.,* 1–6 (Jan. 2022).
48. Šiškins, M. *et al.* Nanomechanical probing and strain tuning of the Curie temperature in suspended Cr2Ge2Te6-based heterostructures. *npj 2D Mater. Appl.* **6** (June 2022).
49. Jiang, S., Xie, H., Shan, J. & Mak, K. F. Exchange Magnetostriction in Two-Dimensional Antiferromagnets. *Nat. Mater.* **19,** 1295–1299 (June 2020).
50. Chittari, B. L. *et al.* Electronic and magnetic properties of single-layer MPX_3 metal phosphorous trichalcogenides. *Phys. Rev. B* **94** (Nov. 2016).
51. Wildes, A. R., Simonet, V., Ressouche, E., Ballou, R. & McIntyre, G. J. The magnetic properties and structure of the quasi-two-dimensional antiferromagnet $CoPS_3$. *J. Phys. Condens. Matter.* **29,** 455801 (Oct. 2017).
52. Joy, P. A. & Vasudevan, S. Magnetism in the layered transition-metal thiophosphates MPS_3 (M=Mn, Fe, and Ni). *Phys. Rev. B* **46,** 5425–5433 (Sept. 1992).
53. Takano, Y. *et al.* Magnetic properties and specific heat of MPS_3 (M=Mn, Fe, Zn). *J. Magn. Magn. Mat.* **272-276,** E593–E595 (May 2004).
54. Šiškins, M. *et al.* Highly Anisotropic Mechanical and Optical Properties of 2D Layered As_2S_3 Membranes. *ACS Nano* **13,** 10845–10851 (Aug. 2019).
55. Landau, L. D., Pitaevskii, L. P. & Lifshitz, E. M. *Electrodynamics of continuous media* 2nd ed. (Butterworth, New York, 1984).

56. Bunch, J. S. *et al.* Electromechanical Resonators from Graphene Sheets. *Science* **315,** 490–493 (2007).

57. Gui, Q. *et al.* Extrinsic-Structured Bimetallic-Phase Ternary Metal Phosphorus Trisulfides Coupled with N-Doped Graphitized Carbon for Superior Electrochemical Lithium Storage. *Adv. Energy Mater.* **11,** 2003553 (Jan. 2021).

58. Liu, Q. *et al.* Magnetic order in XY-type antiferromagnetic monolayer $CoPS_3$ revealed by Raman spectroscopy. *Phys. Rev. B* **103,** 235411 (June 2021).

59. Gibertini, M., Koperski, M., Morpurgo, A. F. & Novoselov, K. S. Magnetic 2D materials and heterostructures. *Nat. Nanotechnol.* **14,** 408–419 (May 2019).

60. Afanasiev, D. *et al.* Controlling the anisotropy of a van der Waals antiferromagnet with light. *Sci. Adv.* **7,** eabf3096 (June 2021).

61. Kim, K. *et al.* Suppression of magnetic ordering in XXZ-type antiferromagnetic monolayer $NiPS_3$. *Nat. Commun.* **10,** 345 (Jan. 2019).

62. Yao-Dong, D. *et al.* A Mössbauer study of the magnetic coupling in iron phosphorous trisulfides. *Chinese Phys.* **13,** 1652 (2004).

63. Zhang, Q. *et al.* Observation of Giant Optical Linear Dichroism in a Zigzag Antiferromagnet $FePS_3$. *Nano Lett.* **21,** 6938–6945 (2021).

64. Zhang, R. & Willis, R. F. Thickness-Dependent Curie Temperatures of Ultrathin Magnetic Films: Effect of the Range of Spin-Spin Interactions. *Phys. Rev. Lett.* **86,** 2665–2668 (May 2001).

3.A. SUPPLEMENTARY INFORMATION

3.A.1. LANDAU THEORY OF SECOND-ORDER PHASE TRANSITIONS AND SPONTANEOUS MAGNETOSTRICTION

Magnetostriction is a coupling between magnetic and mechanical parts of a system. This coupling can be described by an energy term in the total free energy [55], written as:

$$F - F_0 = U_{\mathrm{el}}(z) + a(T - T_{\mathrm{N}})^{2\beta} L_i L_i + B L_i L_i L_i L_i - \sigma_{ij}(z)\lambda_{ijkl} L_k L_l. \tag{3.A.1}$$

Here F is the total free energy of the system in the AF phase at zero magnetic field, F_0 is the free energy of the paramagnetic phase, $U_{\mathrm{el}}(z)$ is the elastic energy of a membrane with deflection z at its centre, T is the temperature and T_{N} is the Néel temperature, L_i are the components of the Néel vector, β is a critical exponent, a and B are positive constants, $\sigma_{ij}(z)$ is the stress tensor and λ_{ijkl} is the magnetostriction tensor. The last term couples the stress to the Néel vector thereby describing the magnetostriction. If we assume the Néel vector to be aligned with the easy axis, equation (3.A.1) simplifies to:

$$F - F_0 = U_{\mathrm{el}}(z) + a(T - T_{\mathrm{N}})^{2\beta} L^2 + B L^4 - \sigma_{ij}(z)\lambda_{ij} L^2, \tag{3.A.2}$$

where L is the magnetic order parameter (i.e. the magnitude of the Néel vector). For notational convenience we write λ_{ij} in dropping the third and fourth index of λ_{ijkl} as only the component where kl corresponds to the easy axis contributes. The elastic energy in a homogeneous membrane is given by [28]

$$U_{\mathrm{el}} = \int\int \frac{S_{ijkl}}{2}\sigma_{ij}(x,y,z)\sigma_{kl}(x,y,z)\,dx\,dy, \tag{3.A.3}$$

where the integration runs over the in plane dimensions of the membrane, z is the membrane deflection at its centre and should not be confused with the out-of-plane coordinate. For ease of notation we will not explicitly write the integration and coordinate dependence from here on. Assuming the membrane thickness does not vary significantly we can take the out-of-plane stress component to vanish, $\sigma_{zx} = \sigma_{zy} = \sigma_{zz} = 0$. equation (3.A.3) then simplifies to

$$\begin{aligned} U_{\mathrm{el}} = {} & \frac{S_{xxxx}}{2}\sigma_{xx}\sigma_{xx} + \frac{S_{yyyy}}{2}\sigma_{yy}\sigma_{yy} + S_{xxyy}\sigma_{xx}\sigma_{yy} \\ & + 2S_{xxxy}\sigma_{xx}\sigma_{xy} + 2S_{yyxy}\sigma_{yy}\sigma_{xy} + 2S_{xyxy}\sigma_{xy}\sigma_{xy}. \end{aligned} \tag{3.A.4}$$

Taking our coordinates such that x, y correspond with the principle stress directions all terms containing σ_{xy} vanish. This simplifies the elastic energy further to

$$U_{\mathrm{el}} = \frac{S_{xxxx}}{2}\sigma_{xx}\sigma_{xx} + \frac{S_{yyyy}}{2}\sigma_{yy}\sigma_{yy} + S_{xxyy}\sigma_{xx}\sigma_{yy}. \tag{3.A.5}$$

Assuming the material has isotropic elastic properties the relevant compliance tensor components are

$$S_{xxxx} = S_{yyyy} = \frac{1}{E} \text{ and } S_{xxyy} = \frac{-\nu}{E}. \tag{3.A.6}$$

Substituting this in to equation (3.A.5) we find

$$U_{\text{el}} = \frac{1}{2E}\sigma_{xx}\sigma_{xx} + \frac{1}{2E}\sigma_{yy}\sigma_{yy} - \frac{\nu}{E}\sigma_{xx}\sigma_{yy}. \tag{3.A.7}$$

By taking the derivative of the free energy with respect to either z or L we find the forces acting on these degrees of freedom, ϕ_L and ϕ_z respectively to be given by

$$-\phi_L = \frac{d(F-F_0)}{dL} = 2a(T-T_{\text{N}})^{2\beta}L + 4BL^3 - 2\sigma_{ij}(z)\lambda_{ij}L, \tag{3.A.8}$$

$$-\phi_z = \frac{d(F-F_0)}{dz} = \left(S_{ijkl}\sigma_{ij}(z) + \lambda_{kl}L^2\right)\frac{d\sigma_{kl}(z)}{dz}. \tag{3.A.9}$$

ORDER PARAMETER AND CRITICAL EXPONENT

In order to find an equation that describes the order parameter as a function of temperature, we find a solution for equation (3.A.8) for the case where $\phi_L = 0$. Aside from the trivial solution $L = 0$, we find for below the transition the additional solution:

$$L^2 = -\frac{a}{2B}(T-T_{\text{N}})^{2\beta} + \frac{\sigma_{ij}\lambda_{ij}}{2B}, \tag{3.A.10}$$

which can be rewritten, using $T_{\text{N}}^* = T_{\text{N}} - (\frac{\sigma_{ij}\lambda_{ij}}{a})^{\frac{1}{2\beta}}$, as[22]:

$$L^2 = \frac{a}{2B}(T_{\text{N}}^* - T)^{2\beta}. \tag{3.A.11}$$

This equation now describes the temperature dependence of the order parameter in a critical region near T_{N} with a corresponding critical exponent β.

MAGNETOSTRICTIVE STRAIN AND RESONANCE FREQUENCY

To assess the magnetostriction contribution to strain and thus the frequency of a rectangular membrane resonator, we need to find stiffness of the membrane from its force-deflection equation. In doing that we analyse equation (3.A.9). First, we describe strain equation for the rectangular membrane at its centre as:

$$\epsilon_{xx}(z) = \epsilon_{0,x} + \frac{c_1}{2}\frac{z^2}{l^2} \tag{3.A.12a}$$

$$\epsilon_{yy}(z) = \epsilon_{0,y} + \frac{c_1}{2}\frac{z^2}{w^2}, \tag{3.A.12b}$$

where c_1 is a geometrical pre-factor that describes the deflection shape of the fundamental mode of vibration [54, 65]. For $w \ll l$ we can neglect the z dependence of $\epsilon_{xx}(z)$. Now, we substitute (3.A.12) to (3.A.9) and using the relation $\sigma_{ij} = C_{ijkl}\epsilon_{kl}$, we find

$$-\phi_z = \left(\frac{E}{1-\nu^2}\epsilon_{0,y} + \frac{\nu E}{1-\nu^2}\epsilon_{0,x} - \lambda_{yy}L^2\right)\frac{c_1}{w^2}z + \frac{E}{1-\nu^2}\frac{c_1^2}{2}\frac{z^3}{w^4}, \tag{3.A.13}$$

where we used that $C_{xxxx} = C_{yyyy} = \frac{E}{1-\nu^2}$ and $C_{yyxx} = C_{xxyy} = \frac{\nu E}{1-\nu^2}$. equation (3.A.13) can be written as

$$-\phi_z = k_1 z - \frac{\lambda_{ij}c_1}{w^2}L^2 z + k_3 z^3, \tag{3.A.14}$$

where k_1 is the elastic linear stiffness and k_3 is the cubic elastic stiffness, given by

$$k_1 = \frac{E}{1-\nu^2}(\epsilon_{0,y} + \nu\epsilon_{0,x})\frac{c_1}{w^2}, \tag{3.A.15}$$

$$k_3 = \frac{E}{1-\nu^2}\frac{c_1^2}{2w^4}. \tag{3.A.16}$$

Assuming small deflections we can neglect the z^3 contribution in equation (3.A.13) and find that the linear stiffness is changed with respect to the purely elastic case. If we consider a rectangular cavity with it's long axis is parallel to the crystalline axis b or a respectively we find:

$$-\phi_{z\,\mathrm{b,a}} = \left(k_1 - \frac{c_1}{w^2}\lambda_{\mathrm{a,b}}L^2\right)z, \tag{3.A.17}$$

where $\lambda_{\mathrm{a,b}}$ are the phenomenological magnetostriction coefficients, chosen such that to couple a and b crystalline directions and L. That leads to a change in the effective linear stiffness $k_{b,a}$:

$$k_{\mathrm{b,a}} = k_1 - \frac{c_1}{w^2}\lambda_{\mathrm{a,b}}L^2, \tag{3.A.18}$$

which can be used to write the frequency equations using $f_{\mathrm{a,b}} = \frac{1}{2\pi}\sqrt{\frac{k_{\mathrm{a,b}}}{m}}$ as:

$$f_{\mathrm{b}} \approx \frac{1}{2\pi}\sqrt{\frac{1}{m}\frac{c_1}{w^2}\left[\frac{E}{1-\nu^2}(\epsilon_{0,\mathrm{a}} + \nu\epsilon_{0,\mathrm{b}}) - \lambda_{\mathrm{a}}L^2\right]}, \tag{3.A.19a}$$

$$f_{\mathrm{a}} \approx \frac{1}{2\pi}\sqrt{\frac{1}{m}\frac{c_1}{w^2}\left[\frac{E}{1-\nu^2}(\epsilon_{0,\mathrm{b}} + \nu\epsilon_{0,\mathrm{a}}) - \lambda_{\mathrm{b}}L^2\right]}, \tag{3.A.19b}$$

where m is the mass of the membrane and where the magnetostrictive strain is defined by:

$$\epsilon_{\mathrm{ms,a}} = \frac{c_1}{mw^2}\lambda_{\mathrm{a}}L^2, \tag{3.A.20}$$

$$\epsilon_{\mathrm{ms,b}} = \frac{c_1}{mw^2}\lambda_{\mathrm{b}}L^2. \tag{3.A.21}$$

Taking the difference of the squares of equations (3.A.19) and assuming $\epsilon_{0,\mathrm{a}} = \epsilon_{0,\mathrm{b}}$, we arrive at the final equation:

$$f_{\mathrm{b}}^2 - f_{\mathrm{a}}^2 = -\frac{1}{4\pi^2}\frac{c_1}{mw^2}\left[\lambda_{\mathrm{b}} - \lambda_{\mathrm{a}}\right]L^2, \tag{3.A.22}$$

which relates the antiferromagnetic order parameter L with the measured resonance frequencies of orthogonal resonators aligned to crystalline axes $f_{\mathrm{a,b}}$ in the ordered phase. Finally, one can show that by plugging equation (3.A.11) into (3.A.22):

$$f_{\mathrm{b}}^2 - f_{\mathrm{a}}^2 \propto (T_{\mathrm{N}}^* - T)^{2\beta}, \tag{3.A.23}$$

which can be used to fit experimental data to extract critical exponent β near the phase transition temperature T_{N}^*.

3.A.2. DERIVATION OF ANISOTROPIC RESONANCE FREQUENCY

Here, we derive the general equation of the resonance frequency of a rectangular cavity oriented at an angle θ with respect to one of the crystalline axes, as schematically shown in figure 3.5. The global coordinate system is defined by the crystallographic axes a and b, along which the material deforms resulting in stresses σ_{aa} and σ_{bb}. The longest side of the cavity, with length l, can be oriented at an arbitrary angle θ with respect to b. Let us

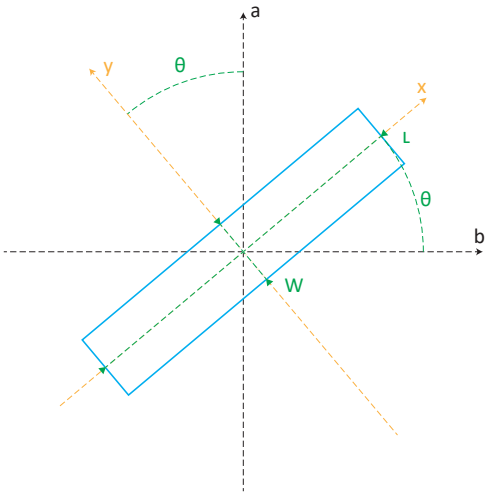

Figure 3.5: **Schematic illustration of rectangular membrane** Rectangular membrane of width w and length l oriented with its long side at an angle θ with respect to the crystalline direction b. The x-y direction refer to the main directions of the rectangular membrane.

first consider a cavity oriented parallel to a crystallographic axis. Since the membranes are very thin, we can assume that the stress in the direction perpendicular to the plane is zero, $\sigma_{cc} = 0$. The membrane's stress tensor can then be expressed as

$$\boldsymbol{\sigma} = \begin{pmatrix} \sigma_{aa} & \sigma_{ab} \\ \sigma_{ba} & \sigma_{bb} \end{pmatrix}_{ab}, \tag{3.A.24}$$

where the subscript $()_{ab}$ indicates that the stress tensor is expressed in the basis of the crystallographic coordinate system. If we assume that there are no shear forces acting on the crystal lattice, $\sigma_{ab} = \sigma_{ba} = 0$, there will be no shear on cavities oriented along the main crystallographic axes. Now, if we consider a rectangular cavity rotated by θ with respect to the crystallographic axes, we can define a rotated xy-coordinate system oriented along the main axis of the rectangle. To express $\boldsymbol{\sigma}$ in this coordinate system we use the tensor transformation rule, $\sigma'_{ij} = q_{ki} q_{lj} \sigma_{kl}$ where q_{ij} are components of the rotation tensor transforming the ab-coordinate system, $\boldsymbol{e}$, into the xy-coordinate system,

$\boldsymbol{e'}$ as $\boldsymbol{e}'_i = q_{ij}\boldsymbol{e}_j$. We then get:

$$\begin{aligned}\boldsymbol{\sigma} &= \begin{pmatrix}\sigma_{xx} & \sigma_{xy}\\ \sigma_{yx} & \sigma_{yy}\end{pmatrix}_{xy}\\ &= \begin{pmatrix}\cos^2(\theta)\sigma_{aa}+\sin^2(\theta)\sigma_{bb} & -\cos(\theta)\sin(\theta)\sigma_{aa}+\sin(\theta)\cos(\theta)\sigma_{bb}\\ -\sin(\theta)\cos(\theta)\sigma_{aa}+\sin(\theta)\cos(\theta)\sigma_{bb} & \sin^2(\theta)\sigma_{aa}+\cos^2(\theta)\sigma_{bb}\end{pmatrix}_{xy}.\end{aligned} \tag{3.A.25}$$

The fundamental resonance frequency of a rectangular membrane oriented at an angle θ with respect to the crystallographic axis can be expressed as

$$f_\theta \approx \frac{1}{2}\sqrt{\frac{1}{\rho}\left(\frac{\sigma_{xx}}{l^2}+\frac{\sigma_{yy}}{w^2}\right)}. \tag{3.A.26}$$

In the case of high-aspect ratio membranes ($w \ll l$), equation 3.A.26 can be approximated to

$$f_\theta \approx \frac{1}{2}\sqrt{\frac{1}{\rho}\frac{\sigma_{yy}}{w^2}} = \frac{1}{2}\sqrt{\frac{1}{\rho w^2}\left(\sin^2(\theta)\sigma_{aa}+\cos^2(\theta)\sigma_{bb}\right)}, \tag{3.A.27}$$

which is (3.2.3) of the main text.

Now, let us consider the constitutive equations of the material:

$$\begin{aligned}c_1 &= E(\epsilon_{\text{fab},aa}-\epsilon_{\text{th},aa}-\epsilon_{\text{ms},aa})\\ &= E\left(\epsilon_{\text{fab},aa}-\int_{T_0}^{T_1}\alpha_{\text{a}}(T)dT-\lambda_{\text{a}}L^2(T_1)\right) = \sigma_{aa}(T_1)-\nu\sigma_{bb}(T_1)\end{aligned} \tag{3.A.28a}$$

$$\begin{aligned}c_2 &= E(\epsilon_{\text{fab},bb}-\epsilon_{\text{th},bb}-\epsilon_{\text{ms},bb})\\ &= E\left(\epsilon_{\text{fab},bb}-\int_{T_0}^{T_1}\alpha_{\text{b}}(T)dT-\lambda_{\text{b}}L^2(T_1)\right) = \sigma_{bb}(T_1)-\nu\sigma_{aa}(T_1),\end{aligned} \tag{3.A.28b}$$

where ϵ_{fab} is the residual fabrication strain at $T = T_0$, ϵ_{th} and ϵ_{ms} are respectively the thermal expansion and magnetostriction contributions to strain, α is the thermal expansion coefficient, λ the magnetostriction coefficient and E is the Young's modulus, which is assumed to be isotropic. We can thus write

$$\sigma_{aa} = c_1+\nu\sigma_{bb} \tag{3.A.29a}$$

$$\sigma_{bb} = c_2+\nu\sigma_{aa}, \tag{3.A.29b}$$

which can be combined in the following expressions for σ_{aa} and σ_{bb}:

$$\sigma_{aa} = \frac{c_1+\nu c_2}{1-\nu^2}, \tag{3.A.30a}$$

$$\sigma_{bb} = \frac{c_2+\nu c_1}{1-\nu^2}. \tag{3.A.30b}$$

We can now rewrite equation 3.A.27 in terms of the different contributions to strain, i.e. residual strain from fabrication (ϵ_{fab}), thermal expansion ($\propto \alpha$) and magnetostriction

($\propto \lambda$):

$$\begin{aligned} f_\theta(T) &= \frac{1}{2}\sqrt{\frac{E}{\rho w^2(1-\nu^2)}\left[\sin^2\theta(c_1+\nu c_2)+\cos^2\theta(c_2+\nu c_1)\right]} \\ &= \frac{1}{2}\sqrt{\frac{E}{\rho w^2(1-\nu^2)}\Big[(\sin^2\theta+\nu\cos^2\theta)(\epsilon_{\mathrm{fab},aa}-\epsilon_{\mathrm{th},aa}-\epsilon_{\mathrm{ms},aa}) \\ &\qquad + (\cos^2\theta+\nu\sin^2\theta)(\epsilon_{\mathrm{fab},bb}-\epsilon_{\mathrm{th},bb}-\epsilon_{\mathrm{ms},bb})\Big]}, \end{aligned} \tag{3.A.31}$$

which is consistent with equation (3.A.19). We can eliminate the pretension ϵ_{fab} terms by considering $\tilde{f}_\theta^{\,2}(T) = f_\theta^2(T) - f_\theta^2(T_0)$. In the following, we assume that the only anisotropic temperature-dependent contribution to the total strain comes from magnetostriction, thus we take $\epsilon_{\mathrm{th},aa} = \epsilon_{\mathrm{th},bb} = \epsilon_{\mathrm{th}}$. By definition of θ we have $b \to \theta = 0°$ and $a \to \theta = 90°$. From equation (3.A.31), we then find, consistent with (3.A.22), that $\tilde{f}_{\mathrm{a}}^2 - \tilde{f}_{\mathrm{b}}^2$ becomes

$$\begin{aligned} \tilde{f}_{\mathrm{a}}^2 - \tilde{f}_{\mathrm{b}}^2 &= \frac{E}{4\rho w^2(1+\nu)}\left(-\epsilon_{\mathrm{ms},aa}+\epsilon_{\mathrm{ms},bb}\right) \\ &= -\frac{E}{4\rho w^2(1+\nu)}(\lambda_{\mathrm{a}}-\lambda_{\mathrm{b}})L^2, \end{aligned} \tag{3.A.32}$$

from which we can directly extract the order parameter. The thermal expansion contribution to strain ϵ_α is proportional to the integral over the temperature of the thermal expansion coefficient α, which is proportional to the Debye specific heat, C_{Debye}, via the Grünesen parameter. Thus, the derivative with respect to temperature of f_θ^2

$$\begin{aligned} \frac{df_\theta^2}{dT} &= \frac{E}{4\rho w^2(1-\nu^2)}\Bigg[(\sin^2\theta+\nu\cos^2\theta)\left(-\alpha-\lambda_{\mathrm{a}}\frac{dL^2}{dT}\right) \\ &\qquad + (\cos^2\theta+\nu\sin^2\theta)\left(-\alpha-\lambda_{\mathrm{b}}\frac{dL^2}{dT}\right)\Bigg] \\ &= \frac{-E}{4\rho w^2(1-\nu^2)}\left[\alpha(1+\nu)+\left(\sin^2\theta(\lambda_{\mathrm{a}}+\nu\lambda_{\mathrm{b}})\frac{dL^2}{dT}+\cos^2\theta(\lambda_{\mathrm{b}}+\nu\lambda_{\mathrm{a}})\frac{dL^2}{dT}\right)\right]. \end{aligned} \tag{3.A.33}$$

can be fitted to $b_1 C_{\mathrm{Debye}} + b_2\frac{dL^2}{dT}$ where b_1 and b_2 are fit parameters, and $\frac{dL^2}{dT}$ is estimated from equation 3.A.32. The results of these fits along with measured data of $\frac{df_\theta^2}{dT}$ are shown in figure 3.6. The polar plots of the resulting $b_1(\theta)$ and $b_2(\theta)$ are shown in figure 3.7, which confirm that the thermal contribution to strain does not exhibit significant anisotropic behavior. From equation (3.A.33), the expected angle dependence of the parameter b_2 is

$$b_2(\theta) = -\left(\frac{E}{4\rho w^2(1-\nu^2)}\right)\left[(\sin^2\theta(\lambda_{\mathrm{a}}+\nu\lambda_{\mathrm{b}})+\cos^2\theta(\lambda_{\mathrm{b}}+\nu\lambda_{\mathrm{a}})\right], \tag{3.A.34}$$

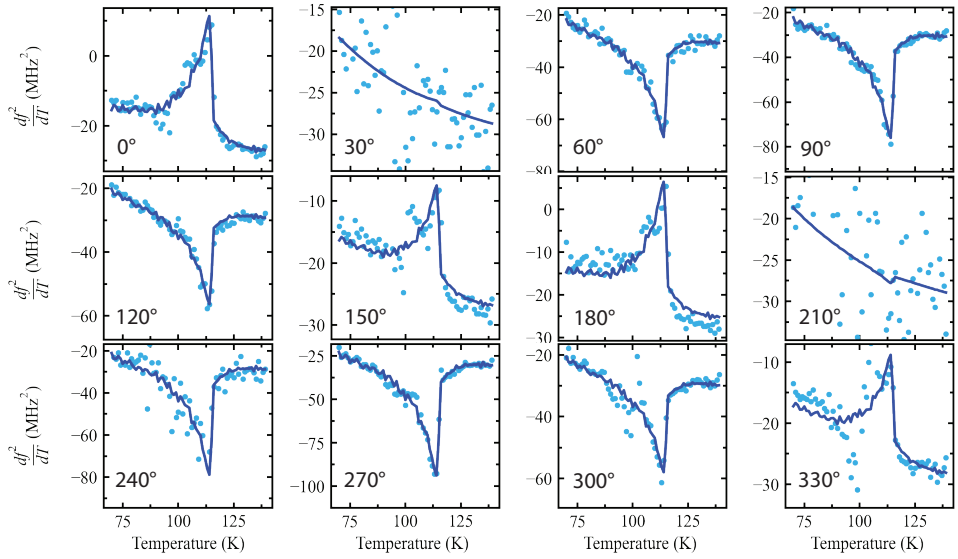

Figure 3.6: **Angle-resolved $\frac{df^2}{dT}$:** Plot of measured (light blue dots) $\frac{df^2}{dT}$ and fit to $b_1 C_{\text{Debye}} + b_2 \frac{dL^2}{dT}$ (blue full line) for all angles of a star-shaped array of $CoPS_3$.

which we use to fit $b_2(\theta)$ in figure 3.7 to $A\sin^2\theta + B\cos^2\theta$ where

$$\frac{A}{B} = \frac{\lambda_a + \nu\lambda_b}{\lambda_b + \nu\lambda_a}. \tag{3.A.35}$$

The fit yields $A/B = -2.062$ and -1.798 for $CoPS_3$ and $A/B = -5.025$ and -8.695 for $FePS_3$.

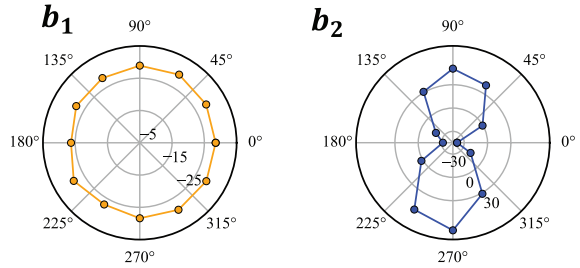

Figure 3.7: **Polar plot of fit parameters b_1 and b_2:** Polar plot of fit parameters b_1 and b_2 from the fits to df^2/dT shown in figure 3.6.

3.A.3. ANISOTROPIC RESONANCE FREQUENCY OF $FePS_3$ RESONATORS

Figure 3.8 shows resonance frequency data measured on $FePS_3$ star-cavity resonators, as presented in figure 3.2 of the main text for $CoPS_3$ and $NiPS_3$ samples. Figure 3.8a shows

the temperature dependence of the resonance frequency of membranes oriented along the a-axis (in red) and b-axis (in blue). Similarly to $CoPS_3$, the opposite strain along a and b arising from spontaneous magnetostriction results in opposite behaviour of the resonance frequency near the transition temperature T_N. The resulting anisotropic response is further illustrated in the map plot of resonance frequency as a function of temperature and angles in figure 3.8b and in the polar plot of $f_{res}(70\,K) - f_{res}(140\,K)$ in figure 3.8c.

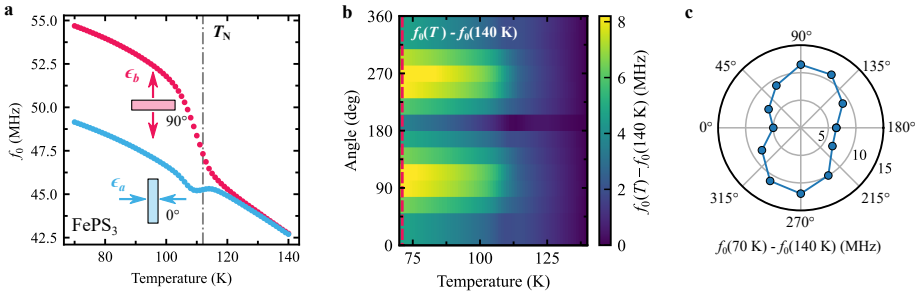

Figure 3.8: **Angle-resolved resonance frequency data of $FePS_3$ membranes. a,** Temperature dependence of f_{res} of a $FePS_3$ rectangular membrane orientated at 0° (blue) and 90° (red) with respect to the b crystallographic axis. Note that $f_{0,0°}$ and $f_{0,90°}$ are proportional to the strain ϵ_a and ϵ_b respectively, see equation (3.2.2). The dashed-dotted grey line indicates the transition temperature T_N. **b,** Resonance frequency difference, $f_{res}(T) - f_{res}(140\,K)$, as a function of angle θ with respect to b-axis and temperature. **c,** Polar plot of $f_{res}(70\,K) - f_{res}(140\,K)$ taken along the red dashed line in (b).

3.A.4. ORDER PARAMETER RELATED FREQUENCY DIFFERENCE $\tilde{f}_B^2 - \tilde{f}_\theta^2$

We have shown how to relate the difference $f_b^2 - f_a^2$ to the antiferromagnetic order parameter through the magnetostriction induced strain at the phase transition $\epsilon_{ms,aa} = \lambda_a L^2$ and $\epsilon_{ms,bb} = \lambda_b L^2$. In general, $\tilde{f}_b^2 - \tilde{f}_\theta^2$ is also proportional to L^2, where $\tilde{f}_\theta^2$ is the pretension corrected resonance frequency of a rectangular cavity oriented at an angle θ with respect to the b-axis. We show this quantity for the $CoPS_3$ and $FePS_3$ star-cavity resonators in figure 3.9a,d by plotting $\tilde{f}_b^2 - \tilde{f}_\theta^2$ as a function of angle and temperature in figure 3.9b,e. Figure 3.9c,f shows the polar plot of $\tilde{f}_b^2 - \tilde{f}_\theta^2$ taken along the red dashed line in 3.9b,e.

This relation of $\tilde{f}_b^2 - \tilde{f}_\theta^2$, for $\theta \neq 90°$, with the order parameter is observed for the thicker samples ($t > 10$ nm) and it is exploited to have a better estimate of the critical parameters β and T_N as discussed in 3.A.5. For thinner resonators every irregularity, like wrinkles or tears, can strongly affect their mode shapes. In some cases, these imperfections can drastically change the resonance frequency of the fundamental mode, as well as its temperature dependence. Therefore, when analysing the critical behaviour of thin flakes, we choose only the most pristine and unaffected membranes fabricated out of a single flake by optical inspection to minimise the chance of being affected by these irregularities.

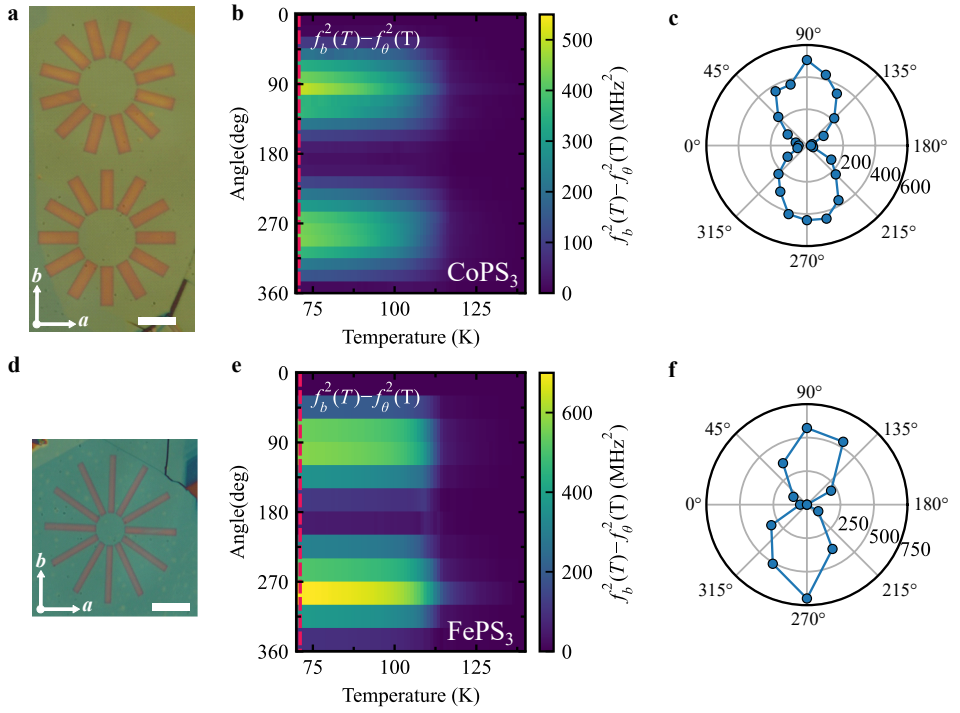

Figure 3.9: **Angle-resolved data of $f_{\mathbf{b}}^2 - f_\theta^2 \propto L^2$ of CoPS$_3$ and FePS$_3$ membranes. a, d,** Optical image of the CoPS$_3$ (a) and FePS$_3$ (d) resonators. Scale bar 12 μm. **b,** Resonance frequency difference, $f_{\mathrm{b}}^2 - f_\theta^2 \propto L^2$, as a function of angle θ and temperature of the CoPS$_3$ sample in (a). **c,** Polar plot of $f_{\mathrm{b}}^2 - f_\theta^2$ taken along the red dashed line in (b). **e,f** follows the same structure as (b,c) for the FePS$_3$ sample in (d).

3.A.5. CRITICAL CURVE FIT

To extract critical parameters β and T_{N} shown in figure 3.3 and 3.4 of the main text, we fit the order parameter related difference $f_{\mathrm{b}}^2 - f_{\mathrm{a}}^2 \propto L^2$ to the power law $A_\theta(1 - T/T_{\mathrm{N}})^{2\beta}$. The experimental determination of critical parameters is often debated due to the difficulty of extracting from one set of data, three strongly correlated parameters, β, T_{N} and A_θ. In addition, finite size effects are known to smear the transition which usually results in a non-zero tail of the order parameter in the paramagnetic state and makes it harder to unambiguously determine the critical temperature. Also, the choice of the temperature interval for the fit is not universal and it is often arbitrary.

In order to have a better estimate of the critical exponents from our experiments, we compute $f_{\mathrm{b}}^2 - f_\theta^2$ for all θ in a star and fit the data to $A_\theta(1 - T/T_{\mathrm{N}})^{2\beta}$. For each star, we then calculate the average value and standard deviation of the critical parameters T_{N} and β weighted by the error from the fit, $T_{\mathrm{N,err}}$ and β_{err}.

We start with an initial guess, which denote T_{N}^*, for T_{N} by extracting the maximum of the derivative of $f_{\mathrm{b}}^2 - f_\theta^2$ with respect to temperature as shown in figure 3.10. We then fit the $A_\theta(1 - T/T_{\mathrm{N}})^{2\beta}$ to $f_{\mathrm{b}}^2 - f_\theta^2$ over the range $[\alpha T_{\mathrm{N}}^*, T_{\mathrm{N}}^*]$, for α varying between $[0.85, 0.95]$ allowing A, T_{N}, β to vary. We define the total error for each α to be $T_{\mathrm{N,err}} + \beta_{\mathrm{err}}$, where

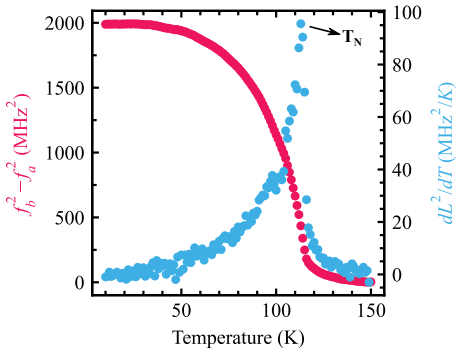

Figure 3.10: **First estimate of T_N from the derivative of the order parameter.** A plot showing $\tilde{f}_b^2 - \tilde{f}_a^2$ in red and its temperature derivative in blue. The temperature at which the derivative shows a maximum is used as the initial guess for T_N.

$T_{N,err}$, β_{err} are the standard deviation errors of the fit. We take the extracted T_N, β with corresponding $T_{N,err}$, β_{err} to be ones given the fit corresponding to the α minimizing the total error. We repeat this process for each θ yielding a distribution of T_N, β. The weighted mean of this distribution is calculated as follows:

$$\overline{\beta} = \frac{1}{N} \sum_{\theta} \beta \frac{\beta_{err,min}}{\beta_{err}}, \tag{3.A.36}$$

where N is the number of cavity pairs and $\beta_{err,min}$ the β_{err} of the pairing with smallest β_{err}. We then fit a normal distribution with $\overline{\beta}$ as mean to the distribution of β where we weigh each β by $\frac{\beta_{err,min}}{\beta_{err}}$, from which the standard deviation is extracted. Using the same process to calculate the mean an standard deviation of the transition temperature, T_N. The resulting parameters for each sample are listed in Table 3.2.

Material	Sample	t (nm)	β	T_N (K)
$CoPS_3$	1	33	0.28 ± 0.017	115.7 ± 0.38
$CoPS_3$	2	52	0.311 ± 0.025	117 ± 0.35
$CoPS_3$	3	52	0.298 ± 0.034	116.1 ± 0.18
$CoPS_3$	4	8	0.195 ± 0.0446	107.8 ± 2.65
$CoPS_3$	5	8.6	0.218 ± 0.002	102.5 ± 1.3
$FePS_3$	1	60	0.208 ± 0.0328	112.7 ± 0.87
$FePS_3$	2	40	0.203 ± 0.03	109.1 ± 0.37
$FePS_3$	3	10	0.194 ± 0.023	110.2 ± 0.48
$FePS_3$	4	7	0.206 ± 0.047	107.9 ± 0.76
$NiPS_3$	1	48	0.218 ± 0.016	150.7 ± 0.7

Table 3.2: **Critical exponents of MPS_3 samples.** Critical exponents, β and T_N, for $CoPS_3$, $FePS_3$ and $NiPS_3$ samples of different thicknesses, extracted following the procedure described in section 3.A.5

REFERENCES

22. Šiškins, M. *et al.* Magnetic and electronic phase transitions probed by nanomechanical resonators. *Nat. Commun.* **11,** 2698 (June 2020).

28. Landau, L. D. & Lifshitz, E. M. *Theory of Elasticity* 3rd ed. (Elsevier, 1986).

54. Šiškins, M. *et al.* Highly Anisotropic Mechanical and Optical Properties of 2D Layered As_2S_3 Membranes. *ACS Nano* **13,** 10845–10851 (Aug. 2019).

55. Landau, L. D., Pitaevskii, L. P. & Lifshitz, E. M. *Electrodynamics of continuous media* 2nd ed. (Butterworth, New York, 1984).

65. Bunch, J. S. *Mechanical and electrical properties of graphene sheets* (Ph.D. thesis, Cornell University Ithaca, NY, 2008).

4

Highly Anisotropic Mechanical Response of the Van der Waals Magnet $CrPS_4$

Semiconducting van der Waals magnets exhibit a rich physical phenomenology with different collective excitations, such as magnons or excitons, that can be coupled, thereby offering new opportunities for optoelectronic, spintronic, and magnonic devices. In contrast with the well-studied van der Waals ferromagnets CrI_3 or Fe_3GeTe_2 which are isotropic, $CrPS_4$ is a layered metamagnet with a high optical and magnon transport anisotropy. Here, we investigate the structural anisotropy of $CrPS_4$ above and below the magnetic phase transition by fabricating nanomechanical resonators consisting of thin layers of $CrPS_4$. A large anisotropy is observed in the resonance frequency of resonators oriented along the crystalline a- and b-axis, indicative of a lattice expansion along the b-axis, boosted at the magnetic phase transition, and a rather small continuous contraction along the a-axis. This behavior in the mechanical response differs from that previously reported in van der Waals magnets, such as $FePS_3$ or $CoPS_3$, and can be understood from the quasi-one-dimensional nature of $CrPS_4$. The results pinpoint $CrPS_4$ as a promising material in the field of low-dimensional magnetism and show the potential of mechanical resonators for unraveling the in-plane structural anisotropy coupled to the magnetic ordering that, in a broader context, can be extended to studying structural modifications in other two-dimensional materials and van der Waals heterostructures.

Parts of this chapter have been published in [66].

4.1. INTRODUCTION

ANISOTROPY is a fundamental property necessary to fully understand the behaviour of low-dimensional materials [67]. For instance, long-range magnetic order was long thought to be forbidden in the two-dimensional (2D) limit, as per the Mermin-Wagner theorem [16], but this theorem can be circumvented if magnetic anisotropy is present, as this allows for the stabilization of different magnetic configurations [59]. Anisotropic behaviours are not limited to magnetic systems as they can also be observed in for example the electronic, optical, and structural properties. In fact, these anisotropic properties are often coupled, offering a fruitful avenue for the control of collective excitations, such as excitons, phonons, or magnons, and allowing the design of new devices in fields such as magnonics, spintronics, optoelectronics, or information storage and processing [68, 69]. In this regard, van der Waals magnets with in-plane anisotropy offer unique opportunities, both in the fundamental understanding of these materials and in terms of applications, as recently shown by the exciton-magnon coupling reported for CrSBr or the fabrication of spintronic and magnonic devices based on 2D magnets, reported in [70–74] among others.

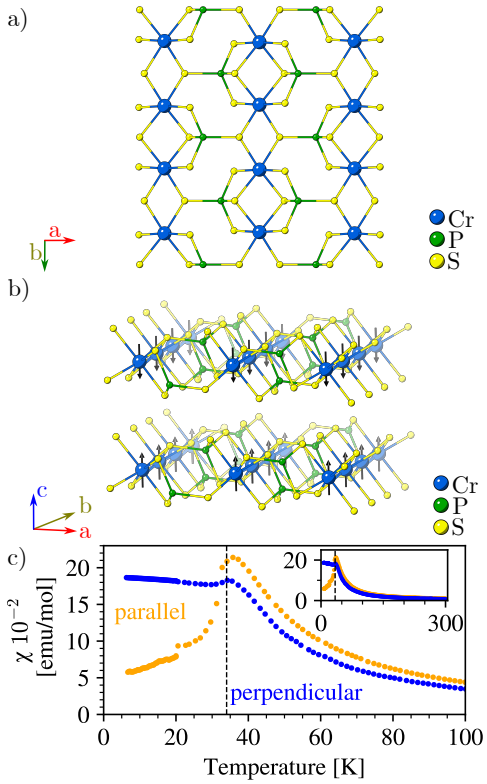

Figure 4.1: **a)** $CrPS_4$ crystal structure along the ab-plane, in which CrS_6 octrahedra form quasi-1D chains (up-down) connected via PS_4 tetrahedra. The crystallographic a- and b-axis are indicated using red and green arrows, respectively. The Cr, P, and S atoms are colored blue, green, and yellow respectively. **b)** Layered structure of $CrPS_4$; same color coding as in a). The magnetic spin structure in the antiferromagnetic phase is indicated by the black arrows through the Cr atoms. They are ferromagnetically aligned in-plane and antiferromagnetically between the planes. **c)** Temperature dependence of the magnetic susceptibility under 1 kOe field applied parallel (orange), and perpendicular (blue) to the c-axis. The transition temperature is indicated with a black dashed line. The parallel and perpendicular susceptibility show different behaviour below the transition. The inset shows the extended temperature range (6 – 300 K) of the same data.

A promising van der Waals magnet exhibiting an interplay between the optical, electrical, magnetic, and structural properties is the magnetic van der Waals semiconductor $CrPS_4$ [75–78]. A single layer of $CrPS_4$ consists of edge-sharing CrS_6 octahedra forming

quasi-one-dimensional (1D) chains along the b-axis that are interconnected along the a-axis by PS_4 tetrahedra, figure 4.1a, thus exhibiting a marked low-dimensional character [78, 79]. Below ca. 34 K, $CrPS_4$ is an A-type antiferromagnet where ferromagnetic layers are coupled antiferromagnetically along the c-axis, see figure 4.1b. We corroborate this by magnetic susceptibility measurements of bulk crystals, using a Quantum Design MPMS-XL-5 magnetometer, the results of which are shown in figure 4.1c, and are in agreement with previous results in literature, which reports a rich magnetic phase diagram, including spin-flop and spin-flip transitions [75, 80, 81].

Optically, it exhibits a marked anisotropic behaviour, as determined by Raman spectroscopy or photoluminescence measurements; excitonic emission is furthermore tuneable by temperature and thickness [76–78, 82]. $CrPS_4$ can be thinned down to the single layer limit while preserving its magnetic ordering [83], and thin-layers have been incorporated into electronic devices, showing magnetic states controllable by a gate voltage [84]. In addition, the insulating nature of $CrPS_4$ at low temperatures is ideal for the electrical excitation and detection of magnons [70], and the fabrication of multi-bit read-only memories [85]. Despite the exciting properties of $CrPS_4$ described above, the role of the underlying in-plane anisotropic structural behaviour remains still unexplored.

Here, we take advantage, on the one hand, of the van der Waals nature of $CrPS_4$ for fabricating nanomechanical resonators based on the layered structure of the material and, on the other hand, of the high sensitivity of nanomechanical resonators to the strain concomitant to a structural modification [22, 34, 48, 86, 87]. We observe a large in-plane structural anisotropy while cooling down, exhibiting a striking opposite mechanical behaviour along the a- and b-axes. We also find indications of a previously unreported structural transition above 120 K.

4.2. RESULTS AND DISCUSSION

Crystals of $CrPS_4$ are grown by chemical vapor transport, see section 4.4. Thin layers of $CrPS_4$ are mechanically exfoliated from their bulk counterpart and deterministically transferred on top of cavities etched in a SiO_2 on Si substrate, thereby forming a nanomechanical resonator. Typical flake thicknesses suitable for covering homogeneously the cavities are in the range of 40 – 120 nm. Developing chemical routes for reaching atomically thin layers of $CrPS_4$ with larger lateral sizes may enable to study the mechanical properties of $CrPS_4$ down to the 2D limit. The fundamental mechanical resonance is characterized as a function of the temperature using a laser interferometry technique, see figure 4.2a and section 4.4. In particular, our experimental configuration is based on an optical interferometer where the $CrPS_4$ membrane acts as the moving mirror, and the silicon surface at the bottom of the drum as the fixed mirror. Thus, by focusing a red laser (Helium-Neon laser, λ = 632.8 nm) on the $CrPS_4$ membrane, we can track its motion since the amplitude of the vibration modifies the cavity length and, therefore, constructive or destructive interference takes place. The interference changes the intensity of the reflected light from the cavity, which is detected with a photodiode. Another mechanism that plays a role is the modulated absorption of the light by the $CrPS_4$ drum [88]. The motion of the membrane is triggered photothermally by focusing a blue diode laser on it (λ = 405 nm). The resonance frequency depends on the geometry, the material properties (Young's modulus, density, and Poisson's ratio) as well as the strain.

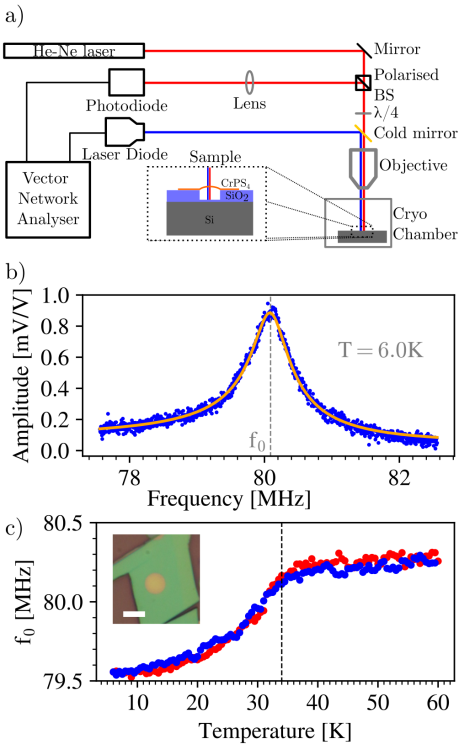

Figure 4.2: **a)** Schematics of the measurement setup. The vector network analyser (VNA) power modulates a laser diode (λ = 405 nm), as to actuate the vibrations of the drum in the cryo-chamber. Motion is read out with a photodiode connected to the VNA using a He-Ne laser (λ = 632 nm), a polarised beam-splitter (BS), and a quarter-wave plate ($\lambda/4$) to create an interferometer. Note, that the red and blue laser paths are offset for clarity but in reality they are coincident. The zoom-in of the sample shows a schematic cut-through. **b)** Representative frequency response, measured at 6 K. The blue dots are the experimental data and the orange line is a harmonic oscillator fit to them, defining the resonance frequency (gray dashed line), indicated by f_0. **c)** Resonance frequency as a function of temperature between 6 and 60 K. There is no significant difference between the heating (red) and cooling (blue) cycles. The inset shows an optical microscope image of a circular drum sample. The scale bar is 4 μm. Data shown in panels **b)** and **c)** correspond to a 120 nm thick $CrPS_4$ flake.

Therefore, variations in the temperature imply a contraction or expansion of the unit cell of the material that causes tensile or compressive strain and, consequently, modifies the resonance frequency. Thus, an enhancement (decrease) of the resonance frequency relates to a compression (expansion) of the unit cell [22].

4.2.1. CIRCULAR CAVITY

A typical resonance response of a circular resonator is shown in figure 4.2b. This response is fitted using a Lorentzian function as shown by the orange curve in figure 4.2b. From this fit the resonance frequency, f_0, is extracted. Since this resonance frequency is the lowest in the spectrum, we attribute it to the fundamental mode. The dependence of the fundamental resonance frequency on temperature, is shown in figure 4.2c.

A clear change in the resonance frequency over the measured temperature range is present: in the region between 60 and 40 K the frequency slowly decreases with decreasing temperature, whereas in the region below 40 K this decrease becomes stronger until around 28 K where the decrease becomes weaker appearing to level out at 10 K. No significant thermal hysteresis between the heating and cooling cycles is observed (compare the blue and red dots). A decrease in the resonance frequency, also called softening, implies a decrease in tensile strain in the material. Since in this case, the decrease occurs solely as a response to a change in temperature, this softening implies an expansion of the crystal lattice when cooling down, indicative of a negative thermal expansion coef-

ficient (TEC). This is comparable to previous results on the 2D magnet $Cr_2Ge_2Te_6$ [48], also displaying an softening response. Here, softening is somewhat unexpected as the related compounds of transition metal thiophosphates (such as $FePS_3$, $MnPS_3$, $CoPS_3$ or $NiPS_3$) [22, 34], show an increase of f_0 with decreasing temperature (hardening). Previously reported measurements on the same material, $CrPS_4$, by Li *et al.* [89], also show a hardening response in contrast to our results.

4.2.2. RECTANGULAR CAVITIES

A possible reason for the difference with the previously reported measurements is the fact that those measurements were done on a beam geometry for which alignment of the crystal is relevant, especially for anisotropic materials such as $CrPS_4$. Therefore we further investigate the anisotropic contributions to this strain behaviour. In order to isolate the contributions of different crystallographic axes we create star samples, which consist of an array of rectangular cavities arranged radially with a rotational offset of 30 degrees. By transferring a flake of $CrPS_4$ over the entire star multiple rectangular drums are created each with a different orientation with respect to the crystallographic axes [34]. By combining two star patterns with an offset with respect to each other of 15 degrees, the angular resolution is increased, albeit requiring larger flakes of the material. An optical image of such a sample is given in figure 4.3a. The crystallographic a- and b-axes are determined as reported by Lee *et al.* [78]; they are indicated by the red and green arrows, respectively.

We then compare the resonance frequencies of the cavities with their short axis along the a- and b-axis respectively, see figure 4.3b. Strikingly different behaviour is observed between the two directions. For the b-axis, a softening of the mode occurs while cooling, similar to the observation for circular drums, indicative of decreasing tensile and a negative TEC. In contrast, the resonance frequency of the a-axis orientation shows a small increase in the resonance frequency over the same temperature range. This increase indicates increasing tensile strain while lowering the temperature; there is no significant feature present near the phase transition point in this case.

This behaviour can be understood as a result of an expansion between the Cr centers along the quasi-1D chains (b-axis), which is enhanced upon the magnetic phase transition, and a rather steady and small compression for the orthogonal direction, that does not exhibit a discontinuity at the phase transition. These findings are in line with the reported crystal structure above and below the magnetic transition, where an expansion of the b-axis is observed while cooling from 60 to 4 K [81]. For completeness, the temperature dependence for different angular directions is presented in figure 4.3c, which emphasizes the clear anisotropic dependence of the resonance frequency and thus the lattice constants of the material. Similar trends are observed for other circular and star drums (see sections 4.A.1 and 4.A.2), manifesting the robustness of the underlying physical phenomena. Overall, we observe a pronounced negative thermal expansion along the b-axis and a small positive thermal expansion along the a-axis. The presence of such a uniaxial negative TEC is a typical fingerprint of highly anisotropic systems, as occurring in related compounds including metal halides, oxychlorides, or CrSBr [68, 90–92]. This difference in the thermal expansion coefficients along the a- and b-axes that appears below 120 K and persists down to low temperature may arise from differences in

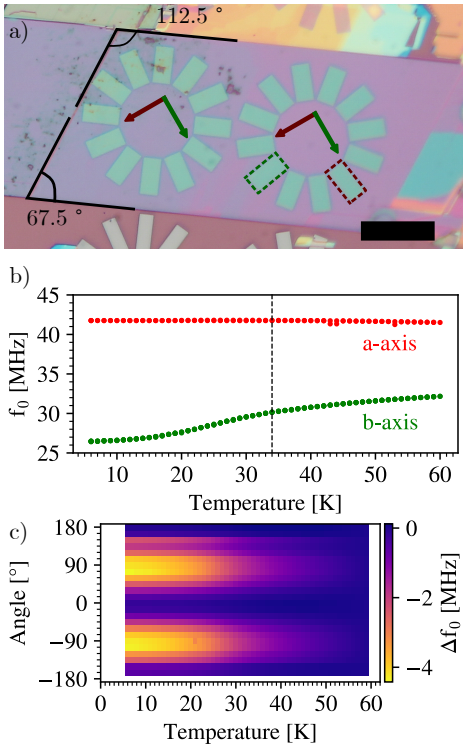

Figure 4.3: **a)** Optical microscopy picture of a star sample, displaying two arrays of rectangular cavities covered by a flake of $CrPS_4$. In the lower left corner of the flake, the fracture angle is highlighted and measured to be 67.5°. From this and the opposite angle of 112.5° the crystallographic axes are determined. The crystallographic a- (red) and b-axis (green) are indicated by colored arrows. The cavity highlighted red and green respectively correspond to the cavity with its short axis aligned along the a- (0°) and b-axis (90°) respectively. The scale bar is 20 μm. **b)** Resonance frequency as a function of temperature between 6 and 60 K for two cavities of the same flake with their short axes aligned along the crystallographic a-axis (red) and b-axis (green). There is a clear difference between the two directions, with the a-axis showing no significant change in resonance frequency, and the b-axis showing a transition behavior similar to that seen in circular drums (figure 4.2) when crossing the phase transition (black dashed line). **c)** Relative frequency change (color coded) with respect to 60 K as a function of temperature. The angle corresponds to the angle the short axis of the cavity makes with the crystallographic a-axis; the cavity with the short axis parallel to the crystallographic a-axis corresponds to 0°. Data shown in panels **b)** and **c)** correspond to a 75 nm thick $CrPS_4$ flake.

the Grüneisen parameter along the different crystal axes, which leads to an increasing anisotropy that eventually can contribute to the magnetic phase transition at lower temperature. These results may motivate further research on the $CrPS_4$ properties at temperatures well above the magnetic transition.

4.2.3. PHASE TRANSITION

Above about 120 K, figure 4.4a shows that the frequencies along the a- and b-axis exhibit the same temperature dependence. This indicates an equal expansion of the lattice for both axes as temperature decreases. However, around 120 K, the distance between the green and red curves starts to become larger, indicating a smaller expansion rate for the b-axis. Indeed, at $T \simeq 80$ K we observe an upturn in the slope for the b-axis in the resonance frequency vs. temperature dependence, shifting from a positive slope at low temperatures, which indicates an expansion of the b-axis while cooling down from 80 K to 6 K, in line with the neutron experiments in bulk $CrPS_4$ reported by Calder *et al.* [81] or Peng *et al.* [93], to a negative one, indicating a compression of the b-axis while cooling from room temperature down to 80 K. This structural anisotropy enhancement around 120 K is to our knowledge unreported in literature. This increased anisotropy and ex-

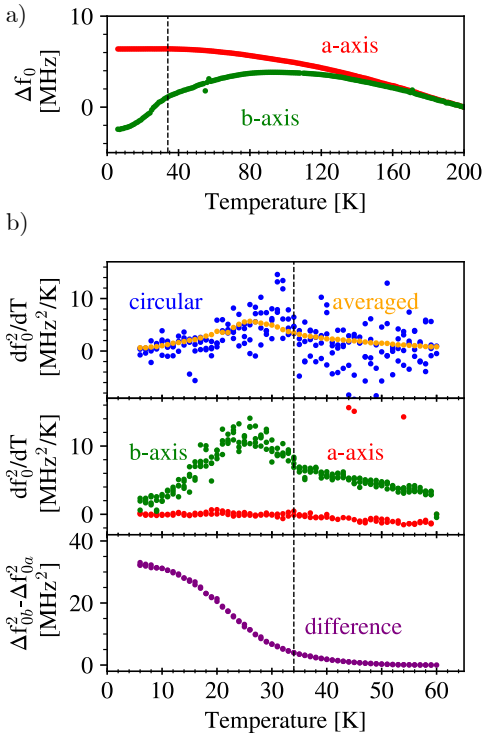

Figure 4.4: **a)** Relative change in resonance frequency w.r.t. its value at 200 K as a function of temperature between 6 and 200 K for two cavities of the same flake with their short axis aligned along the crystallographic a-axis (red) and b-axis (green). The data is the extended version from the data shown in figure 4.3.b and serves to highlight that for temperatures above 120 K the two axes have the same behavior. **b) Top panel**: derivative of the frequency squared with respect to temperature as a function of temperature of a circular cavity (blue) and averaged over all rectangular cavities in a star sample (orange). The average shows a peak around 25 K, whereas the circular cavity has a peak closer to 30 K. **Middle panel**: derivative of the frequency squared with respect to temperature as a function of temperature for two rectangular cavities with their short axis aligned along the a- (red) and b-axis (green) respectively. The a-axis shows no clear variation with temperature whereas the b-axis shows a peak around 25 K. **Bottom panel**: difference between the change in frequency squared for two rectangular cavities with their short axis aligned along the b- and a-axis respectively. The bulk transition temperature is indicated with the vertical black dashed line. Data shown in panels **a)** and **b)-c)** correspond to a 120 nm and 75 nm thick $CrPS_4$ flake, respectively.

pansion of the quasi-1D chains along the b-axis upon cooldown illustrates the interplay between lattice parameters and magnetic order that, based on the change in slope of the $f_0(T)$ curve, indicates that magnetic ordering also has a substantial influence on the lattice parameters, leading to further chain expansion.

Near the magnetic phase transition, the change in frequency for the green curve (b-axis) is even more pronounced. In contrast, the red curve (a-xis) shows a flattening off as temperature decreases with no clear features. To further characterise the behavior near the transition we investigate the temperature derivative of the frequency squared, $\frac{df_0^2}{dT}$, as it is shown that this quantity is proportional to the specific heat [22]. It is expected to have an anomaly at the phase transition. Plotting the $\frac{df_0^2}{dT}$ as a function of temperature, figure 4.4b, we find that in the case of a circular drum this $\frac{df_0^2}{dT}$ exhibits a peak around 30 K, below the expected transition temperature of 34 K. An even lower peak at 26 K is found for the average behaviour of a star sample, which is calculated by adding up the response of all cavities with different angles and dividing the total by the number of cavities involved.

Comparing the $\frac{df_0^2}{dT}$ of the two different crystallographic axes a peak around 26 K is

present for the b-axis while no such feature is present along the a-axis, see the middle panel of figure 4.4b. The fact that no sign of the phase transition is visible in the a-axis can be understood from the fact that the coupling between $\frac{df_0^2}{dT}$ and the specific heat is dependent on the TEC. Since the TEC along the a-axis around the transition is very small, as can be seen from the fact that the frequency does not vary with temperature, this coupling along the a-axis is extremely weak.

Since $\frac{df_0^2}{dT}$ is proportional to the TEC of the material [22], the data of figure 4.4b can be used to estimate the TEC along the two crystalline directions. By using the approximate frequency for a rectangular drum of high aspect ratio [34]:

$$f_0 \approx \frac{1}{2}\sqrt{\frac{E}{\rho w^2}\epsilon}, \tag{4.2.1}$$

we find an adjusted formula for the TEC in rectangular drums,

$$\alpha = -\frac{4\rho w^2}{E}\frac{df_0^2}{dT}(T) + \alpha_{Si}(T). \tag{4.2.2}$$

Here, α is the TEC, E is the Young's modulus, ρ the density, and w the length of the cavity along its short direction. $CrPS_4$ is expected to have an anisotropic Young's modulus [94], with the values along the a- (E_a) and b-axis (E_b) being respectively $E_a = 99.23$ GPa and $E_b = 64.53$ GPa, (see section 4.A.3) [95]. The values for the density, (ρ), and the width of the cavity, (w), are 2.9×10^3 Kg m^{-3} [96], and 4 μm, respectively. For $\alpha_{Si}(T)$ we use the data of Lyon *et al.* [97]. At 26 K, the temperature of the peak in $\frac{df_0^2}{dT}$, this results in a TEC along the a- and b-axis of 2×10^{-8} and -4×10^{-5} K^{-1}, see section 4.A.3. This large difference in TEC between the a- and b-axis, of 3 orders of magnitude, highlights the importance of anisotropy of $CrPS_4$.

The reason for the discrepancy between the peak in $\frac{df_0^2}{dT}$ and the expected transition temperature is unclear but can have several origins. It can be that the transition temperature is shifted from the bulk value simply by going to thinner samples of the material as it transitions to the value of a monolayer. However, the samples in this study are still quite thick, ranging from 40 to 165 nm, for which such a large effect would be surprising.

Another reason for the deviation from bulk value can be that the strain in these samples shifts the transition temperature [22, 48]. Since we do not apply any external strain, the strain responsible for this shift at the transition temperature should be due to the thermal expansion induced strain accumulated upon cooldown of the samples or by strain induced during fabrication. However, the strain required to account for the observed shift is much larger than can be rationalized by the temperature induced strain or is generally observed from fabrication induced strain.

A third reason can be that there is an additional contribution in the $\frac{df_0^2}{dT}$ which dominates the peak caused by the anomaly in the specific heat. Magnetostriction, which couples the strain in the system and the magnetic order and is present below the transition, can give such a contribution. Since strain, or equivalently pressure, modifies the bond distances and with that the superexchange pathways, and via the Goodenough-Kanamori-Arderson superexchange mechanism the magnetic exchange. An example of

which is reported by Bud'ko *et al.* [80], showing a suppression of the Néel temperature of bulk $CrPS_4$ while applying hydrostatic pressure.

Assuming the magnetostrictive coupling coefficient to be temperature independent we expect a peak in the $\frac{df_0^2}{dT}$ which coincides with the steepest slope in the order parameter. The temperature dependence of the order parameter corresponds with the slope of $\Delta f_{0b}^2 - \Delta f_{0a}^2$, see the bottom panel of figure 4.4b, as this quantity is proportional to the order parameter squared, L^2, [34]. So the curve in this figure gives an impression of the temperature dependence of the order parameter. Surprisingly the curve does not follow the standard shape from mean-field theory as the change at the transition temperature is not as abrupt. A possible explanation is the anisotropy that is not due to the magnetic order present in the system, but further research is needed to verify this. Comparing the point of steepest slope of $\Delta f_{0b}^2 - \Delta f_{0a}^2$ with the observed peak of the star sample in figure 4.4b we find that they coincide at 26 K. This suggest that magnetostriction has a significant influence on the peak in $\frac{df_0^2}{dT}$.

4.3. CONCLUSION

In conclusion, we have probed by nanomechanical resonators a large structural anisotropy in thin layers of the van der Waals metamagnet $CrPS_4$. While cooling down, we observe a continuously increasing tensile strain along the a-axis, but a decreasing tensile strain along the b-axis, that is largely enhanced upon the magnetic phase transition. This suggests an increase in the distances between the Cr^{3+} ions along the quasi-1D chain direction. Our results highlight $CrPS_4$ as a van der Waals magnet that is relevant for low-dimensional magnetism due to its marked anisotropic behaviour, in stark contrast with the most common isotropic 2D magnets, such as CrI_3 [98]. We also show that when using nanomechanical resonators for studying van der Waals magnets, careful choice of geometry is needed to account for anisotropic effects. This provides an important insight for future research directions, such as the anisotropic mechanical coupling in van der Waals heterostructures formed by distinct 2D materials or the role of collective excitations, like magnons or excitons, in the 2D limit.

4.4. EXPERIMENTAL SECTION

4.4.1. CRYSTAL GROWTH

Crystals of $CrPS_4$ are grown following a solid-state reaction inside a sealed evacuated quartz tube (pressure 5×10^{-5} mbar, length: 50 cm, internal diameter: 14 mm) with a stoichiometric amount of Cr (99.99 %, Alfa-Aesar), P (> 99.99%, Sigma-Aldrich) and S (99.99 %, Sigma-Aldrich). A three-zone furnace is used, with the material placed in the leftmost zone, with a temperature gradient of 750/650/700 °C. The temperature is kept constant for 21 days and rapidly quenched into water. With this process crystals with a length up to several centimetres are obtained. The obtained crystals were analyzed by energy-dispersive X-ray spectroscopy and by powder X-ray diffraction. The amount of elements obtained was Cr: 23.3 ± 0.5%, P: 14.8 ± 0.4% and S: 61.8 ± 1.5%, in good agreement with the expected ones (Cr: 24.6%, P: 14.7% and S: 60.7 %). The refinement of the X-ray pattern (ICSD 25059) revealed a monoclinic C face center crystal system with C121 space

group and a unit cell determined by $\alpha = \gamma = 90°$ and $\beta = 91.99(1)°$ and $a = 10.841(9)$ Å, $b = 7.247(6)$ Å and $c = 6.100(5)$ Å. The obtained results are in accordance with the ones reported in the literature [75].

4.4.2. BULK MAGNETIC MEASUREMENTS

Variable-temperature (2 – 300 K) direct current (d.c.) magnetic susceptibility measurements were carried out in an applied field of 1.0 kOe with a SQUID magnetometer (Quantum Design MPMS-XL-5).

4.4.3. SAMPLE FABRICATION

Substrates consist of thermal SiO_2 of 285 nm thickness, grown on highly doped (Si^{++}) silicon. The rectangular cavities are defined via e-beam lithography using AR-P 6200 resist. After development, the exposed SiO_2 areas are fully etched via reactive ion etching. The AR-P 6200 resist is stripped in PRS-3000 and the sample is cleaned in an O_2 plasma before stamping. The exfoliation and transfer of multi-layer $CrPS_4$ flakes are done using a combination of polydimethylsiloxane (PDMS) and polycarbonate (PC) transfer methods. First, $CrPS_4$ crystals are exfoliated onto the PDMS through scotch tape. Selected flakes are then transferred to the star-shaped cavities in the SiO_2/Si substrate. For transfer of circular drum samples, the $CrPS_4$ crystals are exfoliated using scotch tape directly on un-etched Si/SiO_2 substrates. Selected flakes are then transferred to circular-shaped cavities in the SiO_2/Si substrate using PC on PDMS [99].

4.4.4. LASER INTERFEROMETRY

Samples are mounted on a heater stage which is cooled down to 4 K using a Montana Instruments Cryostation s50 cryostat with optical access. A blue diode laser ($\lambda = 405$ nm) is used to excite the membrane optothermally via AC power modulation from a vector network analyzer (VNA). Displacements are detected by focusing a red He-Ne laser beam ($\lambda = 632$ nm) on the cavity formed by the membrane and Si substrate. The reflected light, which is modulated by the position-dependent membrane motion, is recorded by a photodiode and processed by a phase-sensitive VNA. Laser spot size is $\sim 1\,\mu$m.

4.4.5. ATOMIC FORCE MICROSCOPY

Samples are mounted in a Cypher AFM platform from Asyllum Research under atmospheric conditions and scanned using Bruker FASTSCAN-A tips. In order to minimise contamination of the samples AFM was performed after all other measurements.

REFERENCES

16. Mermin, N. D. & Wagner, H. Absence of Ferromagnetism or Antiferromagnetism in One- or Two-Dimensional Isotropic Heisenberg Models. *Phys. Rev. Lett.* **17,** 1133 (Nov. 1966).

22. Šiškins, M. *et al.* Magnetic and electronic phase transitions probed by nanomechanical resonators. *Nat. Commun.* **11,** 2698 (June 2020).

34. Houmes, M. J. A. *et al.* Magnetic order in 2D antiferromagnets revealed by spontaneous anisotropic magnetostriction. *Nat. Commun.* **14,** 8503 (Dec. 2023).

48. Šiškins, M. *et al.* Nanomechanical probing and strain tuning of the Curie temperature in suspended Cr2Ge2Te6-based heterostructures. *npj 2D Mater. Appl.* **6** (June 2022).

59. Gibertini, M., Koperski, M., Morpurgo, A. F. & Novoselov, K. S. Magnetic 2D materials and heterostructures. *Nat. Nanotechnol.* **14,** 408–419 (May 2019).

66. Houmes, M. J. A. *et al.* Highly Anisotropic Mechanical Response of the Van der Waals Magnet CrPS4. *Adv. Funct. Mater.* **34,** 2310206 (2024).

67. Da Gao, Z. *et al.* Anisotropic Mechanics of 2D Materials. *Adv. Eng. Mater.* **24,** 2200519 (Nov. 2022).

68. Uniaxial negative thermal expansion behavior of β-CuSCN. *Appl. Phys. Lett.* **118,** 222105 (May 2021).

69. Diederich, G. M. *et al.* Tunable interaction between excitons and hybridized magnons in a layered semiconductor. *Nat. Nanotechnol.* **18,** 23–28 (Dec. 2022).

70. De Wal, D. K. *et al.* Long-distance magnon transport in the van der Waals antiferromagnet CrPS4. *Phys. Rev. B* **107,** L180403 (May 2023).

71. Hwangbo, K. *et al.* Highly anisotropic excitons and multiple phonon bound states in a van der Waals antiferromagnetic insulator. *Nat. Nanotechnol.* **16,** 655–660 (Mar. 2021).

72. Kang, S. *et al.* Coherent many-body exciton in van der Waals antiferromagnet NiPS3. *Nature* **583,** 785–789 (July 2020).

73. Boix-Constant, C. *et al.* Probing the Spin Dimensionality in Single-Layer CrSBr Van Der Waals Heterostructures by Magneto-Transport Measurements. *Adv. Mater.* **34,** 2204940 (Oct. 2022).

74. Bae, Y. J. *et al.* Exciton-coupled coherent magnons in a 2D semiconductor. *Nature* **609,** 282–286 (Sept. 2022).

75. Peng, Y. *et al.* Magnetic Structure and Metamagnetic Transitions in the van der Waals Antiferromagnet CrPS4. *Adv. Mater.* **32,** 2001200 (July 2020).

76. Riesner, M. *et al.* Temperature dependence of Fano resonances in CrPS4. *J. Chem. Phys.* **156,** 54707 (Feb. 2022).

77. Gu, P. *et al.* Photoluminescent Quantum Interference in a van der Waals Magnet Preserved by Symmetry Breaking. *ACS Nano* **14,** 1003–1010 (Jan. 2020).

78. Lee, J. *et al.* Structural and Optical Properties of Single- and Few-Layer Magnetic Semiconductor CrPS4. *ACS Nano* **11,** 10935–10944 (Nov. 2017).

79. Diehl, R. & Carpentier, C.-D. The structural chemistry of indium phosphorus chalcogenides. *Acta Crystallogr.* **B34,** 1097 (Apr. 1978).

80. Bud'Ko, S. L., Gati, E., Slade, T. J. & Canfield, P. C. Magnetic order in the van der Waals antiferromagnet CrPS4: Anisotropic H-T phase diagrams and effects of pressure. *Phys. Rev. B* **103,** 224407 (June 2021).

81. Calder, S. *et al.* Magnetic structure and exchange interactions in the layered semiconductor CrPS4. *Phys. Rev. B* **102,** 024408 (July 2020).

82. Kim, S. *et al.* Photoluminescence Path Bifurcations by Spin Flip in Two-Dimensional CrPS4. *ACS Nano* **16,** 16385–16393 (Oct. 2022).

83. Son, J. *et al.* Air-Stable and Layer-Dependent Ferromagnetism in Atomically Thin van der Waals CrPS4. *ACS Nano* **15,** 16904–16912 (Oct. 2021).

84. Wu, F. *et al.* Gate-Controlled Magnetotransport and Electrostatic Modulation of Magnetism in 2D Magnetic Semiconductor CrPS4. *Adv. Mater.,* 2211653 (June 2023).

85. Qi, S. *et al.* Giant electrically tunable magnon transport anisotropy in a van der Waals antiferromagnetic insulator. *Nat. Commun.* **14,** 1–8 (May 2023).

86. Lee, M. *et al.* Study of charge density waves in suspended 2H-TaS2 and 2H-TaSe2 by nanomechanical resonance. *Appl. Phys. Lett.* **118,** 193105 (May 2021).

87. López-Cabrelles, J. *et al.* Chemical Design and Magnetic Ordering in Thin Layers of 2D Metal-Organic Frameworks (MOFs). *J. Am. Chem. Soc.* **143,** 18502–18510 (Nov. 2021).

88. Davidovikj, D. *Two-dimensional membranes in motion* PhD thesis (TU Delft, 2018).

89. Li, B.-L. *et al.* Very high-frequency, gate-tunable $CrPS_4$ nanomechanical resonator with single mode. *Opt. Lett.* **48,** 2571–2574 (May 2023).

90. Dove, M. T. & Fang, H. Negative thermal expansion and associated anomalous physical properties: review of the lattice dynamics theoretical foundation. *Rep. Prog. Phys.* **79,** 066503 (May 2016).

91. Colossal positive and negative thermal expansion in the framework material $Ag_3[Co(CN)_6]$. *Science* **319,** 794–797 (Feb. 2008).

92. Das, D., Jacobs, T. & Barbour, L. J. Exceptionally large positive and negative anisotropic thermal expansion of an organic crystalline material. *Nat. Mater.* **9,** 36–39 (Nov. 2010).

93. Peng, Y. *et al.* Controlling Spin Orientation and Metamagnetic Transitions in Anisotropic van der Waals Antiferromagnet CrPS4 by Hydrostatic Pressure. *Adv. Funct. Mater.* **32,** 2106592 (2022).

94. Joe, M., Lee, J. & Lee, C. Dominant in-plane cleavage direction of CrPS4. *Comput. Mater. Sci.* **162,** 277–280 (2019).

95. Joe, M. *et al.* A comprehensive study of piezomagnetic response in $CrPS_4$ monolayer: Mechanical, electronic properties and magnetic ordering under strains. *J. Condens. Matter Phys.* **29** (Aug. 2017).

96. Villars, P. *PAULING FILE in: Inorganic Solid Phases,* SpringerMaterials (online database), Springer, Heidelberg (ed.) SpringerMaterials.

97. Lyon, K. G., Salinger, G. L., Swenson, C. A. & White, G. K. Linear thermal expansion measurements on silicon from 6 to 340 K. *J. Appl. Phys.* **48,** 865–868 (Mar. 1997).

98. Wahab, D. A. *et al.* Quantum Rescaling, Domain Metastability, and Hybrid Domain-Walls in 2D CrI3 Magnets. *Adv. Mater.* **33,** 2004138 (Feb. 2020).

99. Zomer, P. J., Guimarães, M. H. D., Brant, J. C., Tombros, N. & van Wees, B. J. Fast pick up technique for high quality heterostructures of bilayer graphene and hexagonal boron nitride. *Appl. Phys. Lett.* **105,** 013101 (July 2014).

4.A. SUPPLEMENTARY INFORMATION

4.A.1. CIRCULAR DRUMS

This section contains additional measurements on circular drum samples. Figure 4.5 shows the atomic force microscopy (AFM) data, which is used to determine the thickness of the $CrPS_4$ flakes. The results of these measurements are summarised in table 4.1. Figure 4.6 shows additional frequency vs. temperature data similar to that of figure 4.2c of the main text. Note that although there are some variations, such as the absolute value of the frequency the overall behaviour is the same between these measurements despite varying thickness and radii. This shows that the observed behaviour is robust.

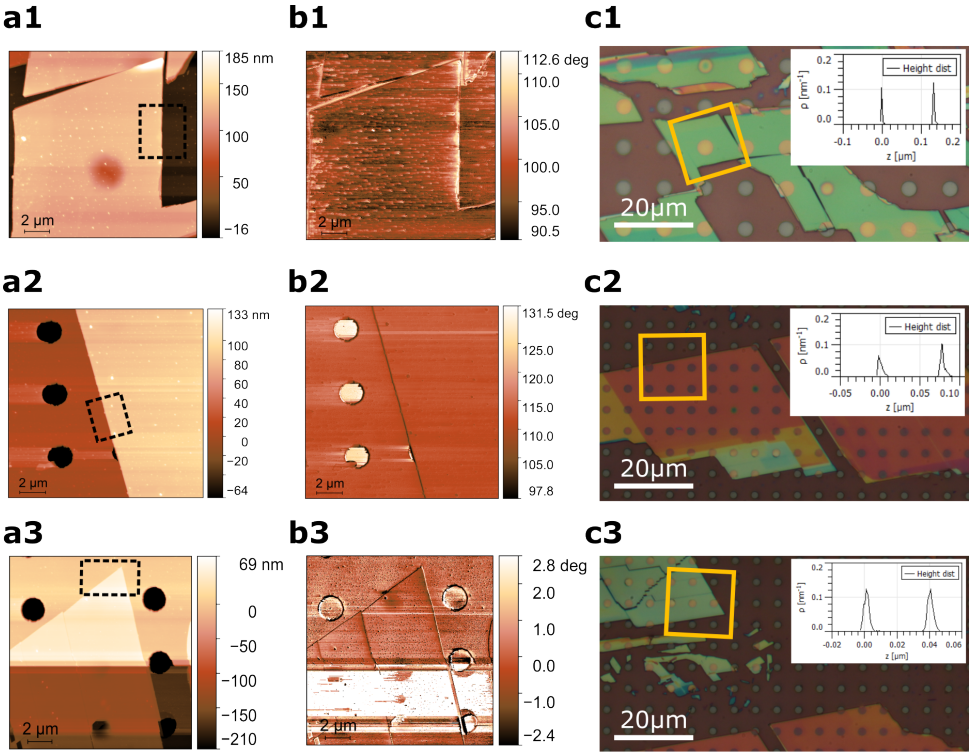

Figure 4.5: **a1,b1,c1)** show AFM height data, AFM phase data, optical image of drum 1. The AFM data corresponds to the yellow outlined area in c1. The thickness of the flake is determined using the height distribution taken in the black dashed box in figure a1; the resulting distribution is shown in the inset in c1. **a2, b2, c2, a3, b3, c3)** show the same information as a1, b1, c1 for drum 2 and 3, respectively.

Sample name	Drum 1	Drum 2	Drum 3
Thickness (nm)	120	80	40
Radius (μm)	3	1	1

Table 4.1: Summary of AFM data for circular drums, showing the thickness and radius.

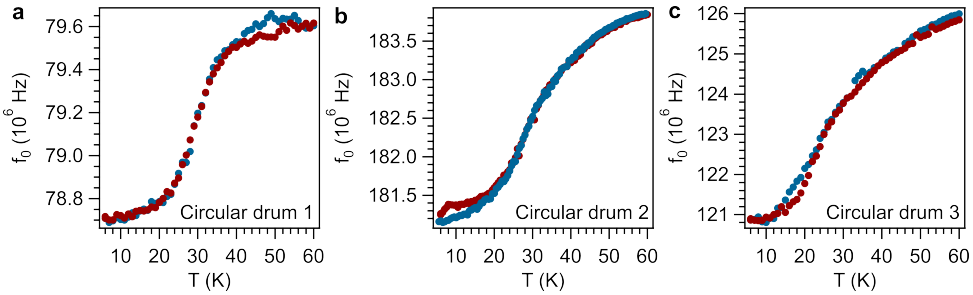

Figure 4.6: **a, b, c)** Additional frequency versus temperature measurements for drums 1, 2, and 3 respectively. The sweeps started at 6 K and the temperature was increased to 60 K and then returned to 6 K. The red points correspond with the heating cycle from 6 to 60 K and the blue points correspond with the cooling cycle from 60 to 6 K. No thermal hysteresis is observed.

4.A.2. STAR SAMPLES

This section contains additional measurements on star samples. Figure 4.7 shows the atomic force microscopy (AFM) data, which is used to determine the thickness of the $CrPS_4$ flakes. The results of these measurements are summarised in table 4.2. Figure 4.8 shows the frequency versus temperature data of stars 1 and 2. Since the alignment of star 1 with the crystal is slightly worse than that of star 2, meaning no cavity is perfectly aligned along either the a- or b-axis, there is some softening observable in the frequency data for all frequencies. Since star 2 is not completely covered by the $CrPS_4$ flake, the angular resolution of its data is lower. Despite this, similar behaviour is observed in both stars. Figure 4.9 shows the frequency data for the a- and b-axis of all stars. All stars show very similar behaviour despite differences in thickness and geometry. Note that with the exception of star 4 all stars show a relative shift of about 4.5 MHz for the b-axis from 6 to 60 K. The reason for the deviation of star 4 is unknown but could be caused by its larger thickness.

Sample name	Star 1	Star 2	Star 3	Star 4	Star 5
Thickness (nm)	75	76	103	165	70
Width (short side) (μm)	5	4	2	4	4
Length (long side) (μm)	10	12	10	12	12

Table 4.2: Summary of AFM data for star samples, showing the thickness, width, and length.

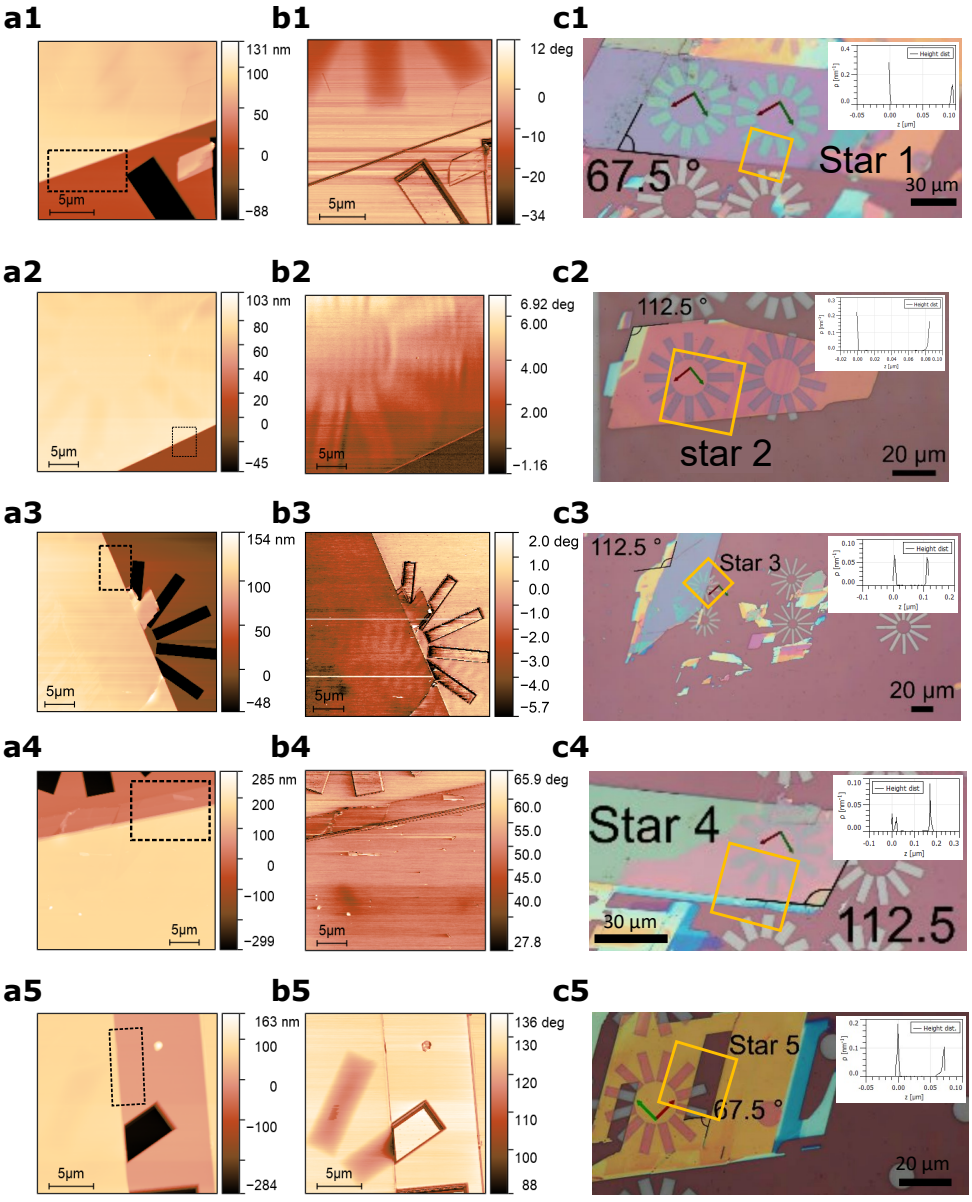

Figure 4.7: **a1,b1,c1)** AFM height data, AFM phase data, optical image of star 1. The AFM data corresponds to the yellow outlined area in c1. The thickness of the flake is determined using the height distribution taken in the black dashed box in figure a1, the resulting distribution is shown in the inset in c1. The measured fracture angles are indicated and labeled, these are used to determine the crystallographic a- and b-axis indicated by the red and green arrows, respectively. **a2-5,b2-5,c2-5)** show the corresponding information as a1, b1, c1 for stars 2, 3, 4, and 5, respectively.

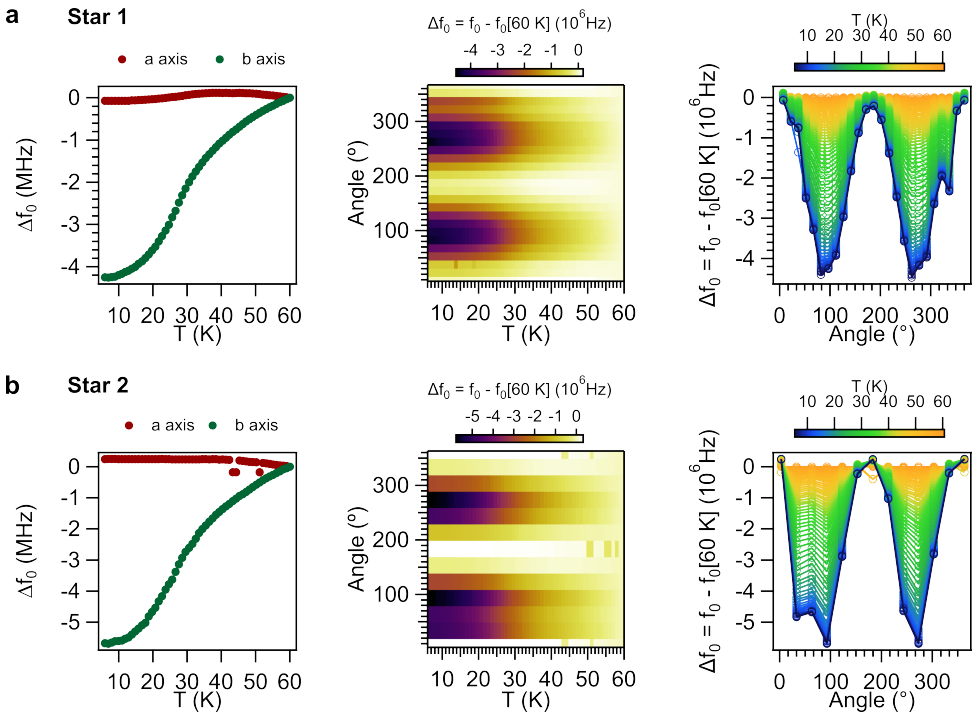

Figure 4.8: **a) Left panel:** Change in resonance frequency relative to 60 K as a function of temperature ($\Delta f_0(T) = f_0(T) - f_0(T{=}60\text{ K})$), between 6 and 60 K for two cavities of star 1 with their short axes aligned along the crystallographic a-axis (red) and b-axis (green). No thermal hysteresis effects are observed. **Center panel:** Relative frequency change (color coded) with respect to 60 K as a function of temperature. The angle corresponds to the angle the short axis of the cavity makes with the crystallographic a-axis; the cavity with the short axis parallel to the crystallographic a-axis corresponds to 0 deg. **Right panel:** Same data as the center panel now plotted with the relative frequency change on the vertical axis and angle on the horizontal axis. The temperature is color-coded. **b)** Shows the corresponding data as in a) for star 2.

4.A.3. PHASE TRANSITION

DATA FILTERING

To limit the effect of noise in calculating the $\frac{df_0^2}{dT}$ we first apply a smoothing step to the frequency data before squaring and taking the temperature derivative. Without this step features are lost in the noise, particularly in the case of the circular drum. This smoothing is done using a Savitzky-Golay filter with a window size of 3 and degree 1 polynomial.

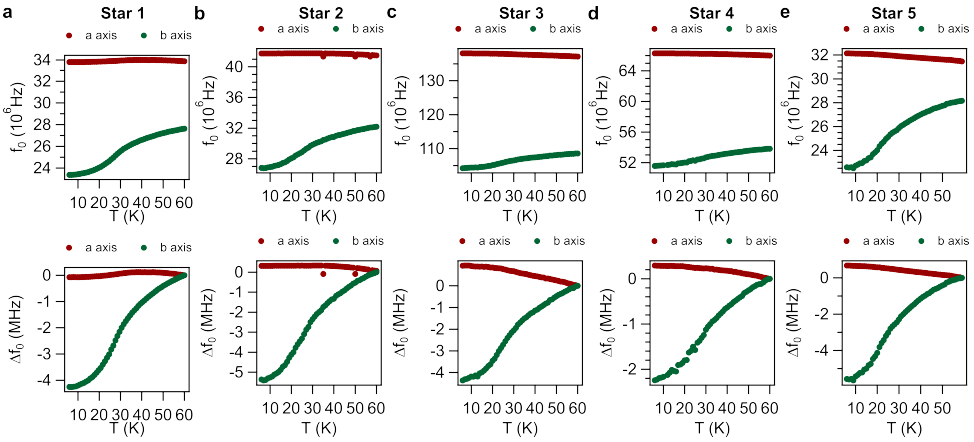

Figure 4.9: **a,b,c,d,e) Top panel:** Resonance frequency as a function of temperature between 6 and 60 K for two cavities with their short axes aligned along the crystallographic a-axis (red) and b-axis (green). of the stars 1, 2, 3, 4, and 5, respectively. **Botom panel:** shows the same data as the top panel now plotted as relative resonance frequency change relative to 60 K, the color coding is the same as in the top panel.

YOUNG'S MODULUS

Joe *et al.*[95], use density functional theory to calculate the elastic constants of $CrPS_4$, from these we calculate the a- and b-axis Young's modulus as

$$E_a = \frac{C_{11}C_{22} - C_{12}^2}{C_{22}}, \tag{4.A.1}$$

$$E_b = \frac{C_{11}C_{22} - C_{12}^2}{C_{11}}, \tag{4.A.2}$$

where $E_{a,b}$ is the Young's modulus along the a- resp. b-axis and C is the elasticity tensor. For C_{11} = 114.4 GPa, C_{22} = 74.4 GPa, and C_{12} = 33.6 GPa we find E_a = 99.23 GPa and E_b = 64.53 GPa.

THERMAL EXPANSION COEFFICIENT

Figure 4.10 shows the same data as the middle panel of figure 4.4b of the main text, converted to a thermal expansion coefficient (TEC) as described in the main text, equation (4.2.2). Apart from the minimum in the b-axis around 26 K, there also appears to be a kink around the phase transition temperature, indicated by the vertical black dashed line. This is an indication of the added contribution of magnetostriction to the TEC.

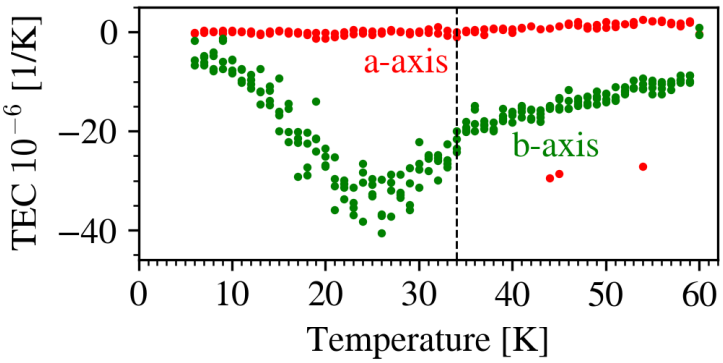

Figure 4.10: The thermal expansion coefficient of a- (red) and b-axis (green) between 6 and 60 K as determined from $\frac{df_0^2}{dT}$ data using equation (4.2.2), as explained in the main text. The black dashed line indicates the bulk transition temperature.

REFERENCES

95. Joe, M. *et al.* A comprehensive study of piezomagnetic response in $CrPS_4$ monolayer: Mechanical, electronic properties and magnetic ordering under strains. *J. Condens. Matter Phys.* **29** (Aug. 2017).

5

THERMO-MAGNETOSTRICTIVE EFFECT FOR DRIVING ANTIFERROMAGNETIC 2D MATERIAL RESONATORS

Magnetostrictive coupling has recently gained interest as a sensitive method for studying magnetism in 2D materials by mechanical means. However, its application in high-frequency magnetic actuators and transducers requires rapid modulation of the magnetic order, which is difficult to achieve with external magnets, especially when dealing with antiferromagnets. Here, we optothermally modulate the magnetization in antiferromagnetic 2D material membranes of metal phosphor trisulfides (MPS_3), to induce a large high-frequency magnetostrictive driving force. From the analysis of the temperature-dependent resonance amplitude, we provide evidence that the force is due to a thermo-magnetostrictive effect, which significantly increases near the Neél temperature, due to the strong temperature dependence of the magnetization. By studying its angle dependence, the effect is observed to follow the anisotropic magnetostriction of the crystal lattice. The presented results show that the thermo-magnetostrictive effect results in a strongly enhanced thermal expansion force near the critical temperature of magnetostrictive 2D materials, which can enable more efficient actuation of nano-magnetomechanical devices and can also provide a route for studying the high frequency coupling between magnetic, mechanical and thermodynamic degrees of freedom down to the 2D limit.

Parts of this chapter have been published in [23].

5.1. INTRODUCTION

Given the strong interest in applications of magnetic devices for sensing, data storage and spintronics, two-dimensional (2D) magnetic materials have been subject of extensive research [100]. However, testing the magnetic properties of suspended 2D materials is challenging due to the small sample volumes, which result in small signals. As an alternative to optical and electronic techniques, recently several works have promoted the use of nanomechanical methods for probing magnetic and thermodynamic properties of suspended 2D membrane resonators such as graphene [101], MoS_2 [102] and $MoSe_2$ [103]. Owing to the strong magnetostrictive coupling between mechanical strain, and magnetism in certain 2D materials [22, 49], nanomechanics has also been used to probe magnetic properties [21, 22, 49, 104], and anisotropies [34]. Instead of probing magnetism by mechanical resonance, in this chapter, we demonstrate the inverse mechanism: driving mechanical resonators via 2D magnetic order through magnetostriction.

Magnetostriciton is the coupling between magnetic order and strain in a crystal. This means that when a crystal is strained its magnetic order changes as well as the reverse, a change in the magnetic order causes a change in the strain in the crystal. This second relation can be seen as a way to provide a driving force to a drum resonator by modulating the magnetic order in the resonator. Using an external magnetic field to provide such a driving force is non trivial, as it requires a strong magnetic field, especially for antiferromagnetic materials as studied in this case, and a modulation of the field at a high frequency, for nanomechanical drum resonators typically in the order of 1-100 MHz.

Therefore using the internal magnetic order of the material provides a simpler way to achieve such magnetostrictive driving, as this internal order can be modulated using temperature. As the magnetic order is particularly sensitive to changes in temperature just below the transition temperature this way of actuation will be most efficient in that temperature regime. In this chapter we modulate optothermally the temperature of the suspended 2D membranes of antiferromagnetic MPS_3 (M = Fe, Co, Ni) compounds, allowing for the magnetization to be varied at high frequencies, causing a large magnetostrictive enhancement of the driving force. We also show that the anisotropy of this driving force corresponds with the anisotropy of the magnetostriction coefficients.

5.2. METHODS AND RESULTS

As in previous chapters the resonators were fabricated using dry transfer of exfoliated crystal flakes using PDMS as transfer polymer on pre-etched substrates of Si with 285 nm of thermally grown SiO_2. A representative sample is shown in figure 5.1a with a schematic cross-section shown in figure 5.1b.

The technique used to study the motion of the suspended MPS_3 membranes is the same as discussed in previous chapters. Using a power modulated blue laser the temperature of the membrane is modulated. Throughout this chapter the power modulation voltage, V_{in}, is held at a constant amplitude. The frequency dependent motion of the membrane is read out using a red laser in the interferometric readout scheme, see 1.4.2. The voltage readout by the detector photodiode will be referred to as V_{out} . The optical actuation power, P_ω, provided by the blue laser is modulated at an angular frequency, ω, so we will model this as $P_\omega = P_0(V_{\text{in}})e^{i\omega t}$, where $P_0(V_{\text{in}})$ is the magnitude of the power

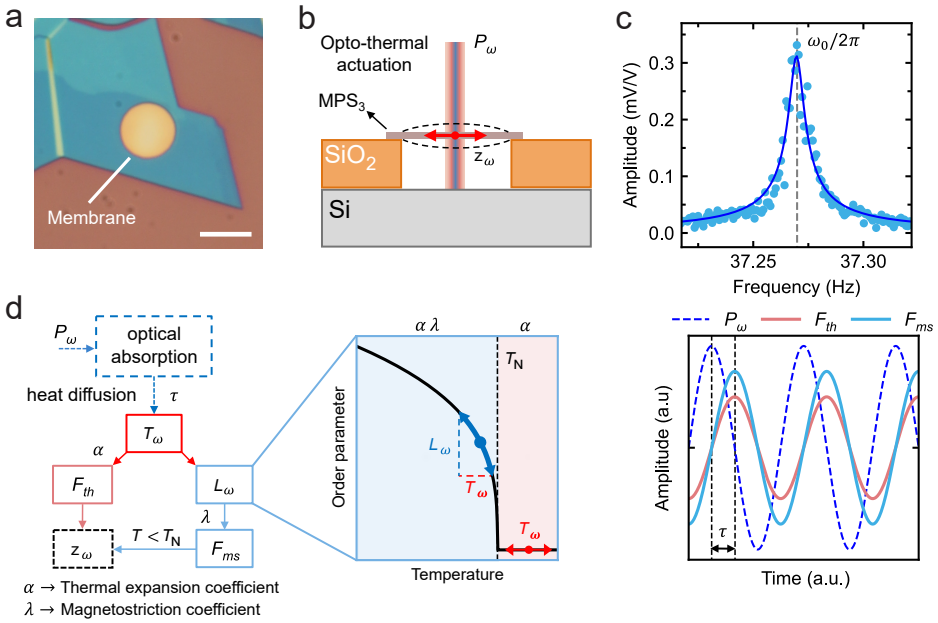

Figure 5.1: **Thermal response characterization of magnetic membranes. (a)** Optical image of a $FePS_3$ membrane resonator (sample Fe-1 in Table 5.1). The scale bar is 6 μm. **(b)** Schematic illustration of the system under study: MPS_3 membrane is optothermally actuated via a power modulated blue laser, P_ω, and its out-of-plane displacement, z_ω, is detected interferometrically with a red laser. The red arrows show the expansion direction. **(c)** Measured amplitude of the fundamental resonance peak (at 120 K) and fit (drawn line) used to extract the resonance frequency, $\omega_0/2\pi$, whose position is indicated by the vertical dashed line. **(d)** Block diagram showing how thermal expansion forces, F_{th}, and magnetostriction forces, F_{ms}, arise from the optothermal actuation and contribute to the membrane's motion. T_ω and L_ω indicate the modulation of temperature and magnetic order parameter respectively. **(e)** Schematic plot of the blue laser power, P_ω, and out-of-phase forces, F_{th}, F_{ms}, resulting from the time delay τ due to heat diffusion.

modulation which is set by the power modulation voltage. When driven at resonance the frequency response, $z_\omega \propto V_{\text{out}}/V_{\text{in}}$, shows a characteristic resonance peak, as shown in figure 5.1c, from which the resonance frequency, $\omega_0/2\pi$, and Q-factor of the resonator can be extracted by fitting a damped harmonic oscillator model.

The force actuating the membrane arises from the delay in the modulation of the temperature, caused by optical absorption of the blue laser, schematically shown in figure 5.1d. This delay in the actuation results in a peak in the imaginary part of the frequency response which is know as a thermal peak [101]. This peak occurs at an angular frequency far below the resonance frequency, $\omega_{\text{th}} << \omega_0$ and corresponds to a characteristic thermal time constant, $\omega_{\text{th}} = 1/\tau$. The low frequency response can be described by [101]:

$$z_\omega = \frac{A}{1 + i\omega\tau}, \tag{5.2.1}$$

where the amplitude A is proportional to the driving force and τ is the membrane's thermal time constant, which is proportional to the material's thermal diffusivity [105, 106].

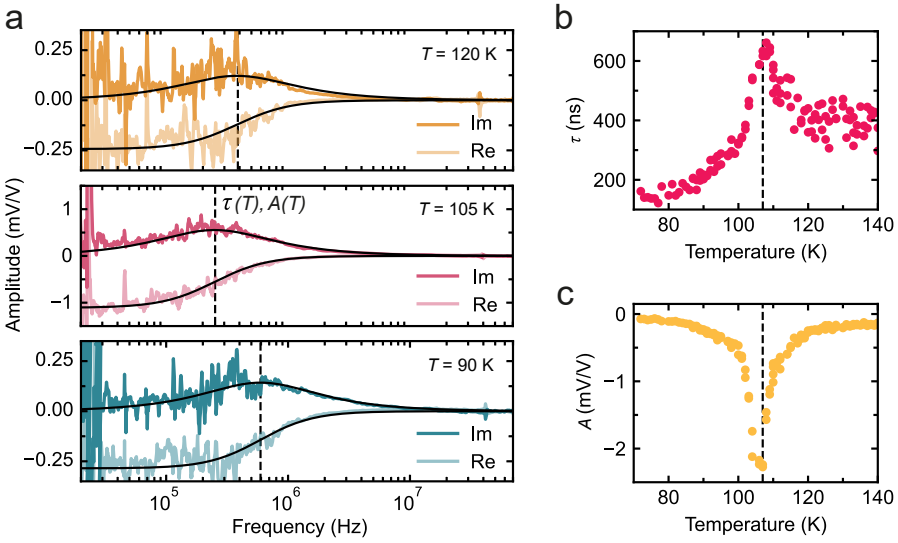

Figure 5.2: **Thermal response vs. temperature.** Measurement data and analysis from $FePS_3$ sample Fe-1. **(a)** Measured real and imaginary component of z_ω as a function of frequency at different temperatures ($T = 90$ K bottom panel, $T = 105$ K middle panel, $T = 120$ K top panel, fit parameters are respectively $\tau = 267, 634$ and 420 ns and $A = -0.28, -1.11$ and -0.24 mV/V). The black solid line indicates the fit to $A/(1 + i\omega\tau)$, used to extract τ and A. Vertical dashed lines highlight the frequency position of the thermal peak, $\omega_{\text{th}}/(2\pi) = 1/(2\pi\tau)$. **(b-c)** Thermal time constant, τ and thermal peak amplitude, A as a function of temperature, extracted from data like in (a). Vertical dashed line indicates the transition temperature, T_N.

We will assume that the time delay between the optical power and the membrane response is dominated by thermal effects [101], see section 5.A.2 for further discussion.

In order to resolve both the resonance frequency and the lower frequency thermal behaviour a wide frequency window is used to measure the frequency response. Figure 5.2a shows three measurements of the frequency response of a $FePS_3$ circular drum resonator, taken at temperatures of 120, 105, and 90 K, as well as a fit using (5.2.1). Using this fit to extract the thermal time constant and the amplitude of the thermal peak we can investigate their temperature dependence, shown in figure 5.2b and 5.2c, respectively. The thermal time constant, figure 5.2b, exhibits a peak with a maximum at the transition temperature of $FePS_3$, indicated by the black dashed line. The amplitude, 5.2c, shows a large dip with a minimum just below the transition temperature, with a value that is 20 times larger than the one at 70 K, well below the magnetic transition. In the following sections we will discuss these results in more detail.

5.3. THERMAL TIME CONSTANT

Given that the specific heat of $FePS_3$ shows a peak near the antiferromagnetic phase transition [22], it is of interest whether the peak in the thermal time constant in figure 5.2b can be accounted for by the anomaly in the specific heat. The thermal time constant

of a circular membrane is approximately given by [102]:

$$\tau = \frac{r^2 \rho c_v}{\mu^2 \kappa}, \tag{5.3.1}$$

where r is the membrane's radius, c_v, ρ and κ are the material's specific heat, density and thermal conductivity and μ^2 is a constant related to the membrane geometry. In figure 5.3a we plot the literature values [107] of the thermal conductivity $\kappa(T)$ of bulk $FePS_3$ and the material's specific heat $c_v \propto \frac{d\omega_0^2}{dT}$ calculated from the measured resonance frequency, $\omega_0/2\pi$, according to the methodology outlined in [22], see section 5.A.3. In figure 5.3b, we use (5.3.1) with $r = 3\,\mu$m, $\rho = 3375$ kg m^{-3}, $\mu^2 = 10$ and the values of κ and c_v shown in figure 5.3a, to calculate the thermal time constant τ (black curve) and compare it to the measured values (red dots). Equation (5.3.1) yields a good correspondence with the experimental data, reproducing the peak shape as well as its magnitude. The qualitative correspondence between the modeled and measured data for $\tau(T)$ in figure 5.3b provides evidence that the measured peak in the thermal time constant is due to the peak in specific heat near T_N. Further analysis of the thermal properties of the membranes can be found in figure 5.7 and 5.8.

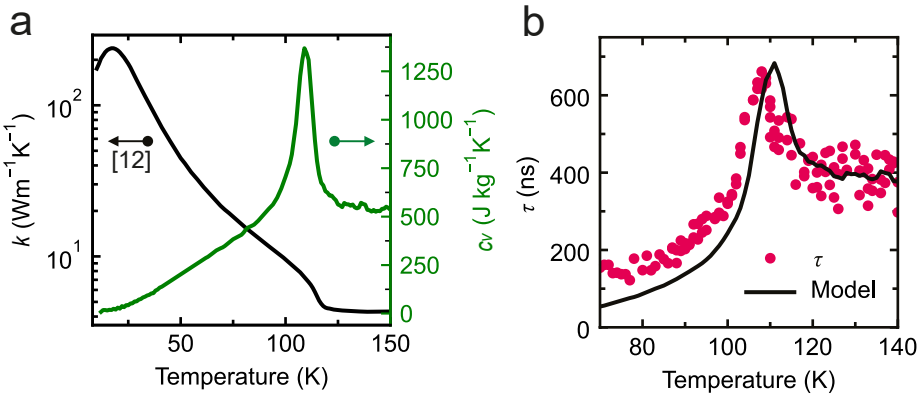

Figure 5.3: **Thermal time constant model.** Measurement data and analysis from $FePS_3$ sample Fe-1. **(a)** Bulk thermal conductivity, κ, (black) from [107] (data adapted with permission) and measured specific heat, c_v, (green) extracted from the resonance frequency, $\omega_0(T)/2\pi$, as described in [22] for $FePS_3$. **(b)** Thermal time constant for the same sample as in (a), calculated from (5.3.1) (black line), with $\mu^2 = 10$, c_v and κ from (a) and measured (red dots).

5.4. AMPLITUDE RESPONSE

We now turn to the large enhancement of the resonator's amplitude near T_N observed in figure 5.2c. To understand this enhancement we first note that the peak height $A(T)$ is determined at a frequency $\omega_{th} = 1/\tau$ which is far below the resonance frequency. At this frequency, the effects of mass and damping can be neglected and the resonator behaves as a spring with stiffness k, and displacement $z_{\omega,th} = F_{\omega,th}/k \propto A$. Since $\omega_0^2 \propto k$

and there is no peak in the resonance frequency near T_N, see figure 5.6 in section 5.A.3, we conclude that the peak in $A(T)$ should be attributed to a large enhancement in the driving actuation force near T_N.

The proposed actuation mechanism is schematically depicted in figure 5.1d-e. The absorption of the power-modulated laser light supplies a time-dependent heating power to the membrane. As a consequence, heat flows from the center of the membrane to the substrate in a time scale determined by the materials' thermal time constant τ. Normally, the resulting temperature rise, T_ω, increases the lattice vibrations that result in an enlarged lattice constant, proportionally to the effective lattice thermal expansion coefficient α of the membrane. However, in the case of an antiferromagnetic membrane below the Néel temperature, T_ω also changes the (staggered) magnetization order parameter, L. If the material is magnetostrictive, then its lattice expands proportionally to λL^2, where λ is the effective magnetostriction coefficient of the membrane.

Thus, when the temperature is optothermally modulated below T_N, the membrane is actuated both by the lattice thermal expansion force, F_{th}, and by the magnetostrictive force F_{ms}, which are both delayed by the characteristic time constant τ with respect to the heating power P_ω, as shown in figure 5.1e. Since the slope of the magnetization versus temperature curve, $L(T)$ is steepest just below T_N, it is expected that the contribution of F_{ms} will also be largest in this temperature range, see below, consistent with the peak in $A(T)$ observed in figure 5.2c.

To analyze the data and models in more quantitative detail, we derive the following equation for the low-frequency ($\omega \ll \omega_0$) mechanical displacement spectrum, z_ω, in section 5.A.5:

$$z_\omega = \left(\alpha + \lambda \frac{\mathrm{d}L^2}{\mathrm{d}T}\right) \frac{RP_0}{1 + i\omega\tau}, \tag{5.4.1}$$

where R is the membrane's thermal resistance. As (5.4.1) shows, the thermal peak amplitude $A(T) = \mathrm{Im}(z_\omega)$ at $\omega = 1/\tau$, is determined by two terms: one containing the effective thermal expansion coefficient α, and the other containing the temperature derivative of the magnetic order parameter L^2. The coefficient α can be expressed in terms of the specific heat considering the thermodynamical relation $\alpha = \dfrac{\gamma}{3KV_M} c_v$, where γ is the Grüneisen parameter, K the bulk modulus, and V_M the molar volume. Assuming that the isotropic contributions to the thermal expansion causing the membrane's motion are only determined by the phononic lattice contribution, then $\alpha \propto c_{\mathrm{Debye}}$, where c_{Debye} is the Debye specific heat:

$$c_{\mathrm{Debye}}(T) \propto T^2 \int_0^{\Theta_D/T} \frac{x^3 e^x}{(e^x - 1)^2}\, dx. \tag{5.4.2}$$

For the analysis of the $FePS_3$ data we use a Debye temperature $\Theta_D = 236$ K [53], while for $CoPS_3$ we use $\Theta_D = 262$ K as estimated from the material bulk modulus[57]. To fit the data using (5.4.1), we employ the method from [34] to extract L^2, from the angle-resolved resonance frequency of rectangular resonators, see section 5.A.6 for more details on this analysis. Figure 5.4a shows the fits of the $A(T)$ data of a rectangular $CoPS_3$ resonator of sample Co-1, which is shown in figure 5.4c, to $A(T) = a_1 c_{\mathrm{Debye}} + a_2 \dfrac{dL^2}{dT}$ with a_1 and a_2 as fit parameters. The dashed lines highlight the individual contributions to A from the

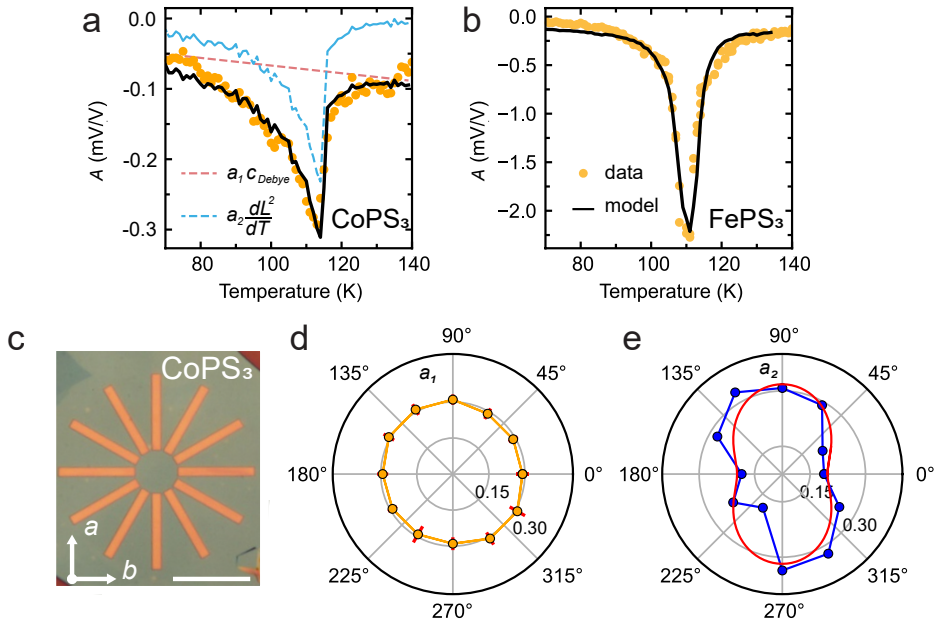

Figure 5.4: **Actuation mediated by the magnetostriction effect.** **(a)** Measured thermal peak amplitude, A, (orange) with fit to $a_1 c_{\mathrm{Debye}} + a_2 \frac{dL^2}{dT}$ (black) on a rectangular resonator of the $CoPS_3$ sample Co-1, where a_1 and a_2 are fit parameters. The dashed colored lines indicate the individual contributions of the Debye term (light red) and magnetostriction term (light blue). **(b)** Same as (a) for $FePS_3$ sample Fe-1. **(c)** Optical image of the star-shaped array resonators of $CoPS_3$ (sample Co-1) measured to investigate angle dependance of $a_1(\theta)$ and $a_2(\theta)$. Scale bar is 12 μm. The arrows indicate the crystallographic directions a and b.**(d-e)** Polar plots of a_1 in orange (d) and a_2 in blue (e) as extracted from fits to $A(\theta)$ for sample Co-1. In (e) the red curve is a fit to $b_1 \sin^2\theta + b_2 \cos^2\theta$. The angle θ is defined with respect to the crystallographic b-axis.

thermal expansion (light red) and magnetostriction force (light blue). The fitted curve (black) corresponds well to the measured $A(T)$ data, providing evidence of the correctness of (5.4.1) and the applicability of the presented analysis. Figure 5.4b shows the same analysis on $A(T)$ for $FePS_3$ sample Fe-1, again resulting in a good correspondence to the data. In this case, since $A(T)$ is measured on a circular $FePS_3$ drum on which $L(T)$ is difficult to obtain using the method from [34], L^2 is calculated from resonance frequency measurements on separate rectangular $FePS_3$ resonators (as shown in figure 5.12 of section 5.A.6), assuming the same temperature dependence of the magnetization holds for the circular resonator. Section 5.A.7 shows additional data on all rectangular cavities of sample Co-1 (figure 5.13), as well as another $FePS_3$ drum (sample Fe-2 in figure 5.14) and $NiPS_3$ drums (samples Ni-1,2,3 in figure 5.15), demonstrating the reproducibility of the effect.

5.5. ANISOTROPY

In [34] it was shown that the magnetostriction coefficient in MPS_3 materials is anisotropic, therefore it is interesting to investigate if the thermo-magnetostrictive driving force also

depends on the crystal orientation. We study this by applying the aforementioned analysis to determine the a_1 and a_2 fit parameters for all rectangular $CoPS_3$ resonators of sample Co-1. As derived in section 5.A.8, the parameters are expected to follow the angular dependence described by:

$$a_1 = -\frac{P_0 E \eta_{ph} R_{ph}}{(1+\nu)}, \tag{5.5.1}$$

$$a_2 = -\frac{P_0 E \eta_m R_m}{(1-\nu^2)}\left[(\lambda_a + \nu\lambda_b)\sin^2\theta + (\lambda_b + \nu\lambda_a)\cos^2\theta\right], \tag{5.5.2}$$

where η_{ph} and η_m are respectively the fractions of heat absorbed by the phononic and magnetic baths, ν is the Poisson ratio, E is the Young's modulus, $\lambda_{a,b}$ are the magnetostriction coefficients along the a and b crystallographic axes, and θ is defined with respect to the b direction. Thus, from (5.5.1) we expect a_1 to be isotropic, which agrees with the polar plot in figure 5.4d showing the extracted a_1 parameters from the fit to angle-resolved data measured on the rectangular $CoPS_3$ resonators. Similarly, $a_2(\theta)$ reproduces the anisotropic function (5.5.2), as shown via a fit (red line in figure 5.4e) to a function of the form $b_1 \sin^2\theta + b_2 \cos^2\theta$. The qualitative agreement with (5.5.2) provides additional evidence that the driving force is of magnetostrictive origin, and is consistent with earlier observations of the anisotropy in the magnetostriction coefficient of $CoPS_3$ [34].

5.6. CONCLUSION

We present evidence that resonators of antiferromagnetic 2D materials can be driven via a thermo-magnetostrictive effect. The effect was shown to be present in $FePS_3$, $CoPS_3$, and $NiPS_3$ resonators, and can lead to strong enhancement of the thermomechanical force below the Neél temperature, because its magnitude scales with the temperature derivative of the square of the staggered magnetization $\frac{dL^2}{dT}$. Despite its magnetic nature, the effect does not require application of external magnetic fields, and is also effective in antiferromagnetic materials, because the magnetic order is varied by optothermal modulation.

As a consequence of the anisotropy in the magnetostriction coefficient, we observe a strong crystal orientation dependence in the amplitude of the thermo-magnetostrictive driving force. Besides providing a route towards driving magnetic nanomechanical resonators, the observed high-frequency magnetostrictive effects can provide further insights into the interplay between motion, thermodynamics, magnetic order, and mechanical strain in the 2D limit.

REFERENCES

21. Lee, M. *et al.* Study of charge density waves in suspended 2H-TaS_2 and 2H-$TaSe_2$ by nanomechanical resonance. *Appl. Phys. Lett.* **118,** 193105 (May 2021).

22. Šiškins, M. *et al.* Magnetic and electronic phase transitions probed by nanomechanical resonators. *Nat. Commun.* **11,** 2698 (June 2020).

23. Baglioni, G. *et al.* Thermo-Magnetostrictive Effect for Driving Antiferromagnetic Two-Dimensional Material Resonators. *Nano Lett.* **23,** 6973–6978 (2023).

34. Houmes, M. J. A. *et al.* Magnetic order in 2D antiferromagnets revealed by spontaneous anisotropic magnetostriction. *Nat. Commun.* **14,** 8503 (Dec. 2023).

49. Jiang, S., Xie, H., Shan, J. & Mak, K. F. Exchange Magnetostriction in Two-Dimensional Antiferromagnets. *Nat. Mater.* **19,** 1295–1299 (June 2020).

53. Takano, Y. *et al.* Magnetic properties and specific heat of MPS_3 (M=Mn, Fe, Zn). *J. Magn. Magn. Mat.* **272-276,** E593–E595 (May 2004).

57. Gui, Q. *et al.* Extrinsic-Structured Bimetallic-Phase Ternary Metal Phosphorus Trisulfides Coupled with N-Doped Graphitized Carbon for Superior Electrochemical Lithium Storage. *Adv. Energy Mater.* **11,** 2003553 (Jan. 2021).

100. Wang, Q. H. *et al.* The Magnetic Genome of Two-Dimensional van der Waals Materials. *ACS Nano* **16,** 6960–7079 (2022).

101. Dolleman, R. J. *et al.* Optomechanics for thermal characterization of suspended graphene. *Phys. Rev. B* **96,** 165421 (Oct. 2017).

102. Dolleman, R. J. *et al.* Transient thermal characterization of suspended monolayer MoS_2. *Phys. Rev. Mater.* **2,** 114008 (Nov. 2018).

103. Morell, N. *et al.* Optomechanical Measurement of Thermal Transport in Two-Dimensional MoSe2 Lattices. *Nano Lett.* **19,** 3143–3150 (2019).

104. Šiškins, M. *et al.* Nanomechanical probing and strain tuning of the Curie temperature in suspended $Cr_2Ge_2Te_6$-based heterostructures. *npj 2D Mater. Appl.* **6** (June 2022).

105. Zener, C. Internal Friction in Solids I. Theory of Internal Friction in Reeds. *Phys. Rev.* **52,** 230–235 (Aug. 1937).

106. Lifshitz, R. & Roukes, M. L. Thermoelastic damping in micro- and nanomechanical systems. *Phys. Rev. B* **61,** 5600–5609 (Feb. 2000).

107. Haglund, A. *Thermal Conductivity of MXY_3 Magnetic Layered Trichalcogenides* (Ph.D. thesis, University of Tennessee, Knoxville, 2019).

5.A. SUPPLEMENTARY INFORMATION

5.A.1. EXPERIMENTAL METHODS AND MEASURED SAMPLES

SAMPLE FABRICATION

MPS_3 flakes are stamped onto a substrate of 285 nm thermal SiO_2, grown on highly doped (Si^{++}) silicon. Cavities are defined via e-beam lithography using AR-P 6200 resist. After development, the exposed SiO_2 areas are fully etched via reactive ion etching. The AR-P 6200 resist is stripped in PRS-3000 and the sample is cleaned in an O_2 plasma before stamping. The exfoliation and transfer of multi-layer MPS_3 flakes is done using a PDMS transfer method. First, MPS_3 crystals are exfoliated onto the PDMS through scotch tape. Selected flakes are then transferred either on the circle-shaped or on the star-shaped cavities in the SiO_2/Si substrate.

LASER INTERFEROMETRY

The samples are mounted in a 4K cryostat (Montana Instruments Cryostation s50) with optical access. An intensity-modulated blue laser (405 nm) causes the membrane to heat up, resulting in its deflection due to thermal expansion. The motion of the membrane is detected via cavity optomechanics using a red He-Ne laser (632 nm). The suspended membrane acts as a moving mirror and the bottom of the cavity as a fixed mirror in a low-finesse Fabry-Perot cavity. The reflected red laser light from the cavity is redirected to a photodetector, which is connected to a vector network analyzer (VNA) in order to measure transmission between the blue laser modulation and the signal on the photodetector in a homodyne detection scheme. The sample is mounted on a heater stage used to control the sample local temperature inside the cryostat with 10 mK precision. Measurements are performed at incident laser power of $< 10\ \mu$W for the red laser and $< 1\ \mu$W for the blue laser. Figure 5.5 shows a schematic of the experimental setup described.

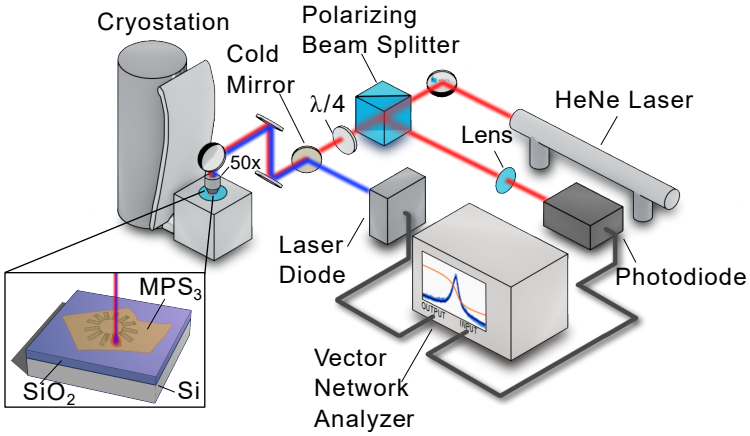

Figure 5.5: **Experimental setup.** Schematic of the interferometry setup.

CRYSTAL GROWTH

Crystal growth of MPS_3 (M = Ni, Fe, Co) was performed following a solid-state reaction inside a sealed evacuated quartz tube (pressure $\sim 5 \times 10^{-5}$ mbar). I_2 was used as a transport agent to obtain large crystals. A three zone furnace was used, where a tube with the material was placed in the leftmost zone. The leftmost side was then heated up to 700 °C in 3 hours so that a temperature gradient of 700 / 650 / 675°C was established. The other two zones were heated up in 24 hours from room temperature to 650 °C and kept at that temperature for one day. The temperature was kept constant for 28 days and cooled down naturally. With this process crystals with a length up to several centimeters are obtained. Detailed description of the crystal growth and characterization can be found in earlier work [22].

MEASURED SAMPLES

Table 5.1 shows an overview of the measured samples of MPS_3 resonators, along with their dimensions and flake thickness as measured via atomic force microscopy.

Sample	Material	Resonator geometry	Dimensions	t (nm)
Fe-1	$FePS_3$	Circular drum	$r = 6\,\mu$m	16
Fe-2	$FePS_3$	Circular drum	$r = 4\,\mu$m	21
Fe-3	$FePS_3$	Star cavity array	$w = 2\,\mu$m, $l = 16\,\mu$m	40
Co-1	$CoPS_3$	Star cavity array	$w = 2\,\mu$m, $l = 16\,\mu$m	30
Ni-1	$NiPS_3$	Circular drum	$r = 4\,\mu$m	16
Ni-2	$NiPS_3$	Circular drum	$r = 4\,\mu$m	20

Table 5.1: **Measured samples.** Overview of the MPS_3 samples studied. Reported are the material, the resonator's geometry, the resonator's dimensions (radius, r, for circular drums and width, w, and lenght, l, for rectangular membranes in star cavity) and thickness, t, as determined by atomic force microscopy.

5.A.2. SOURCES OF DELAY BETWEEN MEMBRANE DISPLACEMENT AND OPTICAL ACTUATION

In the following, we discuss the possible sources for time delay between the modulation of the actuating blue laser and the membrane displacement. As argued in [101], the heating power caused by the modulated intensity can be treated as instantaneous as photoexcited carriers lose their energy to phonons on time scales of a few picoseconds. Then, the heating power will increase the membrane temperature in a time scale determined by the membrane thermal time constant τ. Thus, the resulting force acting on the membrane will also be delayed by τ with respect to the optical actuation. Additional mechanical delays are neglected, since for frequencies far below the membrane's resonance frequency, the membrane motion will be in phase with the actuating force.

Other sources of delay, intrinsic to the measurement setup are taken into account by pointing directly the blue laser to the photodiode to obtain a calibration curve c_ω for the

frequency response f_ω. The corrected frequency response is given by

$$f_{\text{corr},\,\omega} = \frac{f_\omega}{c_\omega}. \tag{5.A.1}$$

This,leaves the thermal time constant of the system as the dominant source of delay. Additional delays between the change in temperature and change in magnetization causing the magnetostriction force are neglected as the data is well represented by a single time constant model.

5.A.3. SPECIFIC HEAT FROM RESONANCE FREQUENCY

Following the model from [22], we derived the specific heat c_ν from the temperature derivative of the resonance frequency $f_0 = \omega_0/2\pi$ as

$$c_\nu = 3\left(\alpha_{\text{Si}} - \frac{1}{\xi^2}\frac{df_0^2}{dT}\right)\frac{EV_M}{3\gamma(1-2\nu)}, \tag{5.A.2}$$

where α_{Si} is the thermal expansion coefficient of Si, E is the Young's modulus, ν is the Poisson ratio, $\gamma \approx \frac{3}{2}\frac{1+\nu}{2-3\nu}$ is the Grüneisen parameter, V_M is the molar volume and $\xi = \frac{2.4048}{\pi d}\sqrt{\frac{E}{\rho(1-\nu)}}$, with ρ the density of the material and d the diameter of the circular resonator.

The c_ν of $FePS_3$ shown in figure 5.3a is computed via (5.A.2) from the resonance frequency data shown in figure 5.6, with $E = 103$ GPa, $\nu = 0.304$, $\rho = 3375$ kg m^{-3}.

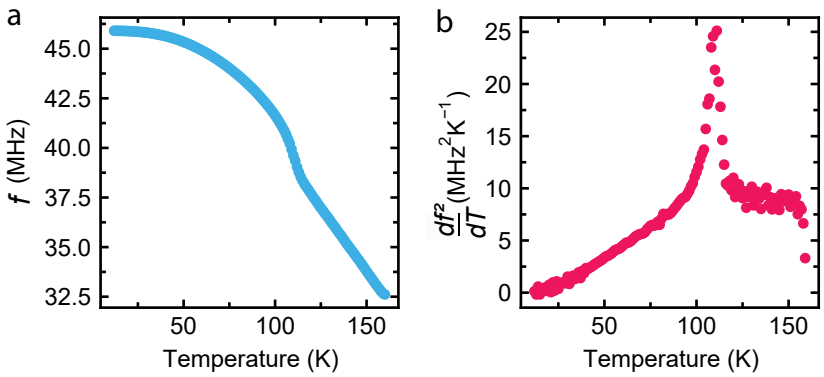

Figure 5.6: **Data on $\omega_0/2\pi$ for sample Fe-1 a).** Temperature dependent resonance frequency, $\omega_0(T)/2\pi$ of sample Fe-1. **b).** Derivative of the frequency squared with respect to temperature of $\omega_0/2\pi$ from (a).

5.A.4. THERMAL CONDUCTIVITY FROM THERMAL TIME CONSTANT

Instead of using the literature value of κ to determine τ as done in the main text, we could also use the measured value of τ to estimate the membrane's thermal conductivity κ. Such an analysis would be of particular interest for materials whose bulk values of

κ are not reported, like for $CoPS_3$, or to study thermal conductivity in the thin limit. However, we note that prior knowledge of the material's mechanical properties, such as Young's modulus and Poisson ratio, are needed to estimate c_v from $\frac{d\omega_0^2}{dT}$. We also note that more clarification is needed to account for the relatively high value of the parameter $\mu^2 = 10$ compared to previous work [102], where a value of $\mu^2 = 5$ was found close to the theoretical value for a circular membrane of $\mu^2 = 5.783$. Despite the fact that we

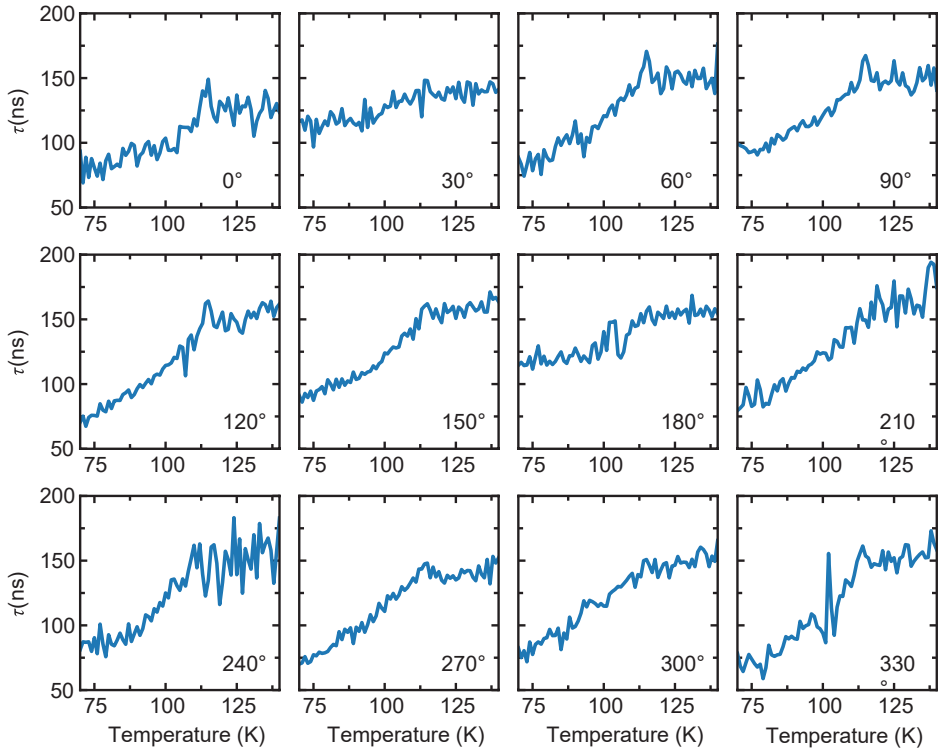

Figure 5.7: **Angle-resolved thermal time constant in $CoPS_3$ resonators.** Thermal time constant rectangular cavities at different orientation with respect to the crystallographic axis of the Co-1 sample.

do not yet obtain a full quantitative agreement between the model and theory, here we present an estimate of the angle-resolved thermal conductivity, k, of $CoPS_3$ from the thermal time constants, τ measured on the rectangular resonators of sample Co-1 (these are shown in figure 5.7). We calculate k as [106]

$$k = \frac{w^2 \rho c_v}{\pi^2 \tau}, \tag{5.A.3}$$

where $w = 2\ \mu$m is the width of the resonator, $\rho = 3257$ kg m^{-3}, and c_v is the bulk specific heat taken from [58]. The resulting k for all resonators is shown in figure 5.8.

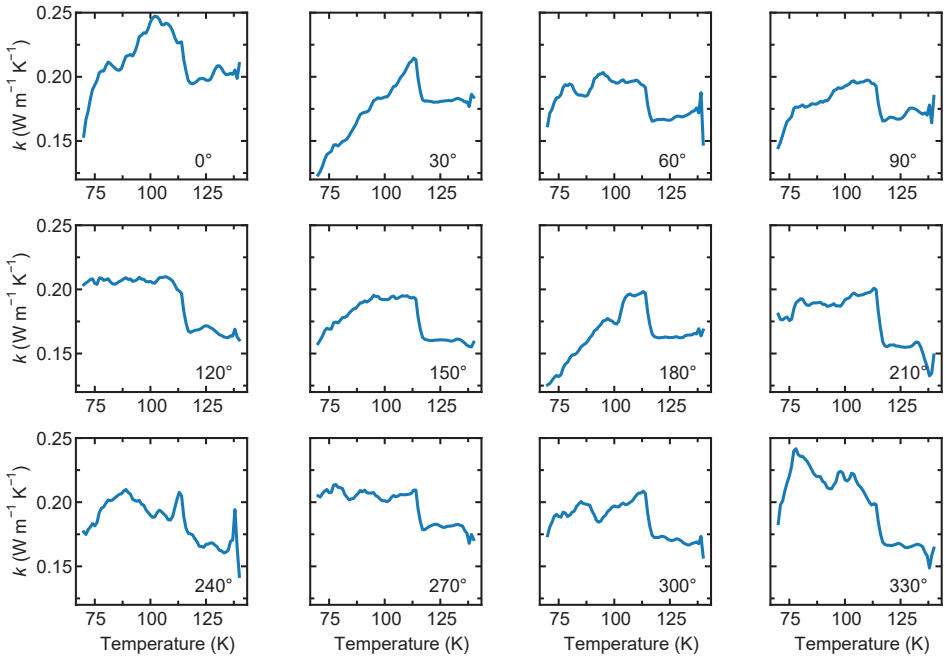

Figure 5.8: **Angle-resolved thermal conductivity in $CoPS_3$ resonators.** Estimated thermal conductivity of rectangular cavities at different orientation with respect to the crystallographic axis of the Co-1 sample. The thermal conductivity is calculated from τ data shown in figure5.7 using (5.A.3)

5.A.5. OPTOTHERMAL ACTUATION OF MAGNETIC MEMBRANES

Here we derive (5.4.1) of the main text. Let us consider the temperature dynamics of the system under optothermal actuation from the power-modulated blue laser, $P_\omega = P_0 e^{i\omega t}$. We start by treating separately the temperature dynamics of the magnetic and phononic systems as $T_{\omega,\mathrm{ph}}$ and $T_{\omega,\mathrm{m}}$, as illustrated in figure 5.9. The fraction of power absorbed from P_ω by each system is determined by the phononic absorption fraction, η_{ph}, and magnetic absorption fraction, η_{m}. The temperature dynamics of the two systems is expressed as a simple RC system:

$$C_{\mathrm{ph}} \frac{dT_{\omega,\mathrm{ph}}}{dt} + \frac{1}{R_{\mathrm{ph}}} T_{\omega,\mathrm{ph}} = P_0 e^{i\omega t}, \tag{5.A.4}$$

$$C_{\mathrm{m}} \frac{dT_{\omega,\mathrm{m}}}{dt} + \frac{1}{R_{\mathrm{m}}} T_{\omega,\mathrm{m}} = P_0 e^{i\omega t}, \tag{5.A.5}$$

where C and R are the system's thermal capacitance and thermal resistance. Thus, the temperature dynamics of the phononic and magnetic systems is given by:

$$T_{\omega,\mathrm{ph}} = \frac{\eta_{\mathrm{ph}} R_{\mathrm{ph}}}{1 + i\omega\tau_{\mathrm{ph}}} P_0 e^{i\omega t}, \tag{5.A.6}$$

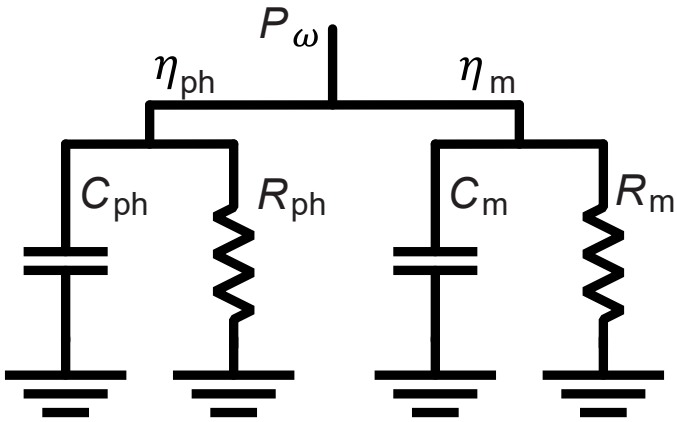

Figure 5.9: **Equivalent circuit illustration of the phononic and magnetic thermal system.** The input power, P_ω, from the blue laser is absorbed with different fractions, η_{ph} and η_m, by the phononic and magnetic systems. The corresponding temperature dynamics is determined by the system thermal resistance, R, and capacitance, C.

$$T_{\omega,m} = \frac{\eta_m R_m}{1 + i\omega\tau_m} P_0 e^{i\omega t}, \tag{5.A.7}$$

where $\tau_{ph} = R_{ph}C_{ph}$ and $\tau_m = R_m C_m$ are the time constants of the two systems.

Below T_N, the temperature modulation T_ω determines changes in the thermal expansion force, $F_{th} = \alpha T$, where α is the thermal expansion coefficient and the magnetostriction force, $F_{ms} = \lambda L^2(T)$, where λ is a magnetostriction coefficient and L the order parameter. When $\omega \ll \omega_0$, the membrane behaves simply as a spring with stiffness k, such that its motion is given by $z_\omega = F_\omega / k$. Thus, given the force modulation resulting from T_ω we get

$$z_\omega = \frac{1}{k}\left(\alpha T_{\omega,ph} + \lambda \frac{dL^2}{dT_{\omega,m}} T_{\omega,m}\right). \tag{5.A.8}$$

Substituting (5.A.6) and (5.A.7) in (5.A.8) yields:

$$z_\omega = \frac{1}{k}\left(\alpha \frac{\eta_{ph} R_{ph} P_0}{1 + i\omega\tau_{ph}} + \lambda \frac{dL^2}{dT_{\omega,m}} \frac{\eta_m R_m P_0}{1 + i\omega\tau_m}\right). \tag{5.A.9}$$

Since the measured data is well represented by a single time constant model, we assume that the temperature dynamics of the phononic and magnetic systems are the same, $\tau_{ph} = \tau_m$ and $\eta_{ph} = \eta_m$. Thus, (5.A.9) is (5.4.1) of the main text.

5.A.6. ORDER PARAMETER FROM RESONANCE FREQUENCY

As derived in [34], the general equation of the resonance frequency, f_θ, of a magnetic rectangular membrane oriented at an angle θ with respect to the crystalline axes is given

by:

$$f_\theta(T) = \frac{1}{2}\sqrt{\frac{E}{\rho w^2(1-\nu^2)}\left[(\sin^2\theta + \nu\cos^2\theta)(\bar{\epsilon}_a + \epsilon_{\lambda,a}) + (\cos^2\theta + \nu\sin^2\theta)(\bar{\epsilon}_b + \epsilon_{\lambda,b})\right]}, \tag{5.A.10}$$

where $\bar{\epsilon}_{a,b} = \epsilon_{0,a,b} + \epsilon_{\alpha,a,b}$, with $\epsilon_{0,a,b}$ the residual fabrication strain and $\epsilon_{\alpha,a,b}$ the thermal expansion strain and $\epsilon_{\lambda,a,b} = \lambda_{a,b}L^2$ are the magnetostrictive strain along the a-axis and b-axis. Under the assumption that the only anisotropic temperature-dependent contribution to the total strain comes from magnetostriction ($\epsilon_{\alpha,a} = \epsilon_{\alpha,b}$), we have

$$\tilde{f}_a^2 - \tilde{f}_b^2 = \frac{E}{4\rho w^2(1+\nu)}(\lambda_a - \lambda_b)L^2, \tag{5.A.11}$$

where $\tilde{f}^2 = f^2(T) - f^2(T_0)$, with T_0 a reference temperature, is the pretension corrected resonance frequency.

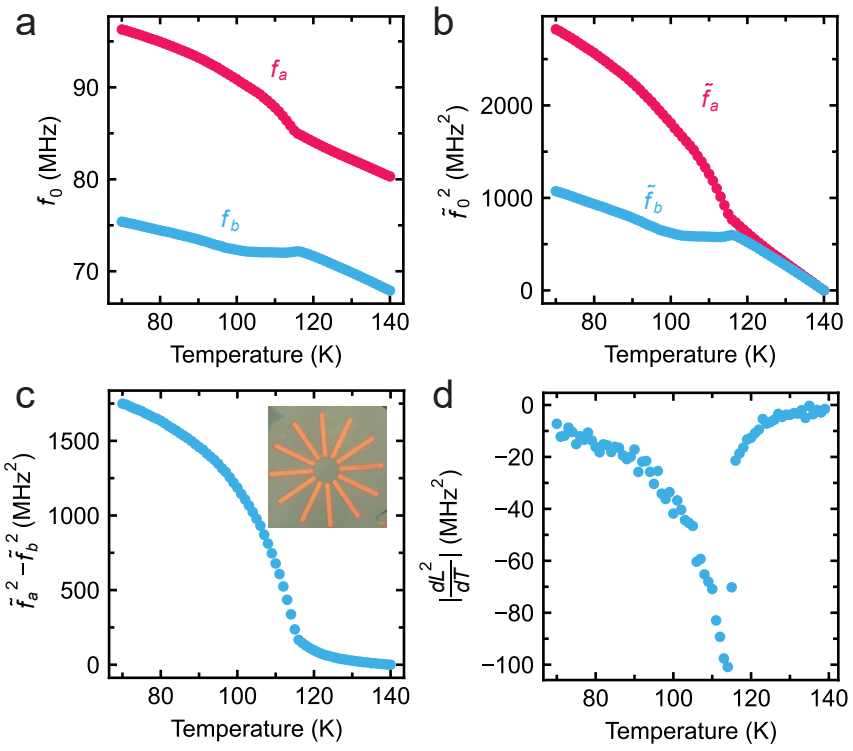

Figure 5.10: **Magnetostriction force from resonance frequency of $CoPS_3$.** Measurements and analysis performed on sample Co-1. **(a)** Bare resonance frequency, $f_\theta(T)$, measured on rectangular membranes oriented along the main crystallographic axes. **(b)** Pretension corrected resonance frequency, $\tilde{f}^2 = f^2(T) - f^2(T_0)$, with T_0 = 140K. **(c)** Difference between corrected resonance frequencies, $\tilde{f}_a^2 - \tilde{f}_b^2$, proportional to the magnetic order parameter, L^2. The inset shows the $CoPS_3$ sample Co-1. **(d)** The temperature derivative of (c).

We use (5.A.11) to extract magnetostriction force, $F_{\text{ms}} \propto \frac{dL^2}{dT}$, used to model the

thermal peak amplitude, $A(T)$, in the main text. Figure 5.10 shows the steps of this analysis for the Co-1 sample, also shown in the inset of figure 5.10c. The bare resonance frequencies f_a and f_b measured on rectangular cavities oriented along a and b crystallographic axis are shown in figure 5.10a. First, we compute the pretension corrected resonance frequency, shown in figure 5.10b, with $T_0 = 140$ K, to remove the contribution of ϵ_0 in (5.A.10). Then, following (5.A.11), the difference between $\tilde{f}^2$ for membranes oriented along different axes is proportional to L^2 (figure 5.10c). Finally, the temperature dependance of the magnetostriction force F_{ms} is found by taking the temperature derivative of $\tilde{f}_a^2 - \tilde{f}_b^2$, as shown in figure 5.10d.

Figure 5.11 shows how the resulting magnetostriction force is combined with the Debye model of specific heat to fit the experimental data of the thermal peak amplitude of a rectangular membrane of sample Co-1. The results of this analysis performed for all rectangular membranes of sample Co-1 are shown in figure 5.13.

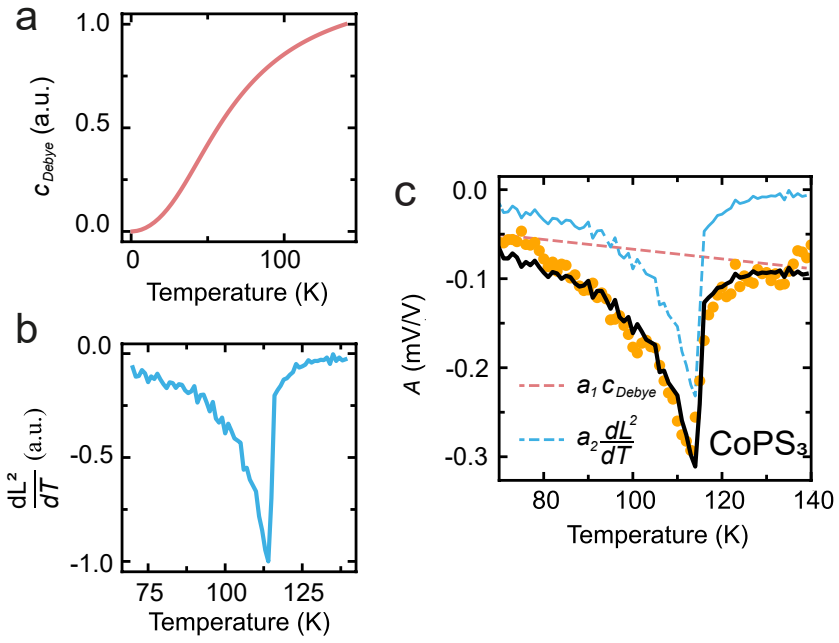

Figure 5.11: **Model for thermal peak amplitude.** Thermal peak amplitude fit on a rectangular resonator of sample Co-1. **(a)** Debye model of the phononic specific heat with $\Theta_D = 262$ K. **(b)** Magnetostriction force extracted from antiferromagnetic order parameter, L. **(c)** Thermal peak amplitude data (orange dots) compared to model (black) and contributions from phononic specific heat (light red) and magnetostriction force (light blue).

In figure 5.12, we show the same analysis as done in figure 5.10 for the $FePS_3$ sample Fe-3. We use the resulting temperature dependence of the magnetostriction force from figure 5.12d to model the thermal peak amplitude data of the $FePS_3$ sample Fe-1 in figure 5.4 and of the sample Fe-2 in figure 5.14.

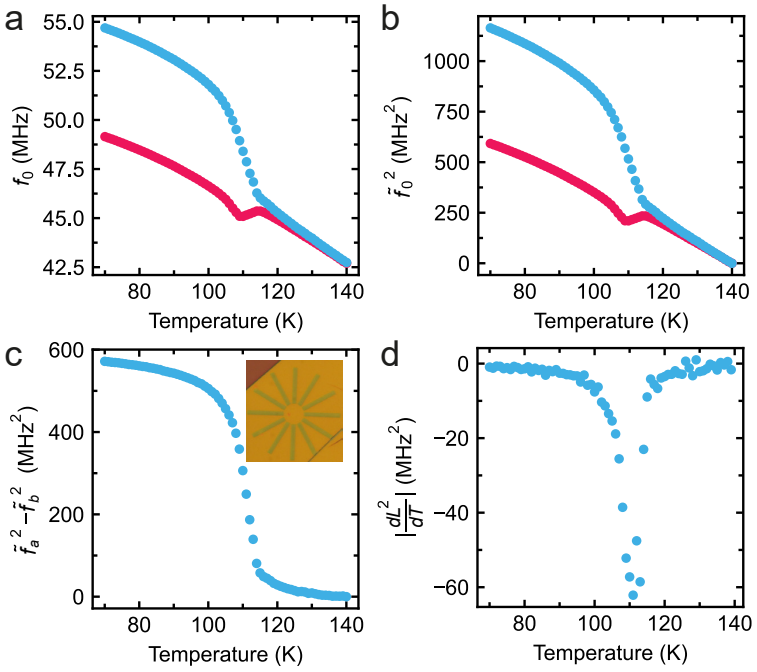

Figure 5.12: **Magnetostriction force from resonance frequency of $FePS_3$.** Measurements and analysis performed on sample Fe-3 **(a)** Bare resonance frequency, $f_\theta(T)$, measured on rectangular membranes oriented along the main crystallographic axes. **(b)** Pretension corrected resonance frequency, $\tilde{f}^2 = f^2(T) - f^2(T_0)$, with $T_0 = 140$K. **(c)** Difference between corrected resonance frequencies, $\tilde{f}_a^2 - \tilde{f}_b^2$, proportional to the magnetic order parameter, L^2. The inset shows the $FePS_3$ sample Fe-3. **(d)** The temperature derivative of (c).

5.A.7. ADDITIONAL DATA ON MPS_3 RESONATORS

Figure 5.13 shows the result of the analysis done in section 5.A.6 for the thermal peak amplitude measured on all rectangular cavities of sample Co-1. The resulting fit parameters $a_1(\theta)$ and $a_2(\theta)$ are listed in table 5.2 plotted in figure 5.4d-e.

Figures 5.14-5.15 show additional data on $FePS_3$ (sample Fe-2) and $NiPS_3$ (sample Ni-1,2) resonators. Interestingly, in $NiPS_3$ no peak is observed at the phase transition on the thermal time constant data. The large enhancement of the thermal peak amplitude, A is still observed. Further analysis and theoretical work on thermal peak amplitude data might allow the extraction of the order parameter, L, of $NiPS_3$ from the measured A instead.

Angle	0°	30°	60°	90°	120°	150°	180°	210°	240°	270°	300°	330°
a_1	-0.29	-0.29	-0.29	-0.31	-0.31	-0.31	-0.29	-0.29	-0.29	-0.30	-0.31	-0.29
a_2	0.19	0.20	0.29	0.31	0.33	0.28	0.18	0.23	0.18	0.33	0.32	0.25

Table 5.2: **Angle-resolved fit parameters a_1 and a_2** Fit parameters a_1 and a_2 for the plots in figure 5.11.

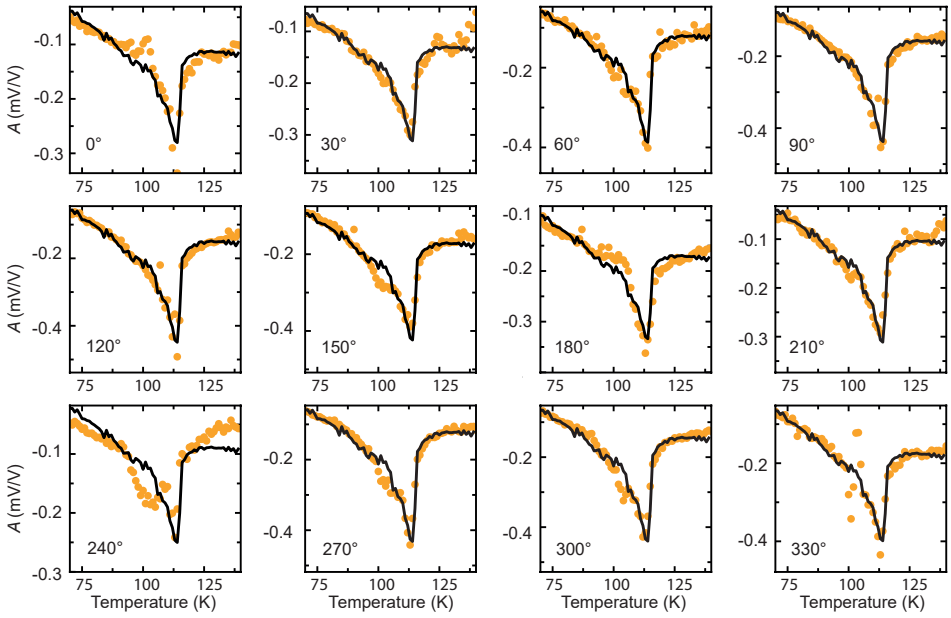

Figure 5.13: **Angle-resolved thermal peak amplitude in $CoPS_3$ resonators.** Thermal peak amplitude data (orange dots) compared to model (black) for rectangular cavities at different orientation with respect to the crystallographic axis of the Co-1 sample.

5.A.8. ANGLE-RESOLVED MEMBRANE DISPLACEMENT

Here we derive the expression of $a_1(\theta)$ and $a_2(\theta)$ used in the main text. Given the stress σ on a rectangular membrane oriented at an angle θ with respect to the crystalline axis:

$$\sigma_x = \sigma_a \cos^2\theta + \sigma_b \sin^2\theta, \tag{5.A.12a}$$

$$\sigma_y = \sigma_a \sin^2\theta + \sigma_b \cos^2\theta. \tag{5.A.12b}$$

If such stress is time dependent, it will actuate the membrane as $z(t) = \gamma_w \sigma_x + \gamma_l \sigma_y$, where γ_w and γ_l are effective expansion coefficients. From the constitutive equations of the materials, we can write

$$\begin{aligned} c_1 &= E(\epsilon_{0,a} + \epsilon_{\alpha,a} + \epsilon_{\lambda,a}) \\ &= E\left(\epsilon_{0,a} - \int_{T_0}^{T_1} \alpha_a(T)dT - \lambda_a L^2(T_1)\right) = \sigma_a(T_1) - \nu\sigma_b(T_1), \end{aligned} \tag{5.A.13a}$$

$$\begin{aligned} c_2 &= E(\epsilon_{0,b} + \epsilon_{\alpha,b} + \epsilon_{\lambda,b}) \\ &= E\left(\epsilon_{0,b} - \int_{T_0}^{T_1} \alpha_b(T)dT - \lambda_b L^2(T_1)\right) = \sigma_b(T_1) - \nu\sigma_a(T_1), \end{aligned} \tag{5.A.13b}$$

where ϵ_0 is residual fabrication strain at $T = T_0$, α is the thermal expansion coefficient, λ the magnetostriction coefficient and E is the Young's modulus, which is assumed to be

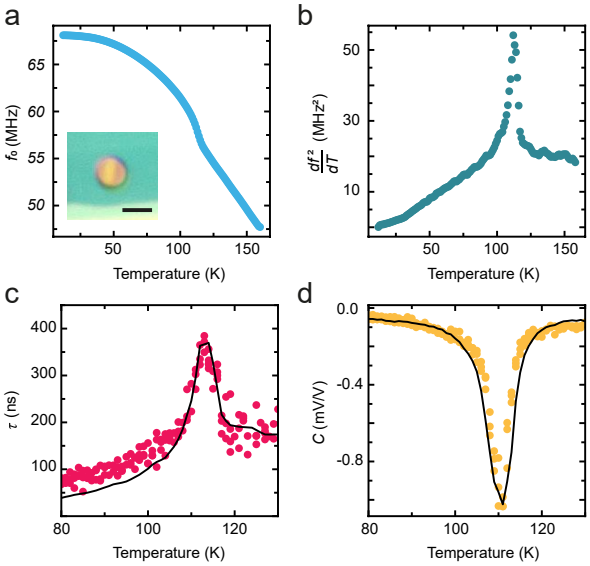

Figure 5.14: **Additional data on $FePS_3$ resonators.** Measurements data and analysis performed on sample Fe-2. **(a)** Temperature dependent resonance frequency, $f_0(T)$. The inset shows the $FePS_3$ sample Fe-2. Scale bar is 4 μm. **b** Derivative with respect to temperature of f_0 from (a). **(c)** Comparison between measured τ (red dots) and model (black line). The model is calculated from Eq. 1 from the main text with c_v from df^2/dT in (b), κ from bulk [107] and $\mu^2 = 10$. **(d)** Thermal peak amplitude data (orange dots) compared to model (black).

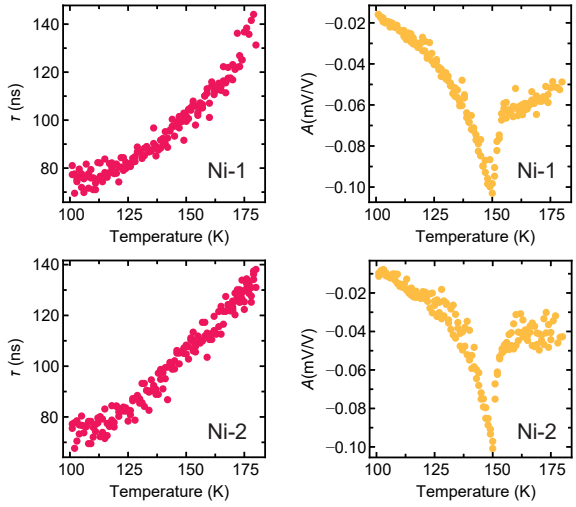

Figure 5.15: **Additional data on $NiPS_3$ resonators. (Left)** Thermal time constant of the $NiPS_3$ resonators. **(Right)** Thermal peak amplitude of the $NiPS_3$ resonators.

isotropic. We can thus write

$$\sigma_a = c_1 + \nu\sigma_b\,, \tag{5.A.14a}$$
$$\sigma_b = c_2 + \nu\sigma_a\,, \tag{5.A.14b}$$

which can be combined in the following expressions for σ_a and σ_b:

$$\sigma_a = \frac{c_1 + \nu c_2}{1-\nu^2}\,, \tag{5.A.15a}$$
$$\sigma_b = \frac{c_2 + \nu c_1}{1-\nu^2}\,. \tag{5.A.15b}$$

We consider separately the temperature dynamics of the magnetic and phononic systems as $T_{\omega,\mathrm{m}}$ and $T_{\omega,\mathrm{ph}}$ as in 5.A.7 and 5.A.6. The membrane displacement can thus be expressed as

$$\begin{aligned} z_\theta(t) &= \gamma_w \sigma_x(T_{\omega,\mathrm{ph}}(t), T_{\omega,\mathrm{m}}(t)) + \gamma_l \sigma_y(T_{\omega,\mathrm{ph}}(t), T_{\omega,\mathrm{m}}(t)) \\ &\approx \gamma_w \left[\frac{\partial\sigma_x}{\partial T_{\omega,\mathrm{ph}}} T_{\omega,\mathrm{ph}}(t) + \frac{\partial\sigma_x}{\partial T_{\omega,\mathrm{m}}} T_{\omega,\mathrm{m}}(t)\right] \\ &\quad + \gamma_l \left[\frac{\partial\sigma_y}{\partial T_{\omega,\mathrm{ph}}} T_{\omega,\mathrm{ph}}(t) + \frac{\partial\sigma_y}{\partial T_{\omega,\mathrm{m}}} T_{\omega,\mathrm{m}}(t)\right]. \end{aligned} \tag{5.A.16}$$

Assuming that thermal expansion is isotropic ($\alpha_x = \alpha_y$) and that it only depends on $T_{\omega,\mathrm{ph}}$ and that magnetostriction only depends on $T_{\omega,\mathrm{m}}$ we have

$$\frac{\partial c_1}{\partial T_{\omega,\mathrm{ph}}} = -E\alpha(T_{\omega,\mathrm{ph}})\,, \qquad \frac{\partial c_1}{\partial T_{\omega,\mathrm{m}}} = -E\lambda_a \frac{\partial L^2}{\partial T_{\omega,\mathrm{m}}}(T_{\omega,\mathrm{m}})\,, \tag{5.A.17a}$$
$$\frac{\partial c_2}{\partial T_{\omega,\mathrm{ph}}} = -E\alpha(T_{\omega,\mathrm{ph}})\,, \qquad \frac{\partial c_2}{\partial T_{\omega,\mathrm{m}}} = -E\lambda_b \frac{\partial L^2}{\partial T_{\omega,\mathrm{m}}}(T_{\omega,\mathrm{m}})\,, \tag{5.A.17b}$$

Thus, combining (5.A.16) and (5.A.17) we get:

$$\begin{aligned} z_\theta(t) = -\frac{P_0 E}{(1-\nu^2)}\Bigg[&\frac{(\gamma_w+\gamma_l)\eta_{\mathrm{ph}} R_{\mathrm{ph}}(1+\nu)}{1+i\omega\tau_{\mathrm{ph}}}\alpha + \\ &+ \frac{\eta_{\mathrm{m}} R_{\mathrm{m}}}{1+i\omega\tau_{\mathrm{m}}}\Big((\gamma_w(\lambda_a+\nu\lambda_b) + \gamma_l(\lambda_b+\nu\lambda_a))\cos^2\theta \\ &+ (\gamma_w(\lambda_b+\nu\lambda_a) + \gamma_l(\lambda_a+\nu\lambda_b))\sin^2\theta\Big)\Bigg]. \end{aligned} \tag{5.A.18}$$

For high aspect-ratio rectangular membranes ($w \ll l$), it is possible to neglect the force along the long axis $\gamma_w \ll \gamma_l$ such that

$$\begin{aligned} z_\theta(t) = -\frac{P_0\gamma_l E}{(1-\nu^2)}\Bigg[&\frac{\eta_{\mathrm{ph}} R_{\mathrm{ph}}(1+\nu)}{1+i\omega\tau_{\mathrm{ph}}}\alpha \\ &+ \frac{\eta_{\mathrm{m}} R_{\mathrm{m}}}{1+i\omega\tau_{\mathrm{m}}}\Big((\lambda_b+\nu\lambda_a)\cos^2\theta + (\lambda_a+\nu\lambda_b)\sin^2\theta\Big)\Bigg], \end{aligned} \tag{5.A.19}$$

from which (5.5.1) and (5.5.2) for $a_1(\theta)$ and $a_2(\theta)$ of the main text are extracted.

REFERENCES

22. Šiškins, M. *et al.* Magnetic and electronic phase transitions probed by nanomechanical resonators. *Nat. Commun.* **11,** 2698 (June 2020).

34. Houmes, M. J. A. *et al.* Magnetic order in 2D antiferromagnets revealed by spontaneous anisotropic magnetostriction. *Nat. Commun.* **14,** 8503 (Dec. 2023).

58. Liu, Q. *et al.* Magnetic order in XY-type antiferromagnetic monolayer $CoPS_3$ revealed by Raman spectroscopy. *Phys. Rev. B* **103,** 235411 (June 2021).

101. Dolleman, R. J. *et al.* Optomechanics for thermal characterization of suspended graphene. *Phys. Rev. B* **96,** 165421 (Oct. 2017).

102. Dolleman, R. J. *et al.* Transient thermal characterization of suspended monolayer MoS_2. *Phys. Rev. Mater.* **2,** 114008 (Nov. 2018).

106. Lifshitz, R. & Roukes, M. L. Thermoelastic damping in micro- and nanomechanical systems. *Phys. Rev. B* **61,** 5600–5609 (Feb. 2000).

107. Haglund, A. *Thermal Conductivity of MXY_3 Magnetic Layered Trichalcogenides* (Ph.D. thesis, University of Tennessee, Knoxville, 2019).

6

NONLINEAR DYNAMICS AND MAGNETO-ELASTICITY OF NANODRUMS NEAR THE PHASE TRANSITION

Nanomechanical resonances of two-dimensional (2D) materials are sensitive probes for condensed-matter physics, offering new insights into magnetic and electronic phase transitions. Despite extensive research, the influence of the spin dynamics near a second-order phase transition on the nonlinear dynamics of 2D membranes has remained largely unexplored. Here, we investigate nonlinear magneto-mechanical coupling to antiferromagnetic order in suspended $FePS_3$-based heterostructure membranes. By monitoring the motion of these membranes as a function of temperature, we observe characteristic features in both nonlinear stiffness and damping close to the Néel temperature T_N. We account for the experimental observations with an analytical magnetostriction model in which these nonlinearities emerge from a coupling between mechanical and magnetic oscillations, demonstrating that magneto-elasticity can lead to nonlinear damping. Our findings thus provide insights into the thermodynamics and magneto-mechanical energy dissipation mechanisms in nanomechanical resonators due to the material's phase change and magnetic order relaxation.

Parts of this chapter have been published in [108].

6.1. INTRODUCTION

THE mechanical properties of two-dimensional (2D) materials have been extensively studied [109, 110] due to their potential for use in a variety of applications, such as sensing [110–112] and energy transduction [113–115]. Owing to its superior sensitivity to applied forces, the motion of these membranes can be coupled to various degrees of freedom [113, 115], ranging from coupling to photons [116, 117], phonons [118–120] and electrons [21, 121, 122], to an interaction between multiple resonators at a distance [120, 123]. Their small mass and ultra-thin nature also make them highly susceptible to geometric nonlinearities [124], leading to internal resonances [125, 126] and various nonlinear dissipation mechanisms [114, 118, 125, 127] that can dictate their motion dynamics at relatively small amplitudes.

Recently, there has been a growing interest in using nanomechanical vibrations of 2D materials as practical nodes for inferring elastic and thermodynamic properties of 2D membranes [113]. Examples include nonlinear dynamic characterization of their elastic properties [124], probing magnetic [22, 34, 49, 87, 104, 128, 129] and electronic phase transitions [21, 22]. Among them, the ability of these membranes to detect the magnetic phase change in the absence of an applied magnetic field [22, 87, 104] has opened up new avenues for developing self-sensitive magnetic nano-electromechanical (NEMS) devices [113, 115]. This approach relies on the coupling between the magnetic and mechanical properties of the 2D material, which allows for highly sensitive detection of magnetisation [34, 49] and thermodynamics of magnetic phases [22, 104]. Furthermore, since these freestanding 2D materials are easily driven to the nonlinear regime of mechanical motion [124, 125], the comprehensive studies and analysis of nonlinear dynamics become important given that their magneto-elastic interactions and microscopic dissipation pathways are inherently linked.

Here, we explore the effect of magneto-elastic coupling and magnetic order on the nonlinear dynamics of antiferromagnetic membranes made of $FePS_3$-based heterostructures. We study the changes in both nonlinear stiffness and nonlinear damping as a result of the antiferromagnetic phase transition near the Néel temperature T_N of $FePS_3$ [22, 38]. Consequently, we describe these experimental observations with a magnetostriction model, revealing and providing a description of the magneto-mechanical dissipation mechanism as a previously unexplored source of nonlinear damping in 2D material membranes.

6.2. MEASUREMENT SETUP

We create a freestanding membrane by suspending a 9.5 ± 0.6 nm thin layer of $FePS_3$ over a pre-defined circular cavity with a radius, $r = 1.5$ μm, in a Si/SiO_2 substrate, figure 6.1. We cover the $FePS_3$ membrane with multi-layer graphene (MLG) of 2.0 ± 0.7 nm thickness in order to electrically contact the membrane and improve thermal conductivity of the structure [101, 130]. These MLG/$FePS_3$ heterostructure membranes are then placed in an optical closed-cycle cryostat chamber and cooled to cryogenic temperatures. The temperature of the sample is controlled using a local sample heater located directly under the sample. We interferometrically measure the amplitude of the membrane's fundamental mode of vibration, x, in response to the low-power opto-thermal drive at several

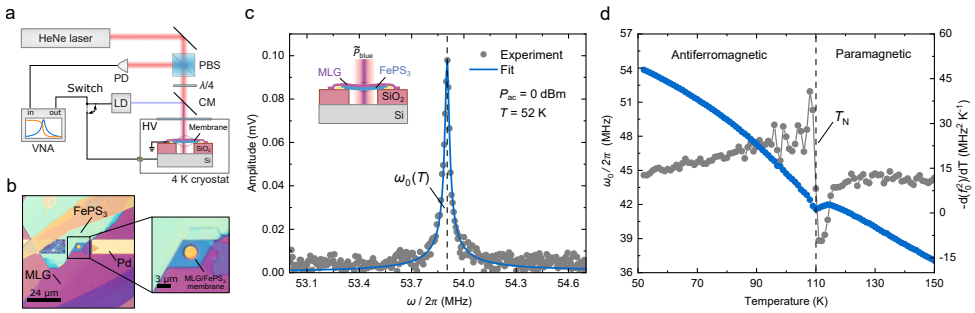

Figure 6.1: Membrane resonator made of MLG/$FePS_3$ heterostructure. **a** Schematic of the laser interferometer measurement setup, see section 6.8. PD is the photodiode, LD - the laser diode, CM - the cold (dichroic) mirror, PBS - the polarized beam splitter, VNA - the vector network analyzer. **b** Optical image of the sample. **c** The measured fundamental resonance peak of the membrane (filled grey dots) at opto-thermal drive excitation power $P_{ac} = 0$ dBm. The solid blue line is fit of the linear damped harmonic oscillator model. The inset shows the schematic of the device cross-section. A vertical dashed line indicates extracted ω_0. **d** The resonance frequency ω_0 as a function of temperature, extracted from the fit similar to (c) (filled blue dots). Connected grey dots are the corresponding derivative of the f_0^2. A vertical dashed line indicates T_N.

temperatures [22, 131], see section 6.8 and figure 6.1a-c. By fitting the measured resonance peak (grey-filled dots) to the linear harmonic oscillator model (solid blue line) we extract the corresponding resonance frequency $\omega_0(T) = 2\pi f_0(T)$, as shown in figure 6.1c.

We measure $f_0(T)$ in the temperature range from 52 to 150 K as shown in figure 6.1d. In the vicinity of $T \sim 110$ K (vertical dashed line in figure 6.1d) the resonance frequency $f_0(T)$ exhibits the antiferromagnetic-to-paramagnetic phase transition-related anomaly. This becomes even more prominent in the temperature derivative of $f_0^2(T)$ (filled grey dots in figure 6.1d). This quantity, the temperature derivative of $f_0^2(T)$, is related to specific heat $c_v(T)$ of the material through thermal expansion coefficient and Grüneisen parameter [22]. Thus, the temperature at which the discontinuity in $-\frac{\mathrm{d}f_0^2(T)}{\mathrm{d}T}$ occurs can be used as a measure of T_N [22, 104]. This is further supported by the fact that the measured T_N also corresponds to a peak in inverse quality factor $Q^{-1}(T)$, which is expected to arise near the phase transition temperature [22, 104, 123], see section 6.A.1.

After characterising the dynamics of the membrane in the linear regime and at a low opto-thermal driving force, we increase the drive from 0 to 8 dBm to achieve higher force levels and observe features of the nonlinear motion [124]. Figure 6.2a displays a Duffing response measured at $T = 52$ K and 8 dBm. By varying the direction of the frequency sweep the bi-stability of the amplitude behaviour becomes clear. By further increasing P_{ac}, we observe a corresponding decrease in responsivity of the resonance peak, shown in figure 6.2b. This indicates the presence of nonlinear damping in the system, which becoming more apparent at higher amplitudes of motion [125]. We measure the amplitude of membrane motion around $f_0(T)$ at a drive power of 8 dBm in the temperature range from 52 to 150 K. The result of which is shown in figure 6.2c. The vertical dashed line indicates the measured $f_0(T)$ in the linear regime from figure 6.1d.

Two noteworthy observations can be made: first, the position of the resonance peak at a higher driving power is shifted to higher frequencies near T_N, indicating a change in

linear membrane stiffness k_1, corresponding to a change in the strain [22]; secondly, the peak amplitude of the Duffing response and its associated frequency change depending on the magnetic state of the membrane with the largest effect near T_N, indicating a change in nonlinear membrane stiffness k_3 [124], see figure 6.2c and section 6.A.2. In order to exclude optical effects coming from the excitation laser as a cause of this behaviour, we performed control experiments on multiple samples using both optical and electrical excitation, where an AC voltage V_{ac} signal is applied between the global Si backgate of the chip and the conducting top layer of MLG. Since we obtain similar results for both the electrostatic and the optothermal drive we conclude that the reported observations are intrinsic to the resonator and not related to the driving mechanism, see section 6.A.3.

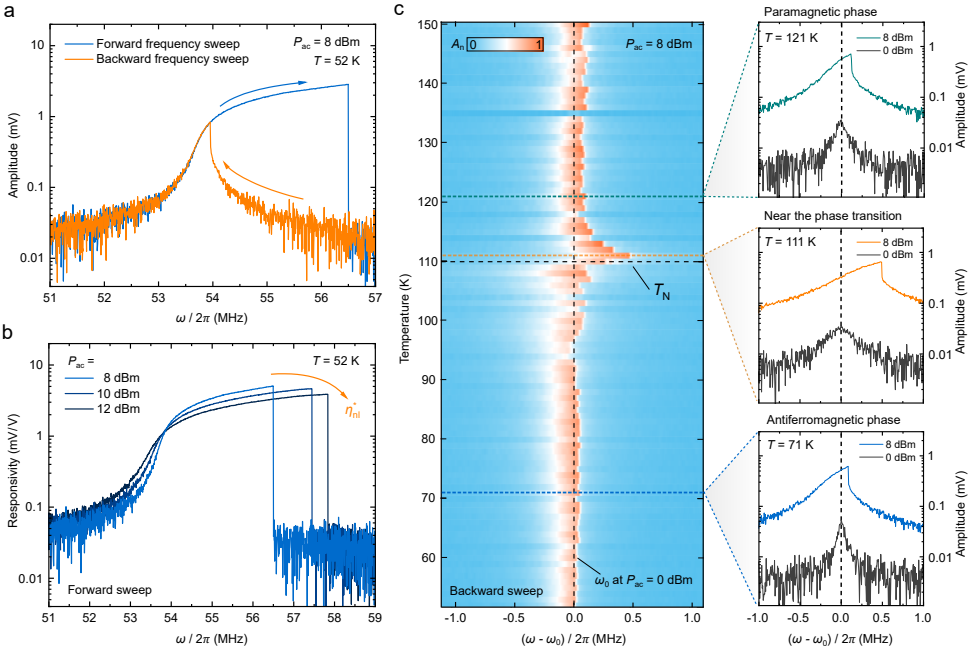

Figure 6.2: Nonlinear dynamics of a MLG/$FePS_3$ membrane. **a** The measured Duffing response and amplitude branches of the resonance peak from figure 6.1c at higher excitation power (P_{ac} = 8 dBm). **b** The measured resonance peak responsivity, i.e., the amplitude response normalized by dividing by the drive-power, at 8, 10 and 12 dBm for the same temperature from (a) indicating the presence of nonlinear damping η^*_{nl}. **c** Left panel: Colour map of the normalized amplitude, as in panel b, measured as a function of temperature for backward frequency sweeps with respect to the linear resonance frequency $\omega_0(T)$ shown in figure 6.1d. The Néel temperature T_N from figure 6.1d is indicated with a black dashed horizontal line. Right panel: measured frequency response around ω_0 corresponding to dashed line cuts from the left panel at three temperature points corresponding to different magnetic phases. The linear response measured at P_{ac} = 0 dBm is included as the black line

6.3. FITTING NONLINEAR RESPONSE

We utilize a dedicated algorithm to fit the measured nonlinear response at different temperatures in the vicinity of T_N. Our approach involves fitting the experimental data with the Duffing-van der Pol equation, see equation (6.8.7) and section 6.A.4, as depicted in figure 6.3a. To avoid an over-parameterised fitting procedure and reduce the uncertainty of the fit, we first extract quality factors $Q(T)$ and $\omega_0(T)$ from the linear resonance peak at low drive levels. Next, we extract the relative driving force $F_\omega(T)$ by fitting the off-resonance response to a harmonic oscillator model. After obtaining all the linear parameters, we extract the Duffing term $k_3^*(T)$ at $P_{ac} = 10$ dBm from the slope of the backbone curve of the nonlinear frequency response [125], figure 6.3b. Consequently, we fix this value while fitting the forward frequency sweep response, thereby extracting the van der Pol-type nonlinear damping term $\eta_{nl}^*(T)$ using an optimizer algorithm, see section 6.A.4. Figure 6.3c shows the extracted nonlinear damping term for the temperature range $52 - 150$ K. At a higher driving power and as the temperature decreases, a sharp drop in $k_3^*(T)$ is observed at $T < T_N$. This feature coincides with a peak in $\eta_{nl}^*(T)$ at approximately the same temperature.

6.4. THEORETICAL MODEL

The pronounced features in both $k_3^*(T)$ and $\eta_{nl}^*(T)$ close to T_N shown in figure 6.3b and c indicate the softening of nonlinear stiffness as well as a prominent increase in the nonlinear dissipation in the antiferromagnetic phase of $FePS_3$, suggesting the magnetic origin of the effect. Therefore, we model the system by considering the elastic potential energy as a function of the membrane displacement at its centre, U_{el}, and the magnetic free energy, U_m, of $FePS_3$, coupled via spontaneous magnetostriction, U_{ms} [22, 34, 55], see section 6.A.5:

$$\begin{aligned} U_T &= U_{el} + U_m + U_{ms} \\ &= \left[\frac{k_1}{2}x^2 + \frac{k_3}{4}x^4\right] + \\ &\quad \left[U_{m,0} + \frac{a(T - T_N)}{2}L^2 + \frac{B}{4}L^4\right] + \left[\frac{\lambda_{ij}\sigma_{ij}(x)}{2}L^2\right], \end{aligned} \tag{6.4.1}$$

where $\sigma_{ij}(x)$ is the amplitude-dependent stress tensor, L the antiferromagnetic order parameter in the direction of the easy-axis of $FePS_3$, λ_{ij} the magnetostriction tensor, $U_{m,0}$ is the magnetic energy in the paramagnetic state, and a, B are phenomenological positive constants [55, 134]. By minimizing equation (6.4.1) with respect to L at a static deformation $\omega = 0$, the ground state order parameter L_0 is obtained, see section 6.8 and section 6.A.5. When the membrane is in motion and the magnetic system is out of equilibrium, the order parameter is stress- and time-dependent, $L(t) \simeq L_0 + L_\omega(t)$. The rate at which $L(t)$ approaches the ground state L_0, figure 6.3f, is described by the kinetic equation [135–137]:

$$\frac{dL}{dt} = -\kappa\frac{\partial U_T}{\partial L}, \tag{6.4.2}$$

where t is the time and κ the phenomenological kinetic coefficient, which we assume to be temperature-independent for simplicity.

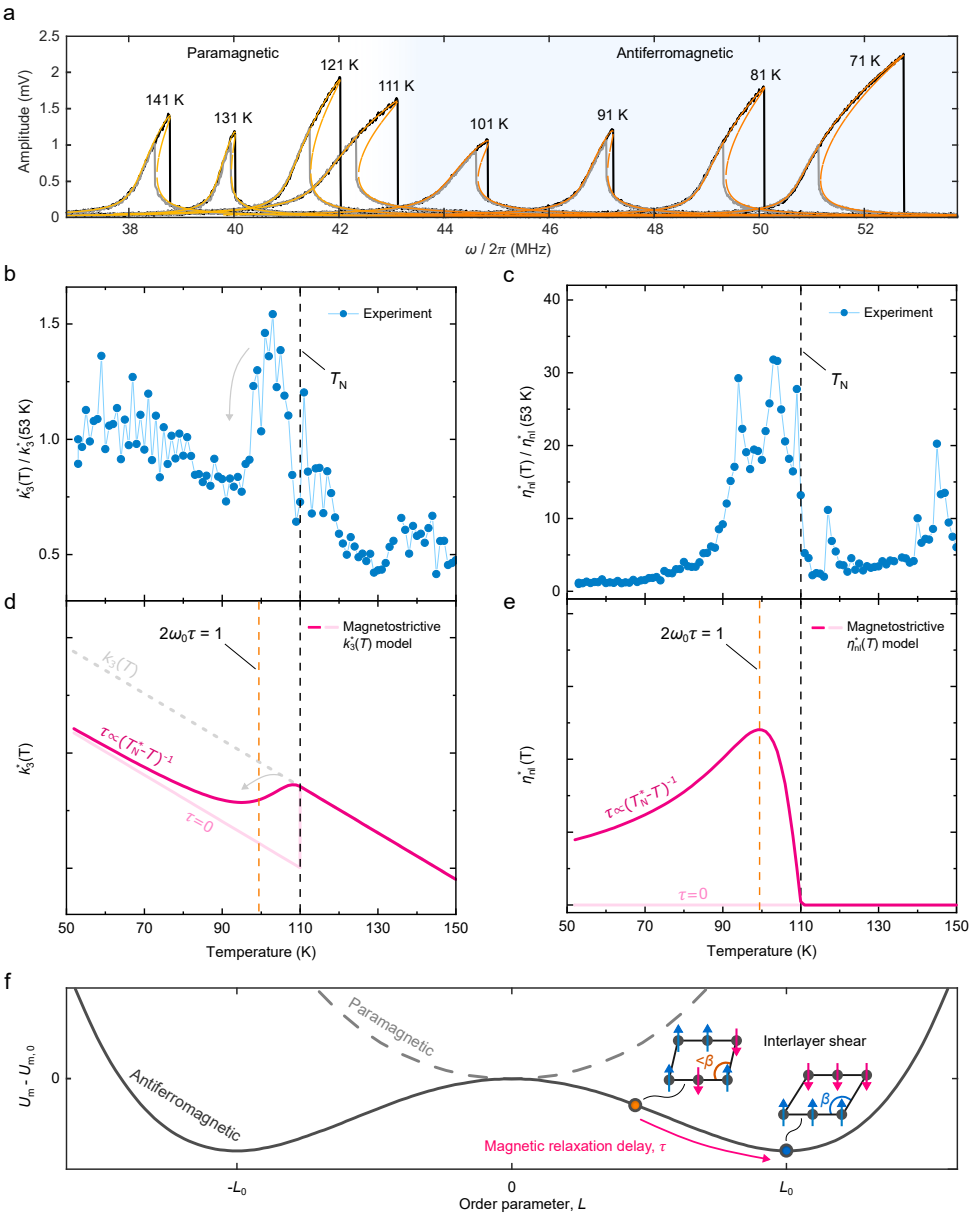

Figure 6.3: Temperature dependence of the nonlinear stiffness k_3^* and nonlinear damping η_{nl}^* of a magnetostrictive membrane resonator. **a** Fit of equation (6.8.7) (orange solid lines) to the measured amplitude for forward frequency sweep (black solid lines) and backward frequency sweeps (grey solid lines) at $P_{ac} = 10$ dBm and the temperature point indicated. The right side of the panel, light blue region, schematically indicates the antiferromagnetic phase of the membrane. **b** Connected blue dots - the measured $k_3^*(T)$, extracted from the fits shown in (a), normalized by the value at 53 K. **c** Connected blue dots - the measured $\eta_{nl}^*(T)$, extracted from the fits shown in (a), normalized by the value at 53 K. **d** and **e** Solid magenta lines - the nonlinear stiffness and nonlinear damping model of equations (6.4.6) and (6.4.7) respectively at $\omega = \omega_0(T)$ from figure 6.1d and $\tau^{-1}(T) = 2\kappa a\left(T_N^* - T\right)$ from Zhou et al. [132] for $h = 9.5$ nm, solid light lines - the model of equations (6.4.6) and (6.4.7) at the same $\omega = \omega_0(T)$ and $\tau = 0$, see section 6.A.5. Dashed light line in (d) - non-magnetic $k_3(T)$ slope extracted by a linear fit to $T > 110$ K region in (b). Vertical dashed orange lines in (d) and (e) - the temperature point at which $2\omega_0\tau = 1$, producing a maximum in the nonlinear damping $\eta_{nl}^*(T)$. **f** Schematic of the magnetic free energy of the system with un-relaxed (orange dot) and relaxed ground (blue dot) states indicated. Magnetic sub-lattice relaxation dynamics is accompanied by a slow interlayer shear deformation with a change in the monoclinic angle β [132, 133] schematically indicated in insets, which hypothetically may have the dominant contribution to τ.

We further describe the driven coupled magneto-mechanical system by linearizing equation (6.4.2) near L_0 together with obtaining the equation of motion associated with the generalized coordinate, x. We define the Lagrangian $\mathscr{L} = \frac{1}{2}m\dot{x}^2 - U_\mathrm{T}$ and use the Euler-Lagrange equations to obtain a system of coupled dynamic equations:

$$\dot{L}_\omega + \frac{L_\omega}{\tau} + \lambda\kappa L_0\sigma_\omega = 0, \tag{6.4.3}$$

$$m\ddot{x} + k_1 x + k_3 x^3 + \frac{\lambda}{2}L^2\frac{\partial\sigma(x)}{\partial x} = F_\omega\cos(\omega t) - \left(\frac{m\omega_0}{Q} + \eta_\mathrm{nl}x^2\right)\dot{x}, \tag{6.4.4}$$

where $\sigma = \sigma_0 + \sigma_\omega$ with static σ_0 and dynamic σ_ω stress contributions, F_ω the amplitude of periodic driving force, λ the phenomenological magnetostriction coefficient that corresponds with the coupling of in-plane membrane stress to the order parameter in the direction of the easy axis L and $\tau = \left[2\kappa a\left(T_\mathrm{N}^* - T\right)\right]^{-1}$, the magnetic relaxation time constant of the $FePS_3$ layer [132, 135, 136], see section 6.8 and section 6.A.5.

Typically, magnetic relaxations in antiferromagnets occur on timescales of the order of picoseconds [40, 60, 138]. However, in the case of $FePS_3$ long nanosecond-scale relaxation times are required to relax the magnetic sub-lattice near T_N due to the strong coupling between the ordering of spins and the lattice, particularly to the slow process of interlayer shear[132, 133], schematically shown in figure 6.3f. We hypothesise that this slow spin-shear relaxation mechanism in $FePS_3$ may have the dominant contribution to the magnetic time constant τ in equation (6.4.3), and hereinafter consider the experimentally measured spin-shear $\tau(T)$ from the work of Zhou et al. [132], see section 6.A.5. The L_ω term then induces oscillations in L, which can lag the membrane motion at sufficiently large τ [132, 133] producing a delay in the coupled magneto-mechanical system.

Solving the coupled system of equations (6.4.3) and (6.4.4) using the harmonic balance method, we obtain the steady-state amplitude-frequency response, see section 6.8 and section 6.A.5. We find that when the membrane is in motion, the linear and nonlinear stiffness as well as the nonlinear damping coefficients are renormalized by the additional magnetic terms, which yield the following steady-state equation of Duffing-van der Pol type [125]:

$$\left(\frac{3k_3^*}{4}a_\mathrm{s}^3 + m(\omega_0^2 - \omega^2)a_\mathrm{s}\right)^2 + \left(\eta_\mathrm{nl}^* a_\mathrm{s}^3 + \frac{m\omega_0}{Q}a_\mathrm{s}\right)^2\omega^2 = F_\omega^2, \tag{6.4.5}$$

in which, $x = a_\mathrm{s}\cos(\omega_0 t)$, with a_s the steady-state amplitude, m the effective mass of the resonator, $m\omega_0^2 = k_1^* = k_1 + \lambda L_0^2\frac{Ec_3}{2r^2}$ the renormalized linear stiffness, k_3^* the renormalized nonlinear stiffness:

$$k_3^* = \begin{cases} k_3 - \frac{\lambda^2}{12B}\frac{E^2c_3^2}{r^4}\frac{1}{1+4\omega^2\tau^2} & T < T_\mathrm{N}^* \\ k_3 & T > T_\mathrm{N}^*, \end{cases} \tag{6.4.6}$$

and η_nl^* the magnetic nonlinear damping term of van der Pol type [125, 139]:

$$\eta_\mathrm{nl}^* = \begin{cases} \eta_\mathrm{nl} + \frac{\lambda^2}{2B}\frac{E^2c_3^2}{r^4}\frac{\tau}{1+4\omega^2\tau^2} & T < T_\mathrm{N}^* \\ \eta_\mathrm{nl} & T > T_\mathrm{N}^*, \end{cases} \tag{6.4.7}$$

where E is the Young's modulus and c_3 the geometric numerical factor which depends on membrane's Poisson ratio [124].

6.5. DISCUSSION

Renormalization of k_1^* and k_3^* leads to two important consequences. First, since the magnetostriction term is quadratic in L, it has the same functional form as the quadratic k_1 term in the magnetic energy and, since k_1 depends on the Néel temperature, it can therefore be considered as a renormalization of T_N. Thus, strain alters the transition temperature as $T_N^* = T_N - \frac{\lambda_{ij}\sigma_{ij}(x)}{a}$, with a a positive constant, which was previously demonstrated by applying a static external force [22]. Consequently, particularly at high amplitude of oscillations, the change of stress due to the membrane motion results in an additional strain compared to the static case, see section 6.A.5 for more details. This strain can reach up to 0.03% in similar systems [140] and consequently reduce T_N^* of $FePS_3$ by a few Kelvins [22]. This produces a corresponding change in k_1 and a shift of the phase transition, as well as the feature of $f_0(T)$ present near T_N, thereby causing the above-mentioned shift of the resonance curve with respect to f_0 at a higher driving power in figure 6.2c, see section 6.A.5. The contribution of the order parameter on effective linear stiffness $k_1^* \propto L_0^2$ is studied and described in detail in a previous work [34].

Second, unlike the renormalization of k_1, which is independent of dynamics of the order parameter L, the renormalization of the nonlinear parameters k_3 and η_{nl} arise from the modulation of the order parameter. As a result, both k_3^* and η_{nl}^* depend on the characteristic time scales of the coupled dynamic system: τ and ω. As follows from equation (6.4.6), k_3^* starts to decrease with $\delta k_3^* \propto -\frac{1}{1+4\omega^2\tau^2}$ when $T < T_N^*$. The same magnetic contribution also leads to a substantial nonlinear damping η_{nl}^* at $T < T_N^*$, which scales as $\delta\eta_{nl}^* \propto \frac{\tau}{1+4\omega^2\tau^2}$ and peaks at $2\omega\tau \simeq 1$, see section 6.8 and section 6.A.5. This behaviour can be understood intuitively: magnetostriction mediates the exchange of the membrane's mechanical energy with a coupled magnetic reservoir, which happens twice for one period of motion due to symmetrical modulation of stress in the up-down geometry of its deflection. If membrane oscillations are much faster than the energy exchange rate to a coupled magnetic reservoir, i.e, if $2\omega \gg 1/\tau$, there is not enough time for it to relax and dissipate energy. On the contrary, when the oscillations are at a much slower timescale $2\omega \ll 1/\tau$, the energy exchange follows the oscillations with a negligible delay, again resulting in minimal dissipation [139]. Thus, the nonlinear damping due to coupling to the order parameter peaks when the relaxation delay is significant and $2\omega\tau \simeq 1$.

Figures 6.3d and e show the derived values for $k_3^*(T)$ and $\eta_{nl}^*(T)$ as described by equations (6.4.6) and (6.4.7) for $\omega = \omega_0$, next to the measured $k_3^*(T)$ and $\eta_{nl}^*(T)$ in figure 6.3b and c. We assume the non-magnetic Duffing constant k_3 to be temperature dependent, providing the additional background-slope in $k_3^*(T)$ below and above T_N^*. As shown in figure 6.3b with a solid magenta line, equation (6.4.6) reproduces the measured decrease of k_3^* in the proximity of T_N^*. The model also reproduces the measured peak in $\eta_{nl}^*(T)$ at $2\omega_0\tau = 1$ as seen in figure 6.3c. Notably, in a hypothetical case where τ is sufficiently small, i.e., $\tau = 0$ in equations (6.4.6) and (6.4.7), the model predicts the discontinuous decrease in $k_3^*(T)$ at T_N^* shown in figure 6.3d, while the magnetic contribution to $\eta_{nl}^*(T)$ completely vanishes as shown in figure 6.3e with light magenta lines.

6.6. MICROSCOPIC ORIGINS

In discussing the physical interpretation of the origin of this nonlinear damping, its microscopic mechanism should be envisioned as a consequence of a nonlinear oscillator's excited vibrational modes scattering off its magnetic energy reservoir [118, 141]. This interaction then is accompanied by the energy transfer of two oscillation quanta ($2\omega_0$) for nonlinear damping [141]. Importantly, a rather general form of the free energy equation and low order of the coupling term suggests that similar effects may appear in systems with other types of non-magnetic phase transitions, for instance, charge density wave [22] or by coupling the mechanical motion to an electronic energy reservoir. Interestingly, this mechanism also finds macroscopic similarities to magnetic internal friction arising due to a delay in Young's modulus relaxation near T_N which occurs in large-scale magnetic solids [136, 137, 142–145]. However, the crucial distinction at the nanoscale is that it affects different mechanical properties at twice the resonance frequency.

Our analysis predicts the observed nonlinear effect in this system appearing solely as a result of modulation of the antiferromagnetic order parameter, L, with dynamic strain via magnetostriction, delayed by a suggested spin-shear relaxation, τ [132, 133]. This is consistent with the fact that in the presented model if $\lambda = 0$ all magnetic contributions to both k_3^* and η_{nl}^* vanish. We note that deviations between theoretical estimates of nonlinear stiffness and damping with experimental data can have multiple sources. Among these are modal interactions of non-magnetic nature in the experiments [125] that have not been accounted for in the model. In addition, deviations near T_N^* may originate in the mean-field approximation of Landau's theory of phase transition, which is not an exact description of van der Waals antiferromagnets in the critical region and rather describes the overall temperature behaviour [34]. Additional effects could also contribute to difference between the presented model and the observations, such as a similar relaxation originating from the thermoelasticity in the system [22]. However, recent experiments show that thermal relaxation time-scales in membranes of $FePS_3$ are up to two orders of magnitude slower [23] than the spin-shear relaxation-related τ considered in this work for comparable sample thicknesses [132]. Therefore, the presence of substantial linear thermoelastic damping and the probed nonlinear damping near T_N are not expected to be a direct consequence of one another [22, 23]. This is further supported by the fact that magneto-mechanical coupling and the associated relaxation mechanisms do not lead to any linear damping terms analytically, see section 6.A.5. Another contribution may come from different nonlinear effects, such as nonlinearities in optothermal response [146, 147], or terms resulting from the nonlinearities in magnetostrictive actuation force [23] present near the magnetic phase transition. Quantitatively evaluating of all these potential causes will require further experimental evidence.

6.7. CONCLUSION

In conclusion, we demonstrated nonlinear nanomechanical coupling to antiferromagnetic order in $FePS_3$-based heterostructure membranes. We provide both experimental evidence and a theoretical descriptions of the mechanism responsible for the renormalization of the nonlinear parameters. We demonstrate a previously unexplored magneto-mechanical dissipation mechanism supported by a phenomenological theory that ac-

counts for magnetostriction. We show that magnetostrictive coupling strongly affects the nonlinear dynamics of magnetic membranes near the magnetic phase transition temperature, even in the absence of an external magnetic field. Our discoveries offer a new understanding of the thermodynamics and energy-dissipation mechanisms related to magneto-mechanical interactions in 2D materials, which is important for future studies of more intricate magnetic systems, such as 2D quantum phases and moiré magnets [148], as well as the development of novel magnetic NEMS and spintronic devices.

6.8. METHODS

6.8.1. SAMPLE FABRICATION AND CHARACTERISATION

We pre-pattern a diced Si/SiO_2 wafer with circular holes using e-beam lithography and reactive ion etching. The holes have a radius of $r = 1.5$ μm and a cavity depth of 285 nm, and the SiO_2 layer acts as electrical insulation between the 2D material membranes and the bottom Si electrode. For electrostatic experiments, Pd electrodes are patterned on top of Si/SiO_2 chips using a lift-off technique to establish electrical contact with the samples. To create suspended membranes, thin flakes of $FePS_3$ and graphite crystals are mechanically exfoliated and transferred onto the chip using an all-dry viscoelastic stamping method [149] immediately after exfoliation. Flakes of van der Waals crystals are exfoliated from high-quality synthetically grown crystals with known stoichiometry, and deterministic stacking is performed to form heterostructures. To prevent degradation, samples are kept in an oxygen-free or vacuum environment directly after the fabrication. Atomic Force Microscopy (AFM) height profile scans and inspection are performed in tapping mode on a Bruker Dimension FastScan AFM. Error bars on reported thickness values are determined by measuring multiple profile scans of the same flake.

6.8.2. LASER INTERFEROMETRY MEASUREMENTS

The sample is mounted on a xy piezo-positioning stage inside a dry optical 4 K cryostat Montana Instruments Cryostation s50. Temperature sweeps are carried out using a local sample heater at a rate of ~ 3 K min^{-1} while maintaining the chamber pressure below 10^{-6} mbar. During data acquisition, the temperature is maintained constant with ~ 10 mK stability. A power-modulated blue diode laser with a wavelength of 405 nm is used to optothermally excite the membrane's motion, and the resulting membrane displacement is measured using an interferometric detection with a He–Ne laser beam of 632 nm. The interferometer records the interfering reflections from the membrane and the Si surface underneath. The data is processed by a vector network analyzer Rohde & Schwarz ZNB4. All measurements are conducted with incident laser powers of $P_{\text{red}} \leq 8$ μW and $P_{\text{blue}} \leq 35$ μW, with a laser spot size of ~ 1 μm. To ensure accuracy in the data acquisition, it is verified that resonance frequency changes due to laser heating are insignificant for all membranes for applied powers upto 15 dBm.

6.8.3. DERIVATION OF ORDER PARAMETER DYNAMICS

In the derivation of antiferromagnetic order parameter relaxation dynamics, we follow closely the approach of Landau-Khalatnikov [135] and Belov-Kataev-Levitin [136, 137]. For simplicity, we assume bi-axial in-plane membrane stress $\sigma(x) = \sigma_{xx} = \sigma_{yy}$. First, we

derive $\sigma(x)$, assuming $x = a_s \cos(\omega_0 t)$, as [124, 140]:

$$\begin{aligned}\sigma(x) =& \sigma_p + \frac{Ec_3}{2r^2}x^2 \\ =& \left[\sigma_p + \frac{Ec_3}{4r^2}a_s^2\right] + \left[\frac{Ec_3}{4r^2}a_s^2\cos(2\omega_0 t)\right] \\ =& \sigma_0 + \sigma_\omega(t)\end{aligned} \tag{6.8.1}$$

where a_s is the steady-state amplitude, σ_p the pre-stress in the membrane due to the fabrication process, and $\sigma_0$and $\sigma_\omega(t)$ are the static and the dynamic stress terms. Then, we derive L_0, the antiferromagnetic order parameter in the ground state, by minimizing the total energy of the magneto-mechanical system (6.4.1) with respect to L at constant bi-axial stress σ_0 such that:

$$\frac{\partial U_T}{\partial L} = \frac{\partial (U_m + U_{ms})}{\partial L} = 0, \tag{6.8.2}$$

resulting in

$$L_0^2 = \frac{a(T_N - T) - \lambda\sigma_0}{B} = \frac{a(T_N^* - T)}{B}, \tag{6.8.3}$$

where λ is a specific magnetostriction coefficient of the λ_{ij} tensor that describes coupling of bi-axial in-plane membrane stress σ_0 to the order parameter L_0 in the direction of the easy axis.

Using this result we linearize the unrelaxed L as $L \simeq L_0 + L_\omega$, where L_ω is the time- and amplitude-dependent dynamic term. When the membrane is in motion and L is out of the equilibrium, the rate of relaxation of L to the equilibrium L_0 is set by the kinetic equation (6.4.2), which using equation (6.8.1) leads to:

$$\frac{dL}{dt} = \frac{dL_\omega}{dt} = -\kappa\frac{\partial (U_m + U_{ms})}{\partial L}. \tag{6.8.4}$$

This equation can be simplified by a Taylor expansion around L_0 assuming $L_\omega \ll L_0$:

$$\frac{dL_\omega}{dt} = \dot{L}_\omega \simeq -\kappa\left[2BL_0^2 L_\omega + \lambda L_0 \sigma_\omega(t)\right], \tag{6.8.5}$$

which rearranges to equation (6.4.3), by taking $\tau = \frac{1}{2\kappa a(T_N^* - T_N)}$ [135]. We note that when $L_\omega \approx L_0$ at $T \approx T_N^*$, higher-order (quintic) nonlinear terms can appear in the motion of the magnetic membrane. We discard these for simplicity.

6.8.4. AMPLITUDE OF NONLINEAR RESONANCE PEAK

We start by solving the first-order differential equation (6.4.3) to obtain the steady-state solution for L_ω in terms of τ:

$$L_{\omega,ss} = -\lambda\kappa L_0 \frac{Ec_3}{4r^2}\frac{\tau\left[\cos(2\omega t) + 2\tau\omega\sin(2\omega t)\right]}{\left(1 + 4\tau^2\omega^2\right)}a_s^2. \tag{6.8.6}$$

We keep the assumption of periodic motion in the form of $x = a_s \cos\omega t$ and plug in the steady state solution in equation (6.4.4) such that $L_\omega = L_{\omega,ss}$. Next we use harmonic

balance method to obtain the amplitude-frequency equation 6.4.5, considering only the fundamental harmonic ω_0, see section 6.A.5:

$$a_s^6\left(\frac{9\gamma^2}{16}+\frac{\xi_{nl}^2\omega^2}{16}\right)+a_s^4\left(\frac{3\gamma(\omega_0^2-\omega^2)}{2}+\frac{\xi_{nl}\omega_0\omega^2}{2Q}\right)+ a_s^2\left((\frac{\omega_0\omega}{Q})^2+(\omega_0^2-\omega^2)^2\right)=\left(\frac{F_\omega}{m}\right)^2, \tag{6.8.7}$$

where $\omega_0^2=\frac{1}{m}\left(k_1+\lambda L_0^2\frac{Ec_3}{2r^2}\right)$ is the re-normalized resonance frequency, $\gamma=\frac{k_3^*}{m}$ the mass-normalized Duffing coefficient and $\xi_{nl}=\frac{\eta_{nl}^*}{m}$ the mass-normalized nonlinear damping coefficient with k_3^* and η_{nl}^* from equations (6.4.6) and (6.4.7), respectively. Further details of the derivation and fitting procedure can be found in section 6.A.5.

REFERENCES

21. Lee, M. *et al.* Study of charge density waves in suspended 2H-TaS_2 and 2H-$TaSe_2$ by nanomechanical resonance. *Appl. Phys. Lett.* **118,** 193105 (May 2021).
22. Šiškins, M. *et al.* Magnetic and electronic phase transitions probed by nanomechanical resonators. *Nat. Commun.* **11,** 2698 (June 2020).
23. Baglioni, G. *et al.* Thermo-Magnetostrictive Effect for Driving Antiferromagnetic Two-Dimensional Material Resonators. *Nano Lett.* **23,** 6973–6978 (2023).
34. Houmes, M. J. A. *et al.* Magnetic order in 2D antiferromagnets revealed by spontaneous anisotropic magnetostriction. *Nat. Commun.* **14,** 8503 (Dec. 2023).
38. Lee, J.-U. *et al.* Ising-Type Magnetic Ordering in Atomically Thin $FePS_3$. *Nano Lett.* **16,** 7433–7438 (Nov. 2016).
40. Němec, P., Fiebig, M., Kampfrath, T. & Kimel, A. V. Antiferromagnetic opto-spintronics. *Nat. Phys.* **14,** 229–241 (Mar. 2018).
49. Jiang, S., Xie, H., Shan, J. & Mak, K. F. Exchange Magnetostriction in Two-Dimensional Antiferromagnets. *Nat. Mater.* **19,** 1295–1299 (June 2020).
55. Landau, L. D., Pitaevskii, L. P. & Lifshitz, E. M. *Electrodynamics of continuous media* 2nd ed. (Butterworth, New York, 1984).
60. Afanasiev, D. *et al.* Controlling the anisotropy of a van der Waals antiferromagnet with light. *Sci. Adv.* **7,** eabf3096 (June 2021).
87. López-Cabrelles, J. *et al.* Chemical Design and Magnetic Ordering in Thin Layers of 2D Metal-Organic Frameworks (MOFs). *J. Am. Chem. Soc.* **143,** 18502–18510 (Nov. 2021).
101. Dolleman, R. J. *et al.* Optomechanics for thermal characterization of suspended graphene. *Phys. Rev. B* **96,** 165421 (Oct. 2017).
104. Šiškins, M. *et al.* Nanomechanical probing and strain tuning of the Curie temperature in suspended $Cr_2Ge_2Te_6$-based heterostructures. *npj 2D Mater. Appl.* **6** (June 2022).

108. Šiškins, M. *et al. Nonlinear dynamics and magneto-elasticity of nanodrums near the phase transition* 2023. arXiv: 2309.09672 [cond-mat.mes-hall].

109. Androulidakis, C., Zhang, K., Robertson, M. & Tawfick, S. Tailoring the Mechanical Properties of 2D Materials and Heterostructures. *2D Mater.* **5,** 032005 (June 2018).

110. Jiang, H., Zheng, L., Liu, Z. & Wang, X. Two-dimensional materials: From mechanical properties to flexible mechanical sensors. *InfoMat* **2,** 1077–1094 (Dec. 2019).

111. Lemme, M. C. *et al.* Nanoelectromechanical Sensors Based on Suspended 2D Materials. *Research* **2020,** 8748602 (July 2020).

112. Rosłoń, I. E., Japaridze, A., Steeneken, P. G., Dekker, C. & Alijani, F. Probing nanomotion of single bacteria with graphene drums. *Nat. Nanotechnol.* **17,** 637–642 (Apr. 2022).

113. Steeneken, P. G., Dolleman, R. J., Davidovikj, D., Alijani, F. & van der Zant, H. S. J. Dynamics of 2D material membranes. *2D Mater.* **8,** 042001 (Aug. 2021).

114. Güttinger, J. *et al.* Energy-dependent path of dissipation in nanomechanical resonators. *Nat. Nanotech.* **12,** 631–636 (July 2017).

115. Bachtold, A., Moser, J. & Dykman, M. Mesoscopic physics of nanomechanical systems. *Rev. Mod. Phys.* **94,** 045005 (Dec. 2022).

116. Kirchhof, J. N. *et al.* Nanomechanical Spectroscopy of 2D Materials. *Nano Lett.* **22,** 8037–8044 (Oct. 2022).

117. Arribas, I. S., Taniguchi, T., Watanabe, K. & Weig, E. M. Radiation Pressure Backaction on a Hexagonal Boron Nitride Nanomechanical Resonator. *Nano Lett.* **23,** 6301–6307 (July 2023).

118. Atalaya, J., Kenny, T. W., Roukes, M. L. & Dykman, M. I. Nonlinear damping and dephasing in nanomechanical systems. *Phys. Rev. B* **94,** 195440 (Nov. 2016).

119. De Alba, R. *et al.* Tunable phonon-cavity coupling in graphene membranes. *Nat. Nanotech.* **11,** 741–746 (June 2016).

120. Luo, G. *et al.* Strong Indirect Coupling between Graphene-Based Mechanical Resonators via a Phonon Cavity. *Nat. Commun.* **9,** 383 (Jan. 2018).

121. Chen, C. *et al.* Modulation of mechanical resonance by chemical potential oscillation in graphene. *Nat. Phys.* **12,** 240–244 (Dec. 2015).

122. Sengupta, S., Solanki, H. S., Singh, V., Dhara, S. & Deshmukh, M. M. Electromechanical resonators as probes of the charge density wave transition at the nanoscale in $NbSe_2$. *Phys. Rev. B* **82,** 155432 (Oct. 2010).

123. Šiškins, M. *et al.* Tunable Strong Coupling of Mechanical Resonance between Spatially Separated $FePS_3$ Nanodrums. *Nano Lett.* **22,** 36–42 (Dec. 2021).

124. Davidovikj, D. *et al.* Nonlinear Dynamic Characterization of Two-Dimensional Materials. *Nat. Commun.* **8,** 1253 (Nov. 2017).

125. Keşkekler, A. *et al.* Tuning Nonlinear Damping in Graphene Nanoresonators by Parametric–Direct Internal Resonance. *Nat. Commun.* **12,** 1099 (Feb. 2021).

126. Keşkekler, A., Arjmandi-Tash, H., Steeneken, P. G. & Alijani, F. Symmetry-Breaking-Induced Frequency Combs in Graphene Resonators. *Nano Lett.* **22,** 6048–6054 (Aug. 2022).

127. Eichler, A. *et al.* Nonlinear damping in mechanical resonators made from carbon nanotubes and graphene. *Nat. Nanotech.* **6,** 339–342 (May 2011).

128. Zhang, T. *et al.* A monolithically sculpted van der Waals nano-opto-electro-mechanical coupler. *Light Sci. Appl.* **11,** 48 (Mar. 2022).

129. Li, X., Sha, X., Yan, N. & Zhang, T. Mechanical Detection of Magnetic Phase Transition in Suspended CrOCl Heterostructures. *Magnetochemistry* **8,** 170 (Nov. 2022).

130. Xu, X. *et al.* Length-dependent thermal conductivity in suspended single-layer graphene. *Nat. Commun.* **5,** 3689 (Apr. 2014).

131. Davidovikj, D. *et al.* Visualizing the Motion of Graphene Nanodrums. *Nano Lett.* **16,** 2768–2773 (Mar. 2016).

132. Zhou, F. *et al.* Dynamical criticality of spin-shear coupling in van der Waals antiferromagnets. *Nat. Commun.* **13,** 6598 (Nov. 2022).

133. Zong, A. *et al.* Spin-mediated shear oscillators in a van der Waals antiferromagnet. *Nature* **620,** 988–993 (Aug. 2023).

134. Landau, L. D. On the theory of phase transitions. *Zh. Eksp. Teor. Fiz.* **7.** [*Ukr. J. Phys.* **53**, 25 (2008)], 19–32 (1937).

135. Landau, L. D. & Khalatnikov, I. M. On the anomalous absorption of sound near a second order phase transition point. *Dokl. Akad. Nauk SSSR* **96,** 469 (1954).

136. Belov, K. P., Katayev, G. I. & Levitin, R. Z. Internal Friction Anomalies in Ferromagnets and Antiferromagnets near the Curie Point. *J. Appl. Phys.* **31,** S153–S156 (May 1960).

137. Belov, K. P., Kataev, G. I. & Levitin, R. Z. Anomalies in internal friction and modulus of elasticity in ferromagnetic near the Curie point. *J. Exptl. Theoret. Phys. (U.S.S.R.)* **37,** 938–943 (1959).

138. Khusyainov, D. *et al.* Ultrafast laser-induced spin–lattice dynamics in the van der Waals antiferromagnet $CoPS_3$. *APL Mater.* **11,** 071104 (July 2023).

139. Schmid, S., Villanueva, L. G. & Roukes, M. L. *Fundamentals of Nanomechanical Resonators* (Springer International Publishing, 2016).

140. Zhang, X. *et al.* Dynamically-enhanced strain in atomically thin resonators. *Nat. Commun.* **11,** 5526 (Nov. 2020).

141. Dykman, M. I. & Krivoglaz, M. A. Spectral distribution of nonlinear oscillators with nonlinear friction due to a medium. *Phys. Status Solidi B* **68,** 111–123 (Mar. 1975).

142. Harada, H., Müller, M. & Warlimont, H. in *Springer Handbook of Condensed Matter and Materials Data* 755–815 (Springer Berlin Heidelberg).

143. Hausch, G. Magnetic exchange energy contribution to the elastic constants and its relation to the anomalous elastic behaviour of invar alloys. *Phys. Status Solidi A* **15,** 501–510 (Feb. 1973).

144. Hausch, G. Magnetovolume effects in invar alloys: Pressure dependence of the Curie temperature. *Phys. Status Solidi A* **16,** 371–376 (Apr. 1973).

145. Postolache, E. *et al.* Comparison of Young's modulus and specific heat anomalies at the magnetic transition in α'-NaV_2O_5. *Solid State Sci.* **2,** 759–766 (Dec. 2000).

146. Barton, R. A. *et al.* Photothermal Self-Oscillation and Laser Cooling of Graphene Optomechanical Systems. *Nano Lett.* **12,** 4681–4686 (Aug. 2012).

147. Dolleman, R. J., Davidovikj, D., van der Zant, H. S. J. & Steeneken, P. G. Amplitude calibration of 2D mechanical resonators by nonlinear optical transduction. *Appl. Phys. Lett.* **111,** 253104 (Dec. 2017).

148. Burch, K. S., Mandrus, D. & Park, J.-G. Magnetism in two-dimensional van der Waals materials. *Nature* **563,** 47 (Oct. 2018).

149. Castellanos-Gomez, A. *et al.* Deterministic Transfer of Two-Dimensional Materials by All-Dry Viscoelastic Stamping. *2D Mater.* **1,** 011002 (Apr. 2014).

6.A. SUPPLEMENTARY INFORMATION

6.A.1. MECHANICAL DISSIPATION IN LINEAR AND NONLINEAR REGIME

We plot the mechanical dissipation, the inverse of a quality factor $Q^{-1}(T)$ of the MLG / $FePS_3$ resonator from figure 6.1 in figure 6.4a. A notable peak is visible at $T_N = 110$ K. We attribute this to an increase of the thermoelastic damping [106, 150] expected near the T_N in magnetic resonators, as $Q^{-1} \propto c_v(T)T$, where $c_v(T)$ is the temperature-dependent specific heat of $FePS_3$ [22, 104, 123].

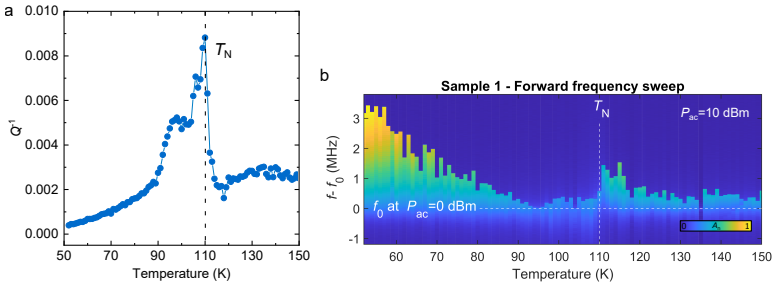

Figure 6.4: Measured mechanical dissipation in linear and nonlinear regime. **a** Inverse quality factor Q^{-1} of the MLG/$FePS_3$ membrane (sample 1) from figure 6.1 of the main text. **b** Normalized amplitude at 10 dBm drive for the forward frequency sweep measurement of the same sample from figure 6.1 of the main text.

The mechanical dissipation at higher drive level and in the nonlinear regime (P_{ac} = 10 dBm) is also manifested as a decrease of maximal measured amplitude for the forward frequency sweep, which is shown in figure 6.4b for the same resonator as shown in figure 6.1. A notable anomaly is visible at $T_N = 110$ K, which we attribute to the observed increase of nonlinear damping as previously discussed.

6.A.2. RENORMALIZATION OF THE DUFFING RESPONSE THROUGH PHASE TRANSITION

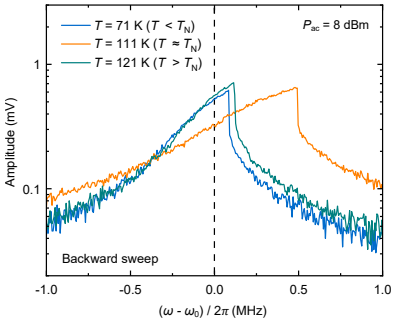

Figure 6.5: The measured resonance peak amplitudes at 8 dBm drive for 71, 111 and 121 K temperature points from figure 6.2c of the main text, superimposed for ease of comparison.

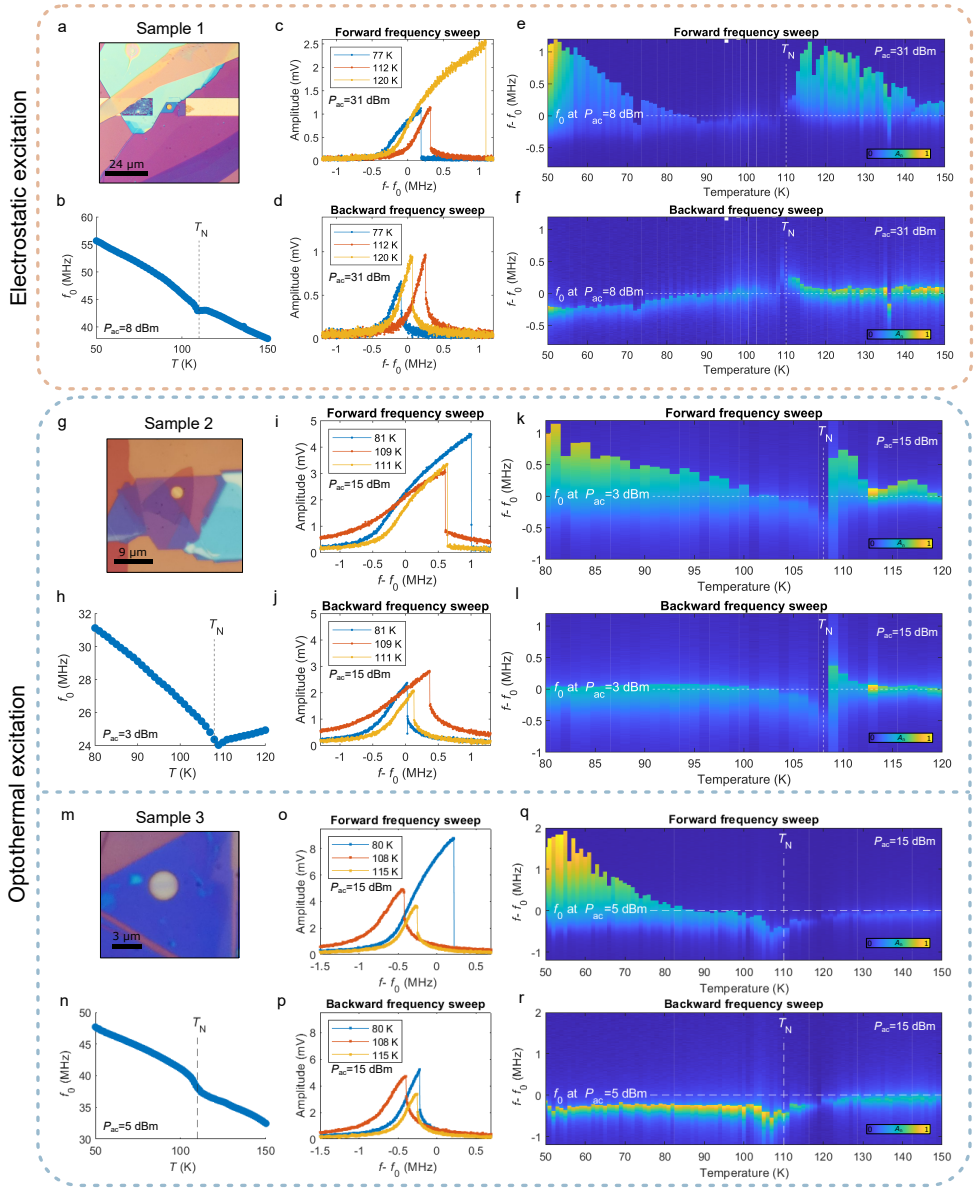

Figure 6.6: Additional measurements on $FePS_3$/MLG samples. **a-f** The $FePS_3$/MLG sample from the main text measured under electrostatic excitation V_{ac} applied to the bottom gate electrode with a DC offset V_{dc} = 10 V. **a** Optical image of the sample. **b** Measured resonance frequency of the fundamental membrane mode f_0 as a function of temperature. **c-f** The Duffing effect and amplitude-frequency branches of the resonance peak at higher drive (P_{ac}) measured for forward (**c**) and backward frequency sweep. **e-f** The colour map of the normalized amplitude measured as a function of temperature in forward (**e**) and backward (**f**) frequency sweep regime around linear resonance frequency f_0 from (b). **g-l** and **m-r** present the data on two additional $FePS_3$/MLG samples measured under opto-thermal excitation. **g-l** and **m-r** follow the same structure as (a-f).

6.A.3. REPRODUCIBILITY OF THE RESULTS

We have performed additional control experiments on multiple $FePS_3$/MLG samples, summarised in figure 6.6, using both optothermal and electrostatic excitation, where an AC voltage, V_{ac}, is applied between the Si backgate of the chip and the conducting top layer of MLG. Since we obtain similar results for the electrostatic drive as for optothermal drive we conclude that the reported observations are intrinsic to the resonator and not related to the driving mechanism.

We note that the qualitatively different behaviours of $f_0(T)$, displayed in figures 6.6b, h, and m, can be well understood considering the interplay between thermal expansion coefficients of materials involved: $FePS_3$, graphene and Si substrate. The resonance frequency of a heterostructure membrane $f_{0,h}(T)$ can be modelled considering the total thermally accumulated tension of the $FePS_3$/MLG heterostructure as a sum of individual tensions in each layer, assuming that the slippage between the layers is negligible [104]:

$$\begin{aligned} f_{0,h}(T) &= \sqrt{\left(\frac{2.4048}{2\pi r}\right)^2 \frac{n_{th}(T)}{\rho h} + f_0^2(T_0)}, \\ &= \sqrt{\left(\frac{2.4048}{2\pi r}\right)^2 \frac{1}{\rho_1 h_1 + \rho_2 h_2}\left[\frac{E_1 h_1}{(1-\nu_1)}\epsilon_{th,1}(T) + \frac{E_2 h_2}{(1-\nu_2)}\epsilon_{th,2}(T)\right] + f_0^2(T_0)}. \end{aligned} \tag{6.A.1}$$

Here, $f_0(T_0)$ is the resonance frequency at a reference temperature T_0 (e.g. room temperature) accounting for the contribution of the pre-tension and the bending rigidity, E the Young's modulus, ν the Poisson ratio, h the layer thickness, ρ the mass density, $n_{th}(T) = \frac{Eh}{(1-\nu)}\epsilon_{th}$ with the thermally accumulated tension at temperature T_i, $\epsilon_{th} = -\int_{T_0}^{T_i} (\alpha_{material}(T) - \alpha_{Si}(T))\, dT$ [22, 151], $\alpha_{Si}(T)$ the literature values for the thermal expansion coefficient of the Si substrate [152], and $\alpha_{material}(T)$ the temperature dependent thermal expansion coefficient of either $FePS_3$ [22] or graphene [153], shown in figure 6.7a.

Thus, we attribute the observed differences in $f_0(T)$ trends to a large contribution of $\alpha_{MLG}(T)$ to the total in-plane stress of the membrane, especially at $T < T_N$,largely depending on the material's thickness ratio. We demonstrate this by plotting equation (6.A.1) in figure 6.7b for two different thicknesses of MLG layer. We use $E_{FePS_3} = 103$ GPa, $\rho_{FePS_3} = 3375$ kgm^{-3}, $\nu_{FePS_3} = 0.304$ for $FePS_3$ [22]. and $E_{MLG} = 1$ TPa, $\rho_{MLG} = 2260$ kgm^{-3}, $\nu_{MLG} = 0.19$ for graphene [154]; From figure 6.7b it is apparent that for the thinner MLG layer in the heterostructure, $f_0(T)$ is expected to monotonically increase with decreasing temperature, similar to samples 1, 3 shown in figure 6.6, while for the thicker MLG layer case, a non-monotonic behaviour can be expected, similar to sample 2.

However, due to the effect of anisotropic magnetostriction found in previous works [34], a downward trend in the frequency response $f_0(T)$ of $FePS_3$-based membrane resonators with decreasing temperature can appear near T_N when stress along the b-axis of the $FePS_3$ crystal dominates, for instance, due to its uneven distribution during the device fabrication. A similar feature in $f_0(T)$ was measured around $T \sim 110$ K shown in figure 6.1d, as also depicted in figure 6.8a.

Utilizing the same material parameters as above and assuming that accumulation of strain in $FePS_3$ layer of this membrane is dominated by the thermal expansion coeffi-

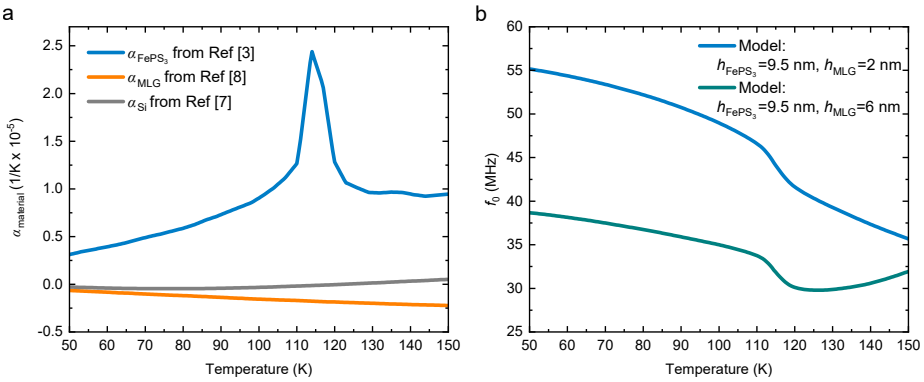

Figure 6.7: Temperature dependence of thermal expansion and resonance frequency of $FePS_3$/MLG heterostructure membranes. **a** Linear thermal expansion coefficients of $FePS_3$ [22], graphene [153] and Si substrate [152]. **b** The resonance frequency model of equation (6.A.1) as a function of temperature and thicknesses of $FePS_3$ and MLG, calculated using the data from (a).

cient along the b-axis of $FePS_3$ crystal (shown in figure 6.8b as taken from Houmes et al. [34]), we calculate the predicted $f_0(T)$ using equation (6.A.1) and plot it in figure 6.8c. We note that the behaviour illustrated in figure 6.1d can be explained and reproduced well using this approach, as the model follows the experimentally measured trend closely, including region near $T \approx T_N$, as demonstrated in figure 6.8d.

6.A.4. EXTRACTING EXPERIMENTAL PARAMETERS

To monitor the change in the stiffness and dissipation of the resonator, we fit the experimental frequency responses to equation (6.8.7) and extract Q, γ, ξ_{nl}, F_ω/m and ω_0. The fitting is done sequentially. First, Q factors are extracted from the linewidths of linear resonance curves at low drive levels, before the onset of nonlinearity. Next, ω_0 is extracted from the peak frequency at low drive levels, assuming it stays constant with increasing drive levels. However, we have sometimes also observed dependency of the fundamental frequency on drive level, possibly due to overheating from the optothermal drive. Thus, we extracted ω_0 for each drive level separately. At the drive levels where the response is nonlinear, we correct for the ω_0 using the inflection of the nonlinear resonance curve, such that $\frac{d^2 a_s}{d\omega^2}|_{\omega_0} \approx 0$, or using the saddle-node bifurcation of the lower solution branch, obtained in the reverse sweep.

After obtaining Q and ω_0, it is possible to extract F_ω/m by fitting the off-resonance response to a harmonic oscillator model, such that $\ddot{x} + \frac{\omega_0}{Q}\dot{x} + \omega_0^2 x = \frac{F_\omega}{m}$. After obtaining all the linear parameters, we extract nonlinear parameters γ and ξ_{nl}. Normalized Duffing coefficient γ is estimated by using the slope of the square of the frequency response since $\gamma = (8\omega_0/3)(\omega_{max} - \omega_0)/a_{s,max}^2$ [155], where ω_{max} is the frequency and a_{max} is the amplitude of the experimental nonlinear resonance peak. Finally, we find ξ_{nl} by matching the peak amplitude i.e., saddle-node bifurcation of the higher solution branch, and by using an optimizer that minimizes the objective $f_{obj} = |a_{s,max}^{sim}(\xi_{nl}) - a_{s,max}|$, where $a_{s,max}^{sim}$ is the peak amplitude of the simulated model. In figure 6.9, we provide additional examples of

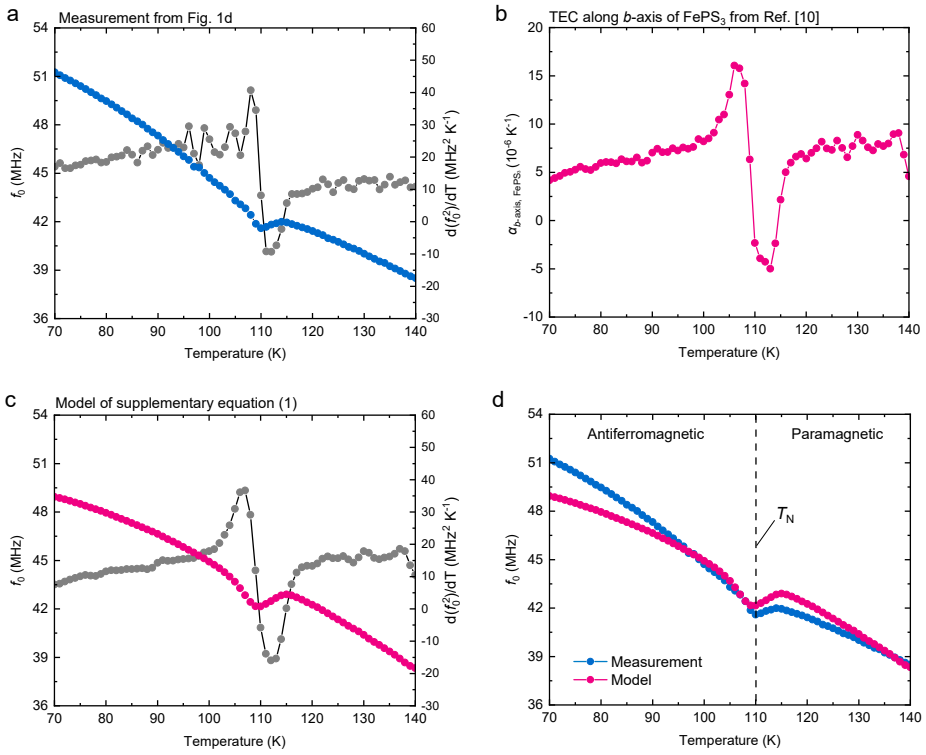

Figure 6.8: Modeling the temperature dependence of resonance frequency of $FePS_3$/MLG heterostructure membrane. **a** The resonance frequency $f_0(T)$ as a function of temperature, from the figure 6.1d of the main text. Connected grey dots are the corresponding derivative of the f_0^2. **b** Linear thermal expansion coefficient of $FePS_3$ along the b-axis from Houmes et al [34]. **c** The predicted resonance frequency $f_0(T)$ as a function of temperature, using the model of supplementary equation (6.A.1). Connected grey dots are the corresponding derivative of the f_0^2. **d** Comparison of $f_0(T)$ from (a) and (c). The vertical dashed line indicates T_N.

the fitted curves for convenience.

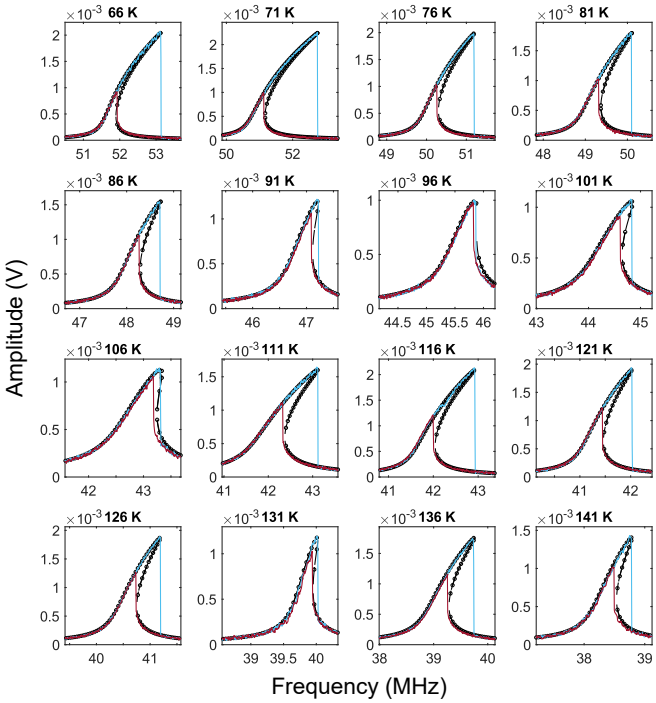

Figure 6.9: Model fits to the experimental data for various temperatures at 10 dBm drive level. The blue line is the experimental forward frequency sweep response, whereas the orange line is in the reverse sweep response. Black circles are the simulated model response.

6.A.5. MAGNETOSTRICTIVE MODEL: DERIVATION OF NONLINEAR STIFFNESS AND DAMPING

DYNAMICS OF ANTIFERROMAGNETIC ORDER PARAMETER

In the derivation of antiferromagnetic order parameter relaxation dynamics, we follow closely the approach of Landau-Khalatnikov [135] and Belov-Kataev-Levitin [136, 137]. The total potential energy of the system can be written as:

$$U_{\mathrm{T}} = U_{\mathrm{el}} + U_{\mathrm{m}} + U_{\mathrm{ms}}, \tag{6.A.2}$$

where U_{el} is elastic potential energy, U_{m} free energy of an antiferromagnet and U_{ms} is magnetostrictive coupling energy term. These take form of:

$$\begin{aligned} U_{\mathrm{el}} &= \frac{k_1}{2}x^2 + \frac{k_3}{4}x^4, \\ U_{\mathrm{m}} &= U_{\mathrm{m},0} + \frac{A}{2}L^2 + \frac{B}{4}L^4, \\ U_{\mathrm{ms}} &= \frac{\lambda_{ij}}{2}\sigma_{ij}(x)L^2, \end{aligned} \tag{6.A.3}$$

where k_1 and k_3 are linear and nonlinear stiffness, $U_{\mathrm{m},0}$ is the magnetic free energy in a paramagnetic state, L is an antiferromagnetic order parameter along the easy-axis of antiferromagnet, while A and B are phenomenological constants, λ_{ij} is the tensor of phenomenological magnetostrictive coefficients, $\sigma_{ij}(x)$ is stress tensor modulated by the membrane deflection x. For notational convenience, we write λ_{ij}, dropping the third and fourth index of λ_{ijkl} as only the component where kl corresponds to the easy axis contributes.

Let us first consider the magnetic energy terms $U_{\mathrm{m}} + U_{\mathrm{ms}}$ that describe the antiferromagnetic phase for uni-axial magnetic anisotropy:

$$U_{\mathrm{m}} + U_{\mathrm{ms}} = U_{\mathrm{m},0} + \frac{A}{2}L^2 + \frac{B}{4}L^4 + \frac{\lambda}{2}L^2\sigma(x), \tag{6.A.4}$$

where $B > 0$, $\sigma(x) = \sigma_{xx} = \sigma_{yy}$ is the in-plane bi-axial stress and λ the specific magnetostriction coefficient of λ_{ij} that describes the coupling of in-plane membrane stress to the order parameter in the direction of the easy axis. In the zero stress condition with $\sigma = 0$ the energy minimum thus shall have extrema that satisfy $\frac{\partial(U_{\mathrm{m}} - U_{\mathrm{m},0})}{\partial L} = 0$, where the $A > 0$ condition describes a disordered (paramagnetic) phase and the $A < 0$ condition an ordered (antiferromagnetic) phase. Consequently, $A = 0$ describes the transition point between these phases. We thus define the antiferromagnetic transition temperature or Néel temperature T_{N} such that it leads to $A = 0$ at T_{N} as:

$$A = a(T - T_{\mathrm{N}})^{2\beta}, \tag{6.A.5}$$

where a is a positive phenomenological constant, T is temperature and $\beta = 0.5$ the critical exponent [55]. By plugging equation (6.A.5) to (6.A.3), we write a full equation for the total potential energy:

$$\begin{aligned} U_{\mathrm{T}} &= U_{\mathrm{el}} + U_{\mathrm{m}} + U_{\mathrm{ms}} \\ &= \left[\frac{k_1}{2}x^2 + \frac{k_3}{4}x^4\right] + \left[U_{\mathrm{m},0} + \frac{a}{2}(T - T_{\mathrm{N}})L^2 + \frac{B}{4}L^4\right] + \left[\frac{\lambda}{2}L^2\sigma(x)\right]. \end{aligned} \tag{6.A.6}$$

We minimize U_{T} with respect to L to find the values of the order parameter in the ground state under the static stress condition $\sigma = \sigma_0$. This leads to:

$$\frac{\partial U_{\mathrm{T}}}{\partial L} = a(T - T_{\mathrm{N}})L + BL^3 + \lambda L\sigma_0 = 0, \tag{6.A.7}$$

where σ_0 is the static stress term of the total in-plane membrane stress, defined as, assuming the flat membrane case and $x \approx a_s \cos(\omega t)$ [124, 140]:

$$\begin{aligned}\sigma(x) =& \sigma_p + \frac{Ec_3}{2r^2}x^2 \\ =& \left[\sigma_p + \frac{Ec_3}{4r^2}a_s^2\right] + \left[\frac{Ec_3}{4r^2}a_s^2\cos(2\omega t)\right] \\ =& \sigma_0 + \sigma_\omega(t),\end{aligned} \tag{6.A.8}$$

where σ_p is the pre-stress in the membrane due to the fabrication process, $\sigma_\omega(t)$ the dynamic stress terms, E the Young's modulus, r the membrane radius, a_s the steady-state amplitude, t the time, ω the drive frequency, and c_3 the geometric numerical factor that depends on membrane's Poisson ratio [156].

Equation (6.A.7) then leads to the antiferomagnetic order parameter in the ground state:

$$L_0 = \pm\sqrt{\frac{a(T_N - T) - \lambda\sigma_0}{B}} = \pm\sqrt{\frac{a(T_N^* - T)}{B}}. \tag{6.A.9}$$

Consequently, one can show that magnetostriction produces the shifted Néel temperature T_N^* as a function of σ_0:

$$T_N^* = T_N - \frac{\lambda\sigma_0}{a}. \tag{6.A.10}$$

One can notice that since σ_0 depends both on σ_p and a_s, a larger steady-state amplitude a_s expected in nonlinear regime (in comparison to a linear regime) would produce a higher stress level σ_0. This can accordingly cause a shift of T_N^* which leads to a resonance frequency difference between different excitation levels near T_N^*, as shown in figure 6.2c.

In contrast, a stressed antiferromagnet in motion satisfies the following relation between L and T_N:

$$L(t)^2 = \frac{a(T_N - T) - \lambda(\sigma_0 + \sigma_\omega(t))}{B} \cong (L_0 + L_\omega(t))^2, \tag{6.A.11}$$

where $L_\omega(t)$ is the dynamic term of the antiferromagnetic order parameter L. When the membrane is in motion, the time dependence of L is related to the energy U_T by the kinetic equation [135–137]:

$$\frac{dL}{dt} = -\kappa\frac{\partial U_T}{\partial L}, \tag{6.A.12}$$

where κ is the kinetic coefficient, that is assumed to be free of anomalies near T_N [135]. Since, from equation (6.A.11), $L(t) = L_0 + L_\omega(t)$ is a sum of the equilibrium L_0 and the additional dynamic term $L_\omega(t)$, produced by the small oscillating stresses $\sigma_\omega(t)$, we can expand $\frac{\partial U_T}{\partial L}$ using a Taylor series around L_0:

$$\frac{dL}{dt} \cong -\kappa\left[\frac{\partial U_T}{\partial L}|_{L_0} + \frac{\partial^2 U_T}{\partial L^2}|_{L_0}(L - L_0) + ...\right], \tag{6.A.13}$$

and obtain, assuming $L_\omega \ll L_0$:

$$-\frac{dL_\omega}{dt} \cong 2\kappa B L_0^2 L_\omega + \kappa\lambda L_0\sigma_\omega(t). \tag{6.A.14}$$

As originally shown by Landau and Khalatnikov [135], the time constant τ, that describes the relaxation of the antiferromagnetic order parameter due to its dynamic term [136, 137], can be found from equation (6.A.14) as:

$$\tau = \begin{cases} \frac{1}{2\kappa a(T_N^* - T)} & T < T_N^* \\ \infty & T > T_N^*, \end{cases} \tag{6.A.15}$$

which further simplifies equation (6.A.14) to:

$$\dot{L}_\omega + \frac{L_\omega}{\tau} + \kappa\lambda L_0 \sigma_\omega(t) = 0. \tag{6.A.16}$$

STEADY-STATE EQUATIONS

We use the method of harmonic balancing to solve for the steady-state amplitude of equation (6.4.4). We approximate the motion by a single harmonic such that $x \approx a_s \cos(\omega t + \psi)$ where a_s is the steady-state amplitude. In order to obtain the steady-state response of the mechanical degree of freedom x, that is coupled to the magnetic order, we define the Lagrangian $\mathscr{L} = \frac{1}{2} m\dot{x}^2 - U_T$, and use the Euler-Lagrange equation as follows:

$$\frac{d}{dt}\frac{\partial \mathscr{L}}{\partial \dot{x}} - \frac{\partial \mathscr{L}}{\partial x} = 0, \tag{6.A.17}$$

which yields:

$$m\ddot{x} + k_1 x + k_3 x^3 + \frac{\lambda}{2}(L_0 + L_\omega)^2 \frac{\partial \sigma}{\partial x} = 0, \tag{6.A.18}$$

where $k_1 = m\omega_0^2$. Assuming that $L_0 \gg L_\omega$ and including linear dissipation related to the quality factor Q, nonlinear damping of van der Pol type [118, 125, 157] η_{nl} and periodic forcing with amplitude F_ω, frequency ω, and phase ψ, coupled equations of motion can be written in the following form:

$$\begin{cases} m\ddot{x} + k_1 x + k_3 x^3 + \frac{\lambda}{2}\left(L_0^2 + 2L_0 L_\omega\right)\frac{\partial \sigma}{\partial x} = F_\omega \cos(\omega t + \psi) - \frac{m\omega_0}{Q}\dot{x} - \eta_{nl} x^2 \dot{x}, \\ \dot{L}_\omega + \frac{L_\omega}{\tau} + \kappa\lambda L_0 \sigma_\omega(t) = 0. \end{cases} \tag{6.A.19}$$

To solve for the steady-state response of the mechanical degree of freedom coupled to the magnetic order, we start by solving the first-order differential equation (6.A.19). Using equations (6.A.15) and (6.A.8), we obtain the steady-state solution for L_ω in terms of τ:

$$\begin{aligned} L_{\omega,ss} &= -\lambda\kappa L_0 \frac{Ec_3}{4r^2}\left[\cos(2\omega t) + 2\tau\omega \sin(2\omega t)\right]\frac{\tau}{1+4\tau^2\omega^2} a_s^2, \\ &= -\lambda\kappa L_0 \left[\sigma_\omega(t) - \tau\frac{\partial \sigma_\omega(t)}{\partial t}\right]\frac{\tau}{1+4\tau^2\omega^2}. \end{aligned} \tag{6.A.20}$$

Consequently, to apply the method of harmonic balancing to the equation (6.A.19), we keep the assumption of periodic motion at the steady state in the form of $x = a_s \cos\omega t$ and plug in the steady state solution of L_ω, such that $L_\omega = L_{\omega,ss}$. Considering only the fundamental harmonic ω and discarding higher order harmonics, we find:

$$\left[\left(\frac{3k_3}{4}-\frac{\lambda^2}{4B}\frac{E^2c_3^2}{4r^4}\frac{1}{\left(1+4\tau^2\omega^2\right)}\right)a_s^3+m(\omega_0^2-\omega^2)a_s\right]\cos\omega t- \tag{6.A.21}$$
$$\left[\left(\eta_{nl}+\frac{\lambda^2\omega}{2B}\frac{E^2c_3^2}{r^4}\frac{\tau}{\left(1+4\tau^2\omega^2\right)}\right)a_s^3+\frac{m\omega_0\omega}{Q}a_s\right]\sin\omega t=F_\omega\cos\psi\cos\omega t-F_\omega\sin\psi\sin\omega t.$$

We equate the coefficients of the fundamental harmonic, namely $\sin\omega t$ and $\cos\omega t$ on both sides and obtain the following steady-state amplitude equation:

$$\left(\left(\frac{3k_3}{4}-\frac{\lambda^2}{16B}\frac{E^2c_3^2}{r^4}\frac{1}{\left(1+4\tau^2\omega^2\right)}\right)a_s^3+m(\omega_0^2-\omega^2)a_s\right)^2 \tag{6.A.22}$$
$$+\left(\left(\eta_{nl}+\frac{\lambda^2\omega}{2B}\frac{E^2c_3^2}{r^4}\frac{\tau}{\left(1+4\tau^2\omega^2\right)}\right)a_s^3+\frac{m\omega_0}{Q}a_s\right)^2\omega^2=F_\omega^2,$$

where $\omega_0^2=\frac{1}{m}\left(k_1+\lambda L_0^2\frac{Ec_3}{2r^2}\right)$ is the re-normalized resonance frequency. From the steady-state amplitude equation, it is possible to see that the coupling to the magnetic order leads to a re-normalized nonlinear damping term η_{nl}^* of a van der Pol type [118, 125, 157] at $T<T_N^*$ such that:

$$\boxed{\eta_{nl}^*=\begin{cases}\eta_{nl}+\frac{\lambda^2}{2B}\frac{E^2c_3^2}{r^4}\frac{\tau}{(1+4\tau^2\omega^2)} & T<T_N^*\\ \eta_{nl} & T>T_N^*\end{cases}}. \tag{6.A.23}$$

Similarly, due to the coupling, the nonlinear stiffness of the Duffing type k_3^* is re-scaled, such that:

$$\boxed{k_3^*=\begin{cases}k_3-\frac{\lambda^2}{12B}\frac{E^2c_3^2}{r^4}\frac{1}{(1+4\tau^2\omega^2)} & T<T_N^*\\ k_3 & T>T_N^*\end{cases}}, \tag{6.A.24}$$

and the linear stiffness k_1^* as:

$$\boxed{k_1^*=\begin{cases}k_1+\lambda L_0^2\frac{Ec_3}{2r^2} & T<T_N^*\\ k_1 & T>T_N^*\end{cases}}. \tag{6.A.25}$$

Thus, the dynamics of the membrane can be effectively described using a single nonlinear differential equation with renormalized linear stiffness as well as Duffing and van der Pol nonlinear damping terms:

$$m\ddot{x}+k_1^*x+k_3^*x^3=F_\omega\cos(\omega t)-\frac{m\omega_0}{Q}\dot{x}-\eta_{nl}^*x^2\dot{x}, \tag{6.A.26}$$

where $\omega_0^2=\frac{k_1^*}{m}$ is the renormalized resonance frequency.

It is worth noting from equation (6.A.23) that η^*_{nl} is significant near $2\tau\omega \approx 1$ and peaks at $2\tau\omega = 1$ [141]. In previous work of Zhou et al. [132], it was shown that in $FePS_3$ the longest magnetostriction-caused lattice relaxation time constant is related to modulation of the monoclinic lattice angle by interlayer spin-shear coupling, which can be in the order of several tens of nanoseconds near T_{N} [132, 133]. These relaxation timescales are indeed expected to lead to $2\tau\omega \approx 1$ and thus hypothetically can cause significant nonlinear damping within the measured range of ω.

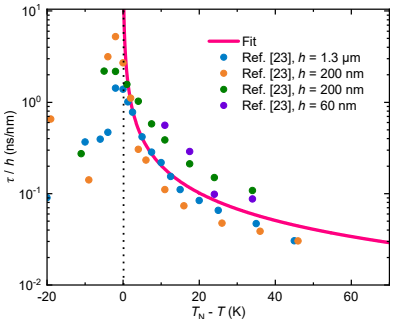

Figure 6.10: Thickness-normalized relaxation time constants $\tau(T)$ reported on samples of various sample thicknesses h from Zhou, F. et al [132]. Solid magenta line - a fit equation (6.A.15) to the data points, with $T^*_N = 115$ K and $\kappa ah = 0.232 \pm 0.019$ ms^{-1}K^{-1}.

We further hypothesise that the spin-shear relaxation $\tau(T)$ from the work of Zhou et al. [132] has the dominant contribution to our experimentally observed delay. By fitting experimental data from Zhou et al. [132] to equation (6.A.15), see figure 6.10, we plot the expected temperature dependence of $k^*_3(T)$ and $\eta^*_{\mathrm{nl}}(T)$ in figure 6.11 for $h = 9.5$ nm, assuming a minor temperature dependence of $k_3(T)$ due to other effects of a non-magnetic nature.

It is worth noting that when τ is insignificant, i.e., $\tau \approx 0$, equation (6.A.24) simplifies to:

$$\begin{cases} k^*_3 = k_3 - \frac{\lambda^2}{12B}\frac{E^2 c_3^2}{r^4} & T < T^*_{\mathrm{N}} \\ k^*_3 = k_3 & T > T^*_{\mathrm{N}} \end{cases}. \tag{6.A.27}$$

This will produce the corresponding behaviour near the phase transition, that we show in figure 6.12 for $k^*_1(T)$ and $k^*_3(T)$, while the magnetic contribution to $\eta^*_{\mathrm{nl}}(T)$ becomes zero.

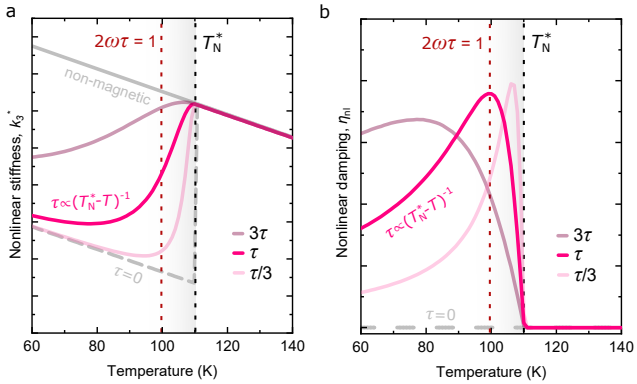

Figure 6.11: Re-normalized nonlinear stiffness k_3^* and nonlinear damping η_{nl} calculated using equations (6.A.23) and (6.A.24) for different values of $\tau(T)$ and $2\omega_0\tau = 1$, as well as results of the fit from figure 6.10 and $\omega(T) = \omega_0(T) = 2\pi f_0(T)$ from figure 6.1c of the main text.

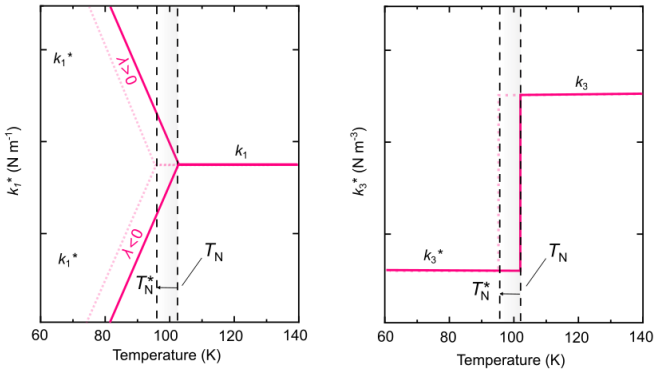

Figure 6.12: Re-normalized k_1^* and k_3^* as a function of temperature at insignificantly small τ ($\tau \approx 0$). The magenta lines correspond with the values without shift of the transition temperature, indicated by the dashed black line labeled T_N. The light lines correspond with the values in case of a shifted transition temperature, indicated by dashed black line labeled T_N^*

REFERENCES

22. Šiškins, M. *et al.* Magnetic and electronic phase transitions probed by nanomechanical resonators. *Nat. Commun.* **11,** 2698 (June 2020).

34. Houmes, M. J. A. *et al.* Magnetic order in 2D antiferromagnets revealed by spontaneous anisotropic magnetostriction. *Nat. Commun.* **14,** 8503 (Dec. 2023).

55. Landau, L. D., Pitaevskii, L. P. & Lifshitz, E. M. *Electrodynamics of continuous media* 2nd ed. (Butterworth, New York, 1984).

104. Šiškins, M. *et al.* Nanomechanical probing and strain tuning of the Curie temperature in suspended $Cr_2Ge_2Te_6$-based heterostructures. *npj 2D Mater. Appl.* **6** (June 2022).

106. Lifshitz, R. & Roukes, M. L. Thermoelastic damping in micro- and nanomechanical systems. *Phys. Rev. B* **61,** 5600–5609 (Feb. 2000).

118. Atalaya, J., Kenny, T. W., Roukes, M. L. & Dykman, M. I. Nonlinear damping and dephasing in nanomechanical systems. *Phys. Rev. B* **94,** 195440 (Nov. 2016).

123. Šiškins, M. *et al.* Tunable Strong Coupling of Mechanical Resonance between Spatially Separated $FePS_3$ Nanodrums. *Nano Lett.* **22,** 36–42 (Dec. 2021).

124. Davidovikj, D. *et al.* Nonlinear Dynamic Characterization of Two-Dimensional Materials. *Nat. Commun.* **8,** 1253 (Nov. 2017).

125. Keşkekler, A. *et al.* Tuning Nonlinear Damping in Graphene Nanoresonators by Parametric–Direct Internal Resonance. *Nat. Commun.* **12,** 1099 (Feb. 2021).

132. Zhou, F. *et al.* Dynamical criticality of spin-shear coupling in van der Waals antiferromagnets. *Nat. Commun.* **13,** 6598 (Nov. 2022).

133. Zong, A. *et al.* Spin-mediated shear oscillators in a van der Waals antiferromagnet. *Nature* **620,** 988–993 (Aug. 2023).

135. Landau, L. D. & Khalatnikov, I. M. On the anomalous absorption of sound near a second order phase transition point. *Dokl. Akad. Nauk SSSR* **96,** 469 (1954).

136. Belov, K. P., Katayev, G. I. & Levitin, R. Z. Internal Friction Anomalies in Ferromagnets and Antiferromagnets near the Curie Point. *J. Appl. Phys.* **31,** S153–S156 (May 1960).

137. Belov, K. P., Kataev, G. I. & Levitin, R. Z. Anomalies in internal friction and modulus of elasticity in ferromagnetic near the Curie point. *J. Exptl. Theoret. Phys. (U.S.S.R.)* **37,** 938–943 (1959).

140. Zhang, X. *et al.* Dynamically-enhanced strain in atomically thin resonators. *Nat. Commun.* **11,** 5526 (Nov. 2020).

141. Dykman, M. I. & Krivoglaz, M. A. Spectral distribution of nonlinear oscillators with nonlinear friction due to a medium. *Phys. Status Solidi B* **68,** 111–123 (Mar. 1975).

150. Sun, Y. & Saka, M. Thermoelastic damping in micro-scale circular plate resonators. *J. Sound Vib.* **329,** 328–337 (Feb. 2010).

151. Morell, N. *et al.* High Quality Factor Mechanical Resonators Based on WSe_2 Monolayers. *Nano Lett.* **16,** 5102–5108 (Aug. 2016).

152. Lyon, K. G., Salinger, G. L., Swenson, C. A. & White, G. K. Linear thermal expansion measurements on silicon from 6 to 340 K. *J. Appl. Phys.* **48,** 865–868 (Mar. 1977).

153. Mann, S., Kumar, R. & Jindal, V. K. Negative thermal expansion of pure and doped graphene. *RSC Adv.* **7,** 22378 (2017).

154. Politano, A. & Chiarello, G. Probing the Young's modulus and Poisson's ratio in graphene/metal interfaces and graphite: a comparative study. *Nano Res.* **8,** 1847–1856 (Apr. 2015).

155. Lifshitz, R. & Cross, M. C. in *Reviews of Nonlinear Dynamics and Complexity* 1–52 (John Wiley & Sons, Ltd, 2008).

156. Davidovikj, D., Scheepers, P. H., van der Zant, H. S. J. & Steeneken, P. G. Static Capacitive Pressure Sensing Using a Single Graphene Drum. *ACS Appl. Mater. Interfaces* **9,** 43205–43210 (Nov. 2017).

157. Catalini, L., Rossi, M., Langman, E. C. & Schliesser, A. Modeling and Observation of Nonlinear Damping in Dissipation-Diluted Nanomechanical Resonators. *Phys. Rev. Lett.* **126** (Apr. 2021).

ACKNOWLEDGEMENTS

As with many (scientific) endeavours, the effort that went into this thesis is not just that of a single person, but of many. So I would like to use the following pages to thank some of the people that helped me get to this point. I say some because I'll undoubtedly forget some people, to which I apologise, and because properly tanking everybody would double the length of this work.

Firstly I want to thank my promotors, without whose guidance this work would not exist. **Peter**, we first talked during the Casimir open days the last Thursday before the lockdowns started. I remember that during the interview we very quickly were just talking about the technical details of the pressure sensors and I think that is quite representative. Your eye for the technical details always forced me to be sharp and although it could sometimes be frustrating the science was only better for it. You are also always coming up with new projects and collaborations, and although I don't know how you manage to be involved with so many, I'm grateful for it. As it gave me the chance to work with SRON and NASA on the detectors, see how ICs are developed in practice, and do a project at the beamline. **Herre**, at first I was a bit scared of you as the big time professor, but that didn't last long once I got to know you. Your hands off approach to supervision allowing me so much freedom to explore often gave me the feeling of being lost for direction, but looking back I really appreciate it. As it thought me how to be independent without ever feeling abandoned as you were always available for help. You taught me a lot about how to be in academia, and I think especially your way of approaching bureaucratic rules did a lot to temper my nature to stress about them. **Peter** and **Herre** you both have a different style of supervision and perspective on the work, but I think this only enriched my experience as your student. I am grateful for you to have been my promotors.

Yaroslav, I want to thank you for being in my committee, but even more so for the great theory discussions, always being available for questions, and the silent stability you bring to the department.

Gary, I want to thank you for being in my committee, I already look forward to your questions as I'm sure they'll be interesting. I loved the many discussions we've had about about anything from physics to society. I also want to say thanks for taking time to awnser my occasional question even though I wasn't in your student.

Alvaro, I know you started as my master student, but it never really felt like that as from the start it was like having another PhD working with me. And I'm very happy you stayed for your PhD. after as I can not imagine what the last year would have looked like without you. We had a lot of adventures together wether it was at the beamline, on conferences, or supervising some master students. I want to say good luck with your PhD. but I am 100% sure you will be great.

Annet, thank you for agreeing to by one of my paranymph and my friend through the years. I still sometimes think back fondly to the china trip which would not have been

as fun without you. I think you said it best yourself, we are able to have a conversation without talking and I'm so happy I get to share that with you.

Martin always kind and happy to help even while working 120% already. Even after these years I'm still so impressed by your amazing dedication and your skill in the cleanroom. I'm a bit proud that I got to learn device fabrication from you and while Covid limited the time we got to go into the cleanroom together it is thanks to you showing me the ropes that I'm now no longer constantly afraid I'll break one of those expensive machines. I wish you good luck with your new group but with you in charge I'm sure it will be great. **Makars** you are really an inspiration to work with. During the start of my PhD you taught me not only the details of the setups and the art of stamping but during the many discussions and conversations you really showed me how to think like an experimental physicist. **Gabriele** while a bit brief it was great having a fellow PhD working on the nanomechanics in the group where everybody else did some form transport. I really remember the time we spend together going back and forth with the equations for the anisotropy paper as we both had this feeling that there should be a way to extract the order parameter from the frequencies, we figured it out in the end.

Yongqing Even though you haven't been around that long in the group I feel like you've always been there. You are so open in discussing ideas and asking questions and are already well on your way to becoming a cleanroom expert. Aside from that you're also a great cook, office mate and friend. **Riccardo** I've only ever seen you in two states, joyfull optimism or complete focus on your work. Your seemingly endless optimism and cheerfulness is infectious, I hope you never lose that. You can get completely absorbed into your work when ever you get a crazy idea or find some cool data and when you find something something cool you tell about it with such enthusiasm that any listener is sure to become excited as well. **Cossimo** It's great to have another GM and board game enthusiast in the group. And between the frisbee lunches and game nights you are also a great scientist, you are very good at explaining what you're doing and are really open for input from everybody. **Thomas Baum** the first thing I always think about when you're mentioned is Kondo something and the second "Tiramisu". You've been my office mate since the start and even though our work didn't really overlap any conversation with you were always full of jokes and interesting insights. Despite the struggle sometimes I'm happy we got to work together a bit when trying to help Giannis in Montana. I'm not sure what you went on to do after your defense, but I'm sure you'll find something that you like as I can't see you settle for anything less. **Jacqueline**, we knew each other already from TA-ing in Leiden, but somehow it took us a few months after I started before we realised we were in the same group. For which I blame Covid. You were always fun to chat to, especially your stories about Chile. **Linde**, it is good to have you in the nanomechanics team. I can imagine it is not easy being the only woman in the group, but I think you are doing good. **Talieh**, you were always very kind and made sure that during group activities everybody was involved. I'm a bit sad that I don't get to be in Delft when you start your own lab as I'm sure it will be great. **Joseph**, it was nice sharing an office with you, you were always open for a quick question. I still walk past the poster you put up about your quantum point contacts thinking how cool that research is. **Samuel**, working with you has been really impressive, you always seem to know everything about every material and know what everybody in the community is doing, al the while doing so

much work yourself. And I also want to thank the rest of the van der Zant lab, **Sergeii**, **Damian**, **Tristan**, **Sebastiaan**, **Jasper**, and all the others the lab would not have been the same without all of you.

Ritesh, Thanks, it is indeed a nice shirt.

I also want to thank the many other people in the **Quantum Nanoscience** department. For the many coffee machine and hallway chats, the party interactions, the fun and interesting talks, shared conferences, and the overall sense of community.

And of course especially my fellow members of the **Culture and Community Committee**, **Sonaski**, **Alvaro**, **Cossimo**, **Jan-Paul**, **Sarah**, **Evert**, **Clinton**, **Talieh**, **Michiel**, **Bowy**, **Tino**, **Lizzy**, **Massimiliano**, **Sonia**, **Maz**, and **Gary**. We had a lot of fun making trying to make QN as nice a place as it could be, wether via organizing parties, the Bytes, furnishing E104, or addressing social issues. I always enjoyed the meetings even with the endless tangents and sometimes frustrating bureaucracy involved.

I also want to thank the many people at **PME**, **Ata**, **Curry**, **Ruben Frederike**, **Xiliang**, **Tufan**, **Farbod**, **Gerard**, and all the others. I was always welcome whether for talks, research coffees, questions, parties or anything else. I always liked hearing about your projects and getting a bit out of the pure physics bubble.

Sten and **Roberto** I want to thank you the many funny moments at conferences. You both have a very sober and a good critical attitude. Showing me how to be excited about cool results while staying grounded in reality. A skill which I think is sometimes undervalued.

My dear **Larissa**, I want thank you for the countless ways in which you are there for me. You support me even when I don't realise I need it and I cannot thank you enough for that. I love you, but you know that already. **Mom and Dad**, thank you for raising me and being there always to support me. I know I'm not easy to communicate with but you never stopped trying and I appreciate that. I love you both. **Hannah**, I know I am not the easiest brother to have, but I am proud to have you as my sister. I am still a bit sad I couldn't be at your graduation, but am happy to see how you and Jard are settling. Much love from your brother. **Suus en Maggie** whose tail wagging each time I got home always cheered up my day.

I want to thank my friends from Leiden, **Annet**, **Casper Barendrecht** and **Martijn de Jong** for the many many many games of Love Letter and Hearts and all the others. My time studying and after would not have been nowhere near as nice without you.

To **Casper van der Esch**, **Lex**, and **I** want to say thank you for being my friends through the year and an always unpredictable group of adventurers to GM for.

My **WDZ** family that taught me so much more than just sailing or lighting fires. I want to especially thank my fellow leaders, **Mariette**, **Niels**, **Lukas**, **Erwin**, **Martijn Righolt**, **Joost**, **Bob**, **Bram**, and the others both green and blue, for the fun and crazy camps and the endless adventures that we shared.

Gert-Jan, I want to thank you for your help. You taught me a lot about myself and really got me unstuck from a dark place.

BIBLIOGRAPHY

1. Novoselov, K. S. *et al.* Electric Field Effect in Atomically Thin Carbon Films. *Science* **306,** 666–669 (Oct. 2004).
2. Novoselov, K. S., Mishchenko, A., Carvalho, A. & Neto, A. H. C. 2D materials and van der Waals heterostructures. *Science* **353,** aac9439 (2016).
3. López-Polín, G. *et al.* Increasing the elastic modulus of graphene by controlled defect creation. *Nature Physics* **11,** 26–31 (Jan. 2015).
4. Chen, W., Gui, X., Yang, L., Zhu, H. & Tang, Z. Wrinkling of two-dimensional materials: methods, properties and applications. *Nanoscale Horiz.* **4,** 291–320 (2019).
5. Gao, W., Zhi, G., Zhou, M. & Niu, T. Growth of Single Crystalline 2D Materials beyond Graphene on Non-metallic Substrates. *Small,* 2311317.
6. Dong, J., Zhang, L. & Ding, F. Kinetics of Graphene and 2D Materials Growth. *Advanced Materials* **31,** 1801583 (2019).
7. Geng, D. & Yang, H. Y. Recent Advances in Growth of Novel 2D Materials: Beyond Graphene and Transition Metal Dichalcogenides. *Advanced Materials* **30,** 1800865 (2018).
8. Sulleiro, M. V., Dominguez-Alfaro, A., Alegret, N., Silvestri, A. & Gómez, I. J. 2D Materials towards sensing technology: From fundamentals to applications. *Sensing and Bio-Sensing Research* **38,** 100540 (2022).
9. Yang, S., Jiang, C. & Wei, S.-h. Gas sensing in 2D materials. *Applied Physics Reviews* **4,** 021304 (May 2017).
10. Baglioni, G. *et al.* Ultra-sensitive graphene membranes for microphone applications. *Nanoscale* **15,** 6343–6352 (2023).
11. Guo, Y. *et al.* Review of the pressure sensor based on graphene and its derivatives. *Microelectronic Engineering* **288,** 112167 (2024).
12. Kim, Y. *et al.* Recent Advances in Functionalization and Hybridization of Two-Dimensional Transition Metal Dichalcogenide for Gas Sensor. *Adv. Eng. Mater.* **26,** 2301063 (2024).
13. Acosta, S. & Quintana, M. Chemically Functionalized 2D Transition Metal Dichalcogenides for Sensors. *Sensors* **24** (2024).
14. Šmejkal, L., Sinova, J. & Jungwirth, T. Beyond Conventional Ferromagnetism and Antiferromagnetism: A Phase with Nonrelativistic Spin and Crystal Rotation Symmetry. *Phys. Rev. X* **12,** 031042 (Sept. 2022).
15. Landau, L., Lifshitz, E. & Pitaevskii, L. *Electrodynamics of Continuous Media: Volume 8* (Elsevier Science, 1995).

16. Mermin, N. D. & Wagner, H. Absence of Ferromagnetism or Antiferromagnetism in One- or Two-Dimensional Isotropic Heisenberg Models. *Phys. Rev. Lett.* **17,** 1133 (Nov. 1966).
17. Hohenberg, P. C. Existence of Long-Range Order in One and Two Dimensions. *Phys. Rev.* **158,** 383–386 (June 1967).
18. Cortie, D. L. *et al.* Two-Dimensional Magnets: Forgotten History and Recent Progress towards Spintronic Applications. *Adv. Funct. Mater.* **30,** 1901414 (2020).
19. Ghiasi, T. S. *et al. Quantum Anomalous Hall and Spin Hall Effects in Magnetic Graphene* 2023. arXiv: 2312.07515 [cond-mat.mes-hall].
20. Yin, P., Lin, Q. & Duan, Y. Applications of Raman spectroscopy in two-dimensional materials. *Journal of Innovative Optical Health Sciences* **13,** 2030010 (2020).
21. Lee, M. *et al.* Study of charge density waves in suspended 2H-TaS_2 and 2H-$TaSe_2$ by nanomechanical resonance. *Appl. Phys. Lett.* **118,** 193105 (May 2021).
22. Šiškins, M. *et al.* Magnetic and electronic phase transitions probed by nanomechanical resonators. *Nat. Commun.* **11,** 2698 (June 2020).
23. Baglioni, G. *et al.* Thermo-Magnetostrictive Effect for Driving Antiferromagnetic Two-Dimensional Material Resonators. *Nano Lett.* **23,** 6973–6978 (2023).
24. Lee, M. *Applied and fundamental studies of vibrating 2D membranes* PhD thesis (Delft Univerisity of Technology, 2021).
25. Kim, C., Yoon, M.-A., Jang, B., Kim, J.-H. & Kim, K.-S. A Review on Transfer Process of Two-dimensional Materials. *Tribology and Lubricants* **36,** 1–10 (Feb. 2020).
26. Schranghamer, T. F., Sharma, M., Singh, R. & Das, S. Review and comparison of layer transfer methods for two-dimensional materials for emerging applications. *Chem. Soc. Rev.* **50,** 11032–11054 (2021).
27. Sadd, M. H. *Elasticity: Theory, Applications, and Numerics* (Elsevier, 2004).
28. Landau, L. D. & Lifshitz, E. M. *Theory of Elasticity* 3rd ed. (Elsevier, 1986).
29. Leissa, A. W. & Qatu, M. S. *Vibrations of continuous systems* (New York: McGraw-Hill, 2011).
30. Landau, L. On the theory of phase transitions. *Ukrainian journal of physics* **53,** 25–35 (2008).
31. Neirotti, J. P. & de Oliveira, M. J. Spontaneous staggered magnetization in antiferromagnetic Heisenberg-Ising chains. *Phys. Rev. B* **54,** 6351–6355 (9 Sept. 1996).
32. Landau, L. D., Lifshitz, E. M., Sykes, J. B. & M.J, K. *Statistical Physics* 3rd ed. (Elsevier, 1980).
33. Gelfand, I. M., Fomin, S. V. & Silverman, R. A. *Calculus of Variations* (Prentice-Hall, Englewood Cliffs, N. J., 1963).
34. Houmes, M. J. A. *et al.* Magnetic order in 2D antiferromagnets revealed by spontaneous anisotropic magnetostriction. *Nat. Commun.* **14,** 8503 (Dec. 2023).
35. Mak, K. F., Shan, J. & Ralph, D. C. Probing and controlling magnetic states in 2D layered magnetic materials. *Nat. Rev. Phys.* **1,** 646–661 (Sept. 2019).

36. Huang, B. *et al.* Layer-dependent ferromagnetism in a van der Waals crystal down to the monolayer limit. *Nature* **546,** 270–273 (June 2017).
37. Gong, C. *et al.* Discovery of intrinsic ferromagnetism in two-dimensional van der Waals crystals. *Nature* **546,** 265–269 (Apr. 2017).
38. Lee, J.-U. *et al.* Ising-Type Magnetic Ordering in Atomically Thin $FePS_3$. *Nano Lett.* **16,** 7433–7438 (Nov. 2016).
39. Telford, E. J. *et al.* Layered Antiferromagnetism Induces Large Negative Magnetoresistance in the van der Waals Semiconductor CrSBr. *Adv. Mater.* **32,** 2003240 (2020).
40. Němec, P., Fiebig, M., Kampfrath, T. & Kimel, A. V. Antiferromagnetic opto-spintronics. *Nat. Phys.* **14,** 229–241 (Mar. 2018).
41. Rahman, S., Torres, J. F., Khan, A. R. & Lu, Y. Recent Developments in van der Waals Antiferromagnetic 2D Materials: Synthesis, Characterization, and Device Implementation. *ACS Nano* **15,** 17175–17213 (Nov. 2021).
42. Mertens, F. *et al.* Ultrafast Coherent THz Lattice Dynamics Coupled to Spins in the van der Waals Antiferromagnet $FePS_3$. *Adv. Mater.,* 2208355 (2022).
43. Boix-Constant, C. *et al.* Probing the Spin Dimensionality in Single-Layer CrSBr van der Waals Heterostructures by Magneto-Transport Measurements. *Adv. Mater.* **34,** 2204940 (2022).
44. Esteras, D. L., Rybakov, A., Ruiz, A. M. & Baldoví, J. J. Magnon Straintronics in the 2D van der Waals Ferromagnet CrSBr from First-Principles. *Nano Lett.* **22,** 8771–8778 (2022).
45. Wang, Y. *et al.* Strain-Sensitive Magnetization Reversal of a van der Waals Magnet. *Adv. Mater.* **32,** 2004533 (2020).
46. Ni, Z. *et al.* Imaging the Néel vector switching in the monolayer antiferromagnet $MnPSe_3$ with strain-controlled Ising order. *Nat. Nanotechnol.* **16,** 782–787 (Apr. 2021).
47. Cenker, J. *et al.* Reversible strain-induced magnetic phase transition in a van der Waals magnet. en. *Nat. Nanotechnol.,* 1–6 (Jan. 2022).
48. Šiškins, M. *et al.* Nanomechanical probing and strain tuning of the Curie temperature in suspended Cr2Ge2Te6-based heterostructures. *npj 2D Mater. Appl.* **6** (June 2022).
49. Jiang, S., Xie, H., Shan, J. & Mak, K. F. Exchange Magnetostriction in Two-Dimensional Antiferromagnets. *Nat. Mater.* **19,** 1295–1299 (June 2020).
50. Chittari, B. L. *et al.* Electronic and magnetic properties of single-layer MPX_3 metal phosphorous trichalcogenides. *Phys. Rev. B* **94** (Nov. 2016).
51. Wildes, A. R., Simonet, V., Ressouche, E., Ballou, R. & McIntyre, G. J. The magnetic properties and structure of the quasi-two-dimensional antiferromagnet $CoPS_3$. *J. Phys. Condens. Matter.* **29,** 455801 (Oct. 2017).
52. Joy, P. A. & Vasudevan, S. Magnetism in the layered transition-metal thiophosphates MPS_3 (M=Mn, Fe, and Ni). *Phys. Rev. B* **46,** 5425–5433 (Sept. 1992).

53. Takano, Y. *et al.* Magnetic properties and specific heat of MPS_3 (M=Mn, Fe, Zn). *J. Magn. Magn. Mat.* **272-276,** E593–E595 (May 2004).

54. Šiškins, M. *et al.* Highly Anisotropic Mechanical and Optical Properties of 2D Layered As_2S_3 Membranes. *ACS Nano* **13,** 10845–10851 (Aug. 2019).

55. Landau, L. D., Pitaevskii, L. P. & Lifshitz, E. M. *Electrodynamics of continuous media* 2nd ed. (Butterworth, New York, 1984).

56. Bunch, J. S. *et al.* Electromechanical Resonators from Graphene Sheets. *Science* **315,** 490–493 (2007).

57. Gui, Q. *et al.* Extrinsic-Structured Bimetallic-Phase Ternary Metal Phosphorus Trisulfides Coupled with N-Doped Graphitized Carbon for Superior Electrochemical Lithium Storage. *Adv. Energy Mater.* **11,** 2003553 (Jan. 2021).

58. Liu, Q. *et al.* Magnetic order in XY-type antiferromagnetic monolayer $CoPS_3$ revealed by Raman spectroscopy. *Phys. Rev. B* **103,** 235411 (June 2021).

59. Gibertini, M., Koperski, M., Morpurgo, A. F. & Novoselov, K. S. Magnetic 2D materials and heterostructures. *Nat. Nanotechnol.* **14,** 408–419 (May 2019).

60. Afanasiev, D. *et al.* Controlling the anisotropy of a van der Waals antiferromagnet with light. *Sci. Adv.* **7,** eabf3096 (June 2021).

61. Kim, K. *et al.* Suppression of magnetic ordering in XXZ-type antiferromagnetic monolayer $NiPS_3$. *Nat. Commun.* **10,** 345 (Jan. 2019).

62. Yao-Dong, D. *et al.* A Mössbauer study of the magnetic coupling in iron phosphorous trisulfides. *Chinese Phys.* **13,** 1652 (2004).

63. Zhang, Q. *et al.* Observation of Giant Optical Linear Dichroism in a Zigzag Antiferromagnet $FePS_3$. *Nano Lett.* **21,** 6938–6945 (2021).

64. Zhang, R. & Willis, R. F. Thickness-Dependent Curie Temperatures of Ultrathin Magnetic Films: Effect of the Range of Spin-Spin Interactions. *Phys. Rev. Lett.* **86,** 2665–2668 (May 2001).

65. Bunch, J. S. *Mechanical and electrical properties of graphene sheets* (Ph.D. thesis, Cornell University Ithaca, NY, 2008).

66. Houmes, M. J. A. *et al.* Highly Anisotropic Mechanical Response of the Van der Waals Magnet CrPS4. *Adv. Funct. Mater.* **34,** 2310206 (2024).

67. Da Gao, Z. *et al.* Anisotropic Mechanics of 2D Materials. *Adv. Eng. Mater.* **24,** 2200519 (Nov. 2022).

68. Uniaxial negative thermal expansion behavior of β-CuSCN. *Appl. Phys. Lett.* **118,** 222105 (May 2021).

69. Diederich, G. M. *et al.* Tunable interaction between excitons and hybridized magnons in a layered semiconductor. *Nat. Nanotechnol.* **18,** 23–28 (Dec. 2022).

70. De Wal, D. K. *et al.* Long-distance magnon transport in the van der Waals antiferromagnet CrPS4. *Phys. Rev. B* **107,** L180403 (May 2023).

71. Hwangbo, K. *et al.* Highly anisotropic excitons and multiple phonon bound states in a van der Waals antiferromagnetic insulator. *Nat. Nanotechnol.* **16,** 655–660 (Mar. 2021).

72. Kang, S. *et al.* Coherent many-body exciton in van der Waals antiferromagnet NiPS3. *Nature* **583,** 785–789 (July 2020).

73. Boix-Constant, C. *et al.* Probing the Spin Dimensionality in Single-Layer CrSBr Van Der Waals Heterostructures by Magneto-Transport Measurements. *Adv. Mater.* **34,** 2204940 (Oct. 2022).

74. Bae, Y. J. *et al.* Exciton-coupled coherent magnons in a 2D semiconductor. *Nature* **609,** 282–286 (Sept. 2022).

75. Peng, Y. *et al.* Magnetic Structure and Metamagnetic Transitions in the van der Waals Antiferromagnet CrPS4. *Adv. Mater.* **32,** 2001200 (July 2020).

76. Riesner, M. *et al.* Temperature dependence of Fano resonances in CrPS4. *J. Chem. Phys.* **156,** 54707 (Feb. 2022).

77. Gu, P. *et al.* Photoluminescent Quantum Interference in a van der Waals Magnet Preserved by Symmetry Breaking. *ACS Nano* **14,** 1003–1010 (Jan. 2020).

78. Lee, J. *et al.* Structural and Optical Properties of Single- and Few-Layer Magnetic Semiconductor CrPS4. *ACS Nano* **11,** 10935–10944 (Nov. 2017).

79. Diehl, R. & Carpentier, C.-D. The structural chemistry of indium phosphorus chalcogenides. *Acta Crystallogr.* **B34,** 1097 (Apr. 1978).

80. Bud'Ko, S. L., Gati, E., Slade, T. J. & Canfield, P. C. Magnetic order in the van der Waals antiferromagnet CrPS4: Anisotropic H-T phase diagrams and effects of pressure. *Phys. Rev. B* **103,** 224407 (June 2021).

81. Calder, S. *et al.* Magnetic structure and exchange interactions in the layered semiconductor CrPS4. *Phys. Rev. B* **102,** 024408 (July 2020).

82. Kim, S. *et al.* Photoluminescence Path Bifurcations by Spin Flip in Two-Dimensional CrPS4. *ACS Nano* **16,** 16385–16393 (Oct. 2022).

83. Son, J. *et al.* Air-Stable and Layer-Dependent Ferromagnetism in Atomically Thin van der Waals CrPS4. *ACS Nano* **15,** 16904–16912 (Oct. 2021).

84. Wu, F. *et al.* Gate-Controlled Magnetotransport and Electrostatic Modulation of Magnetism in 2D Magnetic Semiconductor CrPS4. *Adv. Mater.,* 2211653 (June 2023).

85. Qi, S. *et al.* Giant electrically tunable magnon transport anisotropy in a van der Waals antiferromagnetic insulator. *Nat. Commun.* **14,** 1–8 (May 2023).

86. Lee, M. *et al.* Study of charge density waves in suspended 2H-TaS2 and 2H-TaSe2 by nanomechanical resonance. *Appl. Phys. Lett.* **118,** 193105 (May 2021).

87. López-Cabrelles, J. *et al.* Chemical Design and Magnetic Ordering in Thin Layers of 2D Metal-Organic Frameworks (MOFs). *J. Am. Chem. Soc.* **143,** 18502–18510 (Nov. 2021).

88. Davidovikj, D. *Two-dimensional membranes in motion* PhD thesis (TU Delft, 2018).

89. Li, B.-L. *et al.* Very high-frequency, gate-tunable $CrPS_4$ nanomechanical resonator with single mode. *Opt. Lett.* **48,** 2571–2574 (May 2023).

90. Dove, M. T. & Fang, H. Negative thermal expansion and associated anomalous physical properties: review of the lattice dynamics theoretical foundation. *Rep. Prog. Phys.* **79,** 066503 (May 2016).

91. Colossal positive and negative thermal expansion in the framework material $Ag_3[Co(CN)_6]$. *Science* **319,** 794–797 (Feb. 2008).

92. Das, D., Jacobs, T. & Barbour, L. J. Exceptionally large positive and negative anisotropic thermal expansion of an organic crystalline material. *Nat. Mater.* **9,** 36–39 (Nov. 2010).

93. Peng, Y. *et al.* Controlling Spin Orientation and Metamagnetic Transitions in Anisotropic van der Waals Antiferromagnet CrPS4 by Hydrostatic Pressure. *Adv. Funct. Mater.* **32,** 2106592 (2022).

94. Joe, M., Lee, J. & Lee, C. Dominant in-plane cleavage direction of CrPS4. *Comput. Mater. Sci.* **162,** 277–280 (2019).

95. Joe, M. *et al.* A comprehensive study of piezomagnetic response in $CrPS_4$ monolayer: Mechanical, electronic properties and magnetic ordering under strains. *J. Condens. Matter Phys.* **29** (Aug. 2017).

96. Villars, P. *PAULING FILE in: Inorganic Solid Phases,* SpringerMaterials (online database), Springer, Heidelberg (ed.) SpringerMaterials.

97. Lyon, K. G., Salinger, G. L., Swenson, C. A. & White, G. K. Linear thermal expansion measurements on silicon from 6 to 340 K. *J. Appl. Phys.* **48,** 865–868 (Mar. 1997).

98. Wahab, D. A. *et al.* Quantum Rescaling, Domain Metastability, and Hybrid Domain-Walls in 2D CrI3 Magnets. *Adv. Mater.* **33,** 2004138 (Feb. 2020).

99. Zomer, P. J., Guimarães, M. H. D., Brant, J. C., Tombros, N. & van Wees, B. J. Fast pick up technique for high quality heterostructures of bilayer graphene and hexagonal boron nitride. *Appl. Phys. Lett.* **105,** 013101 (July 2014).

100. Wang, Q. H. *et al.* The Magnetic Genome of Two-Dimensional van der Waals Materials. *ACS Nano* **16,** 6960–7079 (2022).

101. Dolleman, R. J. *et al.* Optomechanics for thermal characterization of suspended graphene. *Phys. Rev. B* **96,** 165421 (Oct. 2017).

102. Dolleman, R. J. *et al.* Transient thermal characterization of suspended monolayer MoS_2. *Phys. Rev. Mater.* **2,** 114008 (Nov. 2018).

103. Morell, N. *et al.* Optomechanical Measurement of Thermal Transport in Two-Dimensional MoSe2 Lattices. *Nano Lett.* **19,** 3143–3150 (2019).

104. Šiškins, M. *et al.* Nanomechanical probing and strain tuning of the Curie temperature in suspended $Cr_2Ge_2Te_6$-based heterostructures. *npj 2D Mater. Appl.* **6** (June 2022).

105. Zener, C. Internal Friction in Solids I. Theory of Internal Friction in Reeds. *Phys. Rev.* **52,** 230–235 (Aug. 1937).

106. Lifshitz, R. & Roukes, M. L. Thermoelastic damping in micro- and nanomechanical systems. *Phys. Rev. B* **61,** 5600–5609 (Feb. 2000).

107. Haglund, A. *Thermal Conductivity of MXY_3 Magnetic Layered Trichalcogenides* (Ph.D. thesis, University of Tennessee, Knoxville, 2019).

108. Šiškins, M. *et al. Nonlinear dynamics and magneto-elasticity of nanodrums near the phase transition* 2023. arXiv: 2309.09672 [cond-mat.mes-hall].

109. Androulidakis, C., Zhang, K., Robertson, M. & Tawfick, S. Tailoring the Mechanical Properties of 2D Materials and Heterostructures. *2D Mater.* **5,** 032005 (June 2018).

110. Jiang, H., Zheng, L., Liu, Z. & Wang, X. Two-dimensional materials: From mechanical properties to flexible mechanical sensors. *InfoMat* **2,** 1077–1094 (Dec. 2019).

111. Lemme, M. C. *et al.* Nanoelectromechanical Sensors Based on Suspended 2D Materials. *Research* **2020,** 8748602 (July 2020).

112. Rosłoń, I. E., Japaridze, A., Steeneken, P. G., Dekker, C. & Alijani, F. Probing nanomotion of single bacteria with graphene drums. *Nat. Nanotechnol.* **17,** 637–642 (Apr. 2022).

113. Steeneken, P. G., Dolleman, R. J., Davidovikj, D., Alijani, F. & van der Zant, H. S. J. Dynamics of 2D material membranes. *2D Mater.* **8,** 042001 (Aug. 2021).

114. Güttinger, J. *et al.* Energy-dependent path of dissipation in nanomechanical resonators. *Nat. Nanotech.* **12,** 631–636 (July 2017).

115. Bachtold, A., Moser, J. & Dykman, M. Mesoscopic physics of nanomechanical systems. *Rev. Mod. Phys.* **94,** 045005 (Dec. 2022).

116. Kirchhof, J. N. *et al.* Nanomechanical Spectroscopy of 2D Materials. *Nano Lett.* **22,** 8037–8044 (Oct. 2022).

117. Arribas, I. S., Taniguchi, T., Watanabe, K. & Weig, E. M. Radiation Pressure Backaction on a Hexagonal Boron Nitride Nanomechanical Resonator. *Nano Lett.* **23,** 6301–6307 (July 2023).

118. Atalaya, J., Kenny, T. W., Roukes, M. L. & Dykman, M. I. Nonlinear damping and dephasing in nanomechanical systems. *Phys. Rev. B* **94,** 195440 (Nov. 2016).

119. De Alba, R. *et al.* Tunable phonon-cavity coupling in graphene membranes. *Nat. Nanotech.* **11,** 741–746 (June 2016).

120. Luo, G. *et al.* Strong Indirect Coupling between Graphene-Based Mechanical Resonators via a Phonon Cavity. *Nat. Commun.* **9,** 383 (Jan. 2018).

121. Chen, C. *et al.* Modulation of mechanical resonance by chemical potential oscillation in graphene. *Nat. Phys.* **12,** 240–244 (Dec. 2015).

122. Sengupta, S., Solanki, H. S., Singh, V., Dhara, S. & Deshmukh, M. M. Electromechanical resonators as probes of the charge density wave transition at the nanoscale in $NbSe_2$. *Phys. Rev. B* **82,** 155432 (Oct. 2010).

123. Šiškins, M. *et al.* Tunable Strong Coupling of Mechanical Resonance between Spatially Separated $FePS_3$ Nanodrums. *Nano Lett.* **22,** 36–42 (Dec. 2021).

124. Davidovikj, D. *et al.* Nonlinear Dynamic Characterization of Two-Dimensional Materials. *Nat. Commun.* **8,** 1253 (Nov. 2017).

125. Keşkekler, A. *et al.* Tuning Nonlinear Damping in Graphene Nanoresonators by Parametric–Direct Internal Resonance. *Nat. Commun.* **12,** 1099 (Feb. 2021).

126. Keşkekler, A., Arjmandi-Tash, H., Steeneken, P. G. & Alijani, F. Symmetry-Breaking-Induced Frequency Combs in Graphene Resonators. *Nano Lett.* **22,** 6048–6054 (Aug. 2022).

127. Eichler, A. *et al.* Nonlinear damping in mechanical resonators made from carbon nanotubes and graphene. *Nat. Nanotech.* **6,** 339–342 (May 2011).

128. Zhang, T. *et al.* A monolithically sculpted van der Waals nano-opto-electro-mechanical coupler. *Light Sci. Appl.* **11,** 48 (Mar. 2022).

129. Li, X., Sha, X., Yan, N. & Zhang, T. Mechanical Detection of Magnetic Phase Transition in Suspended CrOCl Heterostructures. *Magnetochemistry* **8,** 170 (Nov. 2022).

130. Xu, X. *et al.* Length-dependent thermal conductivity in suspended single-layer graphene. *Nat. Commun.* **5,** 3689 (Apr. 2014).

131. Davidovikj, D. *et al.* Visualizing the Motion of Graphene Nanodrums. *Nano Lett.* **16,** 2768–2773 (Mar. 2016).

132. Zhou, F. *et al.* Dynamical criticality of spin-shear coupling in van der Waals antiferromagnets. *Nat. Commun.* **13,** 6598 (Nov. 2022).

133. Zong, A. *et al.* Spin-mediated shear oscillators in a van der Waals antiferromagnet. *Nature* **620,** 988–993 (Aug. 2023).

134. Landau, L. D. On the theory of phase transitions. *Zh. Eksp. Teor. Fiz.* **7.** [*Ukr. J. Phys.* **53**, 25 (2008)], 19–32 (1937).

135. Landau, L. D. & Khalatnikov, I. M. On the anomalous absorption of sound near a second order phase transition point. *Dokl. Akad. Nauk SSSR* **96,** 469 (1954).

136. Belov, K. P., Katayev, G. I. & Levitin, R. Z. Internal Friction Anomalies in Ferromagnets and Antiferromagnets near the Curie Point. *J. Appl. Phys.* **31,** S153–S156 (May 1960).

137. Belov, K. P., Kataev, G. I. & Levitin, R. Z. Anomalies in internal friction and modulus of elasticity in ferromagnetic near the Curie point. *J. Exptl. Theoret. Phys. (U.S.S.R.)* **37,** 938–943 (1959).

138. Khusyainov, D. *et al.* Ultrafast laser-induced spin–lattice dynamics in the van der Waals antiferromagnet $CoPS_3$. *APL Mater.* **11,** 071104 (July 2023).

139. Schmid, S., Villanueva, L. G. & Roukes, M. L. *Fundamentals of Nanomechanical Resonators* (Springer International Publishing, 2016).

140. Zhang, X. *et al.* Dynamically-enhanced strain in atomically thin resonators. *Nat. Commun.* **11,** 5526 (Nov. 2020).

141. Dykman, M. I. & Krivoglaz, M. A. Spectral distribution of nonlinear oscillators with nonlinear friction due to a medium. *Phys. Status Solidi B* **68,** 111–123 (Mar. 1975).

142. Harada, H., Müller, M. & Warlimont, H. in *Springer Handbook of Condensed Matter and Materials Data* 755–815 (Springer Berlin Heidelberg).

143. Hausch, G. Magnetic exchange energy contribution to the elastic constants and its relation to the anomalous elastic behaviour of invar alloys. *Phys. Status Solidi A* **15,** 501–510 (Feb. 1973).

144. Hausch, G. Magnetovolume effects in invar alloys: Pressure dependence of the Curie temperature. *Phys. Status Solidi A* **16,** 371–376 (Apr. 1973).

145. Postolache, E. *et al.* Comparison of Young's modulus and specific heat anomalies at the magnetic transition in α'-NaV_2O_5. *Solid State Sci.* **2,** 759–766 (Dec. 2000).

146. Barton, R. A. *et al.* Photothermal Self-Oscillation and Laser Cooling of Graphene Optomechanical Systems. *Nano Lett.* **12,** 4681–4686 (Aug. 2012).

147. Dolleman, R. J., Davidovikj, D., van der Zant, H. S. J. & Steeneken, P. G. Amplitude calibration of 2D mechanical resonators by nonlinear optical transduction. *Appl. Phys. Lett.* **111,** 253104 (Dec. 2017).

148. Burch, K. S., Mandrus, D. & Park, J.-G. Magnetism in two-dimensional van der Waals materials. *Nature* **563,** 47 (Oct. 2018).

149. Castellanos-Gomez, A. *et al.* Deterministic Transfer of Two-Dimensional Materials by All-Dry Viscoelastic Stamping. *2D Mater.* **1,** 011002 (Apr. 2014).

150. Sun, Y. & Saka, M. Thermoelastic damping in micro-scale circular plate resonators. *J. Sound Vib.* **329,** 328–337 (Feb. 2010).

151. Morell, N. *et al.* High Quality Factor Mechanical Resonators Based on WSe_2 Monolayers. *Nano Lett.* **16,** 5102–5108 (Aug. 2016).

152. Lyon, K. G., Salinger, G. L., Swenson, C. A. & White, G. K. Linear thermal expansion measurements on silicon from 6 to 340 K. *J. Appl. Phys.* **48,** 865–868 (Mar. 1977).

153. Mann, S., Kumar, R. & Jindal, V. K. Negative thermal expansion of pure and doped graphene. *RSC Adv.* **7,** 22378 (2017).

154. Politano, A. & Chiarello, G. Probing the Young's modulus and Poisson's ratio in graphene/metal interfaces and graphite: a comparative study. *Nano Res.* **8,** 1847–1856 (Apr. 2015).

155. Lifshitz, R. & Cross, M. C. in *Reviews of Nonlinear Dynamics and Complexity* 1–52 (John Wiley & Sons, Ltd, 2008).

156. Davidovikj, D., Scheepers, P. H., van der Zant, H. S. J. & Steeneken, P. G. Static Capacitive Pressure Sensing Using a Single Graphene Drum. *ACS Appl. Mater. Interfaces* **9,** 43205–43210 (Nov. 2017).

157. Catalini, L., Rossi, M., Langman, E. C. & Schliesser, A. Modeling and Observation of Nonlinear Damping in Dissipation-Diluted Nanomechanical Resonators. *Phys. Rev. Lett.* **126** (Apr. 2021).

Curriculum Vitæ

Maurits Jan Adriaan Houmes

04-06-1997	Born in Dordrecht, The Netherlands.

Education

2008–2015	Grammar School Johan De Witt gymnasium, Dordrecht
2015–2018	Bachelor Mathematics Leiden University Leiden, The Netherlands
2015–2018	Bachelor Physics Leiden University Leiden, The Netherlands
2018–2020	Master Physics Leiden University Leiden, The Netherlands
2020–2024	PhD. Physics Delft University of Technology Delft, The Netherlands *Thesis:* Magnetostriction in 2D material nanomechanical resonators *Promotors:* Prof. Dr. P. G. Steeneken, Prof. Dr. Ir. H. S. J. van der Zant

Awards

2023	Graphene Study Poster Prize

List of Publications

5. Makars Šiškins, Ata Keşkekler, **Maurits J. A. Houmes**, Samuel Mañas-Valero, Eugenio Coronado, Yaroslav M. Blanter, Herre S. J. van der Zant, Peter G. Steeneken, Farbod Alijani, *Nonlinear dynamics and magneto-elasticity of nanodrums near the phase transition*, Under Review, Preprint: arXiv:2309.09672

4. **Maurits J. A. Houmes**, Samuel Mañas-Valero, Alvaro Bermejillo-Seco, Eugenio Coronado, Peter G. Steeneken, Herre S. J. van der Zant, *Highly Anisotropic Mechanical Response of the Van der Waals Magnet $CrPS_4$*, Adv. Funct. Mater. 2023, 34, 2310206

3. **Maurits J. A. Houmes**, Gabriele Baglioni, Makars Šiškins, Martin Lee, Dorye L. Esteras, Alberto M. Ruiz, Samuel Mañas-Valero, Carla Boix-Constant, Jose J. Baldoví, Eugenio Coronado, Yaroslav M. Blanter, Peter G. Steeneken, Herre S. J. van der Zant, *Magnetic order in 2D antiferromagnets revealed by spontaneous anisotropic magnetostriction*, Nat. Commun. 2023, 14, 8503

2. Gabriele Baglioni, Makars Šiškins, **Maurits J. A. Houmes**, Martin Lee, Dong Hoon Shin, Samuel Mañas-Valero, Eugenio Coronado, Yaroslav M. Blanter, Herre S. J. van der Zant, Peter G. Steeneken, *Thermo-Magnetostrictive Effect for Driving Antiferromagnetic Two-Dimensional Material Resonators*, Nano Lett. 2023, 23, 15, 6973–6978

1. Martin Lee, Johannes R. Renshof, Kasper J. van Zeggeren, **Maurits J. A. Houmes**, Edouard Lesne, Makars Šiškins, Thierry C. van Thiel, Ruben H. Guis, Mark R. van Blankenstein, Gerard J. Verbiest, Andrea D. Caviglia, Herre S. J. van der Zant, Peter G. Steeneken, *Ultrathin Piezoelectric Resonators Based on Graphene and Free-Standing Single-Crystal BaTiO3*, Adv. Mater. 2022, 34, 2204630.